DISSERTATION

SELECTED TECHNIQUES IN RADIOECOLOGY: MODEL DEVELOPMENT AND COMPARISON FOR INTERNAL DOSIMETRY OF RAINBOW TROUT (*ONCORHYNCHUS MYKISS*) AND FEASIBILTIY ASSESSMENT OF REFLECTANCE SPECTROSCOPY USE AS A TOOL IN PHYTOREMEDIATION

Submitted by

Nicole Martinez

Department of Environmental and Radiological Health Sciences

In partial fulfillment of the requirements

For the Degree of Doctor of Philosophy

Colorado State University

Fort Collins, Colorado

Spring 2014

Doctoral Committee:

Advisor: Thomas E. Johnson

John E. Pinder III
Martine C. Duff
Wendy W. Kuhne
Alan K. Knapp

ABSTRACT

SELECTED TECHNIQUES IN RADIOECOLOGY: MODEL DEVELOPMENT AND COMPARISON FOR INTERNAL DOSIMETRY OF RAINBOW TROUT (*ONCORHYNCHUS MYKISS*) AND FEASIBILTIY ASSESSMENT OF REFLECTANCE SPECTROSCOPY USE AS A TOOL IN PHYTOREMEDIATION

Over the past five to ten years, public interest in nuclear energy, decommissioning, and waste management and stewardship has increased, leading to a renewed interest in radioecology (Kuhne 2012), or the study of the relationships between ionizing radiation and the environment (Whicker and Shultz 1982a). Several groups supporting collaborative radioecological research have recently been established, including the European Radioecology ALLIANCE in 2009 (Hinton et al. 2013), the Strategy for Allied Radioecology (STAR) network in 2011 (Kuhne 2012), and the National Center for Radioecology (NCoRE) in the United States in 2011 (Kuhne 2012). The earthquake, tsunami, and subsequent nuclear accident at Fukushima in March of 2011 further emphasized the importance of radioecology in providing timely and technically sound information (such as the transport and fate of radionuclides, potential doses and risks, etc.) for decision making in emergency response as well as in clean up and recovery (Kuhne 2012; Hinton et al. 2013) for both humans and their environment. Although the original and primary aims of the ICRP radiation protection recommendations have been to prevent deterministic effects and minimize stochastic effects to human beings from radiation exposure, the protection framework has recently been extended to include protecting the environment from harmful effects of radiation as well (ICRP 2007, 2008b, 2009).

Radioecology is an interdisciplinary science that encompasses a wide array of topics, including, among others, radiation transport, effects, risk assessment, and remediation (Whicker and Shultz 1982a; Hinton et al. 2013). I consider two topics from different areas of radioecology in this dissertation:

radionuclide uptake and dosimetry as well as an assessment of a technique for potential use in remediation.

Part 1 outlines the development of empirical and computational models for prediction of activity concentration and subsequent radiation dose, respectively, in relevant rainbow trout (*Oncorhynchus mykiss)* organs for selected radionuclides.

Radiation dose rates to biota are typically approximated utilizing dose conversion factors (DCF), which are values for absorbed dose rate per activity concentration in the body or organ (i.e. mGy d^{-1} per Bq g^{-1}). The current methodology employed by both the International Commission on Radiological Protection (ICRP) and within the Environmental Risks from Ionizing Radiation in the Environment (ERICA) Integrated Approach for calculating dose conversion coefficients is to use Monte Carlo modeling of a homogenously distributed radionuclide within an ellipsoidal phantom chosen to represent a particular organism. However, more accurate estimates can be made based on specific absorbed fractions and activity concentrations.

The first study in Part 1 examines the effects of lake tropic structure on the uptake of iodine-131 (^{131}I) in rainbow trout and considers a simple computational model for the estimation of resulting radiation dose. Iodine-131 is a major component of the atmospheric releases following reactor accidents, and the passage of ^{131}I through food chains from grass to human thyroids has been extensively studied. By comparison, the fate and effects of ^{131}I deposition onto lakes and other aquatic systems has been less studied. In this study we reanalyze 1960s data from experimental releases of ^{131}I into two small lakes and compare the effects of differences in lake trophic structures on ^{131}I accumulation in fish. The largest concentrations in the thyroids of trout (*Oncorhynchus mykiss*) may occur from 8 to 32 days post initial release. DCFs for trout for whole body as well as thyroid were computed using Monte Carlo modeling with an anatomically-appropriate model of trout thyroid structure. Activity concentration data was used in conjunction with the calculated DCFs to estimate

dose rates and ultimately determine cumulative radiation dose (Gy) to the thyroids after 32 days. The estimated cumulative thyroid doses at 32 days post-release ranged from 6 mGy to 18 mGy per 1 Bq mL^{-1} of initial ^{131}I in the water, depending upon fish size**.**

The subsequent studies in Part 1 seek to develop and compare different, increasingly detailed anatomical phantoms for *O. mykiss* for the purpose of estimating organ radiation dose and dose rates from ^{131}I uptake and from molybdenum-99 (^{99}Mo) uptake. Model comparison and refinement is important to the process of determining both dose rates and dose effects, and we develop and compare three models for *O. mykiss*: a simplistic geometry considering a single organ, a more specific geometry employing anatomically relevant organ size and location, and voxel reconstruction of internal anatomy obtained from CT imaging (referred to as CSUTROUT). Dose Conversion Factors (DCFs) for whole body as well as selected organs of *O. mykiss* were computed using Monte Carlo modeling, and combined with the empirical models for predicting activity concentration, to estimate dose rates and ultimately determine cumulative radiation dose (μGy) to selected organs after several half-lives of either ^{131}I or ^{99}Mo. The different computational models provided similar results, especially for organs that were both the source and target of radiation (less than 30% difference between estimated doses). Although CSUTROUT was the most anatomically realistic phantom, it required much more resource dedication to develop than did the stylized phantom for similar results. Additionally, the stylized phantom can be scaled to represent trout sizes whereas CSUTROUT cannot be. There may be instances where a detailed phantom such as CSUTROUT is appropriate, as it will provide the most accurate radiation dose and dose rate information, but generally, the stylized phantom appears to be the best choice for an ideal balance between accuracy and resource requirements.

Part 2 considers the use of reflectance spectroscopy as a remediation tool through its potential to determine plant stress from metal contaminants. Reflectance spectroscopy is a rapid and non-destructive analytical technique that may be used for assessing plant stress and has potential

applications for use in remediation. Changes in reflectance such as that due to metal stress may occur before damage is visible, and existing studies have shown that metal stress does cause changes in plant reflectance. The studies in Part 2 further investigate the potential use of reflectance spectroscopy as a method for assessing metal stress in plants.

In the first study, *Arabidopsis thaliana* plants were treated twice weekly in a laboratory setting with varying levels (0 mM, 0.5 mM, or 5 mM) of cesium chloride (CsCl) solution, and reflectance spectra were collected every week for three weeks using an ASD FieldSpec Pro spectroradiometer with both a contact probe and a field of view probe at 36.8 and 66.7 cm above the plant. As metal stress is known to mimic drought stress, plants were harvested each week after spectra collection for determination of relative water content and chlorophyll content. A visual assessment of the plants was also conducted using point observations on a uniform grid of 81 points. Two-way ANOVAs were performed on selected vegetation indices (VI) to determine the significance of the effects of treatment level and length of treatment. Linear regression was used to relate the most appropriate vegetation indices to the aforementioned endpoints and to compare results provided by the three different spectra collection techniques. One-way ANOVAs were performed on selected VI at each time point to determine which, if any, indices offered a significant prediction of the overall extent of Cs toxicity. Of the 14 vegetation indices considered, the two most significant were the slope at the red edge position (SREP) and the ratio of reflectance at 950 nm to the reflectance at 750 nm (R_{950}/R_{750}). Contact probe readings and field of view readings differed significantly. Field of view measurements were generally consistent at each height.

The second study investigated the potential use of reflectance spectroscopy as a method for assessing metal stress across four different species of plants, namely *Arabidopsis thaliana, Helianthus annuus, Brassica napus* var. *rapa,* and *Zea mays.* The purpose of this study was to determine whether a quantifiable relationship exists between reflectance spectra and lithium (Li) contamination in each

species of plant considered, and if such a relationship exists similarly across species. Reflectance spectra were collected every week for three weeks using an ASD FieldSpec Pro Spectroradiometer with a contact probe and a field of view probe for plants treated twice weekly in a laboratory setting with 0 mM or 15 mM of lithium chloride (LiCl) solution. Plants were harvested each week immediately after spectra collection for determination of relative water content and chlorophyll content. Linear regression was used to relate the most appropriate vegetation indices (determined by the Pearson correlation coefficient) to the aforementioned endpoints and to compare results provided by the different spectra collection techniques. Two-way ANOVAs were performed on 12 selected vegetation indices (VI) for each species individually to determine the significance of the effects of treatment level and length of treatment on a species basis. Balanced ANOVAs were conducted across all species to determine significance of treatment, time, and species. LiCl effects and corresponding reflectance shifts were significant for *A. thaliana,* but *Z. mays* and *H. annuus* showed little response to LiCl at the treatment level considered in this study, with no significant differences in relative water content or chlorophyll content by treatment level. *B. rapa* reflectance spectra responded similarly to Li exposure as *Z. mays,* but *B. rapa* did have significant differences in relative water content by treatment level. All species demonstrated a potential stimulatory effect of LiCl, with at least one week of increased reflectance in the near-IR. Different VI proved to be the best predictor of endpoint values for each species, with only SIPI and the ratio of reflectance at 1390 nm to the reflectance at 1454 nm (R_{1390}/R_{1454}) common between species. The most significant VI considering all species together was SIPI, although *A. thaliana* effects dominate this result. VI determined separately by CP and FOV were occasionally well-related, but this relationship was inconsistent between species, further supporting the conclusion in the previous study that CP and FOV are not interchangeable. These techniques should either be used as compliments or independently, depending on the application.

ACKNOWLEDGEMENTS

Part 1: The author was supported in part by the CDC/NIOSH Mountain & Plains Educational and Research Center (NIOSH grant number: T42 OH009229-06). The contents herein, however, are solely the responsibility of the author and do not represent the official views of the CDC, NIOSH and MAP ERC. Model computations were performed using the computer resources of the Rocky Mountain Center for Nuclear Computations, Department of Environmental and Radioactive Health Sciences, Colorado State University or on the CRAY CX1 super computer at the Human Monitoring Laboratory, Health Canada, Ottawa, Canada. The author respectfully wishes to acknowledge her immense debt to J.R. Donaldson, S. Kolehmainen, J.K. Miettinen, P.R. Olson, R.F. Palumbo, F.Z. Short, and S. Takatalo, without whose innovative and comprehensive research the present analysis could not have been performed. Additionally: Rafe McBeth, Kevin Capello, Jenelle Parson, Elizabeth Ruedig, Lauren Nagle, David Connick, Katy Swancutt, Chris Schmit, F. Ward Whicker, Daniel Kraus (Daniel's XL Toolbox, version 6.22), Jeanne Brockway, Jean Runyan, Julie Asmus. Part 2: The author would like to respectfully acknowledge Clay Stafford, Eric Caldwell, Erica Stieve-Caldwell, Amanda Wright, and Nate Creazzo for their significant contributions to this work. This project was conducted in conjunction with work accomplished under Contract No. DE-AC09-08SR22470 with the U.S. Department of Energy. This work is supported by U.S. DOE—National Nuclear Security Administration through the Office of Defense Nuclear Non proliferation Research and Development—NA-22 (Grant No. DE-FG52-05NA27035). The author was also partially supported by the post-9/ll GI bill administered by the Veterans' Administration.

In general, incredible support, encouragement, and mentorship has been provided by so many in my life, but especially: my family and friends, everyone in John Till's Risk Assessment group, the yogis and yoginis at Aiken Yoga, the group fitness staff at CSU Campus Recreation and Raintree Athletic Club, and of course, my committee members.

TABLE OF CONTENTS

PART 1: ESTIMATING ORGAN DOSE IN RAINBOW TROUT (*ONCORHYNCHUS MYKISS*) FROM UPTAKE OF SELECTED RADIONUCLIDES

EXECUTIVE SUMMARY

Iodine-131 (^{131}I) is a major component of the atmospheric releases following reactor accidents, and the passage of ^{131}I through food chains from grass to human thyroids has been extensively studied. By comparison, the fate and effects of ^{131}I deposition onto lakes and other aquatic systems has been less studied. The first study: (1) reanalyzes 1960s data from experimental releases of ^{131}I into two small lakes; (2) compares the effects of differences in lake trophic structures on the accumulation of ^{131}I by fish; (3) relates concentrations in fish and fish tissues to that in the water column using empirically estimated uptake (L kg^{-1} d^{-1}) and loss (d^{-1}) parameters; and (4) shows that the largest concentrations in the thyroids of rainbow trout (*Oncorhynchus mykiss*) may occur from 8 to 32 days after initial release. ^{131}I concentration in trout thyroids at 30-days post release may be > 1,000 times that in the water. Estimates of cumulative radiation dose (mGy) to thyroids computed using an anatomically-appropriate model of trout thyroid structure within the Monte Carlo N-particle modeling software predicted cumulative thyroid doses that increased approximately linearly after the first 8 days and resulted in 32-day cumulative thyroid doses that ranged from 6 mGy g^{-1} to 18 mGy g^{-1} per 1 Bq mL^{-1} of initial ^{131}I in the water depending upon fish size. The majority of this dose is due to beta emissions, and the dose varies with positions in the thyroid tissue.

Subsequent studies seek to develop and compare different, increasingly detailed anatomical phantoms for *O. mykiss* for the purpose of estimating organ radiation dose and dose rates from ^{131}I uptake and from molybdenum-99 (^{99}Mo) uptake in multiple organs. Model comparison and refinement is important to the process of determining both dose rates and relating these dose rates to dose effects. Therefore, we develop and compare three models for *O. mykiss*: a simplistic geometry considering a single organ, a more specific geometry employing anatomically relevant organ size and location, and voxel reconstruction of internal anatomy obtained from CT imaging (referred to as CSUTROUT). Dose

Conversion Factors (DCFs) for whole body as well as selected organs of *O. mykiss* were computed using Monte Carlo modeling, and combined with the empirical models for predicting activity concentration, to estimate dose rates and ultimately determine cumulative radiation dose (μGy) to selected organs after several half-lives of either ^{131}I or ^{99}Mo. The different computational models provided similar results, especially for organs that were both the source and target of radiation (less than 30% difference between estimated doses). Although CSUTROUT was the most anatomically realistic phantom, it required much more resource dedication to develop than did the stylized phantom for similar results. Additionally, the stylized phantom can be scaled to represent trout sizes whereas CSUTROUT cannot be. There may be instances where a detailed phantom such as CSUTROUT is appropriate, as it will provide the most accurate radiation dose and dose rate information, but generally, the stylized phantom appears to be the best choice for an ideal balance between accuracy and resource requirements.

CHAPTER 1: INFLUENCE OF LAKE TROPHIC STRUCTURE ON ^{131}I ACCUMULATION IN TROUT THYROIDS WITH CORRESPONDING ESTIMATION OF WHOLE BODY AND THYROID RADIATION DOSE*

1. Introduction

1.1. Radioiodine in the environment

Reactor accidents and above-ground nuclear detonations release iodine isotopes, notably ^{131}I, into the atmosphere with subsequent deposition onto terrestrial, aquatic and marine ecosystems at both regional and global scales (e.g. Crick and Linsley 1984; National Cancer Institute 1999; Gomez-Guzman et al. 2013; Tang and Guo 2012). The fate of this deposition onto terrestrial systems has received most of the research interest because of the sensitivity and efficiency of the grass-cow-milk-child food chain and the resulting dose to relatively radiosensitive child thyroids (National Cancer Institute, 1999).

Aquatic ecosystems may also be sensitive to ^{131}I depositions because of the typically small iodine concentrations in fresh waters, i.e. ≤7 μg L^{-1}, (Poston and Klopfer 1986; Coughtrey et al. 1983; Tiffany et al. 1969; Vanderploeg et al. 1975) and the metabolic requirements for iodine in many aquatic organisms, especially fish. Concentrations of stable iodine in seawater (~60 μg L^{-1}, Poston and Klopfer 1986; Coughtrey et al. 1983) are much higher than those in freshwater systems, and the decreasing concentrations of stable iodine in fish tissues from marine to anadromous to freshwater species indicates that iodine levels in fish muscle are influenced by ambient iodine concentrations (Vanderploeg et al. 1975).

Thyroid hyperplasia (a marked increase in thyroid size and/or activity) was seen in spawning Lake Michigan rainbow trout, but was not seen in either spawning anadromous (steelhead) rainbow trout or in spawning Lake Superior trout that had access to food and water supplemented with iodine.

* Martinez NE, Johnson TE, Pinder JE III. 2014. Influence of lake trophic structure on Iodine-131 accumulation and subsequent cumulative radiation dose to trout thyroids. Journal of Environmental Radioactivity, 131:62-71.

The above evidence suggests that the observed thyroid hyperplasia was due to ambient iodine concentrations < 1.5 µg L^{-1} (Coughtrey et al. 1983; Robertson and Chaney 1953).

The current recommended whole-body iodine concentration ratios are considerably larger for freshwater species than marine species: ~100-400 L kg^{-1} (depending on trophic level) for freshwater species (Yankovich et al. 2013) and 9 L kg^{-1} for marine species (ICRP 2009), suggesting that freshwater species are likely to have considerably higher uptake in response to an acute release of iodine.

The rapid assimilation of ^{131}I by fish following an accidental release is demonstrated by Kryshev (1995) for Kiev Reservoir (Figure 1.1) where ^{131}I concentrations in the reservoir water 5 days following the Chernobyl accident were > 300 Bq L^{-1} and the concentrations in fish muscle were already more than 10 times that in the water.

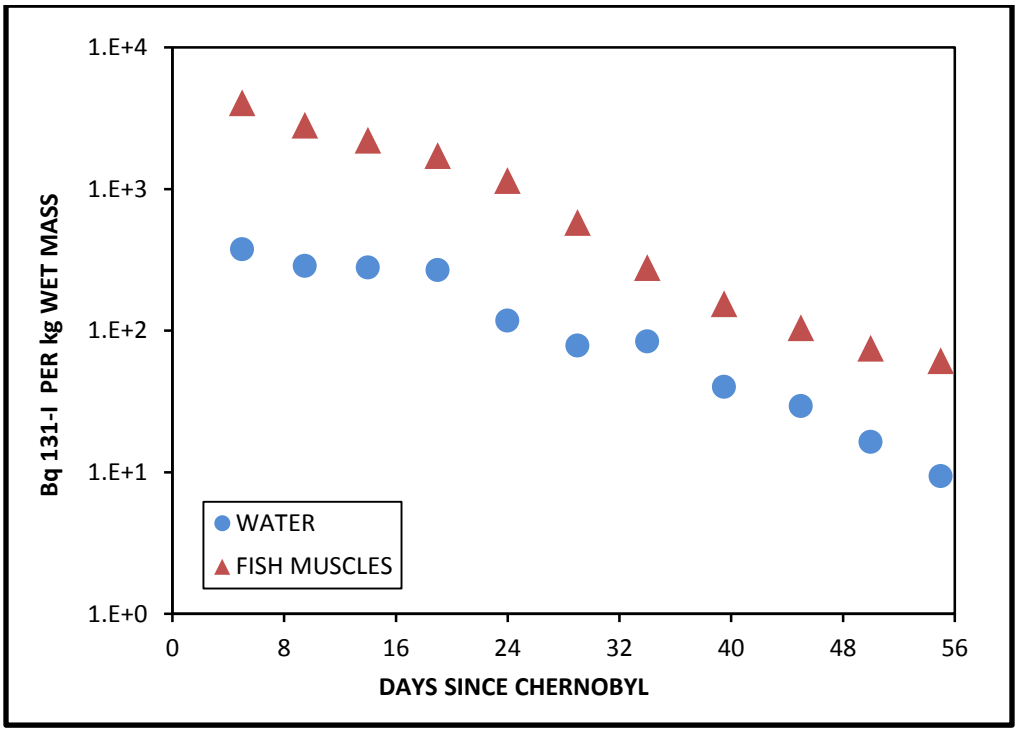

Figure 1.1: ^{131}I in Kiev Reservoir. The wet mass concentrations of ^{131}I in water and fish muscles in the Kiev Reservoir in the days following the Chernobyl accident. After day 25, both water and muscle concentrations are declining at rates similar to that for the radioactive decay of ^{131}I.

Moreover, the iodine concentration in fish thyroids may be many times that in fish muscle (Vanderploeg et al. 1975), and this suggests the possibility that fish thyroids may be receiving damaging or destructive radiation exposures.

Rapid accumulation of radioactive iodine in fish thyroids with resulting degradation of thyroid-mediated functions has been demonstrated for juvenile rainbow trout (*Oncorhynchus mykiss*, the modern synonym for *Salmo gairdnerii*), who accumulated as much as 17% of intraperitoneal injections of 3.7 MBq ^{131}I in their thyroid regions. Following six such monthly injections these fish showed reduced growth rates, reduced skeletal calcification, and absence of sexual development (LaRoche et al. 1965, 1966). Fish on iodine supplemented diets that received similar injections accumulated 3-5% of the ^{131}I in the thyroid region and did not display similar reductions in the thyroid mediated functions. Although there is no dosimetry for this study, comparison of thyroid uptake of ^{131}I provides evidence that fish in environments with higher naturally occurring levels of stable iodine are less vulnerable to the deleterious effects of ^{131}I exposure, i.e., marine or even anadromous fish. To what extent similar damage occurs as a result of ^{131}I deposition on to natural systems depends on the cumulative thyroid dose per Bq of deposited ^{131}I.

Although the fate of ^{131}I deposition onto aquatic systems and their watersheds has received considerable study (Bird et al. 1995a; Bird et al. 1995b; Bird and Schwartz 1996; Gilfedder et al. 2009; Gilfedder et al. 2010), the resulting doses to aquatic organisms have received far less attention. This may be due to the rapid decay of ^{131}I (half-life = 8.041 days; ICRP 2008a) and the perceived limited time for meaningful doses to accumulate.

1.2. Study objectives

In this study we (1) review and reanalyze data on iodine isotopes introduced by accidental releases or purposeful experimental studies into aquatic systems to determine the likely cumulative dose to the thyroid of rainbow trout and (2) relate these doses to properties of the aquatic systems such

as food chain complexity. The study comprises four integrated components: (1) empirical models are developed for these systems to describe the temporal patterns of ^{131}I concentrations in water, plants, invertebrates, fish, and specific fish tissues, especially trout thyroids; (2) the radiation dose rate to thyroids as a function of ^{131}I concentrations (i.e. dose conversion factor; mGy d^{-1} per Bq g^{-1}) is estimated using Monte Carlo simulation in an anatomically appropriate model of rainbow trout thyroid tissue; (3) the dose rate per Bq g^{-1} from the Monte Carlo simulation is applied to the temporal patterns of ^{131}I concentrations in trout thyroids to estimate cumulative thyroid dose per initial ^{131}I Bq mL^{-1} in the water; and (4) cumulative doses from hypothetical and historical cases of ^{131}I contamination were evaluated for their potential to affect trout development and survival.

The current methodology employed by the ICRP and within the ERICA Integrated Approach for approximating radiation dose rates to biota calculates whole body dose conversion factors (DCFs) assuming homogenous distribution of radionuclide within an ellipsoidal phantom, with organs modeled as spheres within the ellipsoid, if included (ICRP 2008b; Gómez-Ros et al. 2008). Organ specific DCFs may be conservatively approximated using mass ratios, although this may considerably overestimate the organ dose (Gómez-Ros et al. 2008). A similar approach is taken in this study; however, we have the benefit of specific anatomical dimensions and activity concentration data and can calculate organ specific DCFs directly.

1.3. Thyroid tissue in fish

Fish thyroid tissue shows various arrangements of location, structure and activity levels. Thyroid tissues may be located in or near the mandible as in other vertebrates (Raine et al. 2005; Singh 1968; Tarrant 1971), near the eyes, or in the kidneys. Thyroid tissue may be nearly absent with its functions assumed by kidney tissues (Geven et al. 2007). It may be simultaneously located in both the mandible and the kidneys with varying levels of thyroid activity between these locations (Chavin and Bouman 1965). Even when located near the mandible as in other vertebrates, it may occur as separate individual

nodules (or tubules) or as clusters of nodules (Raine et al. 2005; Raine and Leatherland 2000; Singh 1968). These variations among and within species have complicated the analysis of ^{131}I accumulation and the estimation of ^{131}I concentrations and concentration ratios for fish.

1.3.1. Sampling fish thyroid tissue

To ensure adequate sampling of thyroid tissue, some studies removed tissue from the mandible area that contained both thyroid and non-thyroid tissue. These samples were described as "thyroid area" samples, and the concentration of ^{131}I in these "thyroid area" samples probably underestimated the ^{131}I concentrations of the true thyroid tissues.

1.3.2. Rainbow trout thyroid activity confined to the mandible area

For rainbow trout immersed in various solutions containing ^{131}I (Hunn and Fromm 1966), the absorbed ^{131}I was concentrated in the mandible area. There was no indication of ^{131}I deposition in the kidneys or other tissues, and this suggests that the mandible area is the only location with active thyroid tissue for this species.

1.4. Data sources for the development of empirical models

Data from two whole-lake studies, Kolehmainen et al. (1969) and Short et al. (1969), were used to develop empirical models relating ^{131}I concentrations in aquatic biota, fish, and fish tissues to time since deposition into the system. Both of these studies involved the experimental release of ^{131}I into small, natural lakes.

1.4.1. Lake Pitkannokanlampi

Kolehmainen et al. (1969) released 6.3×10^{8} Bq of carrier-free ^{131}I into Lake Pitkannokanlampi, a 0.52 ha oligotrophic Finnish lake, with the objective of determining the distribution of the ^{131}I among the lake's water and biota as a function of the time since release. The lake had surface water temperatures of 12 °C, stable iodine concentrations of 3.0 μg L^{-1}, and a simple foodchain (Kolehmainen et al. 1969) of crucian carp (*Carassius carassius*) feeding on green algae (*Oedogonum* sp.). The released ^{131}I was mixed

with surface waters, and the concentrations (i.e. Bq per unit dry mass) of ^{131}I in water, algae, and whole fish were measured periodically for 26, 26, and 40 days, respectively. The data from this study were obtained using interpolation from enlargements of graphics in the published paper.

1.4.2. Fern Lake

Short et al. (1969) released 1.39×10^{11} Bq of carrier-free ^{131}I into Fern Lake, a 9.7 ha, oligotrophic lake near Seattle, Washington in the United States. The lake had surface water temperatures of 22 °C and stable iodine concentrations of < 4 μg L^{-1}. This lake had (1) a more complex biotic community than that of Lake Pitkannokanlampi composed of algae (*Nitella flexis*), amphipods (*Gammarus* sp.), crayfish (*Pacifastacus leniusculus*), and rainbow trout and (2) more complex food chains composed of multiple pathways of ^{131}I movement from the water to the trout. The ^{131}I concentrations (i.e. Bq per unit wet mass) in the water as well as the gills, gastrointestinal (GI) tract, liver, muscle and thyroid tissues of the trout were measured for 28 days. However, the thyroid tissue, as defined and acknowledged by Short et al. (1969) involved "thyroid area" sampling which was necessitated by the difficulty in identifying and separating thyroid tissues from the surrounding tissues. Thus, the reported ^{131}I concentrations for thyroids are probable underestimates of the ^{131}I concentrations in true thyroid tissues. Data from this study were obtained from tables or interpolated from enlargements of graphics in the published paper with the exception that data for fish tissues on day 13 were not used. Fish data on this date were unexplainably ~10X greater than those for both the preceding and following sample dates.

The Fern Lake study also involved the release of 2.2×10^{8} Bq of carrier-free ^{131}I into a 75 L aquarium facility where the biota were confined to cages and could only accumulate ^{131}I by absorption from the water column. The aquarium was maintained at 11.5 °C with stable iodine concentrations < 4 μg L^{-1}. The ^{131}I concentrations in the water, biota and the gills, gastrointestinal tract, liver, muscle and "thyroid area" of the trout were measured periodically for 27 days, and data were obtained from tables or interpolated from enlargements of graphics in the published paper.

2. Materials and methods

2.1. Development of empirical models

Computing an accumulated dose over time to a fish thyroid, or other tissues or biota, requires some form of tabulation, equation, or model that describes the temporal concentration of the radionuclide in that organ. We fitted empirically-derived models to the data obtained from tables and figures in the publications to describe the ^{131}I concentrations in biota and their tissues.

2.1.1. Structure of the empirical model

The following simple uptake and loss rate model was used to model the time varying concentrations of ^{131}I in biota, fish, and fish tissues:

$$\frac{dB(t)}{dt} = \mu \cdot W(t) - k \cdot B(t) \qquad (1\text{-}1)$$

where μ is an uptake constant with units L kg^{-1} d^{-1}, k is a first-order loss rate constant with units d^{-1}, $W(t)$ is the ^{131}I concentration in water, and $B(t)$ is the ^{131}I concentration in biota, whole fish or specific fish tissues. Similar models have been used by Pinder et al. (2009, 2011), Smith et al. (2002), and Thomann (1981) to describe the time-varying radionuclide concentrations in biota. The approach of Eq. 1 has also been used to predict isotope movements through lake food webs (Monte et al. 2003) in the models AQUASCOPE (Smith et al. 2005) and ECOPRAQ (Comans et al. 2001).

The parameters μ and k in Equation 1-1 will be referred to as uptake and loss rather than absorption and elimination because their estimated values may measure more than just physiological processes. For algae, which absorb ^{131}I directly from the water column, μ is an estimate of an absorption rate. For animal biota, μ is not a measure of absorption from the water column or absorption from ingestion of what has been consumed. Rather, it is a measure of the transfer of the radionuclide through the food chain pathways from the water to animal, and the factors affecting μ become increasingly complex with increases in the number of trophic levels and increases in the number of

alternative pathways from the water to the consumer (Pinder et al. 2009). Despite the number of factors affecting μ for consumers, the model has been shown to be able to accommodate these complexities for top predators such as pike (*Esox lucius*; Smith et al. 2002) as well as trophic levels extending from zooplankton, snails, aquatic insect larvae, to fish species of varying trophic levels (Pinder et al. 2011). For whole-body ^{131}I concentrations, k is a measure of loss that incorporates radioactive decay, excretion, as well as losses from the population due to mortality or emigration (Pinder et al. 2009). Losses due to mortality or emigration should be negligible within the short durations of these studies that were performed in mostly confined locations, and the estimated k should be dominated by radionuclide decay and excretion.

When the model is applied to individual fish tissues, the parameters μ and k have different interpretations. The parameter μ may represent (1) increases in ^{131}I concentrations due to absorption and ingestion of additional ^{131}I or (2) the transfer of ^{131}I from other tissues. The parameter k, besides including losses due to radioactive decay and excretion, also includes transfer to other tissues.

2.1.2. Procedures for estimating μ and k in the empirical models

The estimation of μ and k involved a two-step process. First, the declines in ^{131}I concentrations in water following the experimental additions were approximated using a single-component exponential equation (Whicker and Shultz 1982) of the form:

$$W(t) = a \cdot e^{-bt} \tag{1-2}$$

where $W(t)$ is the ^{131}I concentration in water at time t, a is the initial ^{131}I concentration in the water at the time of experimental or accidental release (*i.e.*, t = 0), and b is the rate constant (d^{-1}) for the exponential decline in $W(t)$. In the second step, estimates of μ and k are obtained by fitting the following equation (Whicker and Shultz, 1982) to the time series of ^{131}I concentrations measured in biota or tissues (see Appendix A1 for derivation):

$$B(t)=\left(\frac{\mu\cdot a}{k-b}\right)\left(e^{-bt}-e^{kt}\right)+B(0)e^{-kt} \tag{1-3}$$

where *a* and *b* are from Equation 1-2. In applying Equation 1-3, the initial ^{131}I concentrations in the fish (i.e. *B*(0)) have been treated as negligible. For this study, estimates of *a*, *b,* μ and *k* parameters and their asymptotic standard errors (SE) were obtained using the PROC NLIN procedure of SAS software (SAS Institute, 1989). In addition to the estimates of μ and *k*, two other metrics of the model are important. The first is the time to the maximum value of $B(t)$, and the second is the value of the concentration $B(t)$ at the time of this maximum. We calculate this by determining the value of *t* for which the derivative of $B(t)$ is equal to zero (Equation 1-4 and Equation 1-5):

$$\dot{B}(t)=\left(\frac{\mu\cdot a}{k-b}\right)\left(-be^{-bt}+ke^{kt}\right)=0 \tag{1-4}$$

$$\Rightarrow t_{\max}=\frac{\ln\frac{b}{k}}{b-k} \tag{1-5}$$

2.1.3. Development of empirical models for Lake Pitkannokanlampi

The estimated parameters of *a* and *b* for the Lake Pitkannokanlampi water model were 18 Bq L^{-1} and 0.103 d^{-1}, respectively. The models for algae and carp showed good fit to the data with R^2 = 0.986 and 0.988, respectively. Estimates ($\pm$ SE) for μ and *k* for algae were 4710 $\pm$ 751 L kg^{-1} d^{-1} and 0.802 $\pm$ 0.147 d^{-1}, respectively, and estimates ($\pm$ SE) for μ and *k* for the carp were 47.8 $\pm$ 5.19 L kg^{-1} d^{-1} and 0.170 $\pm$ 0.0243 d^{-1}, respectively. Figure 1.2 illustrates ^{131}I concentrations in water, algae, and carp for Lake Pitkannokanlampi (data from Kolehmainen et al. 1969) along with the model predictions developed from the parameters listed above.

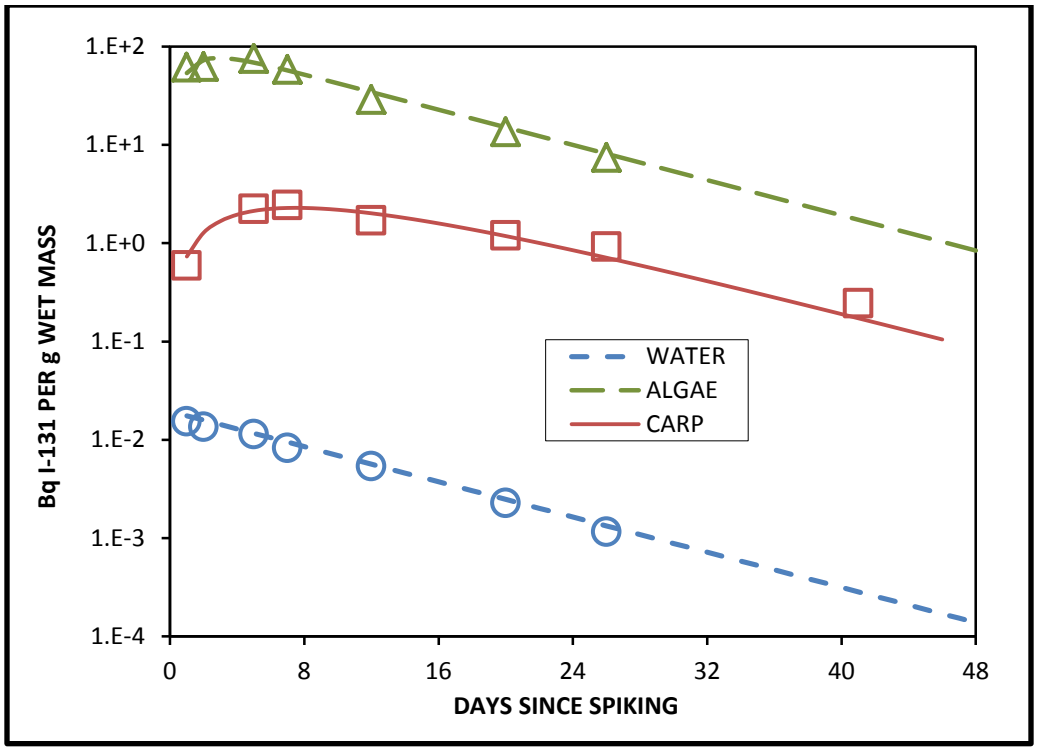

Figure 1.2: ^{131}I in Lake Pitkannokanlampi. The ^{131}I dry mass concentrations in water, algae (Oedogonum sp.) and crucian carp (Carassius carassius) in the days following the release of ^{131}I into Lake Pitkannokanlampi in Finland. The data are from Kolehmainen et al. (1969).

For this simple water-algae-carp food chain, the maximum concentrations for algae and carp occurred before the first half-life of ^{131}I had past. Maximum algae concentrations predicted by the model were 84.4 Bq g^{-1} on day 3. Maximum predicted concentrations for carp were 2.82 Bq g^{-1} on day 7. By day 24, the concentrations of water, algae and carp approached an apparent transient steady state with rates of decline dominated by the physical decay rate of ^{131}I. Although whole-body concentrations for carp approached a transient steady state with the concentrations for water and algae, questions remain concerning the possible internal redistribution of ^{131}I among the carp's internal organs.

Development of empirical models for the Fern Lake aquarium and lake studies

Figure 1.3Figure 1.3 compares the model fits to water, gastrointestinal tract and thyroids (i.e. "thyroid area") of trout in the aquarium, where only absorption of ^{131}I from the water column can occur, and in the lake where ^{131}I accumulation can occur either by absorption or ingestion.

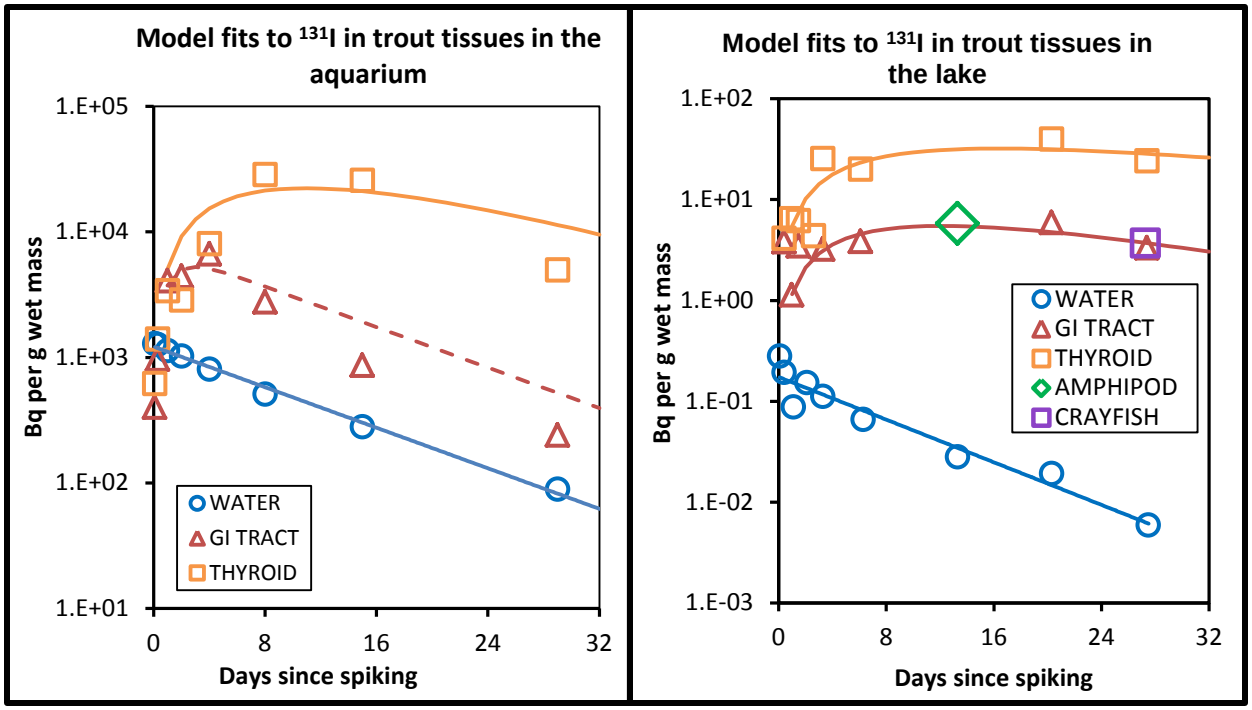

Figure 1.3: ^{131}I in Fern Lake Studies. A comparison of the results and the model fits to water, and the gastrointestinal tracts and thyroids of trout in the aquarium, where only absorption of ^{131}I from the water column can occur, and in the lake, where ^{131}I accumulation can occur either by absorption or ingestion.

In neither environment did a transient steady state occur between the concentrations in the thyroids and the water within 32 days following the ^{131}I release. The fits of the models to the tissue data may be expected to be less accurate than the fits to a fish's whole-body because of the potential internal redistribution of ^{131}I among the different tissues adds an additional source of variation not present in the simpler whole-body data. The R^2 for the aquarium and lake thyroid tissues were 0.867 and 0.915, respectively.

The model's maximum predicted ^{131}I concentrations in "thyroid area" tissues of 22,300 Bq g^{-1} for the aquarium and 32.0 Bq g^{-1} for the lake did not occur until 11 and 16 days after the release. The greater concentrations for thyroids in the aquarium reflect the greater initial ^{131}I concentration in the aquarium water ($a_{lake} = 0.183$ Bq mL^{-1} versus $a_{aquarium} = 1.221$ Bq mL^{-1}). The ratios of concentrations in thyroids to that in water for these days of maximum concentration were 51 and 1,296 L kg^{-1} for the

aquarium and lake, respectively. The greater ratio for the lake reflects the respective estimates (± SE) for $\mu_{thyroid}$ of 4.53 (± 1.42) L kg^{-1} d^{-1} for the aquarium and 33.9 (± 8.54) L kg^{-1} d^{-1} for the lake.

The estimated *k* and the corresponding turnover times for thyroids also differed between the aquarium and the lake. The estimated $k_{thyroid}$ (± SE) in the aquarium was 0.0897 (± 0.0469) d^{-1} which was not significantly different from the radioactive decay rate for ^{131}I. The rate for the lake was 0.0276 (± 0.0197) d^{-1} with an estimated turnover time for ^{131}I in the thyroid of 25.1 days. All of the *k* estimations for the trout tissues in the aquarium were equal to or greater than the 0.0862 d^{-1} decay rate for ^{131}I, while all of the *k* estimations for the trout tissues in the lake were less than 0.0862 d^{-1} (Table 1.1 and Table 1.2).

Table 1.1: The water parameters a, the initial concentration in the water, and b, the first order loss rate from the water column, for the ^{131}I concentrations in the reservoirs, lakes and aquaria included in this analysis. Because of the different methods of estimation 95% confidence intervals are given for a while standard errors are given for b.

Water Body	Initial Water Concentration (Bq L^{-1})		Loss Rate (d^{-1})	
	a	95% Confidence Interval	*b*	SE
Kiev Reservoir	715	518 - 1675	0.0736	0.005
Lake Pitkannokanlampi	18	16 - 19	0.103	0.002
Fern Lake	183	130 - 258	0.122	0.012
Fern Lake – Aquarium	1221	1116 - 1335	0.0929	0.003

Table 1.2: The uptake (μ) and loss rate parameter (k) for biota and fish tissues and their standard errors for the lakes and aquaria included in this study.

Water Body Biotic Component	Uptake Parameter (L kg^{-1} d^{-1}) *μ*	SE	Loss Rate (d^{-1}) *k*	SE
Lake Pitkannokanlampi				
Algae (*Oedogonium* sp.)	4710	751	0.802	0.147
Sponge (*Spongilla lacustris*)	1717	191	0.242	0.035
Lily (*Nuphar luteum*)	514	72.3	1.01	0.163
Carp (*Carassius carassius*)	47.8	5.19	0.170	0.0243

Fern Lake - Aquarium				
Rainbow Trout (*Oncorhynchus mykiss*)				
Gills	13.3	3.33	0.367	0.121
Liver	6.50	3.40	1.06	0.662
Gastrointestinal tract	4.81	1.61	0.854	0.348
Thyroid	4.53	1.42	0.090	0.047
Fern Lake – Lake				
Rainbow Trout				
Gills	4.63	0.520	0.0581	0.0109
Liver	3.76	0.556	0.0201	0.0148
Gastrointestinal tract	7.25	1.55	0.0520	0.0200
Thyroid	33.9	8.54	0.0276	0.0197

As only absorption of ^{131}I from the water column occurs in the aquarium, concentrations in trout tissues other than the thyroid increase rapidly at first but decline at rates faster than in the lake. The observed decline rate for the gastrointestinal tract in the aquarium was faster than the model's prediction for days > 8. Faster than predicted loss rates after day 8 similar to those for gastrointestinal tract also occurred for liver, gill and muscle tissues. These faster than predicted rates coupled with the slower decline rates for the thyroid suggest that the assimilated ^{131}I was becoming preferentially concentrated in the thyroid. It would require whole-body measures of ^{131}I to evaluate the proportions of the ^{131}I being retained preferentially in the thyroid or being lost to excretion

The difference between the temporal patterns illustrated for gastrointestinal tracts and thyroids in the aquarium and those in the lake in Figure 1.3 are due to the continued assimilation of ^{131}I by trout from prey items containing ^{131}I. This is most clearly illustrated by the correspondence of the predicted ^{131}I concentrations in the gastrointestinal tract with those for amphipods at day 13 of 5.8 Bq g^{-1} and crayfish at day 27 of 3.7 Bq g^{-1} (Short et al., 1969). The predicted GI tract concentrations for these days were 5.5 and 3.8 Bq g^{-1}, respectively.

Short et al. (1969) only report ^{131}I concentrations for amphipods and crayfish for these days because these were the days of maximum observed concentrations, which implies that ^{131}I was still

being retained and accumulated by these biota up to this point despite the losses of ^{131}I from the lake due to radioactive decay.

The (1) tissue loss rates for k in the lake being less than the isotope decay rate, (2) the longer times to maximum ^{131}I concentrations in trout tissues for the lake, (3) the continuing presence of ^{131}I in food items, and (4) the correspondence of concentrations for food items and those for the gastrointestinal tract imply that the maximum concentrations for trout tissues and the persistence of larger concentrations in Fern Lake are due, at least in part, to the continuing persistence of ^{131}I in intermediate organisms in the complex food chains leading to trout. This result is analogous to the greater accumulation of PCB concentrations by lake trout (*Salvelinus namaycush*) feeding on more diverse and complex food webs (Rasmussen et al. 1990).

Although variations among lakes in water temperature, stable iodine content, food chain complexity, and other factors may affect the values of μ and k, the estimates of 33.9 ($\pm$ 8.54) L kg^{-1} d^{-1} and 0.0276 ($\pm$ 0.0197) d^{-1} from Fern Lake are, at present, the best available estimates of ^{131}I accumulation and loss for thyroids of free-swimming fish in impacted environments and will be used in subsequent assessments of ^{131}I radiation dose to rainbow trout thyroids. It should also be noted that μ and k in this analysis have been estimated for yearling fish of approximately 0.20 m in length, and fish of differing sizes may demonstrate alternative values of these parameters.

2.2. Development of MCNP simulation

The structure, arrangement, and composition of rainbow trout thyroid tissue was modeled within the Monte Carlo N-particle (MCNP) transport code, version 5.1.60 (Briesmeister 2000; X-5 Monte Carlo Team 2003), to appropriately model radiation transport through said tissue. The resultant tabulation of energy deposition was then combined with empirically derived ^{131}I concentrations in the "thyroid area" to determine radiation dose to thyroid tissues.

2.2.1. Modeling the follicle structure of rainbow trout thyroid tissue

Thyroid tissue, as it occurs in juvenile rainbow trout of approximately 9 cm in length, consists of follicles (or tubules) formed by an exterior tissue layer of epithelial cells surrounding a fluid-filled lumen. These follicles may occur singularly or in clusters and are of irregular sizes; diameters of follicles range from < 0.05 mm to > 0.25 mm) (Raine et al. 2005). These clusters occur intermittently along the ventral aorta (Raine et al. 2005), spanning a total length of about 2.7 mm.

Thyroid tissues were simplified into uniformly sized tubules within the MCNP program. Each tubule was made up of two concentric cylinders: an inner cylinder representing the lumen, with length 0.88 mm and diameter 0.065 mm, and an outer cylinder representing the tubule as a whole, with length 0.9 mm and diameter 0.075 mm. The epithelial cell "sheath," i.e. the area between the cylinders, was therefore uniformly 0.01 mm thick. Radiation transport also depends on the density and elemental composition of a medium; currently, fish specific tissue data is not available. Therefore, the representative lumen and epithelial cells were given densities (1.03 g cm^{-3} and 1.05 g cm^{-3} respectively) and elemental compositions of human lymph fluid and thyroid tissues (ICRU 1989).

Because electron-probe, X-ray microanalyses have shown iodine to be primarily contained in the epithelial cells (Suzuki 1985), the ^{131}I was limited to the epithelial casing around the lumen. Therefore, using the mass ratio of thyroid tubule to epithelial casing, an ^{131}I concentration of 1 Bq g^{-1} wet mass in "thyroid area" tissue indicates average ^{131}I concentrations in the epithelial casings of 3.713 Bq g^{-1} wet mass, with uniform distribution of ^{131}I across and between casings.

2.2.2. Modeling the clusters of follicles

Thyroid tissue was ultimately represented by two clusters of nine tubules each, longitudinally arranged within the mandible area of the fish, to achieve an anatomically relevant representation of thyroid clusters that did not involve unmanageable complexity. Each cluster was composed of three

rows of three tubules; tubules within a cluster were linearly offset to mimic the trout's arbitrary arrangement of thyroid tubules (Figure 1.4).

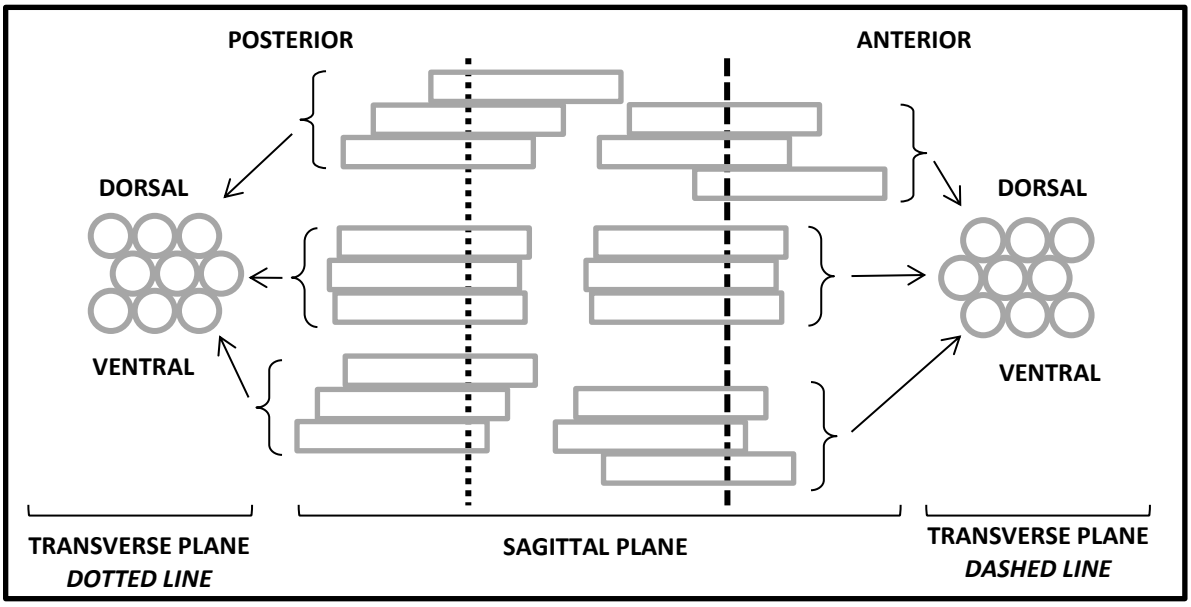

Figure 1.4: Model thyroid structure. Diagram of the modeled tubule structure simulating the follicular clusters inthe rainbow trout. Top views of each layer of tubules are associated with the end on view of the stacking of the layers.

This offset resulted in an overall cluster length of about 1.5X the length of an individual tubule. Although offset, tubules within a cluster shared a common cross-sectional (i.e. transverse) plane (Figure 1.4). The modeled thyroid bundle spanned a total length of 2.75 mm, approximating the 2.7 mm length of juvenile rainbow trout thyroid tissues reported by Raine et al. (2005).

To account for the portion of radiation emitted from the thyroid that is subsequently scattered back to the thyroid by surrounding tissue, the thyroid structure was modeled within an ellipsoid representing the body of a rainbow trout (Figure 1.5).

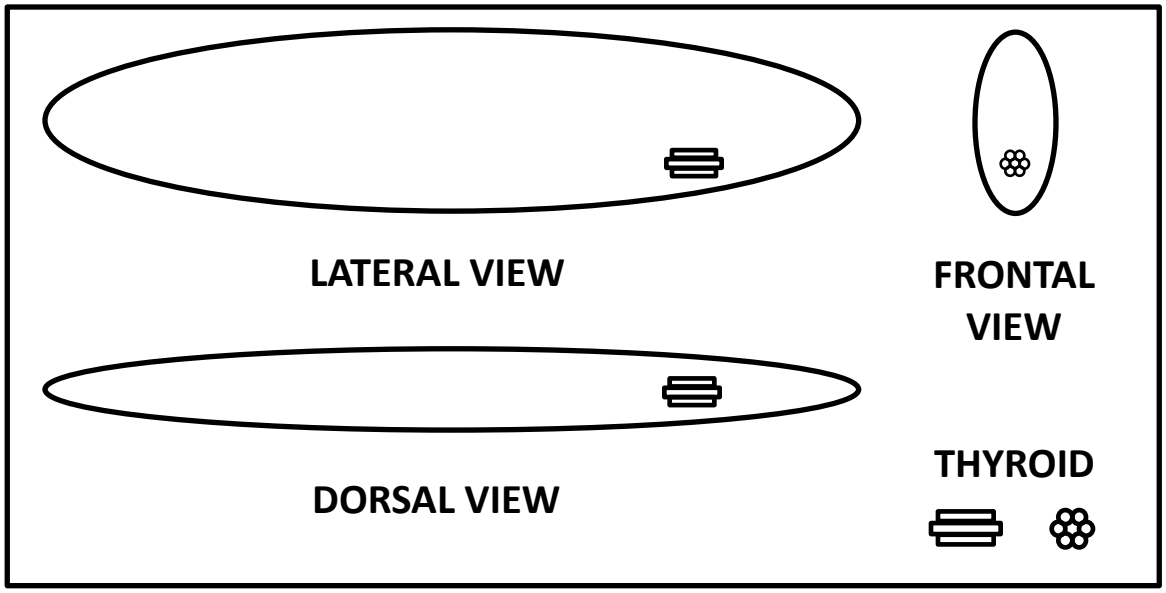

Figure 1.5: Thyroid cluster positions. Positioning of the model thyroid clusters (not to scale) within the model trout body which has length:depth: width ratios of 9:2:1.

This ellipsoid was defined to have a length:depth:width of 9:2:1 (Raine et al. 2005) and a tissue density of 1.05 g cm^{-3} (human skeletal muscle, ICRU 1989). The mass ratio of the modeled thyroid to fish body was 3 x 10^{-5}, which corresponds to mass ratios reported in the literature for rainbow trout (Vanderploeg et al. 1975). The addition of a water body around the fish contributed considerably to run time but did not significantly affect the dose to thyroid (less than 1% difference), so was therefore not included in the MCNP simulation here.

2.2.3. Determination of the dose conversion factor.

To simulate ^{131}I decay and estimate the corresponding energy deposited per disintegration, MCNP software simulated 10^7 ^{131}I disintegrations (10^7 chosen to optimize variance reduction with run time), distributed randomly across locations in the tubule sheaths. The locations and magnitudes of resultant energies deposited in the tubule sheaths were tabulated, with separate tabulations made for each tubule sheath. Energies deposited in the tubule epithelials (the tissue of biological significance and interest) were tabulated and analyzed; energies deposited in the lumen and surrounding fish tissues were recorded, but a detailed analysis is not included as it would be beyond the scope of this paper.

Separate randomizations and tabulations were made for beta particles and gamma photons corresponding to ^{131}I decay. Total deposited energy tabulated was normalized by simulated disintegrations, i.e. MCNP output reports energy deposited per disintegration (MeV dis^{-1}).

The initial energies of beta particles or gamma radiations emitted from the simulated disintegrations were randomly selected from appropriate frequency distributions specified in the MCNP program. The initial beta energies were randomly selected from a continuous distribution of possible energies ranging up to a maximum energy of 0.8069 MeV with an average energy of 0.1821 MeV (Stabin and CQP 2002). Gamma energies were randomly selected from either 0.364 MeV with probability 0.817 or 0.637 MeV with probability 0.072 with lower probability energies not being considered (Stabin and CQP 2002).

The tabulation of energies (MeV) deposited were made using the tally function in MCNP that records the sum of all energies deposited in the tissue by that particle type as well as its secondary particles (i.e. the *f8 tally; X-5 Monte Carlo Team 2003). A dose conversion factor (DCF) of $0.013824 \cdot E$ mGy d^{-1} per Bq g^{-1} (where E is the energy deposited per disintegration (MeV dis^{-1}) and 0.013824 is the appropriate unit conversion) was determined directly from the MCNP output.

2.3. Additional fish models

Three fish models of different sizes were constructed and compared. These three models represented rainbow trout of lengths 9, 36, and 63 cm and are referred to hereafter as juvenile, small, and average, respectively. Masses and sizes of the fish bodies and thyroids were obtained by proportionally increasing the dimensions of the juvenile fish by a factor of 4 (small fish) and 7 (average fish) (Table 1.3).

Table 1.3: Selected dimensions of different size fish models.

	Length (cm)	Mass (kg)	Total thyroid mass (mg)	Thyroid epithelial thickness (μm)
Juvenile	9	0.010	0.296	10
Small	36	0.633	18.97	40
Average	63	3.394	101.7	70

2.4. Determination of cumulative doses

The empirical models developed were combined with the MCNP simulation to compute cumulative doses to the thyroid epithelial tissues from the decay of ^{131}I. First, the predicted ^{131}I concentrations in thyroids as a function of time, $B(t)$, were converted to ^{131}I concentrations in epithelial tissues (i.e., 3.713 Bq g^{-1} epithelial tissue per g thyroid tissue described above). Concentrations of ^{131}I in the epithelial tissue were then multiplied by the DCF obtained from MCNP to acquire a dose rate. The dose rate was then integrated over time to determine a cumulative dose.

The dose rate, $\dot{D}(t)$, at time *t* is given by Equation 1-6:

$$\dot{D}(t) = \mathrm{DCF} \cdot 3.713 \cdot B(t) = \mathrm{DCF} \cdot 3.713 \cdot \left(\frac{\mu \cdot a}{k-b} \right) \left(e^{-bt} - e^{-kt} \right) \tag{1-6}$$

The cumulative dose, $D(t)$, is then Equation 1-7:

$$D(t) = \mathrm{DCF} \cdot 3.713 \cdot \left(\frac{\mu \cdot a}{k-b} \right) \left(\frac{1}{b} \left(e^{-bt} - 1 \right) + \frac{1}{k} \left(1 - e^{-kt} \right) \right) \tag{1-7}$$

3. Results

3.1. Energy deposition by tubule

Although the distribution of ^{131}I among the tubule sheaths was uniform in the model, the distribution of energy deposited by the decay of ^{131}I was not uniform. Figure 1.6 maps the energy deposited per tubule as a function of tubule position for both beta and gamma energies.

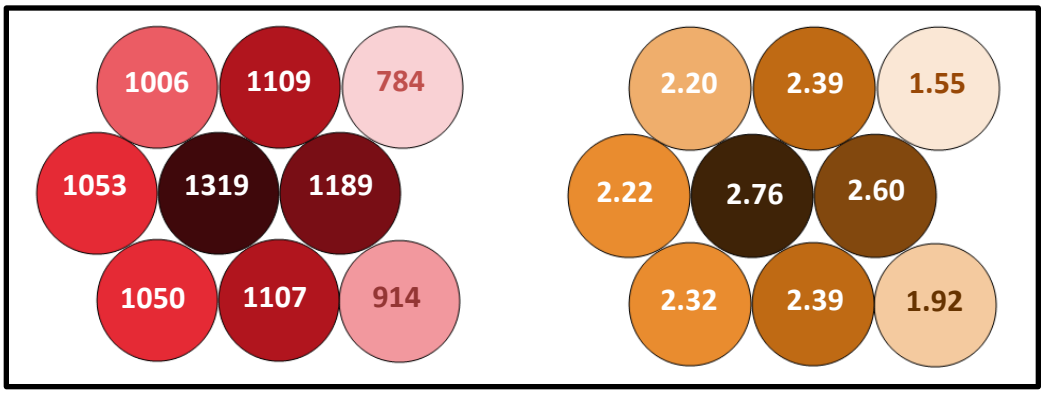

Figure 1.6: Variations of energy deposition in model thyroid epithelial. Cross-sectional views of the tubules in one of the two model clusters relating the energy absorbed by the tubule sheath with its placement within the cluster. Separate energies, expressed in units of eV, are given for both beta (left, shown in red) and gamma (right, shown in brown) emissions.

3.2. Predicted cumulative doses to thyroid per of initial ^{131}I concentration in the water

The dose conversion factor for juvenile trout was 2.647×10^{-4} mGy d^{-1} g Bq^{-1}. Figure 1.7 demonstrates the model's prediction ($\mu_{thyroid} = 33.945$ mL $g^{-1}d^{-1}$ and $k_{thyroid} = 0.0276$ d^{-1}) of cumulative ^{131}I radiation dose to the thyroid epithelial cells of the juvenile trout for a scenario where the initial ^{131}I concentration in the water, *a*, ranges from 0.1 to 5 Bq mL^{-1}, and the concentration in the water declines solely due to radioactive decay (i.e. $b = 0.0862$ d^{-1}) for the first 4 half-lives of ^{131}I.

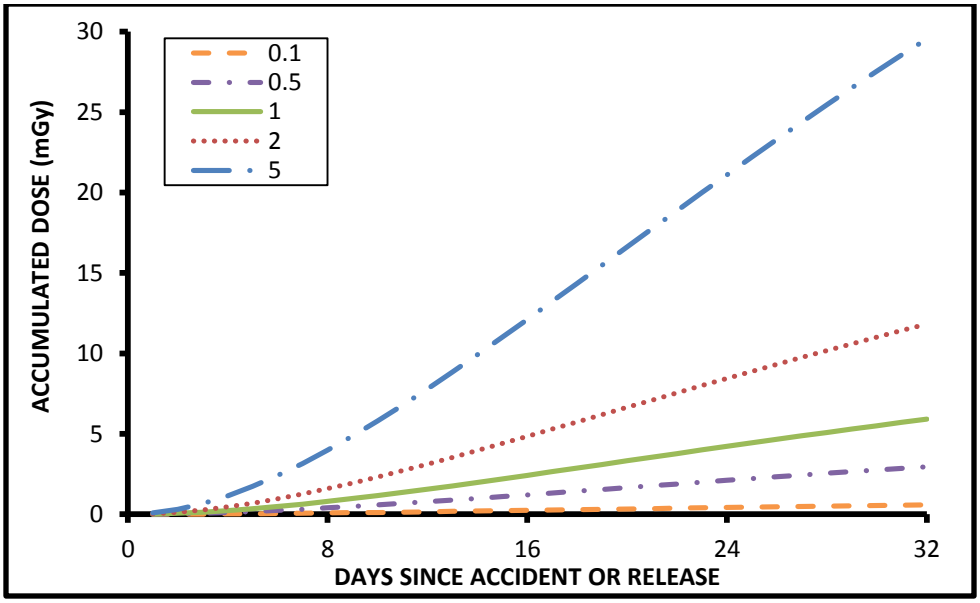

Figure 1.7: Cumulative radiation dose to thyroid resulting from five different initial water concentrations.

Predictions are limited to the first 32 days because the uncertainty of the extent to which the passage of ^{131}I through the food chains will continue to support the predictions beyond day 27 is unknown. The cumulative dose for each of these scenarios initially increases slowly as ^{131}I concentrations in the thyroid increase, but after day 8, the doses show an almost linear rate of increase due to the maintenance of relatively constant ^{131}I concentrations in the thyroids (Figure 1.3). Because of this nearly-linear increase, the ratio of the cumulative dose over the first 32 days to the initial ^{131}I concentration in the water is approximately 5.9 mGy per Bq mL^{-1} for this range of initial concentrations.

3.3. DCFs and subsequent thyroid radiation dose for different size fish

The dose conversion factors for small and average fish were 6.061×10^{-4} and 8.065×10^{-4} mGy d^{-1} g Bq^{-1}, respectively. The predicted doses to the thyroid epithelials therefore differed markedly for fish of different sizes. For the scenario of an initial water concentration of 1 Bq mL^{-1} and losses due solely to radioactive decay (Figure 1.8; $b = 0.0862\ \mathrm{d}^{-1}$), the ratios of cumulative dose to initial water concentration were 13.5 mGy per Bq mL^{-1} for the small fish and 18.0 mGy per Bq mL^{-1} for the average fish.

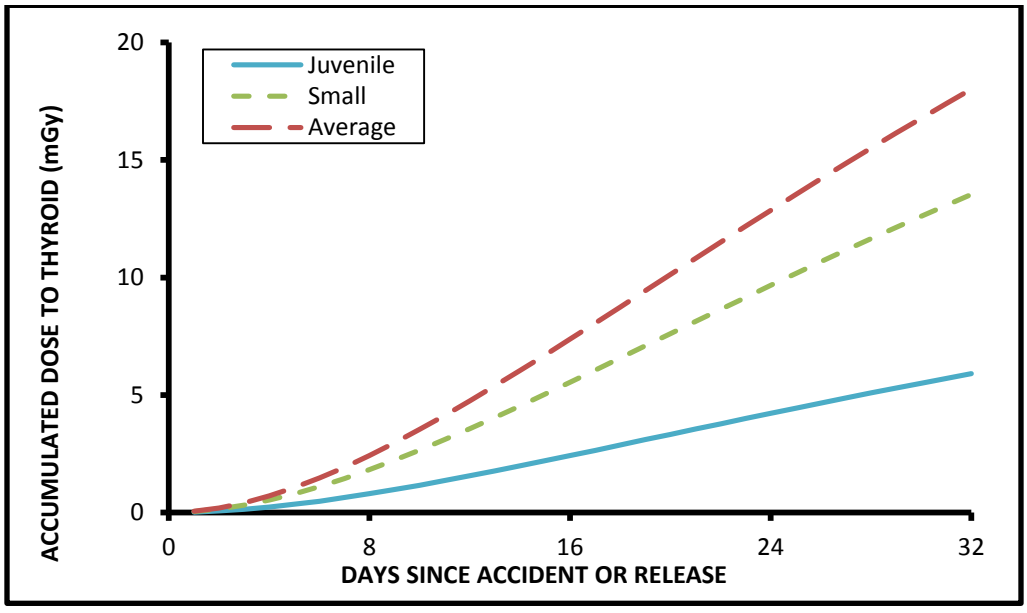

Figure 1.8: Model predictions for different size fish; the predictions are for fish of lengths 0.09 (juvenile), 0.36 (small) and 0.63 m (average).

The ICRP's reference trout (ICRP 2008b, 2009) was not considered in our analysis because its dimensions are not proportional to the rainbow trout (Raine et al. 2005) used in MCNP geometry development. However, the range of whole body DCFs determined by our model (details not shown) were consistent with DCF for internal exposure of trout to ^{131}I (ICRP 2008b), implying that our thyroid DCFs are likely applicable to similarly-sized reference trout.

4. Discussion

4.1. Sources of error in estimated cumulative dose

The predicted 5.9 mGy per Bq mL^{-1} initial water concentration for juvenile trout may be considered an underestimate of the accumulated dose because it is based the "thyroid area" concentrations of Short et al. (1969) that are used to define the ^{131}I concentrations in the epithelial cells. The "thyroid area" concentrations of Short et al. (1969) may underestimate the ^{131}I concentrations in actual thyroid tissues; for example, if a cylinder simulating the sampled area was circumscribed about the thyroid clusters with dimensions of the total length and width spanned by the thyroid bundle (i.e., with a diameter of 0.6 mm and length of 2.75 mm), the mass ratio of "thyroid area" to thyroid epithelial shells would be 10.227, compared to 3.713, which would result in a 2.75X larger cumulative dose to the thyroid than predicted above. The greater the sampling margins, the more of an underestimate the original predicted dose will be.

Alternatively, the predictions maybe overestimates because processes in the lake may cause the ^{131}I concentrations in the water to decline at rates greater than that solely due to decay. However, the rate of decline of the water concentration has a smaller effect on the accumulated dose than the initial concentration. Increasing the rates of decline by factors of 1.5 and 2 (i.e, $b = 1.5 \cdot 0.0862\,\mathrm{d}^{-1}$ and $b = 2 \cdot 0.0862\,\mathrm{d}^{-1}$) results in ratios of dose to initial water concentration of 2.6 and 2 mGy per Bq mL^{-1}, respectively. It should be noted that the model is not appropriate for rates of decline in water

concentrations that are significantly less than the rate of radioactive decay because these rates of decline imply the continuing additions of ^{131}I to the water.

4.2. Variation in energy deposition among tubules within a cluster

The energy deposited per tubule varied depending on position of the tubule within the cluster: there was an approximate factor of 2 differences between energy deposited to the central tubules and that deposited to tubules on the periphery of the cluster for both beta and gamma energies. This is because radiation from tubule sheaths is emitted in all directions; tubules on the periphery of the cluster receive radiation from a fewer number of neighboring tubules than do centrally located tubules.

Whether differences in doses to epithelial sheaths actually differ by this much in a fish is questionable; the arrangement of the follicles is far less regular than that in the model. Follicle clusters in the fish involve follicles of different cross-sectional areas that are therefore less regularly arranged. Although the variation in energy deposition among fish follicles may be less than that for the model's tubules, variations in dose rates among follicles will likely occur and may be better simulated by more anatomically correct tubule arrangements. Furthermore, the variation in follicle sizes implies variation in ^{131}I assimilation among follicles with corresponding differences in energy deposition in that and surrounding follicles.

4.3. Predicted doses for larger-sized fish

As fish size increased a proportionally greater amount of energy was deposited in the thyroid per unit mass, which is the result of the increased tubule sheath dimensions. The probability that interactions will occur between beta or gamma radiations and the media through which they travel increases with the distance travelled (*i.e.*, the distance through the tissue thickness). For juvenile fish where the thickness of the tubule sheaths is 10 µm, the radiations may readily pass through the surrounding thyroid tissues and deposit minimal energy. Increasing the thickness of the tubule sheaths

to 40 µm and 70 µm in the small and average fish respectively, increases the likelihood (e.g. frequency) of radiation-tissue interactions.

5. Conclusions

5.1. Predicted thyroid doses to fish in the Kiev Reservoir

The Figure 1.7 scenario for an initial ^{131}I concentration of 1 Bq mL^{-1} is not completely hypothetical. The ^{131}I data in the water of Kiev Reservoir in Figure 1.1 involved initial concentrations of approximately 1 Bq mL^{-1} ($a = 0.715$ Bq mL^{-1}) and rates of decline ($b = 0.074$ d^{-1})similar to that for radioactive decay. Using the model above ($\mu_{\text{thyroid}} = 33.945$ mL g^{-1} d^{-1} and $k_{\text{thyroid}} = 0.0276$ d^{-1}) and the conditions in Kiev Reservoir, the predicted 32-day cumulative dose to a fish thyroid is 4.6 mGy, 10.6 mGy, and 14.1 mGy for a juvenile, small, and average rainbow trout respectively.

The calculated thyroid doses correspond to dose rates less than 1 mGy d^{-1}. Only whole body dose rate risk data is available for this type of fish, and at dose rates that are above 1 mGy d^{-1} (ICRP 2009). It is known that radioiodine exposures can negatively affect aspects of fish growth and development that are mediated by thyroidal hormones (LaRoche et al. 1965, 1966), yet currently no information is available linking risk of occurrence to thyroid radiation dose levels associated with ^{131}I exposure.

5.2. Trophic complexity and the linearly increasing cumulative doses

The model may err in the prediction of actual dose rates and consequently the cumulative dose over time, but the pattern of the nearly-linearly increasing cumulative doses is not a function of the accuracy of the MCNP model's predictions. The pattern is a product of the maintenance of nearly constant ^{131}I concentrations in the thyroids (Figure 1.3) due to the continuing ingestion of ^{131}I from the trout's prey item components of the complex food web of Fern Lake. These nearly constant ^{131}I concentrations in the thyroids result in nearly constant dose rates, and these nearly constant dose rates result in linearly increasing cumulative doses with time. Where similar complex food webs exist in other

aquatic systems, continuing increases in cumulative doses beyond the 1st and 2nd half-lives of ^{131}I can be expected to occur.

CHAPTER 2: DEVELOPMENT AND COMPARISON OF THREE COMPUTATIONAL MODELS FOR ESTIMATION OF ORGAN DOSE IN RAINBOW TROUT FROM UPTAKE OF IODINE-131*

1. Introduction

1.1. Current methodology in radiation protection of the environment

Radiation dose rates to biota are typically approximated utilizing dose conversion factors (DCF), which are values for absorbed dose rate per activity concentration in the body or organ (i.e. mGy d^{-1} per Bq g^{-1}). The current methodology employed by both the ICRP and within the ERICA Integrated Approach (Larsson 2008) for calculating dose conversion coefficients is to use Monte Carlo modeling of a homogenously distributed radionuclide within an ellipsoidal phantom[1] chosen to represent a particular organism (ICRP 2008b; Gómez-Ros et al. 2008; Ulanovsky and Pröhl 2006, 2008). It has been shown that when computing whole-body DCF, the assumption of a homogenous distribution will result in an uncertainty of less than 30% for both electrons and photons (Gómez-Ros et al 2008). However, if a radionuclide is not homogeneously distributed but instead concentrates in a particular organ (e.g. iodine-131 (^{131}I) in thyroid) a much higher dose will be received by the organ or tissue than by the whole body. To address such situations, organs have been generically modeled as spheres within the ellipsoid phantom (ICRP 2008b), but this simplicity may be insufficient to accurately represent the complex and variable nature of organ structure and arrangement within different types of organisms. In computing DCFs for these spheres, the ratios of whole-body to organ mass offer conservative conversions of whole-

* Martinez NE, Johnson TE, Capello K, Pinder JE. 2014. Development and comparison of computational models for estimation of absorbed organ radiation dose in rainbow trout (*Oncorhynchus mykiss*) from uptake of iodine-131. Physics in Medicine and Biology. Submitted.

[1] The word "phantom" has traditionally been used in the radiation protection community to mean a physical phantom representing the human body. However, with the advent of computational models, the generic "phantom" has also been used to refer to a mathematically defined three-dimensional model, as distinct from a physiological computational model related to, say, respiration or blood flow (Xu and Eckerman 2010); both "phantom" and "model" here to refer to computational anatomical models.

body to organ specific DCF (Gómez-Ros et al. 2008), but may considerably overestimate the organ dose. More accurate estimates of organ dose can be made using specific absorbed fractions and activity concentrations.

1.2. Study objective and justification

Establishment of appropriate screening levels in the regulatory paradigm requires incorporation of sufficient knowledge of dose effects; the ICRP currently lists no derived consideration reference levels for organs, meaning that specific risks associated with organ dose rates are unavailable (ICRP 2008b). Model comparison and refinement is important to the process of determining both dose rates and dose effects, and here we develop and compare three models for rainbow trout (*Oncorhynchus mykiss*): a simplistic geometry considering a single organ, a more specific geometry employing anatomically relevant organ size and location, and voxel reconstruction of internal anatomy obtained from CT imaging. We consider the dose rates to the thyroid, GI tract, and liver of rainbow trout from uptake of ^{131}I, where the time-varying concentrations of ^{131}I in these organs have been previously determined for the first 32 days following an ^{131}I release into the freshwater system (Martinez et al. 2014). Iodine-131 is a major component of the atmospheric releases following reactor accidents, and although the fate of ^{131}I deposition onto lakes and other aquatic systems has been studied considerably (e.g. Bird et al. 1995a; Bird et al. 1995b; Bird and Schwartz 1996; Gilfedder et al. 2009; Gilfedder et al. 2010), the resulting doses to aquatic organisms have received less attention. The goal of this study is determination of accuracy of and variation among increasingly true-to-life radiation transport models to compare and assess the most appropriate anatomical approximations for computing radiation dose to biota. Appropriateness is evaluated as the ratio of perceived increase in accuracy relative to the increased effort required to construct more anatomically accurate phantoms. For this analysis it is assumed that the DCF from the most anatomically correct phantoms are the most accurate.

1.3. Existing computational models

Computational phantoms have found extensive use through incorporation into Monte Carlo based radiation transport computer codes for application in radiation dosimetry, as well as in medical imaging simulation and evaluation (Zaidi and Tsui 2009; Xu and Eckerman 2010). Through the early 2000s there were considered to be two main classes of anthropomorphic computational models (Zaidi and Tsui 2009). The first, stylized phantoms, were first developed in the 1960s and use combinations of simple, equation-based surfaces such as cylinders and spheres for object representation. The second, voxel phantoms, were originally created in the 1980s following the advent of more powerful computing technologies and imaging techniques. Objects in a voxel phantom are represented by three dimensional voxel matrices. A third class of computational phantom emerged in the 2000s as a hybrid of stylized and voxel phantoms (Xu and Eckerman 2010). These hybrid phantoms utilize boundary representation (BREP) geometries and can even be used to simulate movement. However, the translation of this type of phantom for use within radiation transport codes is non-trivial (Xu and Eckerman 2010). In this study we consider the first two classes of phantoms.

1.4. Existing animal phantoms and similar studies

A significant amount of research has been conducted concerning human model development, however work conducted in creating animal models is lacking (Zaidi and Tsui 2009). The initial research and subsequent increase in animal model development over the past decade was motivated by the need for refined preclinical models, and therefore initially focused on laboratory animals (Zaidi and Tsui 2009); although computational models may be used in different applications, the primary focus in early work was on animals as models for humans, or for refining medical imaging techniques for use in human medicine. However, in recent years, there has been increased emphasis on radiation protection of the environment, and some models have been used for this specific end (Mohammadi et al. 2011, 2012;

Caffery and Higley 2013). Table 2.1 lists existing whole body animal phantoms, along with studies that have calculated absorbed fractions or organ dose coefficients using such phantoms.

Table 2.1: Studies that have developed or utilized whole body animal computational phantoms.

Animal	Phantom development	Selected absorbed fraction data	Organ dose coefficients for external photon irradiation
Mouse	Segars et al. 2004 Hindorf et al. 2004 Stabin et al. 2006 Dogdas et al. 2007 Taschereau et al. 2006 Bitar et al. 2007 Mauxion et al. 2013	Mohammadi et al. 2011	Zhang et al. 2012
Rat	Stabin et al. 2006 Wu et al. 2008 Xie et al. 2010a Zhang et al. 2009	Xie et al. 2010a, 2010b Mohammadi et al. 2012	
Frog	Kinase 2008	Mohammadi et al. 2011, 2012	
Crab	Caffery and Higley 2013	Caffery and Higley 2013	
Canine	Padilla et al. 2008 Kramer et al. 2012		

However, this is the first study to consider temporal changes in activity concentration data as applied to organ uptake in various phantom types. One similar study comparing absorbed fractions determined by three different computational phantoms was conducted with rats (Xie et al. 2010a) and found that the stylized phantom might underestimate the self-absorbed S-factors and thus might under predict organ dose.

2. Materials and methods

2.1. Kinetic data for ^{131}I

Computing an accumulated radiation dose over time requires some form equation or model that describes the temporal concentration and location of the particular radionuclide. Martinez et al. (2014) used existing ^{131}I kinetic data (Short et al. 1969) from Fern Lake, Washington to develop

empirically-derived models for the prediction of activity concentration in various biota and tissues, including rainbow trout.

Fern Lake is a 9.7 ha, oligotrophic lake near Seattle, Washington in the United States. The Fern Lake Trace Mineral Metabolism program was a 10-year interdisciplinary research program initiated in 1957 (Donaldson et al. 1959) seeking to improve the productivity of western Washington lakes (Olsen et al. 1967). As part of the Fern Lake program, several radionuclides, including ^{131}I, were released into the lake to understand the fate and transport of the corresponding stable isotopes (e.g. ^{127}I) (Short et al. 1969, 1971). Iodine-131 concentrations in water, various biota, and trout tissues were measured periodically for 27 days, which is the data considered by Martinez et al. (2014). The following simple uptake and loss rate model was used to model the time varying concentrations of ^{131}I in fish tissues:

$$\frac{dB(t)}{dt} = \mu \cdot W(t) - k \cdot B(t) \tag{2-1}$$

where μ is an uptake constant with units L kg^{-1} d^{-1}, k is a first-order loss rate constant with units d^{-1}, $W(t)$ is the ^{131}I concentration in water, and $B(t)$ is the ^{131}I concentration in specific fish tissues. $W(t)$ is approximated using a single-component exponential equation (Whicker and Shultz 1982):

$$W(t) = a \cdot e^{-bt} \tag{2-2}$$

where a is the initial ^{131}I concentration in the water at the time of release (i.e. t = 0), and b is the rate constant (d^{-1}) for the exponential decline in $W(t)$.

For aquatic animal biota, μ is a measure of the transfer of the radionuclide through food chain pathways from the water to animal. The factors affecting μ become increasingly complex with increasing number of trophic levels (Pinder et al. 2009). Despite the number of factors affecting μ for consumers, the model has been shown to be able to accommodate these complexities for varying trophic levels (Smith 2002; Pinder et al. 2011). For whole-body ^{131}I concentrations, k is a measure of loss that incorporates radioactive decay, excretion, and population losses due to mortality or emigration (Pinder

et al. 2009). Population losses should be negligible within the short durations of these studies that were performed in mostly confined locations, so the estimated *k* should be dominated by radionuclide decay and excretion.

The parameters μ and *k* have different interpretations when applied to individual fish tissues. The parameter μ may represent increases in ^{131}I concentrations due to absorption and ingestion of additional ^{131}I or due to the transfer of ^{131}I from other tissues. The parameter *k*, besides including losses listed above, also includes transfer to other tissues. Table 2.2 lists the specific values used for μ and *k* determined by Martinez et al. (2014), and Figure 2.1 shows model fits compared to the Fern Lake data (Short et al. 1969; Martinez et al. 2014).

Table 2.2: Values for empirical parameters used in determination of activity concentration.

Source organ	μ (L kg^{-1} d^{-1})	*k* (d^{-1})
Thyroid	33.95	0.0276
Liver	3.76	0.0201
GI	7.25	0.0520

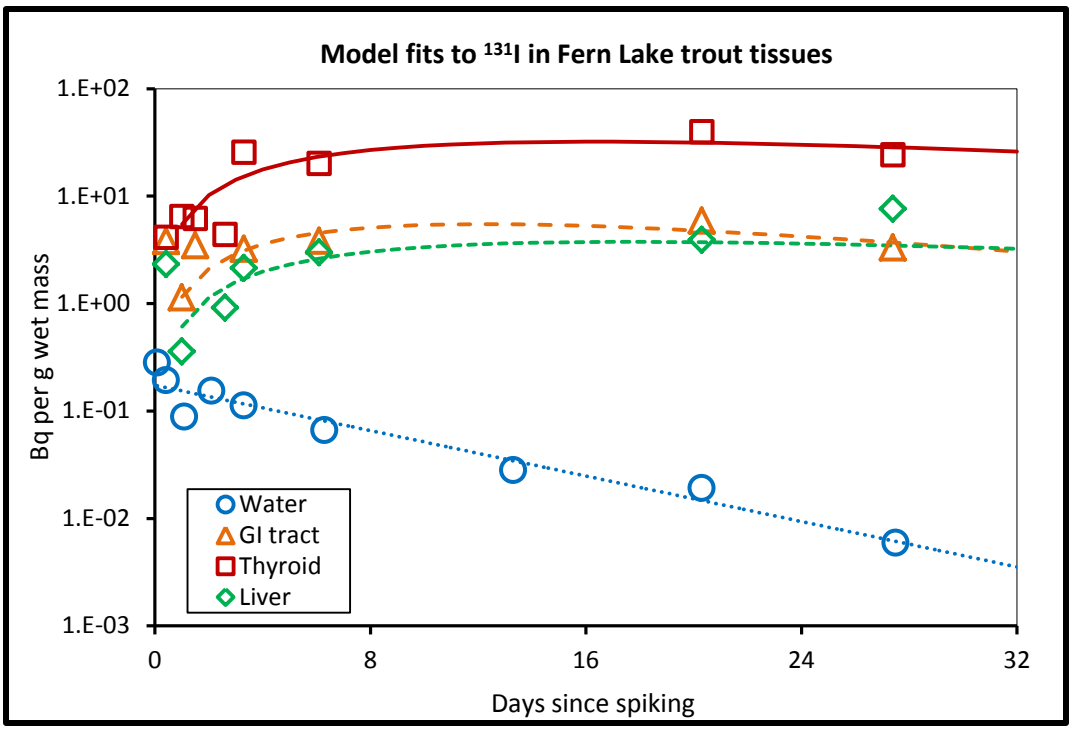

Figure 2.1: A comparison of Fern Lake data and model predictions for activity concentrations in water and O. mykiss thyroid, liver, and the gastrointestinal tracts.

The maintenance of nearly constant ^{131}I concentrations in the thyroid, GI tract, and liver (Figure 2.1) is due to the continuing ingestion of ^{131}I from the trout's prey item components of the complex food web of Fern Lake.

Although variations among lakes in water temperature, stable iodine content, food chain complexity, fish size, and other factors may affect the values of μ and k, the Fern Lake values (Table 2.2) are the best available estimates of ^{131}I accumulation and loss in free-swimming fish, and are used here to calculate and compare organ radiation doses with various rainbow trout phantoms.

2.2. Analysis of fish anatomy

Six deceased trout, including five rainbow trout (*O. mykiss*) and one brown trout (*Salmo trutta*), were caught and donated by a local fisherman in early November 2013. Three fish were caught from lakes, and three were caught from streams and rivers. The largest of these fish, a 0.286 m long female *O. mykiss*, pictured in Figure 2.2 was used to develop the phantoms considered in this paper.

Figure 2.2: Female rainbow trout used as a model in this study.

2.2.1. Image acquisition

To acquire the image set necessary for phantom development, three fish (one lake-caught rainbow trout, one river-caught rainbow trout, and one river-caught brown trout) were given a CT scan at the James L. Voss Veterinary Teaching Hospital in Fort Collins, Colorado (1 mm slices; Gemini TruFlight Big Bore PET/CT, Philips Healthcare, Andover, MA), based on resource availability. Image files obtained from CT (cross-sectional radiographs, referred to as CT slices) are saved in the Digital Imaging and Communications in Medicine (DICOM) file format; DICOM files are the standard file format within the DICOM Standard in medical imaging (National Electrical Manufacturers Association 2011). A DICOM file set consists of an array of two-dimensional (2D) cross-sectional images (CT slices), with each image consisting of a certain amount of pixels. The DICOM files from the fish CT were separated by individual fish, and imported into 3D-Doctor software (version 5.0, AbleSoftware Corp, Lexington, MA). Organs were outlined, i.e. contoured, manually in 3D-Doctor using a Wacom Intuos Pen and Touch Small Tablet (Wacom, Vancourver, WA). Figure 2.3 illustrates the interpretation of three separate CT slices by the application of contour lines around specific tissues of a female rainbow trout.

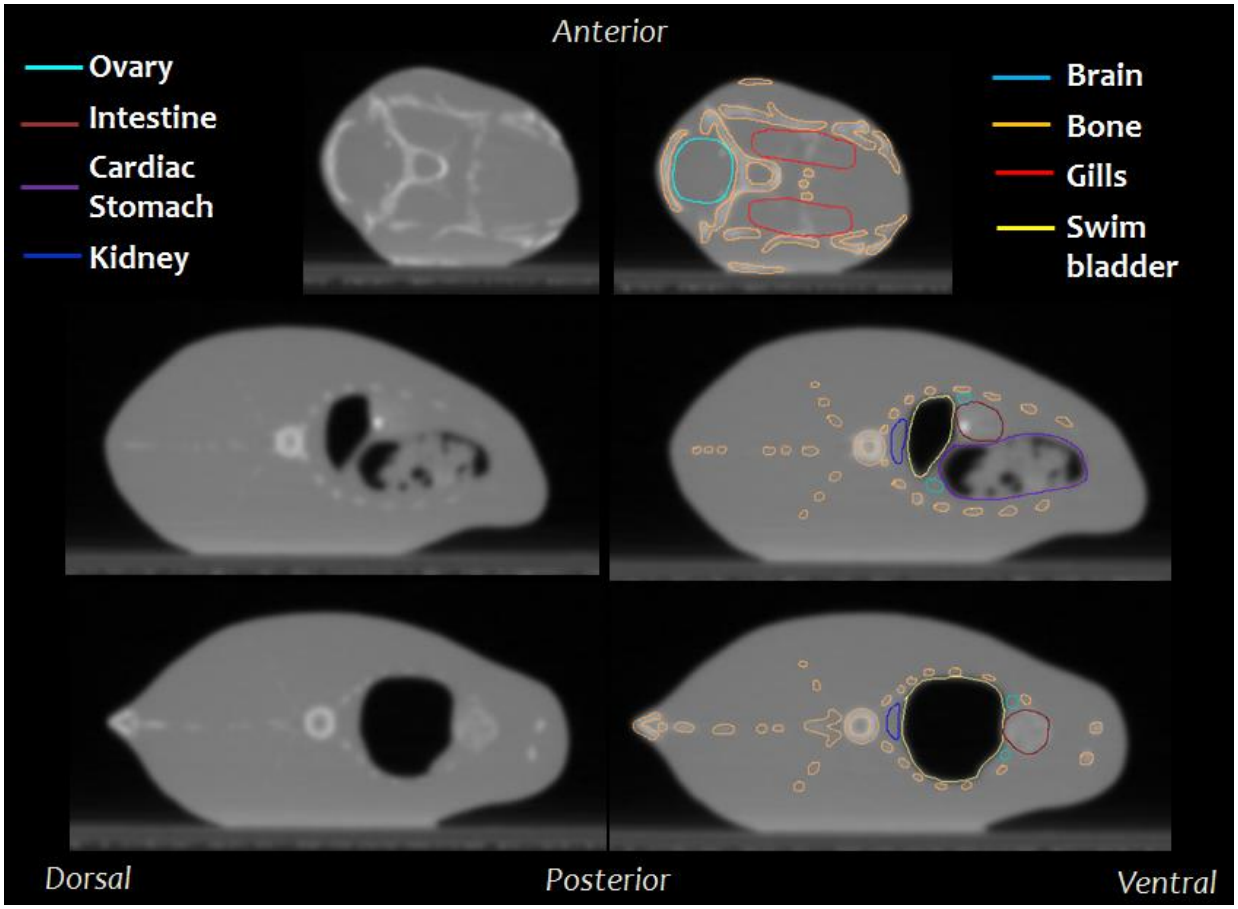

Figure 2.3: Example CT slices without and with organ contours.

2.2.2. Dissection

Four fish, including both rainbow trout that received a CT, were dissected (Figure 2.4) to assist in appropriately identifying organs (Weinreb and Bilstad 1955).

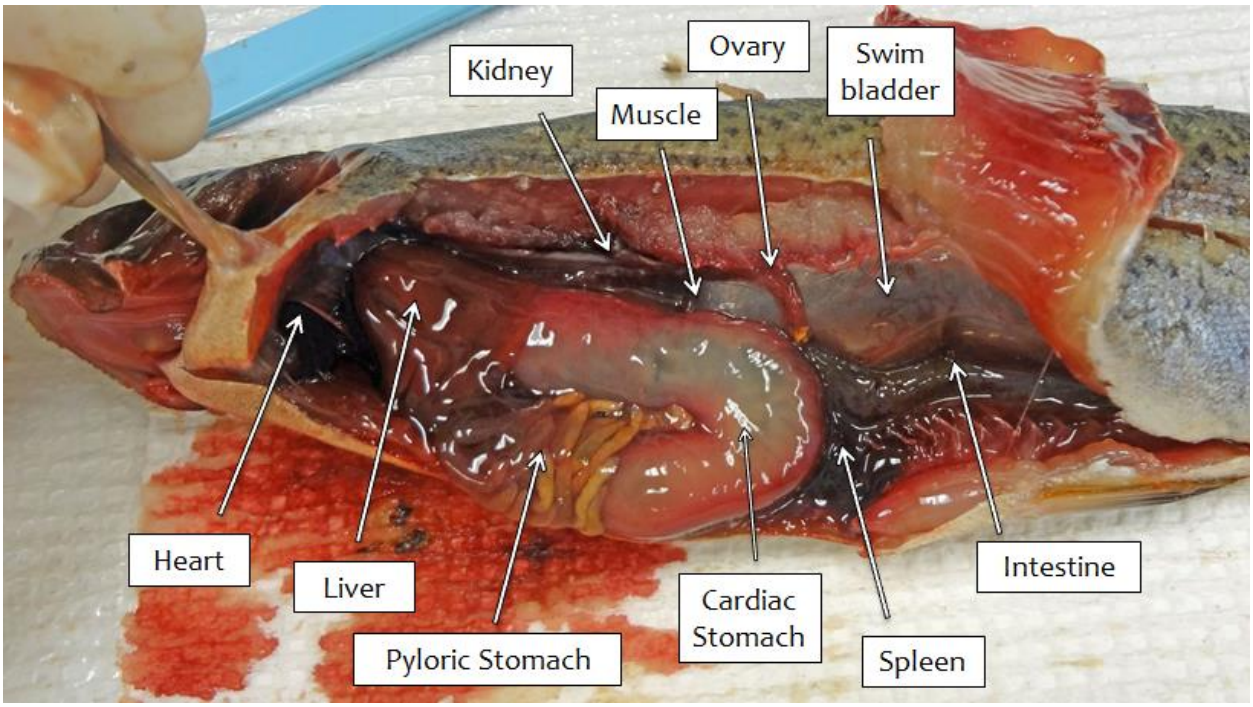

Figure 2.4: Internal organs of a female rainbow trout.

Organs were retained for future determination of tissue elemental composition. Fish samples were kept frozen at -20°C prior to the CT scan, completely thawed for the CT scan, and refrigerated at 4°C post-CT and prior to dissection. Dissected tissue or whole body samples were kept frozen at -20°C after the dissection.

2.3. Overview of phantom creation

The geometric structure, arrangement, and composition of rainbow trout tissues were either modelled with organs represented as simple geometric shapes or modelled using Voxelizer software (developed by the Human Monitoring Laboratory (HML), Health Canada, Ottawa). Voxelizer converts an organ boundary file, which is a set of organ contours created from CT images, into a lattice structure geometry (Kramer et al. 2010) recognizable by the Monte Carlo N-particle (MCNP) transport code (Briesmeister 2000; X-5 Monte Carlo Team 2003) version 5.1.60 or System X version 7.0D, known as MCNP5 and MCNPX respectively (Radiation Safety Information Computational Center, Oak Ridge, TN). MCNP5 and MCNPX were employed for Monte Carlo simulation of radiation transport and energy

deposition based on empirically derived ^{131}I concentrations in various organs to determine radiation dose to desired tissue(s).

Because appropriate trout tissue elemental composition is as of yet unavailable, elemental compositions of tissues in all three models were based on human tissue (ICRU 1989). This is consistent with previous work (Martinez et al. 2014; Kramer et al. 2012; Caffrey and Higley 2013). The exception is the swim bladder, which was assumed to contain air. It should be noted that although there is existing data (e.g. Diem and Lentner 1970) on trout tissue composition from a nutritional standpoint, it is not sufficiently specific for input into MCNP. Tissue samples obtained in this study were retained for subsequent determination of total elemental analysis so that further refinements of these phantoms based on variations among tissue compositions can be made.

2.4. Building phantoms of the fish body

2.4.1. The simplistic phantom

The simplest phantom developed consists of an ellipsoidal fish body containing a thyroid modeled as 18 small cylindrical shells. The thyroid model was based on rainbow trout thyroid anatomy (Raine et al. 2005). A complete description of the simple phantom is described by Martinez et al. (2014), and this simple phantom was rescaled to from the phantom developed by Martinez et al. (2014) to match the size of the scanned fish. The height and width of the body were slightly reduced from the 9:2:1 (length:height:width) ratios utilized in Martinez et al. (2014) in order to fully match the dimensions of the aforementioned fish.

2.4.2. Stylized phantom

A more detailed anatomical phantom was developed from the simplistic phantom; the size, shape, location, and composition of the fish body and thyroid are the same as for the simplistic phantom. Additional stylized organs, including the liver, swim bladder, gastrointestinal tract, ovaries, heart, and brain were added to the model. The location and size of these model organs were

determined by matching their stylized shapes and locations to the corresponding CT slices as illustrated in Figure 2.5.

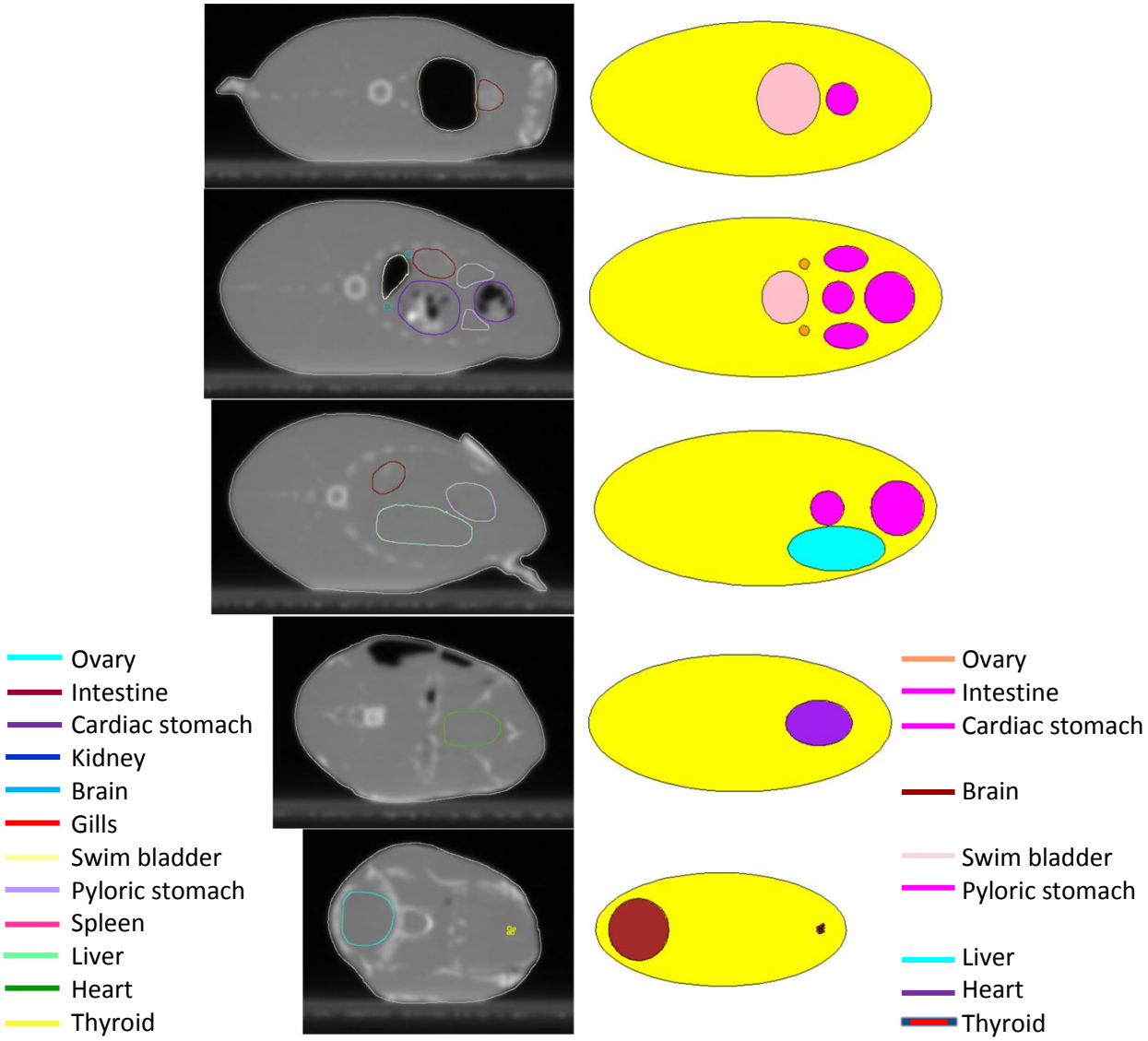

Figure 2.5: Transverse cross sections of anatomical model compared to similar location on CT scan, where the left side of each image is the dorsal side of the fish, and the right side of each image is the ventral side of the fish. From top to bottom images are ordered posterior to anterior.

The details and composition of these model organs is described in Table 2.3 and cross-sectional illustrations of their placements are shown in Figure 2.6.

Table 2.3: Description of representative geometry for organs created in stylized model.

Organ	Description
Body	Ellipsoid
Thyroid	18 cylindrical shells
Liver	Ellipsoid
Swim Bladder	Ellipsoid, rotated 2 degrees from horizontal
GI Tract:	
Intestine	Cylinder, rotated 2 degrees from horizontal
Cardiac Stomach	Cylinder
Pyloric Stomach	2 cylinders
Ovaries	2 cylinders, rotated 5 degrees from horizontal
Heart	Ellipsoid
Brain	Sphere

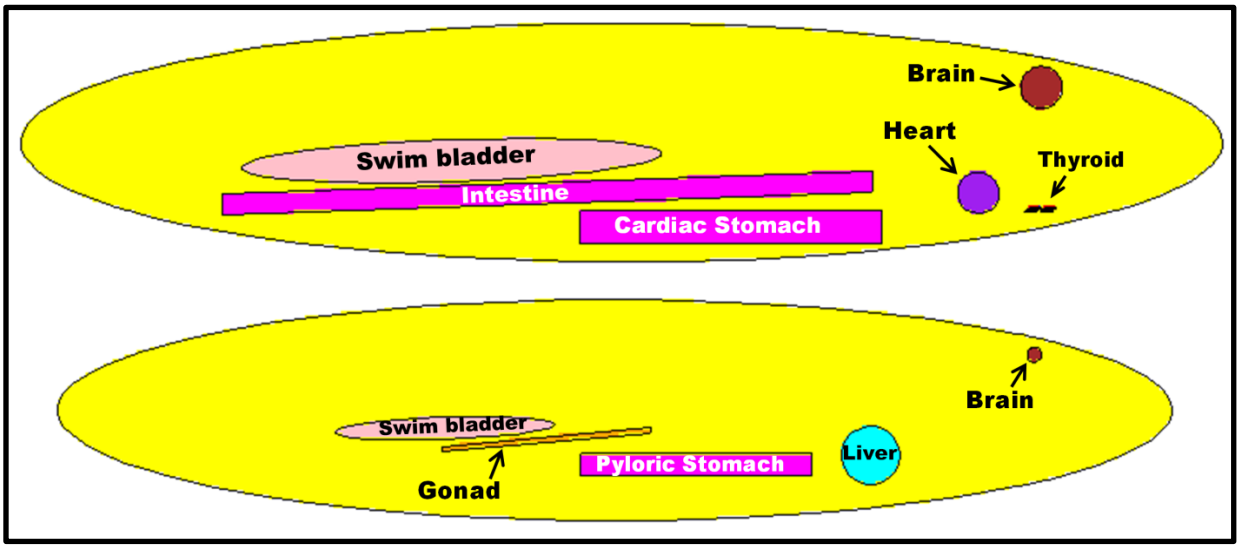

Figure 2.6: Example longitudinal cross sections of the anatomical model: upper section is through the midline of the fish body, the lower is slightly to the lateral left (0.47 cm) of the midline of the body.

The organs were selected for inclusion in the stylized phantom for significant biological relevance (e.g. heart, brain, ovary), tendency to accumulate ^{131}I (e.g. GI tract, liver, thyroid), or for

variation from soft tissue composition (e.g. swim bladder) that would significantly impact radiation transport.

2.4.3. Voxel phantom (CSUTROUT)

There are four general steps in the procedure for creating a voxel phantom (Zaidi and Tsui 2009; Xu and Eckerman 2010). These include: (1) acquiring an appropriate full-body image set (such as from CT, MRI, or cryosection photography); (2) identifying and segmenting organs or other anatomical structures of interest within the image set acquired in step 1; (3) determining density and elemental composition characteristics for tissues identified in step 2; and (4) converting the organ segments (contours) to a three dimensional (3D) volume for visualization (verification of appropriate organ structure) and Monte Carlo implementation.

Step (1), (2), and (3) were discussed in sections 2.2 and 2.3. It should be noted, however, that the thyroid was too small to be seen on CT and was therefore contoured using knowledge of thyroid anatomy (Raine et al. 2005; Martinez et al. 2014). For step (4), once the organ contouring of step (2) was completed, the contour lines were consolidated into a 3D rendering of the two-dimensional contours, shown in Figure 2.7 and Figure 2.8, for visual confirmation of structure.

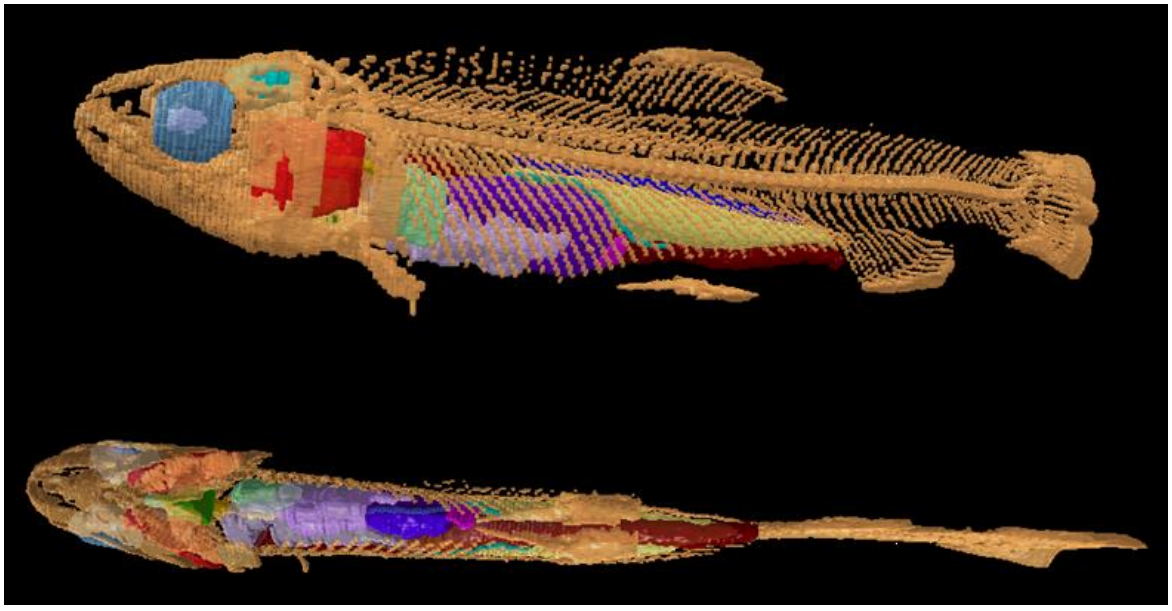

Figure 2.7: Voxel phantom skeleton and internal organs; view from side and bottom.

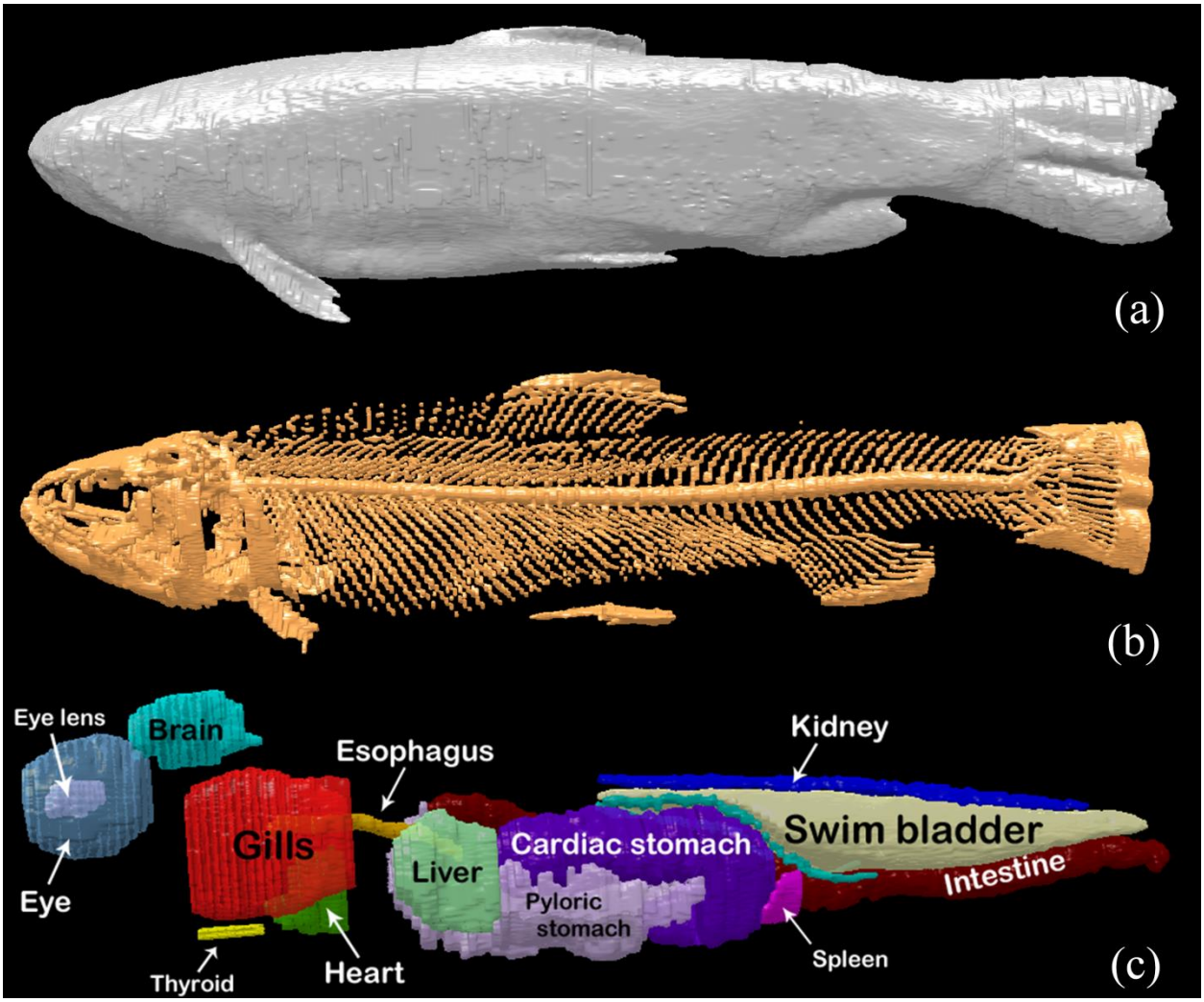

Figure 2.8: Voxel phantom (a) body, (b) skeleton, and (c) internal organs.

Note that the colors in Figure 2.7 and Figure 2.8 correspond to the organs listed in Figure 2.3 and on the CT images in Figure 2.5. Volumes of the contoured organs are listed in Table 2.4, with volumes of the stylized organs included for comparison.

Table 2.4: Organ volume and comparison for stylized and voxel phantoms.

Organ/organ system	Volume (cm^3)		Ratio
	Stylized phantom	Voxel phantom	
Body	212.12	208.47	1.02
Thyroid	2.4E-03	5.9E-03	0.41
Liver/Gallbladder	0.78	0.89	0.88
Swim Bladder	5.70	5.53	1.03

GI Tract	9.15	8.71	1.05
Intestine	3.04	2.74	1.10
Cardiac Stomach	3.69	3.34	1.10
Pyloric Stomach	2.42	2.54	0.95
Esophagus	--	0.10	--
Ovaries	0.20	0.19	1.05
Heart	0.35	0.43	0.81
Brain	0.52	0.61	0.85
Spleen	--	0.07	--
Kidney	--	0.54	--
Eye (Whole)	--	2.09	--
Eye Lens	--	0.10	--
Gills	--	3.52	--
Bone	--	11.58	--
Remaining Tissue (Muscle)	184.85	165.58	1.12
		Minimum	0.41
		Median	1.03
		Maximum	1.12

It should be noted that the GI tract consists of multiple organs. The stylized model GI tract consists of the intestine, cardiac stomach, and pyloric stomach. The voxel model GI tract consists of the same organs as they stylized model, with the addition of the esophagus. However, we consider the esophagus to be a separate organ from the GI tract for a more appropriate comparison to the stylized model. When defining the GI tract as the source organ, an even distribution of the source radionuclide was defined across the intestine, cardiac stomach, and pyloric stomach.

As is often the convention (Xu and Eckerman 2010), we name our phantom to distinguish it from other computational models should other researchers desire to use it; heretofore our complete voxel rainbow trout phantom will be referred to as CSUTROUT.

The completed set of organ contours were combined into a single boundary file using 3D Doctor and imported into Voxelizer software, which converted the file into MCNP lattice geometry (Kramer et

al. 2010). Voxelization is achieved by multiplying the pixel size (determined by image resolution) by the thickness of an image slice, converting the 2D pixels into 3D voxels (Xu and Eckerman 2010). Voxelizer requires minimal user input, needing only specification of boundary file dimensions and pixel size (obtained from 3D Doctor) as well as the desired compression factor. A higher compression factor results in fewer voxels and faster computing time. However, less voxels equates to less resolution (Figure 2.9).

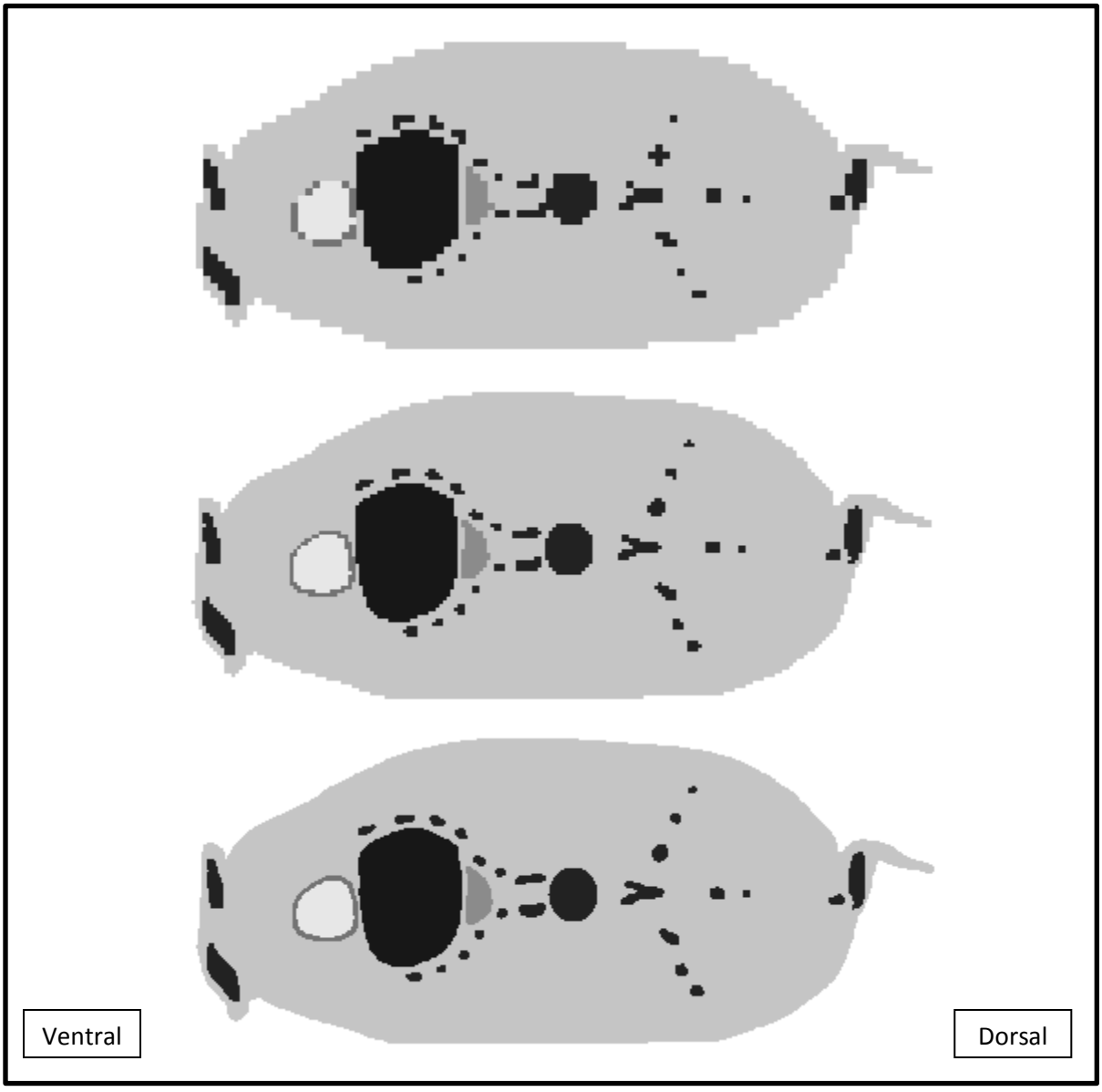

Figure 2.9: Images representing the resolution of different compression factors (exported from Voxelizer). From top to bottom, the images represent a compression factor of 4, 2, and 1 respectively.

Compression factors of 1, 2, and 4 resulted in about 3.0×10^8, 7.5×10^7, and 1.9×10^7 voxels respectively. Because of the lengthy computing time required, a compression factor of 4 was used in this study.

2.5. Source definition and determination of DCF

MCNP software simulated 10^7 ^{131}I disintegrations (10^7 chosen to optimize variance reduction with run time) to mimic ^{131}I decay and estimate the corresponding energy deposited per disintegration. Disintegrations were distributed randomly across the particular source organ. The locations and magnitudes of energies deposited in each organ (whether or not the source) as well as the fish body were tabulated and analyzed. Energies deposited in the thyroid lumen (Raine et al. 2005) and the swim bladder are not of concern as these are non-tissue structures containing fluid and air, respectively, and have no biological significance. Separate MCNP runs were conducted for beta particles and gamma photons corresponding to ^{131}I decay, as well as for different source organs (e.g. thyroid, liver, and GI tract for the stylized and voxel models).

Total deposited energy tabulated was normalized by simulated disintegrations, i.e. MCNP output reports energy deposited per disintegration (MeV dis^{-1}). The initial energies of beta particles or gamma radiations emitted from the simulated disintegrations were randomly selected from appropriate frequency distributions specified in the MCNP program. The initial beta energies were randomly selected from a continuous distribution of possible energies ranging up to a maximum energy of 0.8069 MeV with an average energy of 0.1821 MeV (Stabin and CQP 2002). Gamma energies were randomly selected from either 0.364 MeV with probability 0.817 or 0.637 MeV with probability 0.072 with lower probability energies not being considered (Stabin and CQP 2002).

The tabulation of energies (MeV) deposited were made using *f8 tally function in MCNP, i.e. that tally which records the sum of all energies deposited in the tissue by that particle type as well as its secondary particles (X-5 Monte Carlo Team 2003). A dose conversion factor (DCF) of

$0.013824 \cdot E$ mGy d^{-1} per Bq g^{-1} (where E is the energy deposited per disintegration (MeV dis^{-1}) in the tissue or organ of interest, and 0.013824 is the appropriate unit conversion) was determined directly from the MCNP output.

2.6. Determination of cumulative dose rates and doses

The empirical models developed by Martinez et al. (2014) were combined with the MCNP simulation (see Appendix A2 for example MCNP input) to compute cumulative organ doses from the decay of ^{131}I. First, the predicted ^{131}I concentrations (Bq kg^{-1}) in the source organ as a function of time, $B(t)$, were determined (Equation 2-3) from empirical models described in Martinez et al. (2014):

$$B(t) = \mu \cdot \left(\frac{a}{k-b} \right) \cdot \left(e^{-b \cdot t} - e^{-k \cdot t} \right) \tag{2-3}$$

where μ is the uptake constant (L kg^{-1} d^{-1}) in the body or tissue of interest, k is the loss rate constant (d^{-1}) from the body or tissue of interest, a is the initial concentration in the water (Bq L^{-1}), and b is the rate of loss (d^{-1}) from the water (as described above). Values for a (1 Bq mL^{-1}) were chosen to normalize activity concentration by initial water concentration. Values of b correspond to the decay rate of ^{131}I (0.0862 d^{-1}). Values for μ and k are taken from Martinez et al. (2014) (Table 2.2). Concentrations of ^{131}I in the source organ were then multiplied by the appropriate mass ratio and the DCF (µGy d^{-1} per Bq kg^{-1}) obtained from MCNP to acquire a dose rate (µGy d^{-1}). The dose rate, $\dot{D}(t)$, at time t is given by Equation 2-4:

$$\dot{D}(t) = \text{DCF} \cdot (\text{mass ratio}) \cdot B(t) = \text{DCF} \cdot (\text{mass ratio}) \cdot \mu \cdot \left(\frac{a}{k-b} \right) \cdot \left(e^{-b \cdot t} - e^{-k \cdot t} \right) \tag{2-4}$$

Mass ratios were used to convert activity concentration in the source organ to an equivalent activity concentration for the target organ. In the case that the source and target organs are the same, the mass ratio will be unity.

To determine the time at and magnitude of maximum dose rate, we set the derivative of dose rate to zero, and solve for *t* (Equation 2-5 and Equation 2-6):

$$\ddot{D}(t) = \text{DCF} \cdot (\text{mass ratio}) \cdot \mu \cdot \left(\frac{a}{k-b} \right) \cdot \left(-be^{-bt} + ke^{-kt} \right) \tag{2-5}$$

$$\Rightarrow t_{\max} = \frac{\ln \frac{b}{k}}{b-k} \tag{2-6}$$

Note that calculating the overall maximum dose rate (from all sources) is non-trivial and not explored here. A conservative estimation can be obtained by summing the maximum dose rates from each organ source. The dose rate was then integrated over time to determine a cumulative dose (μGy). The cumulative dose at time *t,* $D(t)$, is then given by Equation 2-7:

$$D(t) = \text{DCF} \cdot (\text{mass ratio}) \cdot \mu \cdot \left(\frac{a}{k-b} \right) \cdot \left(\frac{1}{b}\left(1-e^{-bt}\right) + \frac{1}{k}\left(e^{-kt}-1\right) \right) \tag{2-7}$$

3. Results

Dose and dose rate predictions are limited to the first 32 days because the uncertainty of the extent to which the passage of ^{131}I through the food chains will continue to support the predictions beyond day 27 is unknown (Short et al. 1969; Martinez et al. 2014). Values for μ and *k* will be constant for every phantom, as will the time to the maximum dose rate from each source organ (Table 2.5). Note that "thyroid" in this section refers to the biologically significant portion of the thyroid, or the thyroid epithelial shell discussed in Chapter 1.

Table 2.5: Time to maximum dose rate listed by source organ.

	Time (days) at maximum dose rate (by source organ)
Thyroid	19.43
Liver	22.03
GI	14.78

As the most significant radiation doses will be to the organs that are both the source and target, results are shown below for said organs as well as whole body. Detailed tabulations of results, including all organs, are contained in Appendix A3.

3.1. Simplistic model

The simplistic model considers only the thyroid as a source, with no other organs surrounding it. The maximum dose rate to the thyroid in this model will be 4.72×10^{2} µGy d^{-1}. The maximum dose rate to the whole body will be 2.89×10^{-2} µGy d^{-1}. The progression of cumulative dose in time is shown in Figure 2.10 below.

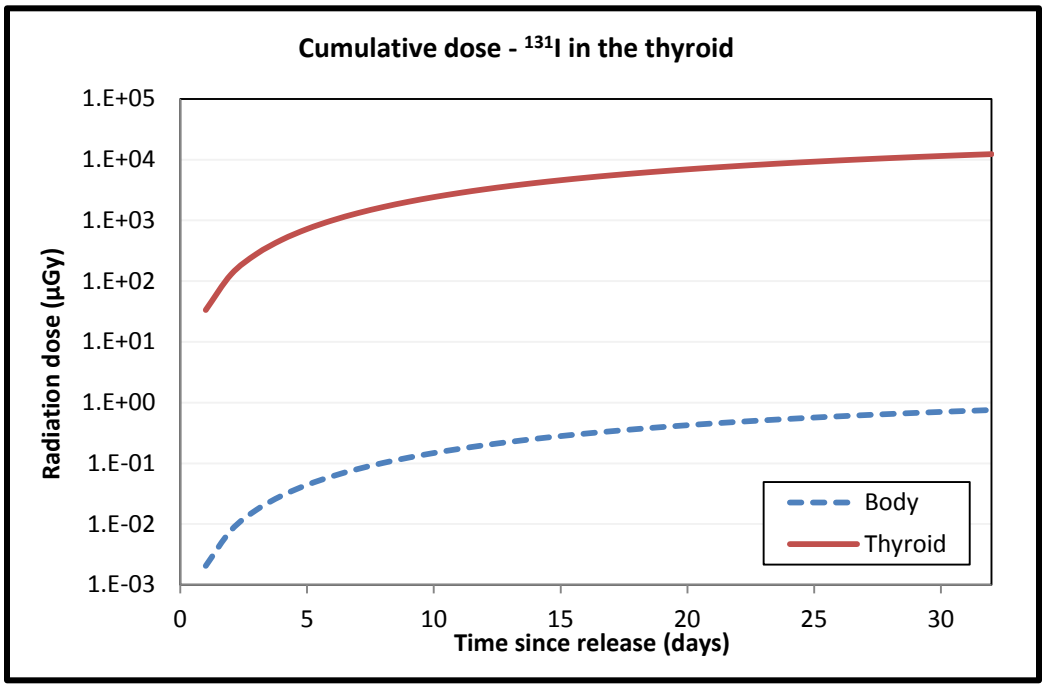

Figure 2.10: Cumulative radiation dose to the thyroid and whole body with the thyroid as the source organ (simplistic phantom).

3.2. Stylized model

The stylized model considers the same thyroid and fish body as does the simplistic model, with eight additional organs. The stylized model also considers radiation dose received from ^{131}I uptake by

the liver and the GI tract. The maximum dose rates to the organs both a source and target in this model are listed in Table 2.6 below, along with whole body dose rates.

Table 2.6: Summary of maximum dose rates by source organ using the stylized model, assuming an initial water concentration of 1 Bq mL^{-1}.

Organ	Maximum dose rate (µGy d^{-1}) by source organ			
	Thyroid	Liver	GI	Total
Whole Body	2.89E-02	5.02E-02	5.01E+00	5.35E+00
Thyroid	4.72E+02	1.22E-02	2.92E-02	4.72E+02
Liver	1.64E-03	7.37E+01	6.12E-02	3.40E+02
GI Tract	3.61E-04	4.78E-02	7.49E-01	7.44E+01
Intestine	2.42E-04	4.63E-02	1.01E+02	1.01E+02
Cardiac Stomach	4.90E-04	6.34E-02	1.01E+02	1.01E+02
Pyloric Stomach	3.19E-04	3.30E-02	1.04E+02	1.04E+02

The progression of cumulative dose in time for each source organ is shown in Figure 2.11 through Figure 2.13 below.

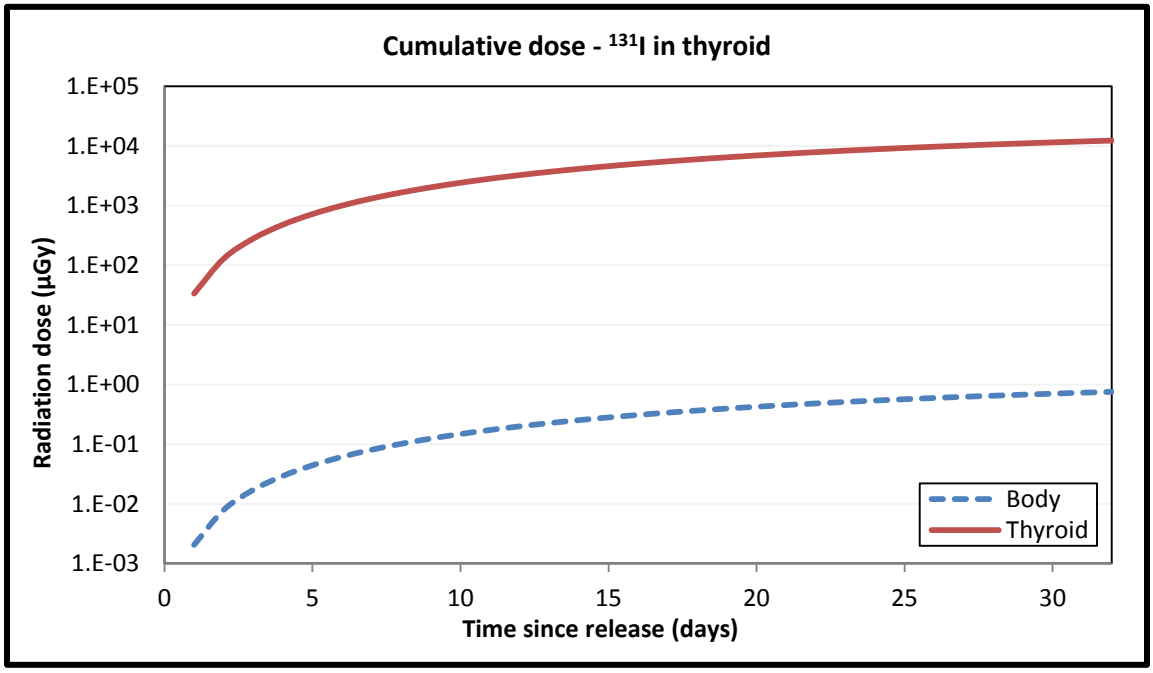

Figure 2.11: Cumulative radiation dose to the thyroid and whole body with the thyroid as the source organ (stylized phantom).

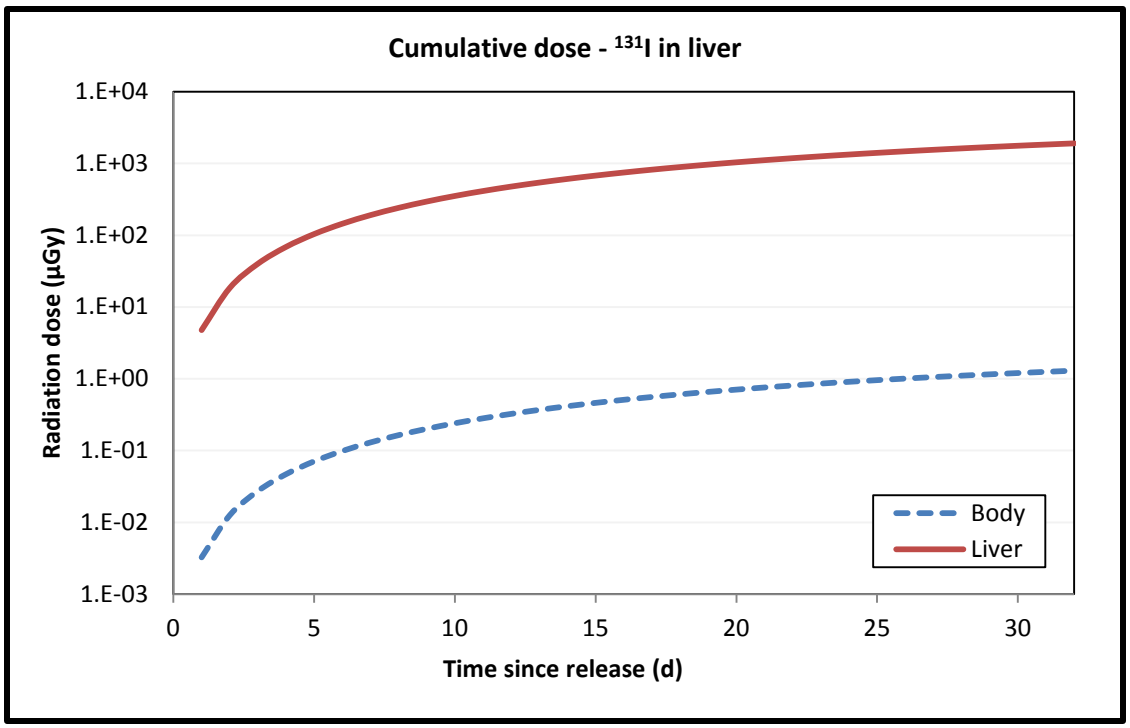

Figure 2.12: Cumulative radiation dose to the liver and whole body with the liver as the source organ (stylized phantom).

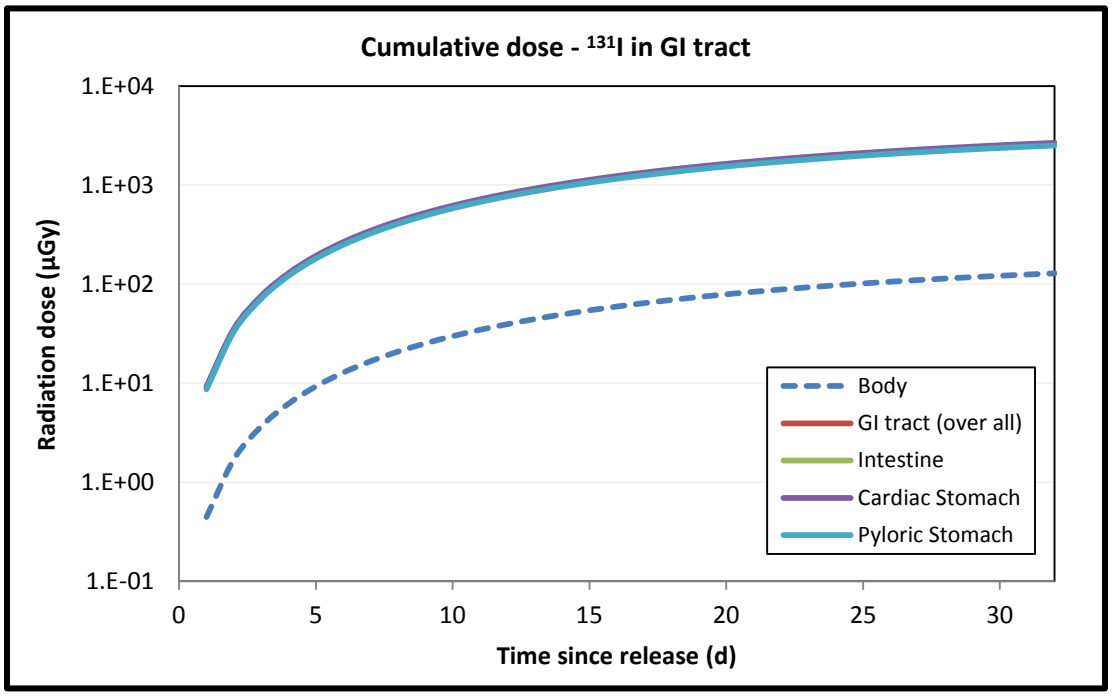

Figure 2.13: Cumulative radiation dose to the GI tract and whole body with the GI tract as the source organ (stylized phantom).

Total cumulative doses received by all organs are shown in Figure 2.14 on a log scale; additional cumulative dose charts are contained in Appendix A3.

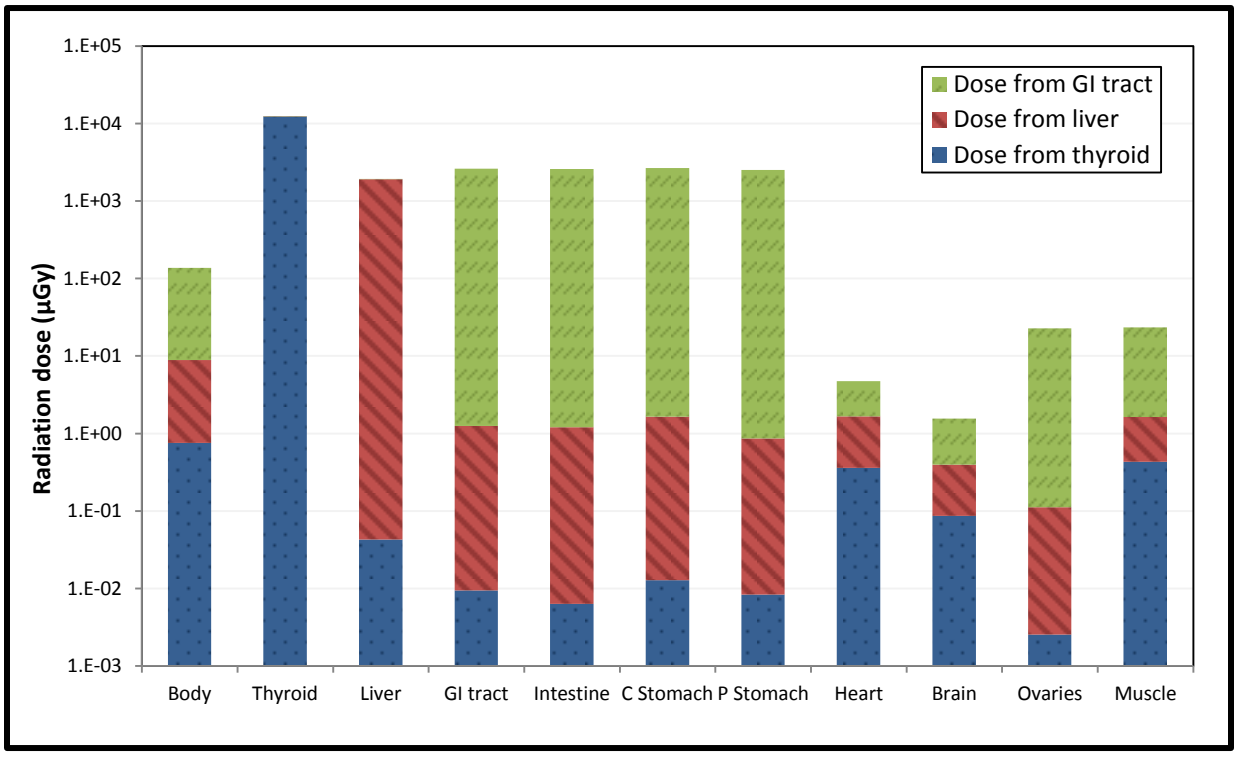

Figure 2.14: Total cumulative (internal) radiation dose from all sources of ^{131}I, radiation dose on a log scale (stylized phantom).

3.3. Voxel model (CSUTROUT)

CSUTROUT consists of a three-dimensional rendering of an actual fish body. It includes the same organs as the stylized model, with seven additional organs. Our dose model using CSUTROUT considers radiation dose received from ^{131}I uptake by the thyroid, liver, and the GI tract. The maximum dose rates to the organs both a source and target in this model are listed in Table 2.7 below, along with whole body dose rates.

Table 2.7: Summary of maximum dose rates by source organ using CSUTROUT, assuming an initial water concentration of 1 Bq mL^{-1}.

Organ	Maximum dose rate (µGy d^{-1}) by source organ			
	Thyroid	Liver	GI Tract	Total
Whole Body	3.67E-02	3.83E-01	4.97E+00	5.43E+00
Thyroid	6.23E+02	4.20E-02	2.09E-01	6.53E+02
Liver	4.32E+02	7.23E+01	2.31E+00	7.46E+01
GI tract	5.53E-03	1.84E-01	9.66E+01	9.67E+01
Intestine	2.01E-03	5.42E-02	9.95E+01	9.96E+01
Cardiac Stomach	1.07E-03	1.11E-01	8.55E+01	8.56E+01
Pyloric Stomach	1.57E-03	3.65E-01	1.08E+02	1.08E+02

The progression of cumulative dose in time for each source organ is shown in Figure 2.15 through Figure 2.17.

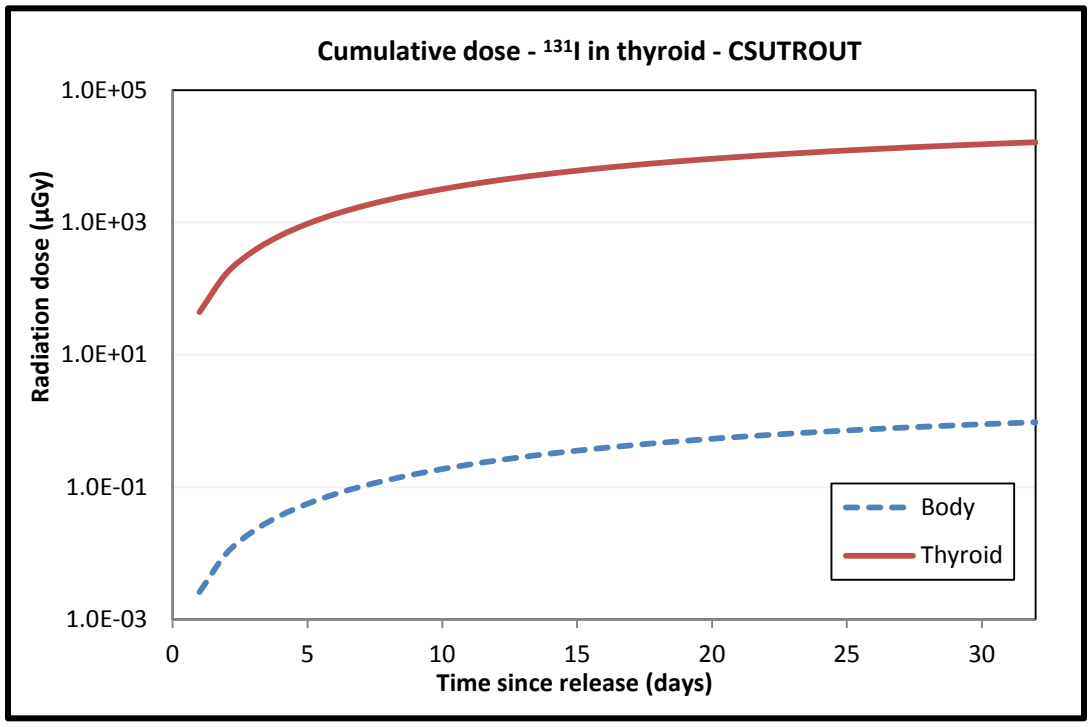

Figure 2.15: Cumulative radiation dose to the thyroid and whole body from ^{131}I distributed in the thyroid; left graph utlizes a log scale on the y-axis to better visualize dose differences.

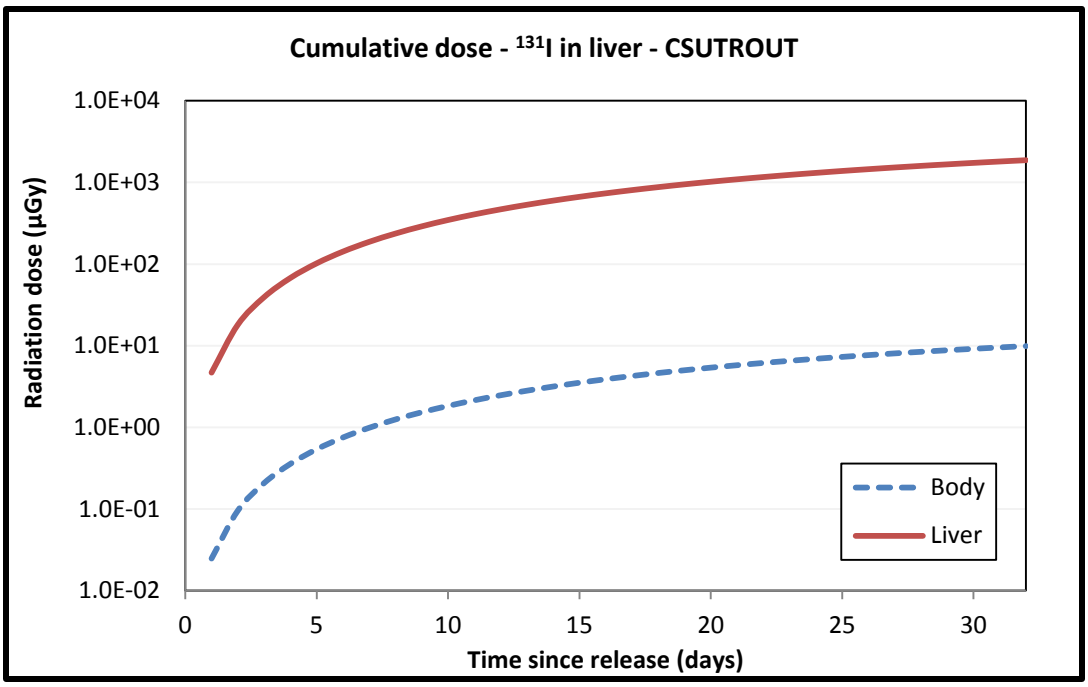

Figure 2.16: Cumulative radiation dose to the liver and whole body from ^{131}I distributed in the liver; left graph utlizes a log scale on the y-axis to better visualize dose differences.

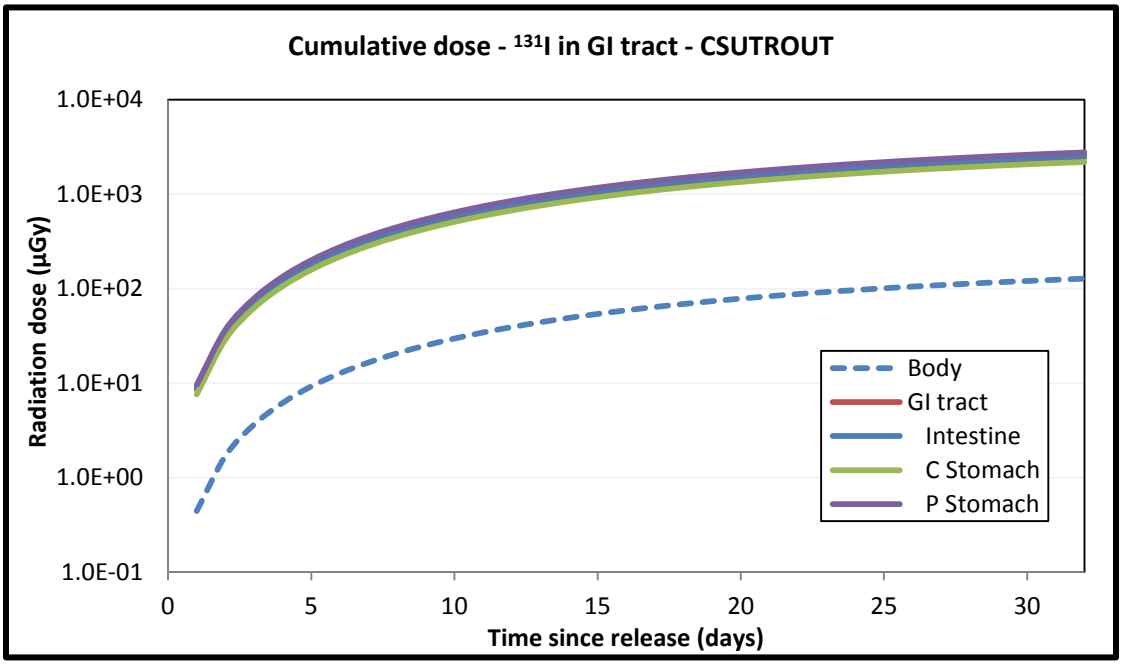

Figure 2.17: Cumulative radiation dose to the GI tract and whole body from ^{131}I distributed in the GI tract; left graph utlizes a log scale on the y-axis to better visualize dose differences.

Total cumulative doses received by all organs are shown in Figure 2.18 on a logarithmic scale; additional cumulative dose charts are contained in Appendix A3.

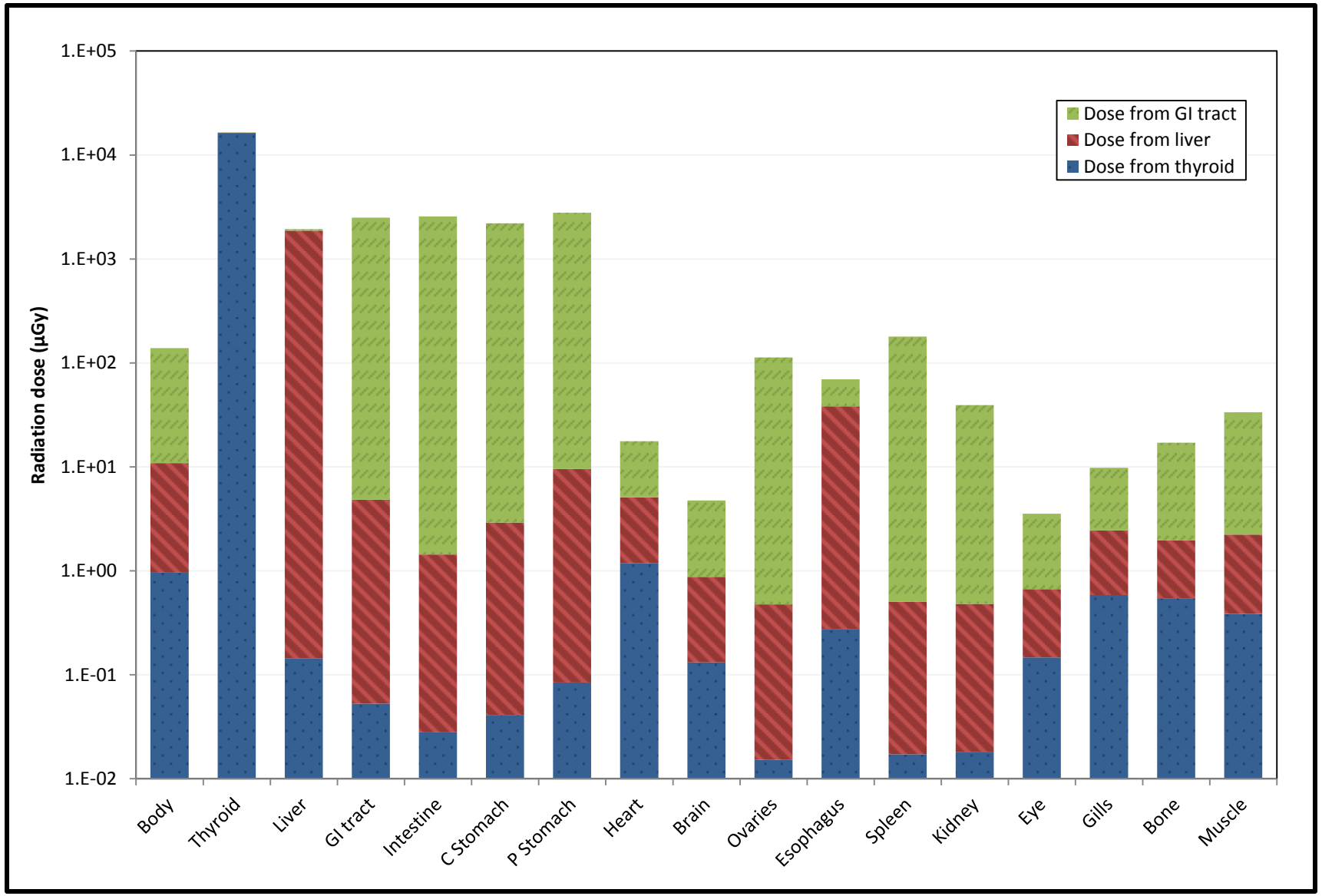

Figure 2.18: Total cumulative (internal) radiation dose from all sources, radiation dose on a log scale.

4. Discussion

4.1. Model comparison

Progressively more detailed phantoms were considered to assess the difference in organ dose and DCFs with improved anatomical realism. Additionally, we consider and compare the use of organ specific DCFs vice the use whole body to organ mass ratios for dose determination. The results for the thyroid and whole body were the same for the simplistic and stylized model. Therefore, we consider only the differences in the stylized phantom and CSUTROUT for organs the models have in common.

4.1.1. Cumulative 32 day dose

Comparisons of cumulative doses received to source-target organs are shown in Figure 2.19 and Figure 2.20.

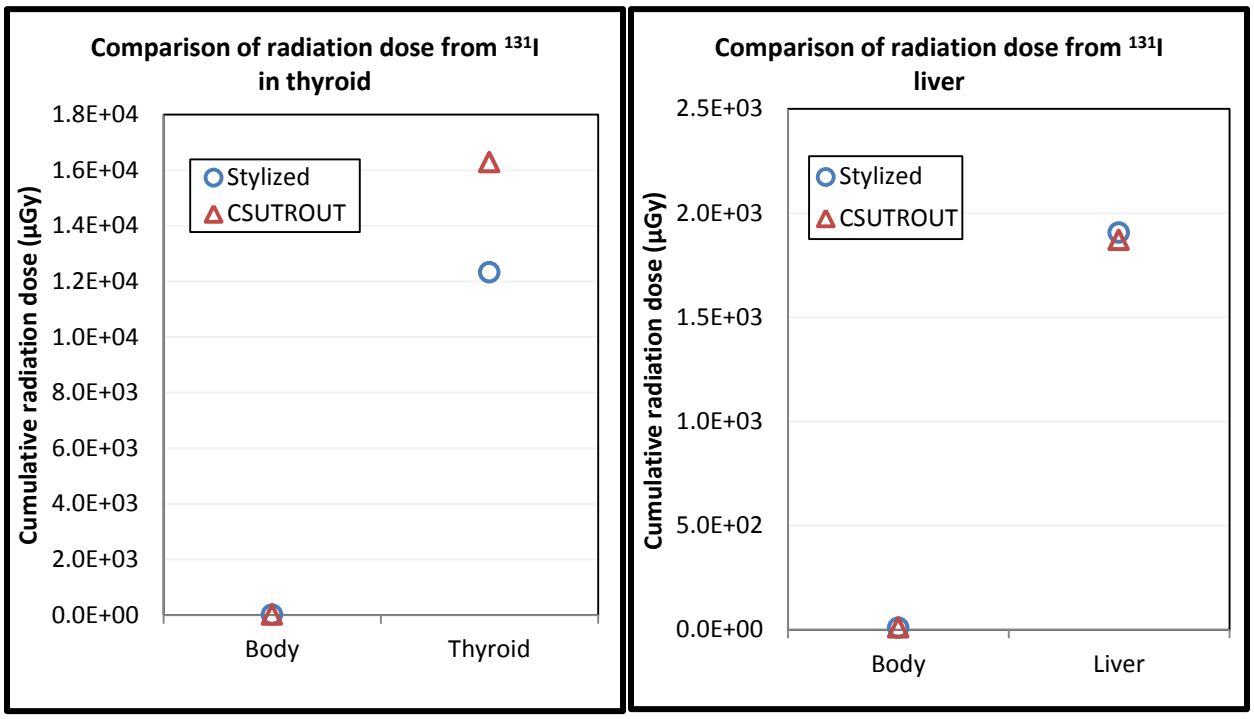

Figure 2.19: Comparison of 32 day cumulative doses received from ^{131}I with the thyroid(left graph) or liver (right graph) as the source organ, as calculated by the stylized phantom and CSUTROUT.

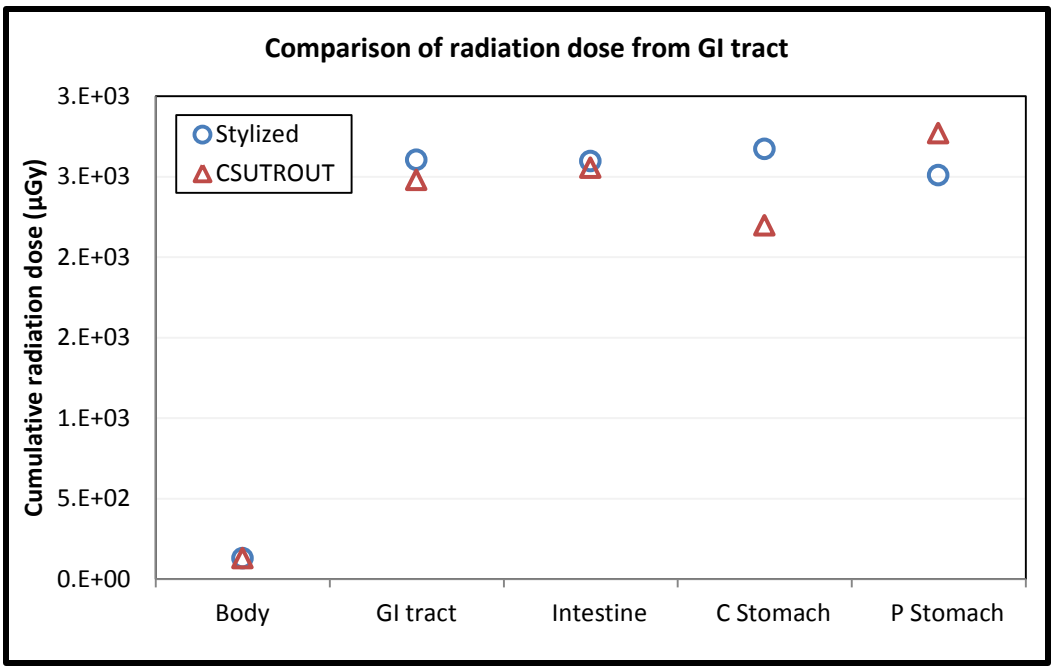

Figure 2.20: Comparison of 32 day cumulative doses received from ^{131}I with the GI tract as the source organ, as calculated by the stylized phantom and CSUTROUT.

The models are similar in prediction of dose, especially for source-target organs. For ^{131}I distributed in the thyroid, the percent differences between model estimates of dose are 24% (0.2 µGy absolute difference) and 28% (3960 µGy absolute difference) for the whole body and thyroid respectively. For ^{131}I distributed in the liver, the percent differences between model estimates of dose are 19.5% (1.8 µGy absolute difference) and 1.8% (35 µGy absolute difference) for the whole body and liver respectively. Considering the GI tract as the source, portions of the GI tract (intestine and stomach) range up to about 20% difference between model estimates of dose, but the doses to the GI tract as a whole organ system are within 110 µGy (about 4.4% difference). The whole body dose estimates for ^{131}I in the GI are only 0.7% different (1 µGy absolute difference). The differences for non-source organs were similar, with the highest doses to these organs due to radiation exposure from the GI tract. The GI tract is a larger organ system than either the liver or thyroid and lies in close proximity to several other organs, meaning a radiation source distributed in the GI tract will have a wider distribution and, in general, a shorter path to other organs; this is particularly relevant for ^{131}I as beta

particles have a relatively short range and will deposit most of their energy just prior to coming to rest (Cember and Johnson 2009).

The larger percent differences for ^{131}I distributed in the thyroid are equated to the difference in size between the thyroid organs of the stylized model and CSUTROUT, as the thyroid in CSUTROUT was not visible on CT and had to be approximated by hand. Results for DCFs as well as details of cumulative doses received to all organs are contained in Appendix A3. A summary of doses received by all organs considered from uptake of ^{131}I is shown in Figure 2.21.

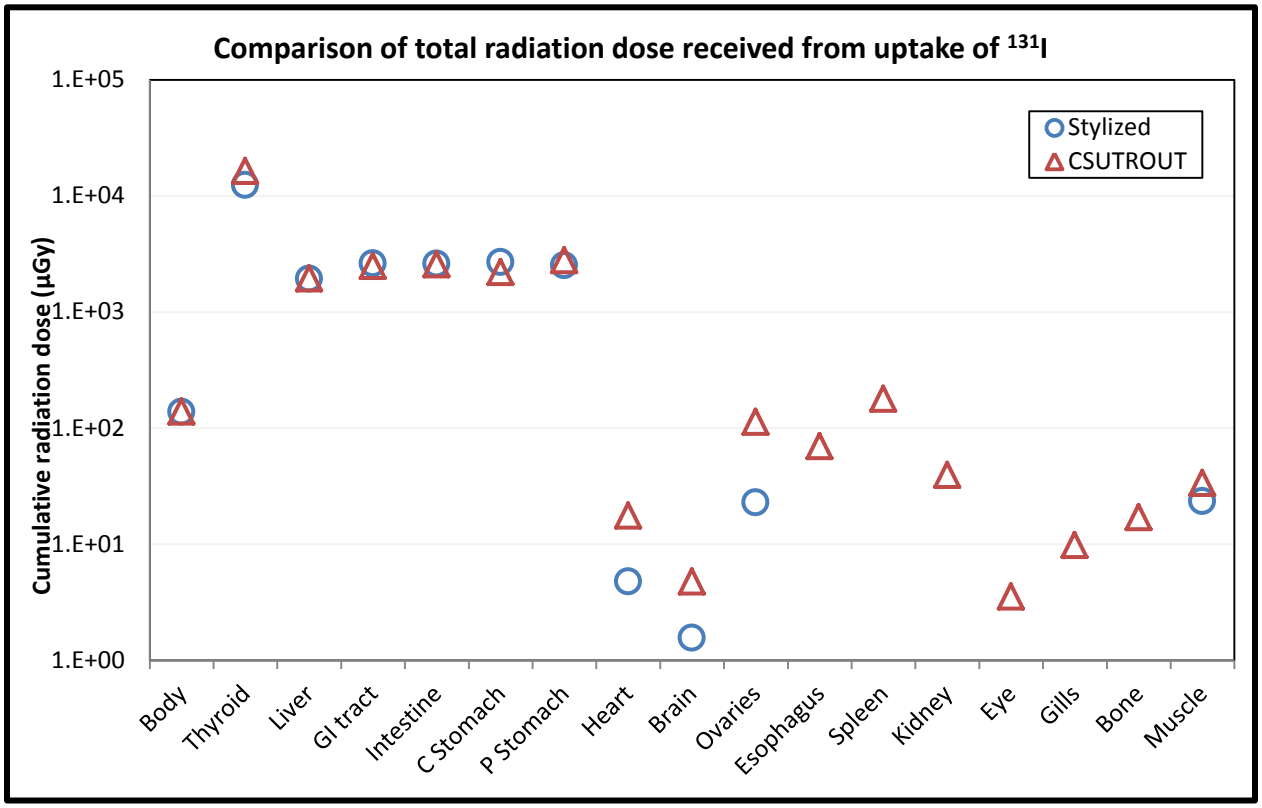

Figure 2.21: Comparison of total cumulative 32 day radiation dose from ^{131}I (log scale) received by organs considered in the stylized model and in CSUTROUT from all internal source organs.

The thyroid received the highest doses (1.23×10^4 and 1.63×10^4 µGy, stylized model and CSUTROUT respectively), due to preferential uptake of ^{131}I. The liver and GI tract will also take up ^{131}I, but to a much lesser extent than the thyroid (Figure 2.1). The highest doses to organs not taking up ^{131}I were to the ovaries (22.8 and 113 µGy using the stylized model and CSUTROUT respectively) and the

spleen (179 µGy, CSUTROUT), although these doses were much lower than doses to the source organs (between 1900 and 16300 µGy).

4.1.2. Factor differences in using mass ratios to calculate organ specific DCF

In the absence of organ-specific data, a conservative estimate of organ specific DCF (Gómez-Ros et al. 2008) is to multiple the whole body DCF by the ratio of the mass of the whole body to the mass of the particular organ of interest:

$$DCF_{organ} = DCF_{whole\ body}\left(\frac{m_{whole\ body}}{m_{organ}}\right) \quad (2\text{-}8)$$

It should be noted that this approach is only valid for organs that are both the source and the target of radiation. The organ specific DCF was calculated directly from MCNP output and then calculated again using the mass ratio approach. The factor difference (ratio) between these two values is shown in Figure 2.22.

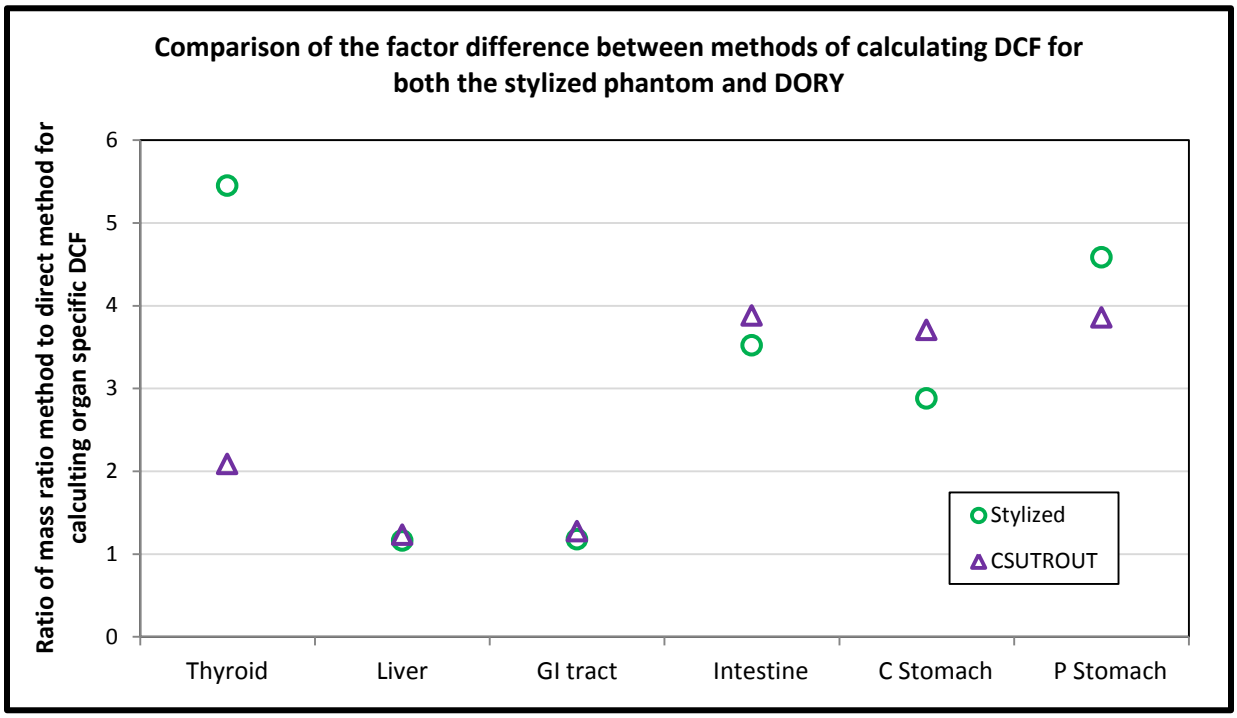

Figure 2.22: Factor difference between calculating organ-specific DCFs directly and by using the mass ratio approach. This factor difference is shown for both the stylized phantom and CSUTROUT.

All factor differences, using either model, are less than 10 for all source-target organs. The differences between models are due to the slight difference in size and location of the particular organs, although these differences are small. The mass ratio approach is therefore a reasonable approximation of organ dose, as suggested by Gómez-Ros et al. (2008), although this approach can only be used for organs that preferentially take up a radionuclide.

4.2. Consideration of fish size using the simplistic model

We consider the simplistic model in comparing size effect on the ability of the mass ratio method to predict organ dose. As seen in section 4.1.2, the thyroid has the greatest difference between the mass ratio method and the direct method for dose approximation (out of the three source-target organs). Therefore, we consider the thyroid here. CSUTROUT cannot be re-sized, although the stylized and simplistic models can be. The DCFs determined by the stylized and simplistic models are the same; therefore we use the previously scaled set of simple models developed in Chapter 1 (Martinez et al. 2014), along with the simplistic model used in this chapter. The effect size has on dose is discussed in Chapter 1, so here we consider data from Chapter 1, not yet shown in detail, to consider the difference fish size will have on the mass ratio prediction of organ radiation dose (or organ dose conversion factors).

Consider the energy deposition distribution shown in Figure 2.23 for fish of different sizes (Table 2.8 contains details of fish dimensions).

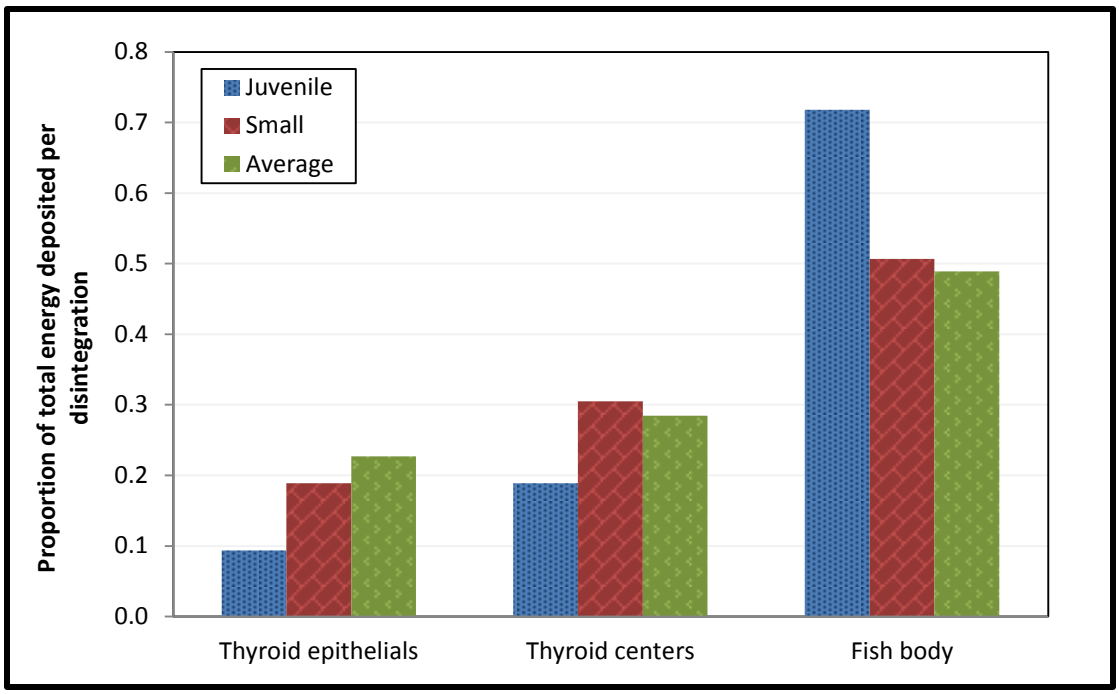

Figure 2.23: Energy distribution by organ and fish size from Chapter 1 data, including beta and gamma emissions from ^{131}I.

Table 2.8: Fish size and corresponding dose conversion factors for both the thyroid epithelial and whole body[2].

Fish reference	Fish size (length, mass)	DCF (µGy d^{-1} kg Bq^{-1})	
		Thyroid epithelial	Total body
Juvenile	90 mm, 9.896 g	2.647E-04	2.830E-03
Current study	286 mm, 222.7 g	5.412E-04	2.947E-03
Small	360 mm, 633.3 g	6.061E-04	3.207E-03
ICRP[3]	500 mm, 1257 g	7.198E-04	3.319E-03
Average	630 mm, 3394 g	8.065E-04	3.556E-03

[2] The juvenile, small, and average fish all have relative dimensions of 9:2:1 (length:width:height), scaled from data in Raine et al. (2005). The simplistic model developed here has a length:width:height of about 11.5:2.3:1, and the ICRP representation developed in the Chapter 1 study has a length:width:height of about 8.3:1.3: 1. However, thyroid dimensions (all) were determined relative to the length of the fish.

[3] The ICRP representation listed here and developed in Chapter 1 uses a soft tissue density of 1 g cm^{-3} to correspond with that listed in ICRP 108 (ICRP 2008). Soft tissue in the other models was assigned a density of 1.05 g cm^{-3} to be consistent with ICRU tissue compositions (ICRU 1989).

More energy will be proportionally deposited in the thyroid of a larger fish than in a smaller fish (see discussion in Chapter 1, Section 4.3). The probability of interactions between beta or gamma radiations and the media through which they travel (e.g. tissue) increases with distance travelled. Also, in addition to having a relatively short range, beta particles will deposit most of their energy towards the end of their range, just prior to coming to a stop (Cember and Johnson 2008). As fish size increased, a larger proportion of energy was deposited in the thyroid per unit mass. More energy was deposited in the larger fish thyroid per until mass due to larger tubule sheath dimensions. Juvenile fish with very thin tubule sheaths (10 μm) will result in radiation readily passing through the thyroid tissues and depositing minimal energy. Increasing the thickness of the tubule sheaths in the larger fish increases the likelihood (e.g. frequency) of radiation tissue interactions.

Because of the differences in relative energy deposition between different fish sizes, DCF for the thyroid and for the whole body will be different. Values for DCFs of the different size simplistic models are shown in Table 2.8 along with fish sizes.

Although DCF will be different, the mass ratios (whole body to thyroid) remain the same. The mass ratio method for estimating thyroid organ dose will therefore give proportionally different results for different size fish. The estimated thyroid radiation dose as calculated by each method, for each size fish, is shown in Table 2.9, along with the ratio between them.

Table 2.9: Organ radiation dose as determined directly using the thyroid DCF and indirectly using mass ratios for different size fish. The ratio between the two approximations is also listed.

	Estimated Organ Radiation Dose (mGy)		Ratio
	Using thyroid DCF	Using mass ratios	
Juvenile	5.90	63.2	10.7
Current study	12.3	67.1	5.4
Small	13.5	71.6	5.3
ICRP	16.1	74.2	4.6
Average	18.0	79.6	4.4

Note that the ratio of the DCFs (whole body to thyroid) will be the same as the ratio of the cumulative organ dose estimations as listed in Table 2.9. The mass ratio method becomes more accurate as fish size increases. The relationship between fish size is shown in Figure 2.24.

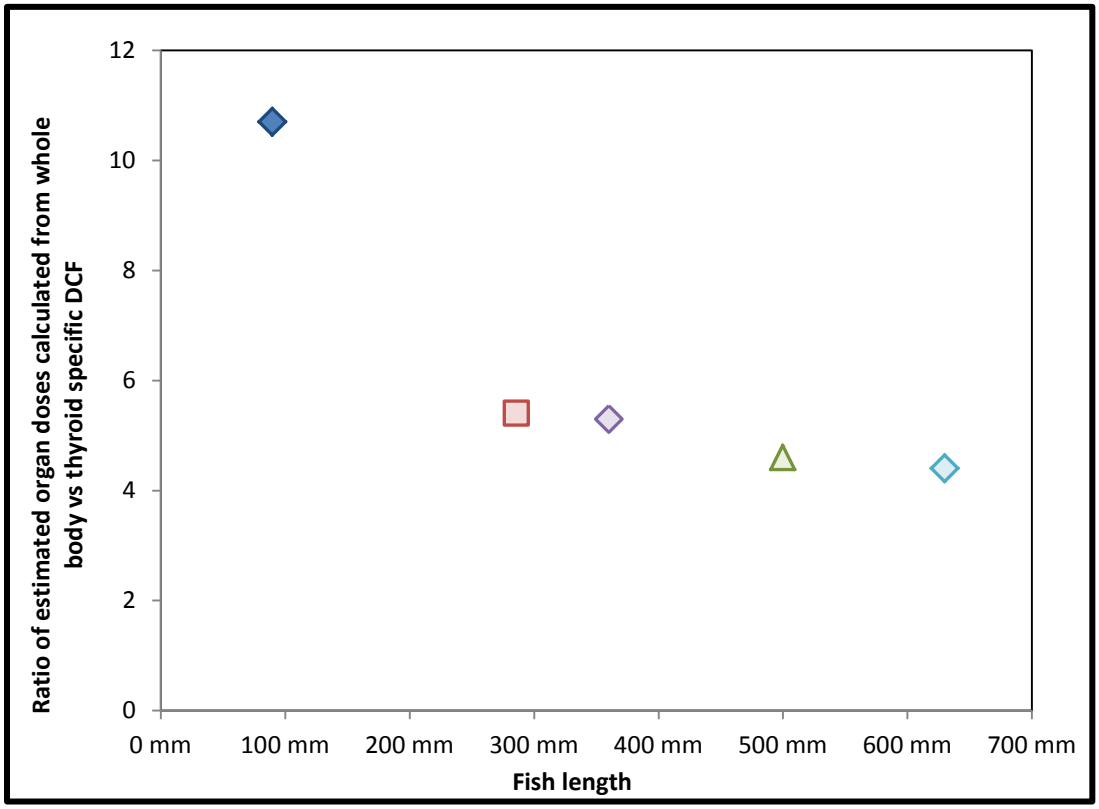

Figure 2.24: Graphical illustration of the ratio of estimated radiation dose calculated by (1) using the whole body DCF and converting to a thyroid DCF using mass ratios to (2) using the thyroid DCF directly for trout of 5 different lengths. Diamonds represent body ratios (length:height:width) of 9:2:1. The square and triangle represent alternate body dimensions as discussed in the text.

Figure 2.25 considers the relationship between fish length and relative accuracy of the mass ratio method for fish of the same relative dimensions.

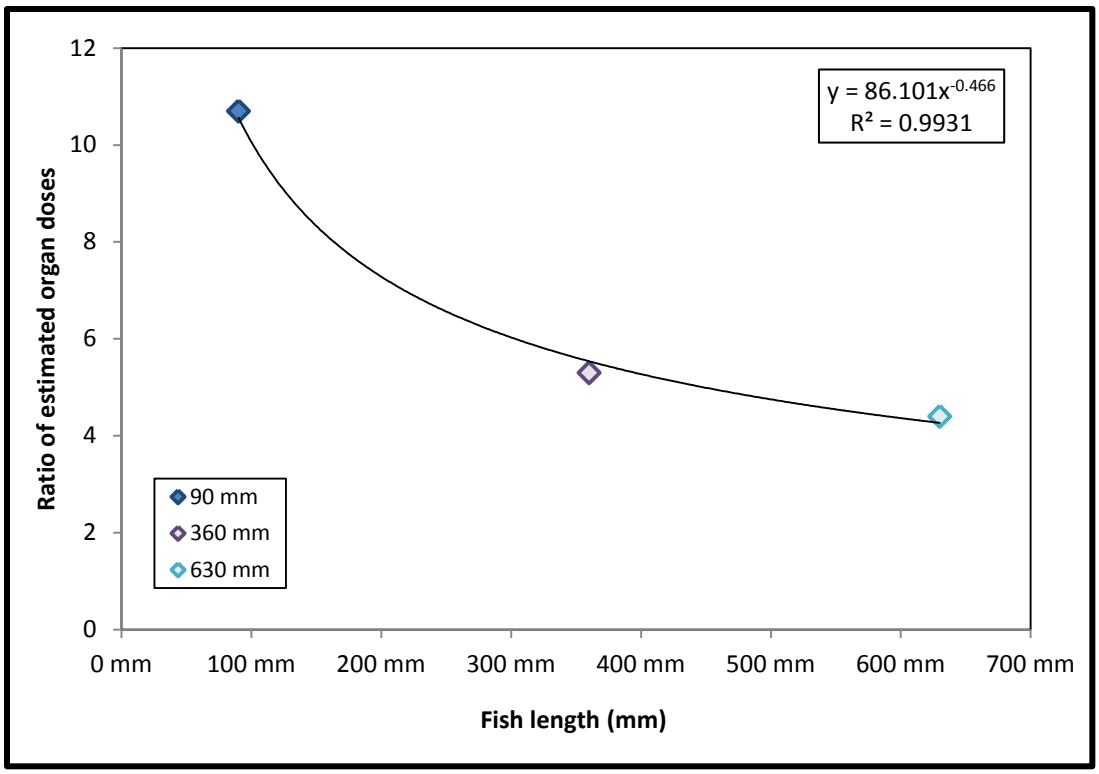

Figure 2.25: Ratio of estimated organ doses, as Figure 2.24, for simplistic models of relative dimensions of 9:2:1 (length:width:height), with fitted power equation and corresponding R^2 value.

The above figures further demonstrate that the mass ratio approach is indeed a valid approximation of organ radiation dose, in agreement with Gómez-Ros et al. (2008). Additionally, this provides an example of the effect size has on how accurate the mass ratio approach will be; for larger animals and larger organs, the mass ratio approach will be more accurate. This follows from the discussion of beta energy deposition in Chapter 1, as larger organs will self-absorb more radiation than smaller organs.

4.3. Model considerations

Although the voxel phantom provides the most anatomically accurate model, the development process is very time-consuming. Although automatic segmentation is an available feature of 3D Doctor, it cannot adequately distinguish the various soft tissue organs. Manual contouring of organs on the original image set is labor-intensive, tedious, and involves user-specific assumptions about anatomy. Additionally, several organs have very low image contrast, making the segmentation nearly impossible,

and other organs, such as the fish thyroid, are so small as to be beyond the resolution of the CT image slices. For organ dose calculations numerous internal organs/tissues have to be identified and contoured; the resulting size of a whole-body computational phantom with organs can potentially be too large for MCNP to process (Xu and Eckerman 2010). The compression factor of the boundary file (organ contours) can be changed to reduce the number of voxels, but resolution is sacrificed.

Whereas stylized phantoms are easily scalable (Martinez et al. 2014), the voxel phantom developed here is fish specific; for different species, sizes, life stages, gender, etc. a different voxel phantom would need to be developed for the most accurate dose assessment. These issues are consistent with voxel phantom development, in general (Xu and Eckerman 2010).

5. Conclusions

5.1. Consideration of the mass ratio approach

Although calculations in this study did not assume a homogenous whole body distribution of radionuclides, calculating organ specific DCF using the mass ratio approach described by Gómez-Ros et al. (2008) was a reasonable approximation for calculating DCFs directly from MCNP output. However, this approach is only valid for organs with preferential uptake of a radionuclide. Therefore, one significant benefit of both the stylized phantom and CSUTROUT is the ability to determine radiation dose in organs due to “cross fire,” i.e. the ability to calculate dose to organs from other organs.

5.2. Optimal phantom choice

Although CSUTROUT was the most anatomically realistic phantom, it required much more resource dedication to develop than did the stylized phantom for similar results. Additionally, the stylized phantom can be scaled to represent trout sizes whereas CSUTROUT cannot be. There may be instances where a detailed phantom such as CSUTROUT is appropriate, as it will provide the most accurate radiation dose and dose rate information for the size, sex, and species considered, but

generally, the stylized phantom appears to be the best choice for an ideal balance between accuracy and resource requirements.

5.3. Utility and implications of model development

The results of this study work towards eventual application and integration into the regulatory paradigm of environmental protection of non-human biota. Either model could be used in demonstrating regulatory compliance in environmental protection, whether at a nuclear power station or a waste repository. Eventually, we would determine specific radiation effects to fish, and use the models developed here to equate effects with certain doses or dose rates.

In addition to establishing environmental benchmarks of health, understanding the biological effects of radiological contaminants in organisms and ecosystems has application in emergency response and recovery as well as resource management. The combination of computational and empirical models could be used for any radionuclide, with available data, to determine activity concentrations and radiation doses to fish. Establishing baseline models, such as discussed in Chapter 1 for ^{131}I, could be used in place of site-specific data as well. Knowledge of the impact of an accidental or purposeful release of radiation would have specific and beneficial utility for fisheries, for fishing communities, and for general assessment and protection of aquatic environment health.

CHAPTER 3: APPLICATION OF PREVIOUSLY DEVELOPED MODELS TO ESTIMATE ORGAN RADIATION DOSE IN FERN LAKE RAINBOW TROUT FROM UPTAKE OF ^{99}MO

1. Introduction

The purpose of this study is to demonstrate the applicability of the models described and developed in previous chapters to an additional radionuclide, namely molybdenum-99 (^{99}Mo). The Fern Lake study discussed in Chapter 1 (Short et al. 1969) consisted of four field experiments, in which phosphorus-32, calcium-45, and ^{99}Mo were applied to the Fern Lake in addition to ^{131}I. We were able to locate the ^{99}Mo data (Short et al. 1971), and although it is limited, we consider it here as an application for our previously developed models.

1.1. Molybdenum in the environment

Molybdenum (Mo) is used as a constituent in numerous alloys, and compounds of Mo are used in lubricants, rubbers, and fertilizers. Anthropogenic sources of Mo in the environment therefore include leaching at molybdenum mines, water contamination during the manufacture of products containing Mo, and use of molybdenum-containing fertilizers. Naturally occurring Mo in the aquatic environment is mostly from the weathering and subsequent runoff to streams and lakes from varying types of rock (Reid 2002).

1.2. Molybdenum uptake and toxicity in fish

Molybdenum is an essential micronutrient in animals and considered to have low toxicity to freshwater fish (e.g. McDonnell 1977) as is supported by several studies focused on salmonids of the genus *Oncorhynchus* (Reid 2002). Concentrations of Mo in *Oncorhynchus mykiss* tissues relative to Mo concentration in the surrounding water (e.g. Short et al. 1971; Ward 1973; Regoli et al. 2012) have been measured and compared to components in the aquatic food chain. It is known that Mo does not biomagnify in aquatic food webs (Regoli et al. 2012), but the mechanistic details of Mo uptake in fish

have not been investigated; additionally, very little is known about the metabolism or mechanism of toxicity of Mo (Reid 2002). Molybdenum concentrations in fish muscle will remain fairly consistent (Ward 1973, Regoli et al. 2012), although concentrations in other organs (specifically the liver) (Ward 1973; Reid 2011) will increase with background levels of Mo. Molybdenum does not accumulate in muscle, and does not distribute homogenously in the fish body.

1.3. Radioactive molybdenum

Molybdenum-99 (^{99}Mo), a radioactive isotope of Mo, is a fission product produced through the neutron bombardment of enriched uranium (^{235}U) in a nuclear reactor (Molinksi 1982; Zolle 2007; Le 2014). Molybdenum-99 can also be produced through neutron activation of molybdenum metal or oxides, but the specific activity of this method is low (Molinski 1982; Le 2014). The half-life of ^{99}Mo is 65.94 hours, and the half-life of its most common daughter, Technetium-99 metastable (^{99m}Tc; 87.7%), is 6.015 hours (ICRP 2008a). ^{99m}Tc-labeled radiopharmaceuticals are widely used in the medical industry, comprising 80-85% of diagnostic nuclear medicine imaging procedures world-wide every year (Zolle 2007; Le 2014).

2. Materials and methods

2.1. Development of models

Computational model development is discussed in detail in Chapter 2. Three increasingly detailed anatomical phantoms for *O. mykiss* were developed and compared for the purpose of estimating organ radiation dose and dose rates from ^{131}I uptake. The results for the simplistic and stylized phantom were the same, so here we consider only the stylized phantom and voxel phantom for comparison of radiation dose due to uptake of ^{99}Mo by Fern Lake rainbow trout.

The methodology behind empirical model development is described in detail by Martinez et al. (2014). For the ^{99}Mo empirical model, we take ^{99}Mo uptake data collected from another Fern Lake (see Chapter 1) experiment (Short et al. 1971) and follow the same procedure described by Martinez et al.

(2014). It should be noted that the ^{99}Mo data were only collected on a few samples following its release into the water column and are somewhat insufficient for the development of a robust empirical model. Multiple data points acquired on a single day were off set randomly by 0.1 days to have sufficient data points for nonlinear regressions. Even so, there were only six and seven observations for liver and GI uptake respectively, and the loss rate, *k,* had to be given a lower bound to force model convergence ($k_{\text{liver}} = 0.005\ \text{d}^{-1}$ and $k_{\text{GI tract}} = 0.01\ \text{d}^{-1}$). Values determined in this process include: *a*, the initial water concentration (Bq L^{-1}); *b*, the loss rate from the water (d^{-1}); μ, the uptake constant (L kg^{-1} d^{-1}) in the body or tissue of interest; and *k,* the loss rate constant (d^{-1}) from the body or tissue of interest. Water parameters are listed in Table 3.1, and organ parameters are listed in Table 3.2.

Table 3.1. The water parameters a, the initial concentration in the water, and b, the first order loss rate from the water column, for the ^{99}Mo concentrations in Fern Lake. Because of the different methods of estimation 95% confidence intervals are given for a *but standard errors are given for* b*.*

Initial Water Concentration (µg L^{-1})			Loss Rate (d^{-1})	
a	95% Confidence Interval		*b*	SE
0.0366	0.0283	- 0.0449	1.4963	0.3343

Table 3.2: The uptake (µ) and loss rate parameter (k) for biota and fish tissues and their standard errors for the lakes and aquaria included in this study.

	Uptake parameter (L kg^{-1} d^{-1})		Loss Rate (d^{-1})	
Organ	μ	SE	*k*	SE
Liver	22.2	3.39	0.005	N/A
Gastrointestinal tract	20.1	3.58	0.01	N/A

The concentrations of stable Mo in Fern Lake water and biota were reported in units of mass (Short et al. 1971), and empirical models were fitted to these data. The specific activity of the ^{99}Mo

solution reported by Short et al. (1971) was $889\,\text{mCi g}^{-1}$ (3.29×10^{13} Bq kg^{-1}) which was the value used in calculating activity concentrations (i.e. the initial activity concentration in water was $a = 1204$ Bq L^{-1}).

2.2. Determination of ^{99m}Tc activity concentration

Activity concentrations of ^{99m}Tc were derived from the relationship between ^{99}Mo and ^{99m}Tc. The relationship between a parent radionuclide and its daughter, assuming a branching ratio of 100%, was described (Equation 3-1) by Bateman (1910):

$$N_d(t) = \frac{\lambda_p}{\lambda_d - \lambda_p} N_p(0)\left(e^{-\lambda_p t} - e^{-\lambda_d t}\right) + N_d(0)e^{-\lambda_d t} \tag{3-1}$$

where $N_d(t)$ is the number of atoms of the daughter nuclide at time *t*, $N_p(t)$ the number of atoms of the parent nuclide at time *t* , λ_p is the parent nuclide decay constant, and λ_d is the daughter nuclide decay constant. If we assume the initial ($t = 0$) concentration of ^{99m}Tc is zero, we convert number of atoms to activity ($A = \lambda N$), and consider the branching ratio between ^{99}Mo and ^{99m}Tc (0.8873, ICRP 2008a) we have Equation 3-2:

$$A_d(t) = \frac{\lambda_d}{\lambda_d - \lambda_p} A_p(0)\left(e^{-\lambda_p t} - e^{-\lambda_d t}\right)(0.8773) \tag{3-2}$$

We know that the activity at time *t* of the parent, ^{99}Mo, is given by Equation 3-3:

$$A_p(t) = A_p(0)e^{-\lambda_p t} \tag{3-3}$$

It follows that the ratio of the parent to daughter at time *t* will be given by Equation 3-4:

$$\frac{A_d(t)}{A_p(t)} = \frac{\lambda_d(0.8773)\left(e^{-\lambda_p t} - e^{-\lambda_d t}\right)}{\left(\lambda_d - \lambda_p\right)e^{-\lambda_p t}} = \frac{\lambda_d(0.8773)\left(1 - e^{\left(-\lambda_d + \lambda_p\right)t}\right)}{\left(\lambda_d - \lambda_p\right)} \tag{3-4}$$

The relative activity of ^{99}Mo and ^{99m}Tc as well as the ratio between them is shown over time in Figure 3.1; the relationship between ^{99}Mo and ^{99m}Tc is referred to as transient equilibrium (Cember and Johnson 2009).

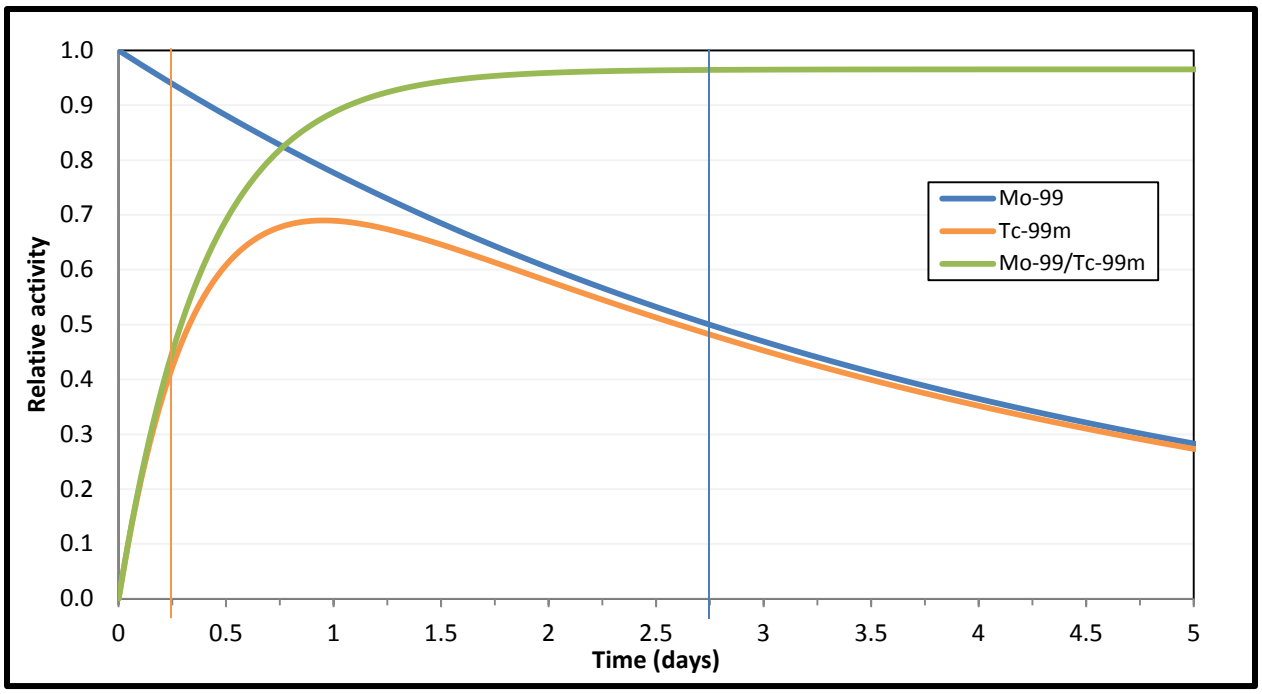

Figure 3.1: Illustration of transient equilibrium for ^{99}Mo and ^{99m}Tc. One half-life of ^{99}Mo is indicated by the light blue vertical line, and one half-life of ^{99m}Tc is indicated by the orange vertical line.

To determine activity concentrations of ^{99m}Tc in the various tissues, we assume the above relationship (Equation 3-4), with the initial release of ^{99}Mo considered to be at $t = 0$, although this does not account for potential differences in the chemistry or physiological behavior of ^{99m}Tc.

2.3. Source definition and determination of DCF

MCNP software simulated 10^7 disintegrations to represent ^{99}Mo or ^{99m}Tc decay and estimate the corresponding energy deposited per disintegration (10^7 chosen to optimize variance reduction with run time). Disintegrations were distributed randomly across the particular source organ. The locations and magnitudes of energies deposited in each organ as well as the fish body were tabulated and analyzed. Energies deposited in the thyroid lumen and the swim bladder are not of concern, because these organs are respectively fluid- and gas-filled and are therefore of no biological significance. Separate MCNP runs were conducted for beta particles and gamma photons corresponding to ^{99}Mo decay, as well as the gamma photon from the ^{99}Mo daughter ^{99m}Tc.

Separate MCNP runs were also conducted for the different source organs (e.g. liver and GI tract). It should be noted that the GI tract consists of multiple organs, namely the intestine, cardiac stomach, and pyloric stomach.

Total deposited energy tabulated was normalized by simulated disintegrations, i.e. MCNP output reports energy deposited per disintegration (MeV dis^{-1}). The initial energies of beta particles or gamma radiations emitted from the simulated disintegrations were randomly selected from appropriate frequency distributions specified in the MCNP program.

The initial beta energies were randomly selected from a continuous distribution of possible energies ranging up to a maximum energy of 1.2141 MeV with an average energy of 0.3891 MeV (Stabin and CQP 2002). Gamma energies for ^{99}Mo were selected from 0.7779, 0.7395, 0.1811, and 0.1405 MeV with respective probabilities of 0.0426, 0.1213, 0.0599, and 0.0452. Gamma energy for ^{99m}Tc was 0.1405 MeV with probability of 0.8906 (Stabin and CQP 2002; ICRP 2008a). Lower probability gammas than the ones listed for both ^{99}Mo and ^{99m}Tc were not considered.

The tabulation of energies (MeV) deposited were made using *f8 tally function in MCNP, i.e. that tally which records the sum of all energies deposited in the tissue by that particle type as well as its secondary particles (Monte Carlo Team 2003). A dose conversion factor (DCF) of $0.013824 \cdot E$ μGy d^{-1} per Bq kg^{-1} (where E is the energy deposited per disintegration (MeV dis^{-1}) and 0.013824 is the appropriate unit conversion) was determined directly from the MCNP output

2.4. Determination of cumulative dose rates and doses

The empirical models developed were combined with the MCNP simulation to compute cumulative organ doses from the decay of ^{99}Mo and the subsequent decay of ^{99m}Tc. Predicted ^{99}Mo concentrations (Bq kg^{-1}) in the source organ as a function of time, $B(t)$, were determined from the above described empirical models using the Equation 3-5:

$$B(t) = \left(\frac{\mu \cdot a}{k - b} \right) \cdot \left(e^{-bt} - e^{-kt} \right) \quad (3\text{-}5)$$

The only difference from the empirical model described above, is that in order to generalize the dose estimation, values for *a* were chosen to normalize activity concentration by initial water concentration (i.e. $a = 1$ Bq mL^{-1}), and values of *b* used corresponded to the decay rate of ^{99}Mo (i.e. $b = 0.252$ d^{-1}). Activity concentrations of ^{99m}Tc were determined as described in section 2.2, and dose and dose rate determinations due to ^{99m}Tc are described in Appendix A1.

Concentrations of ^{99}Mo and ^{99m}Tc in the source organ were then multiplied by the appropriate mass ratio and the DCF (μGy d^{-1} per Bq kg^{-1}) obtained from MCNP to acquire a dose rate (μGy d^{-1}); calculations were done separately for ^{99}Mo and ^{99m}Tc. Methods for calculating dose rate, maximum dose rate, and cumulative dose were the same as in section 2.6; we assume that the maximum dose rate from 99Mo and ^{99m}Tc occurs simultaneously.

3. Results

Dose and dose rate predictions are limited to the first 14 days, because ^{99}Mo concentrations in Fern Lake *O. mykiss* are unreported beyond day 14. Time to maximum dose rate is assumed to occur at the same time for both ^{99}Mo and ^{99m}Tc.

Table 3.3: Time in days post-release of Mo-99 at which the maximum dose rate will occur.

	Time (days) at maximum dose rate (by source organ)
Liver	3.82
GI	3.37

As the most significant radiation doses will be to the organs that are both the source and target, results are shown below for the liver and GI tract as well as the whole body. Detailed tabulations of results, including all organs, are contained in Appendix A3.

3.1. Model predictions of activity concentrations

3.1.1. Liver

Model predictions for liver activity concentration, along with measurement data considered in model development, are shown in Figure 3.2.

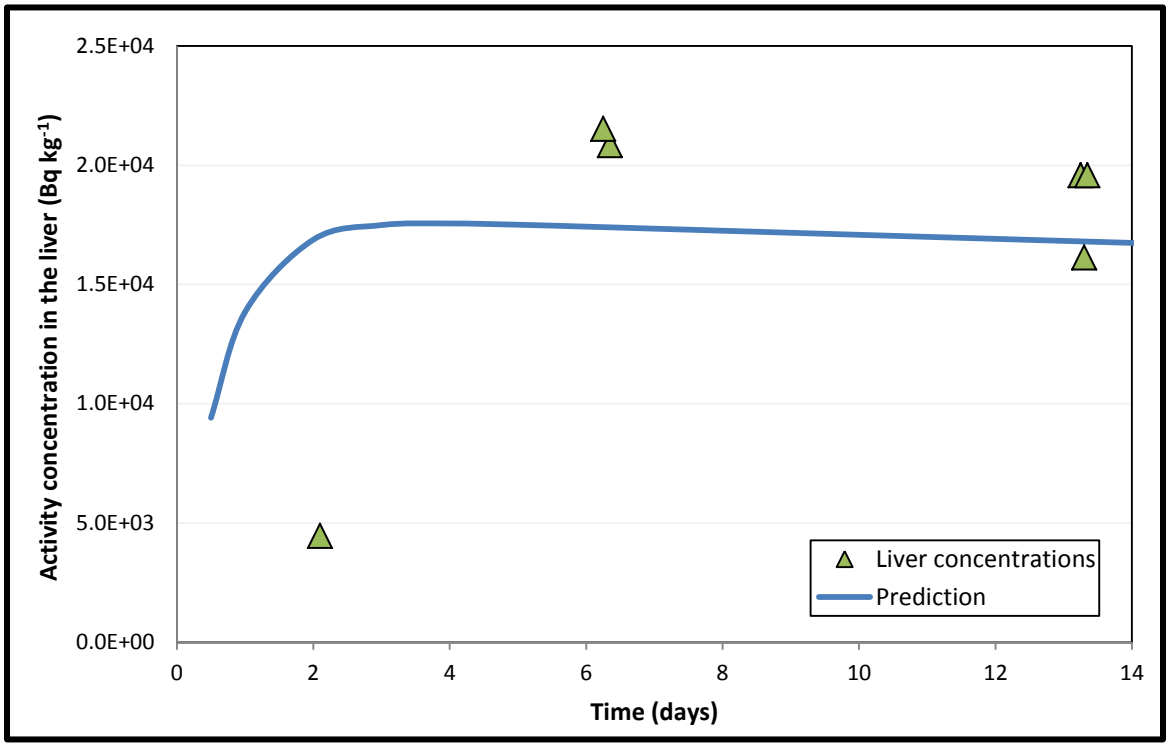

Figure 3.2: Model predictions for temporal activity concentrations of ^{99}Mo in the liver, with data points for measured liver concentrations.

The limitations of the ^{99}Mo data are apparent in Figure 3.2, especially for day 2. However, the rapid accumulation by day 6 and the continuing large concentrations on day 13 support the general form of the predictive model. The principal probable source of error is the approximation to the pattern of Mo accumulation before day 6, but most of the radiation dose, as is indicated by the reported data, occurs after day 6 where the model better approximates the reported concentrations.

The comparison of model predictions for ^{99}Mo concentration and the assumed ^{99m}Tc concentrations are shown in Figure 3.3

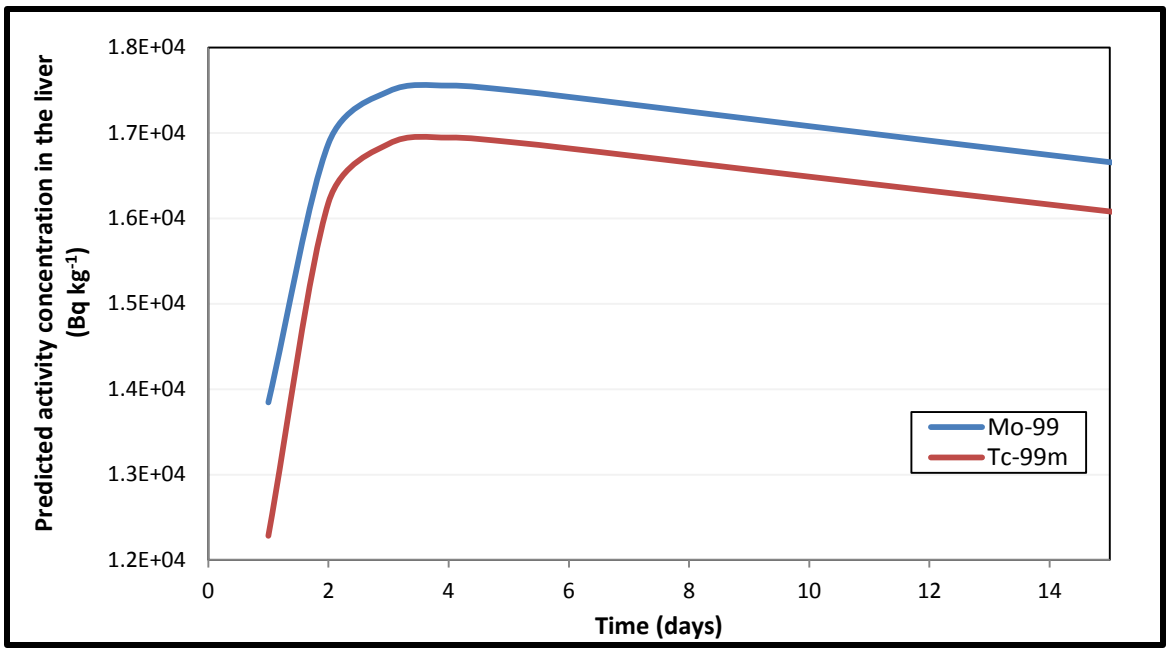

Figure 3.3: Model predictions for activity concentrations in the liver of ^{99}Mo and ^{99m}Tc.

3.1.2. GI tract

Model predictions for GI tract activity concentration, along with measurement data considered in model development, are shown in Figure 3.4.

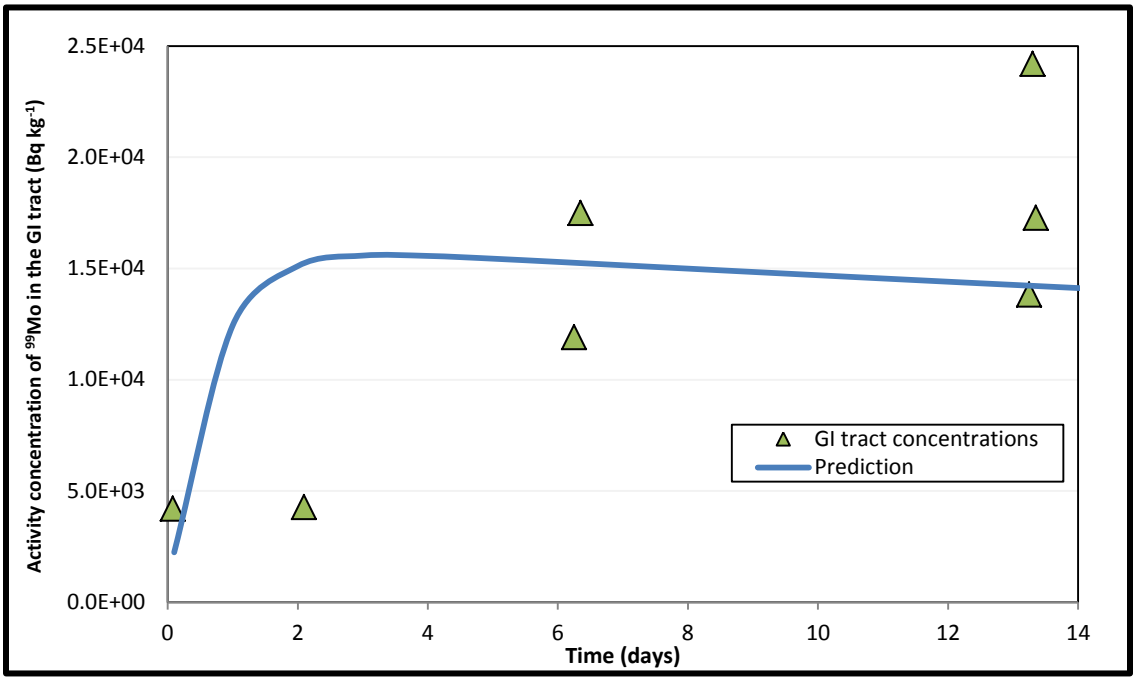

Figure 3.4: Model predictions for temporal activity concentrations of ^{99}Mo in the GI, shown with data points for measured GI tract concentrations.

The limitations of the fitted model are again illustrated for the time before day 6, but again the model is more appropriate for the period from day 6 through day 14 when most of the radiation dose is occurring.

The comparison of model predictions for ^{99}Mo concentration and the assumed corresponding ^{99m}Tc concentrations are shown in Figure 3.5.

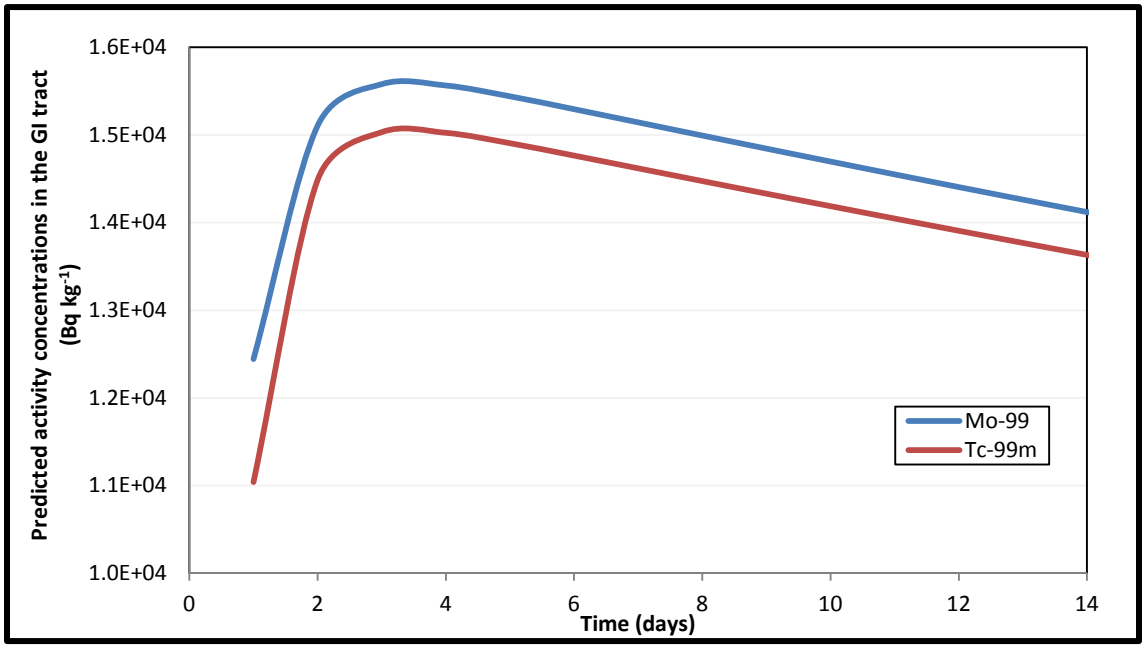

Figure 3.5: Model predictions for activity concentrations in the liver of ^{99}Mo and ^{99m}Tc.

3.2. Stylized phantom

The maximum dose rates to the source-target organs in this model are listed in the Table 3.4.

Table 3.4: Summary of maximum dose rates by source organ, including contribution from ^{99m}Tc.

Organ	Maximum dose rate (µGy d^{-1}) by source organ		
	Liver $t = 3.82$ d	GI Tract $t = 3.37$ d	Total
Whole Body	3.98E-01	4.06E+00	4.46E+00
Liver	8.59E+01	2.63E-02	3.86E-02
GI Tract	6.67E-02	3.22E-02	4.63E-02

Intestine	8.87E-02	6.70E-01	8.66E+01
Cardiac Stomach	2.18E-02	7.35E+01	7.36E+01
Pyloric Stomach	2.75E-02	7.16E+01	7.17E+01

The progression of cumulative dose in time for each source organ is shown in Figure 3.6 and Figure 3.7; the right hand graph is shown on a linear scale, but the left hand graph has a logarithmic scale on the y-axis to better visualize whole body dose.

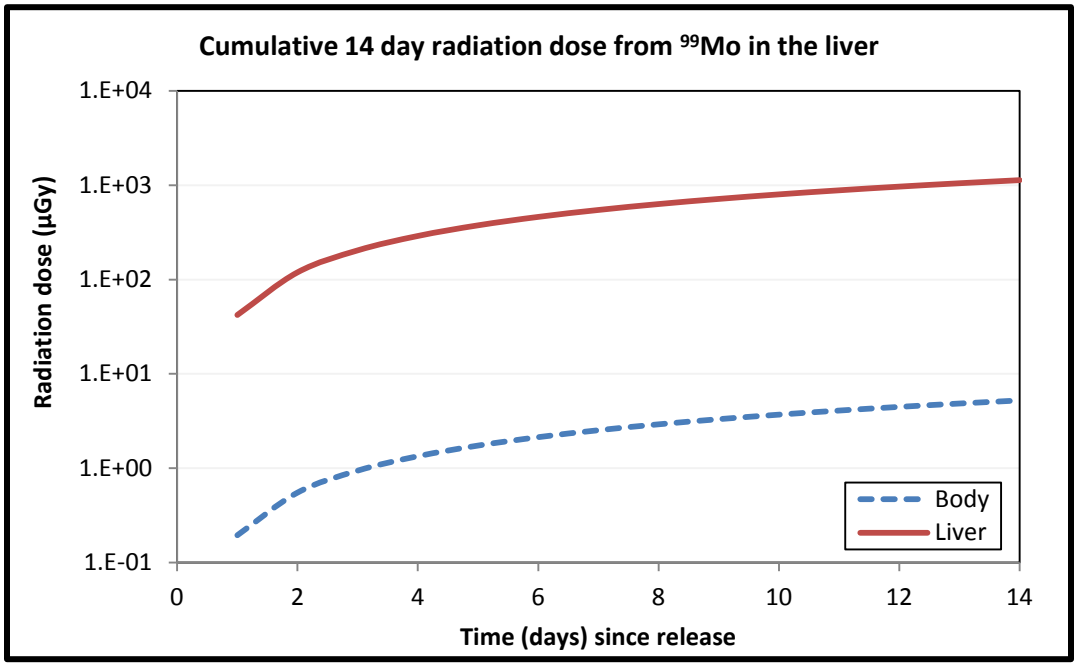

Figure 3.6: Cumulative radiation dose (log scale) to the liver and whole body from ^{99}Mo distributed in the liver, including contribution from ^{99m}Tc.

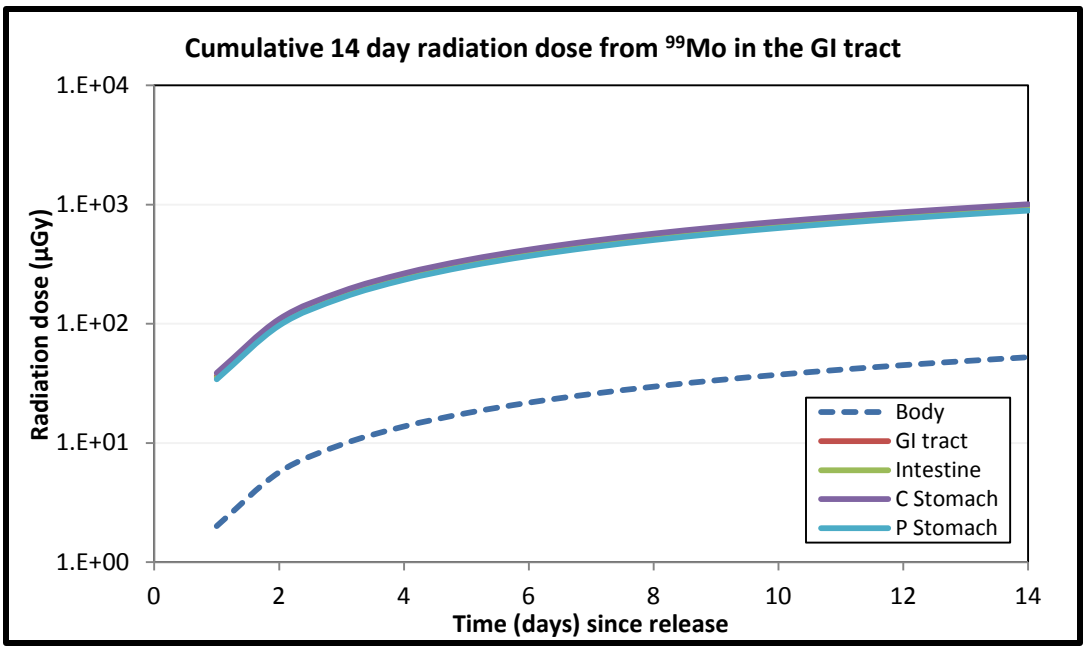

Figure 3.7: Cumulative radiation dose (log scale) to the GI tract and whole body from ^{99}Mo distributed in the GI tract, including contribution from ^{99m}Tc.

Total cumulative doses received by all organs are shown in Figure 3.8 on a log scale; additional cumulative dose charts are contained in Appendix A3.

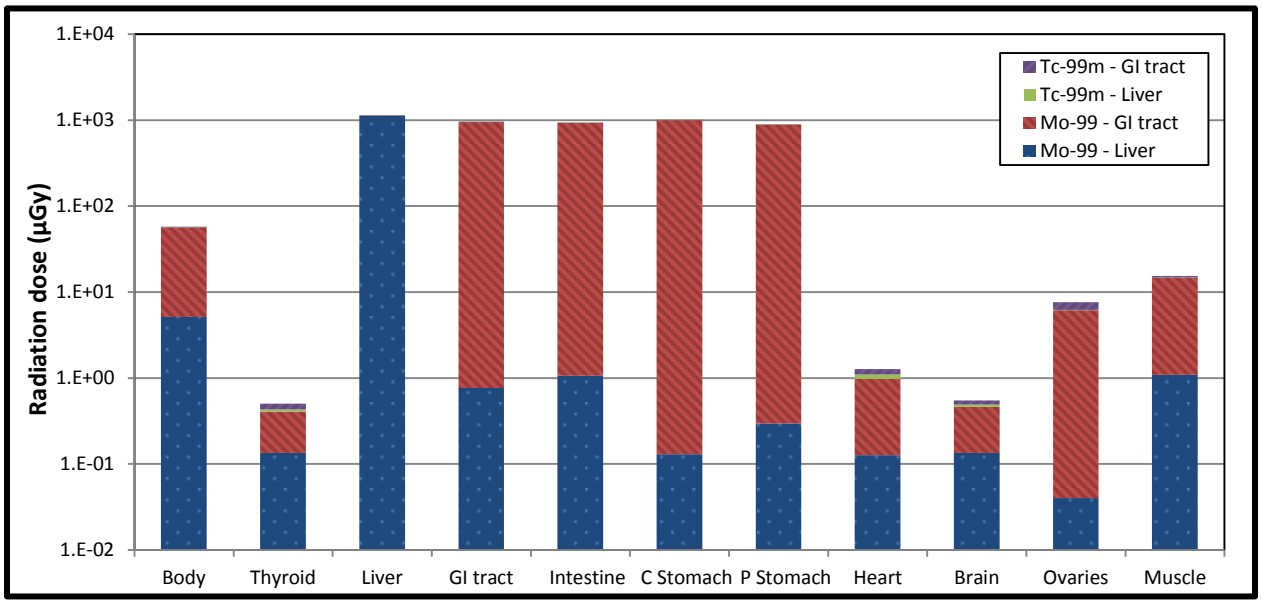

Figure 3.8: Total cumulative (internal) radiation dose from all sources on day 14 post release; radiation dose shown on a log scale.

3.3. CSUTROUT

The maximum dose rates to the source-target organs in this model are listed in the Table 3.5.

Table 3.5: Summary of maximum dose rates by source organ, including contribution from ^{99m}Tc.

Organ	Maximum dose rate (µGy d^{-1}) by source organ		
	Liver $t = 3.82$ d	GI Tract $t = 3.37$ d	Total
Whole Body	4.84E-01	4.02E+00	4. 50E+00
Liver	8.42E+01	2.77E+00	8.70E+01
GI tract	3.45E-01	7.05E+01	7.08E+01
Intestine	5.62E-02	7.09E+01	7.09E+01
Cardiac Stomach	4.69E-01	6.43E+01	6.47E+01
Pyloric Stomach	7.44E-01	7.80E+01	7.88E+01

The progression of cumulative dose in time for each source organ is shown in Figure 3.9 and Figure 3.10 below.

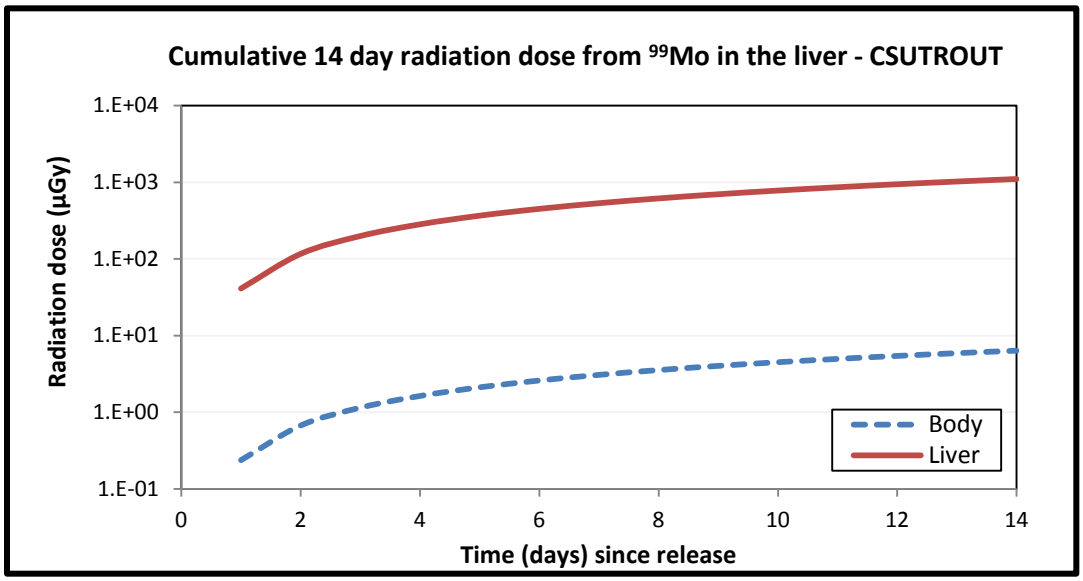

Figure 3.9: Cumulative radiation dose (log scale) to the liver and whole body from ^{99}Mo distributed in the liver, including contribution from ^{99m}Tc.

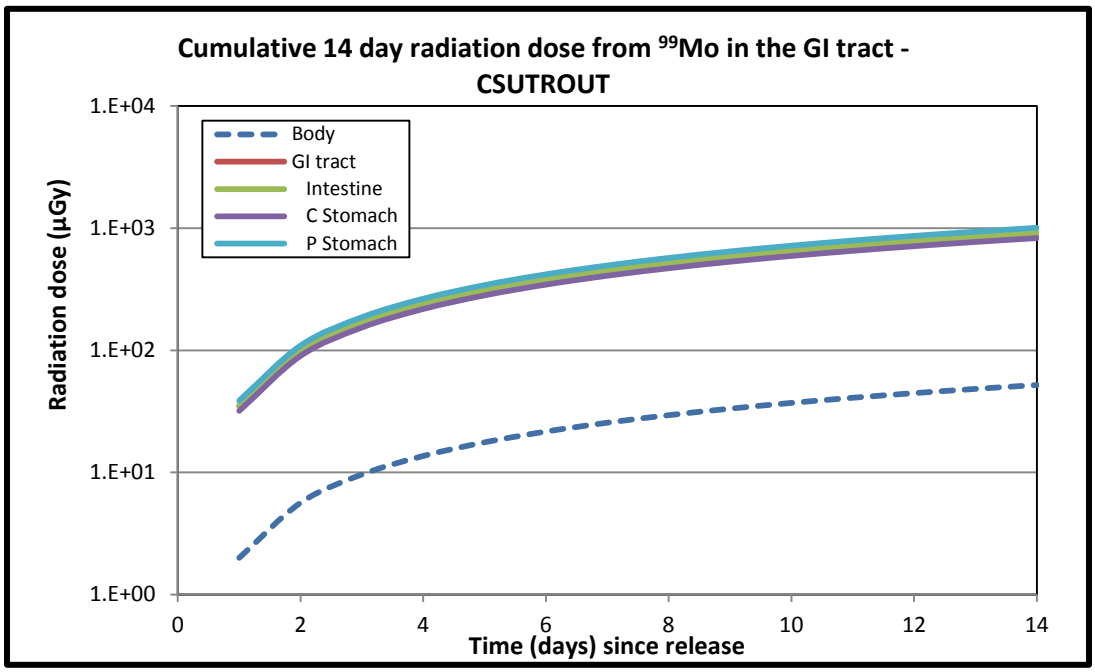

Figure 3.10: Cumulative radiation dose (log scale) to the GI tract and whole body from ^{99}Mo distributed in the GI tract, including contribution from ^{99m}Tc.

Total cumulative dose received from all sources, separated by radionuclide, for each tissue in the model is shown in Figure 3.11; additional cumulative dose charts are contained in Appendix A3.

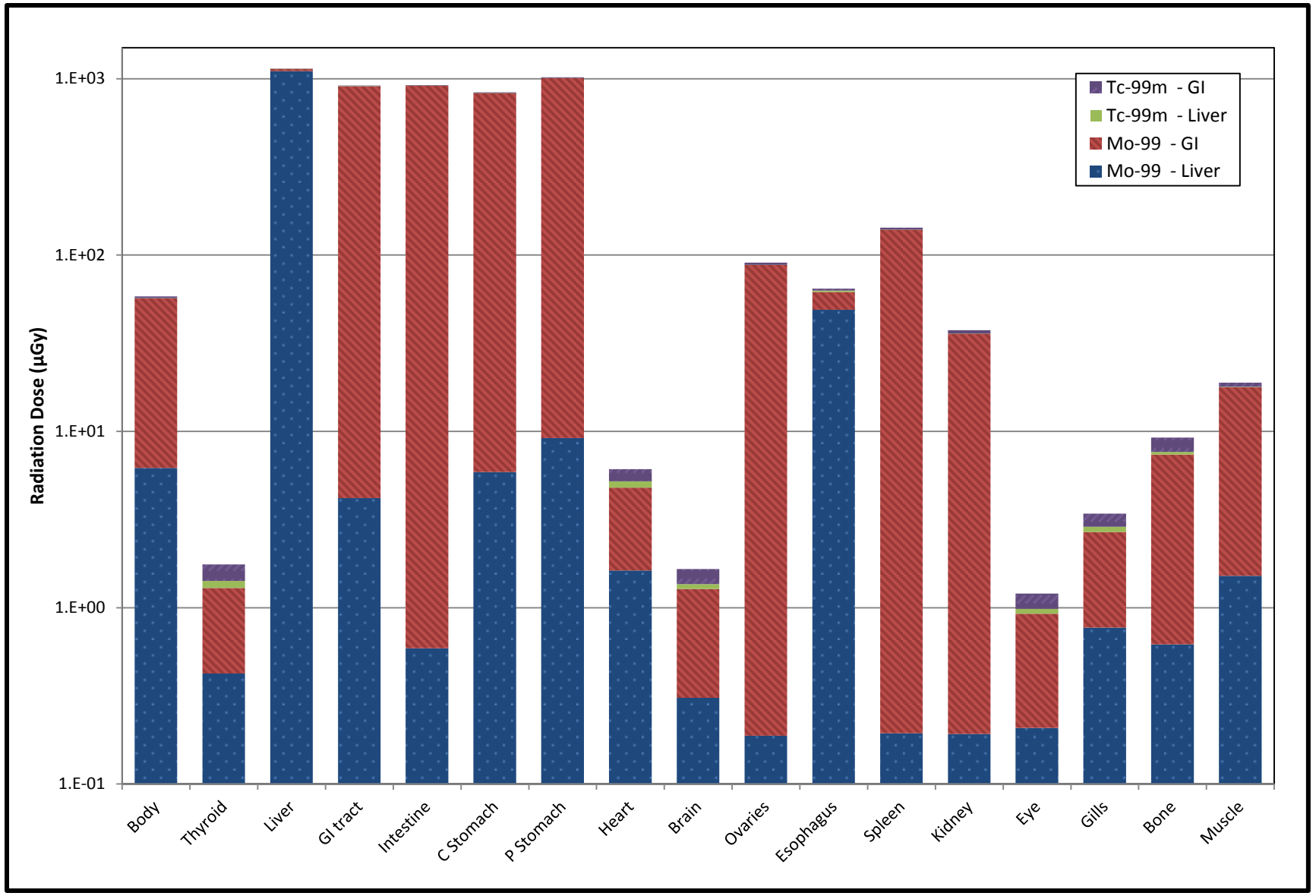

Figure 3.11: Total cumulative (internal) radiation dose from all sources on day 14 post release; radiation dose shown on a log scale.

4. Discussion

4.1. Comparison of dose received from ^{99}Mo and ^{99m}Tc

Doses received from ^{99}Mo were significantly (about two orders of magnitude) greater than the dose received from ^{99m}Tc. This is due to the greater contribution of beta radiation to radiation dose then gamma radiation, as gamma radiation is much more penetrating, depositing most of the energy outside the body of the fish (see Chapter 1 discussion). Doses from each radionuclide are pictured for the liver as the source organ and the GI tract as the source organ in Figure 3.12 and Figure 3.14, respectively for the stylized phantom, and Figure 3.13 and Figure 3.15 for CSUTROUT.

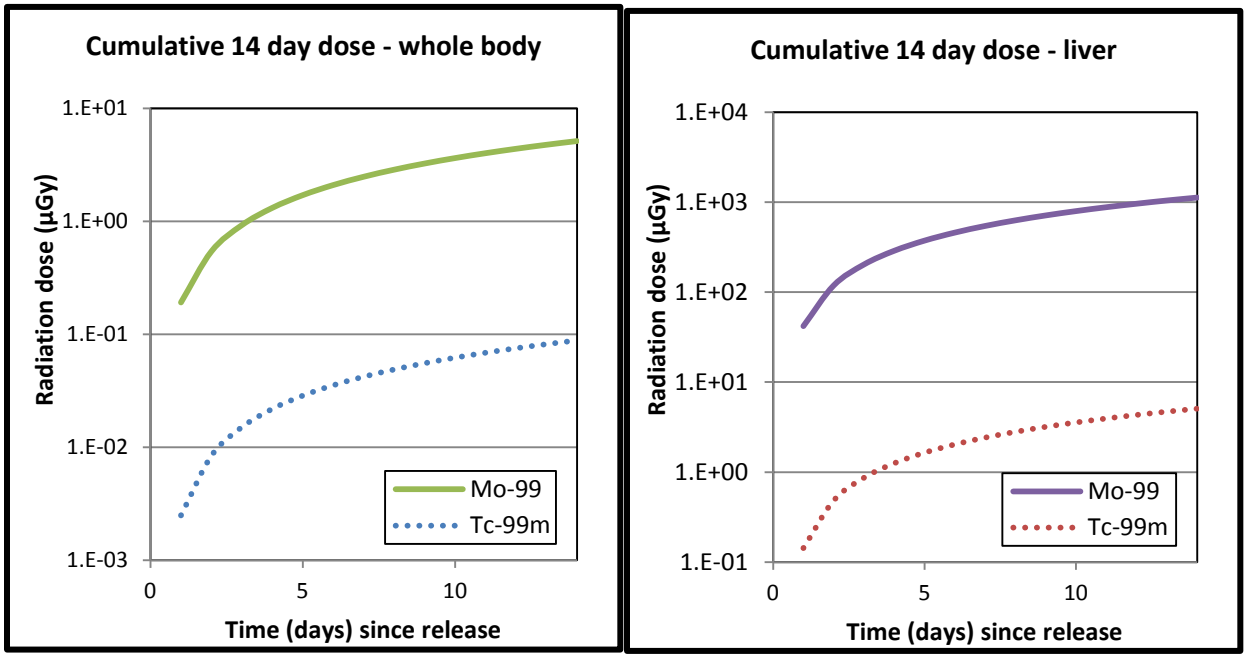

Figure 3.12: Comparison of 14 day cumulative doses received from ^{99}Mo and ^{99m}Tc with the liver as the source organ (stylized phantom).

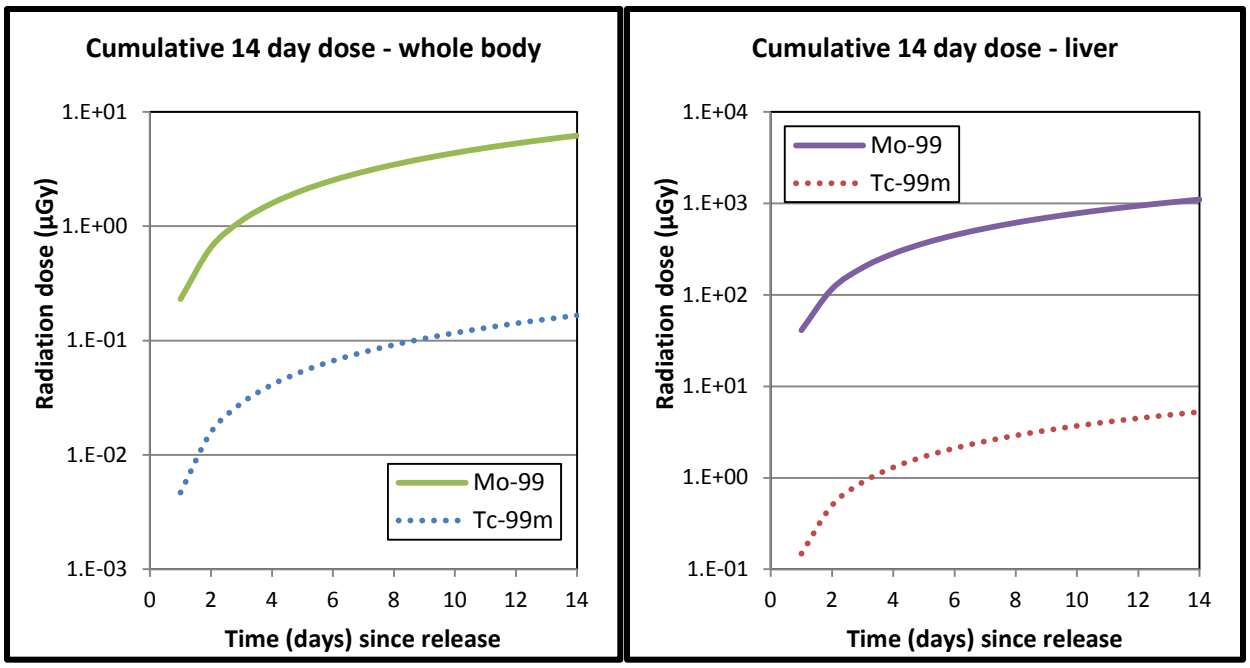

Figure 3.13: Comparison of 14 day cumulative doses received from ^{99}Mo and ^{99m}Tc using CSUTROUT, with the liver as the source organ.

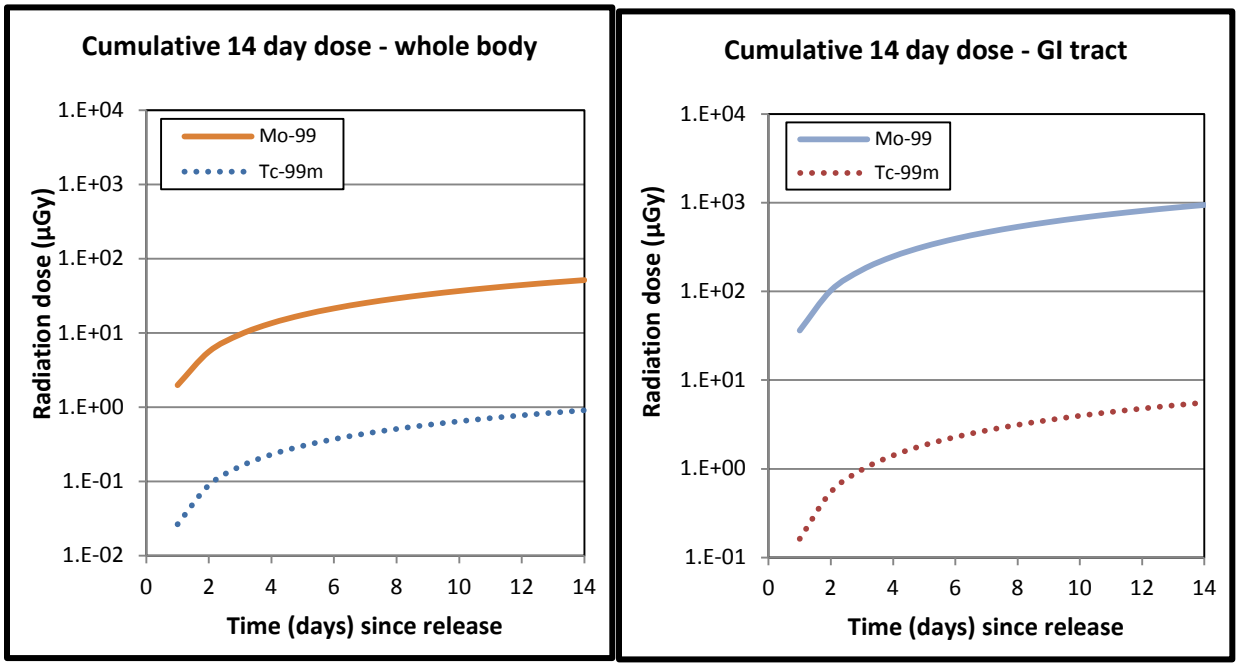

Figure 3.14: Comparison of 14 day cumulative doses received by the GI tract from ^{99}Mo and ^{99m}Tc (stylized phantom).

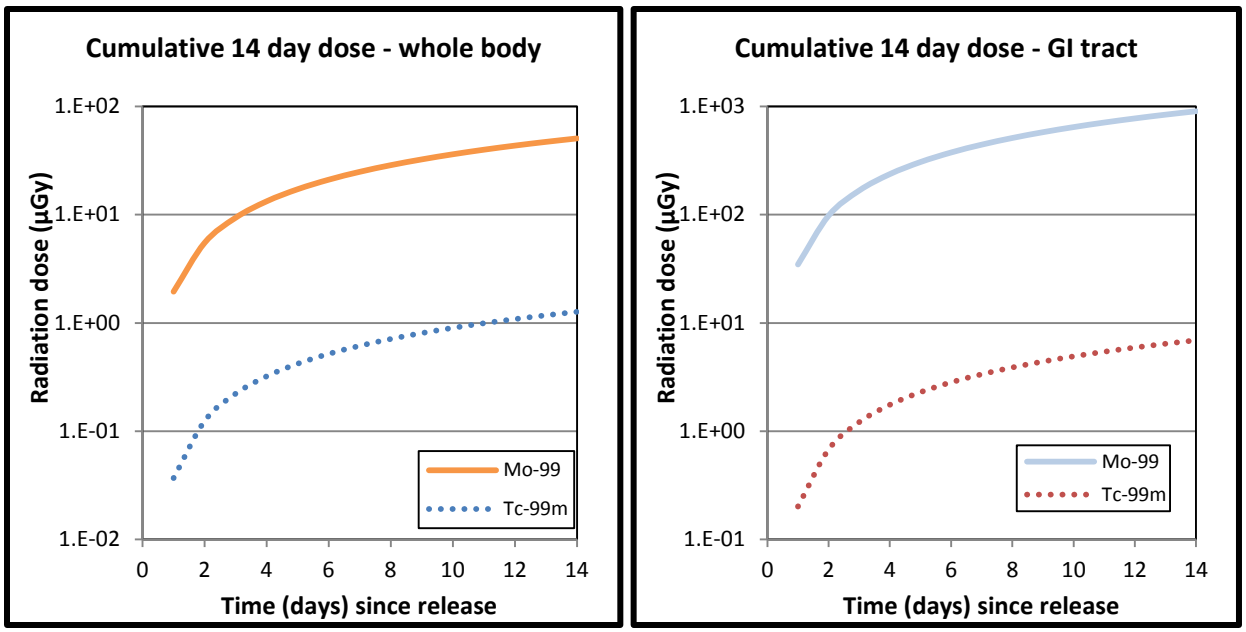

Figure 3.15: Comparison of 14 day cumulative doses received by the GI tract from ^{99}Mo and ^{99m}Tc using CSUTROUT.

4.2. Model comparison

4.2.1. Cumulative 14 day dose

Comparisons of cumulative doses received to source-target organs are shown in Figure 3.16 and Figure 3.17.

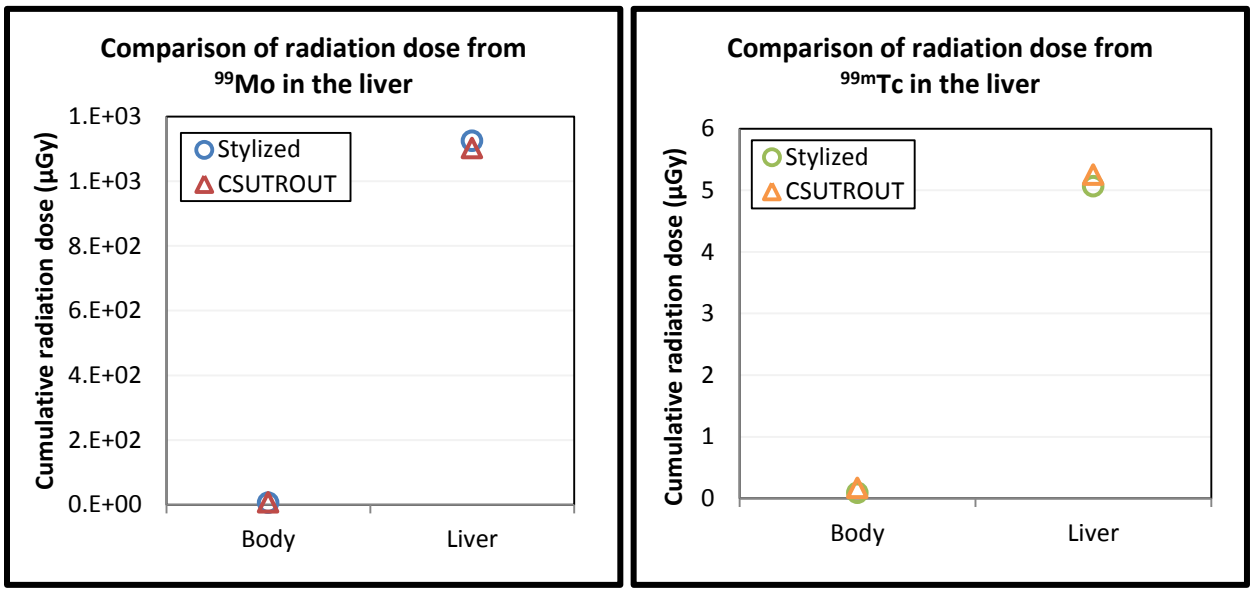

Figure 3.16: Comparison of 14 day cumulative doses received from ^{99}Mo and ^{99m}Tc with the liver as the source organ, as calculated by the stylized phantom and CSUTROUT.

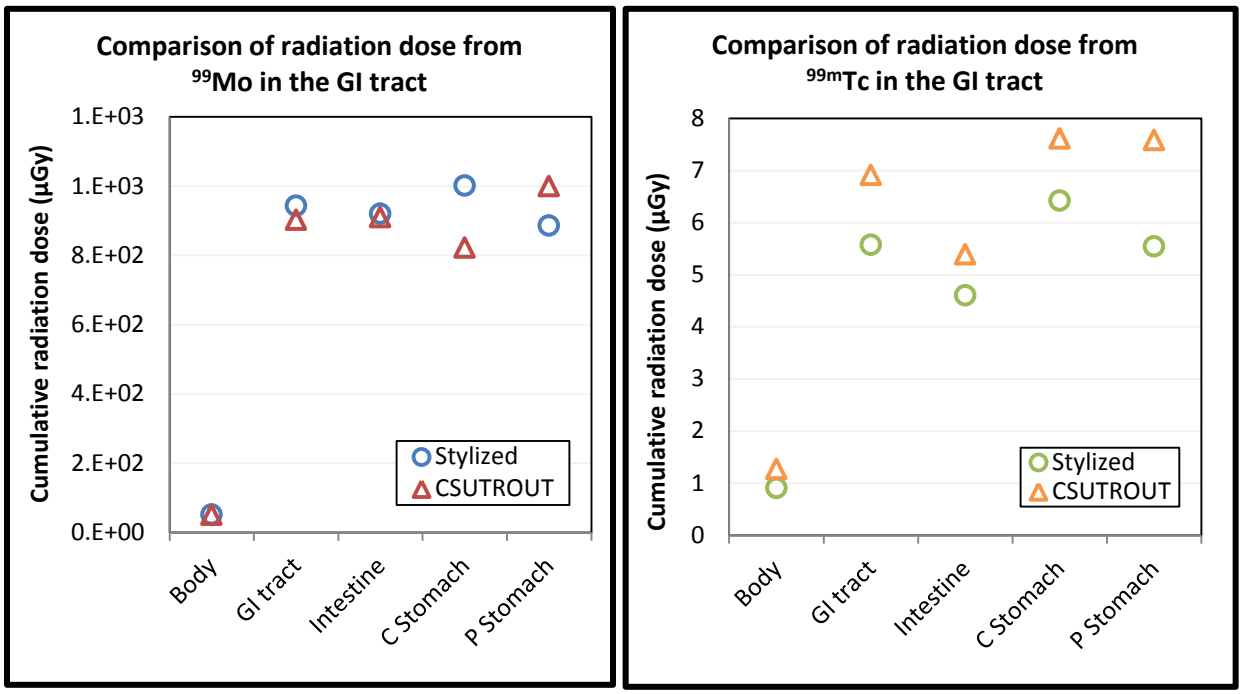

Figure 3.17: Comparison of 14 day cumulative doses received from ^{99}Mo and ^{99m}Tc with the GI tract as the source organ, as calculated by the stylized phantom and CSUTROUT.

The models are similar in prediction of dose, especially for source-target organs. For ^{99}Mo distributed in the liver, the percent differences between model estimates of dose are 18.5% (1 µGy absolute difference) and 1.8% (20 µGy absolute difference) for the whole body and liver respectively. For ^{99m}Tc in the liver, model estimates of dose are within 2 µGy. Considering the GI tract as the source, portions of the GI tract (intestine and stomach) range up to about 19.5% difference between model estimates of dose, but the doses to the GI tract as a whole organ system are within ~40 µGy (about 4.4% difference). The relative difference in dose from ^{99m}Tc is higher than ^{99}Mo; however, the absolute difference is only a few µGy. Differences in DCFs will be similar; DCF details as well as details of cumulative doses received to all organs are contained in Appendix A3.

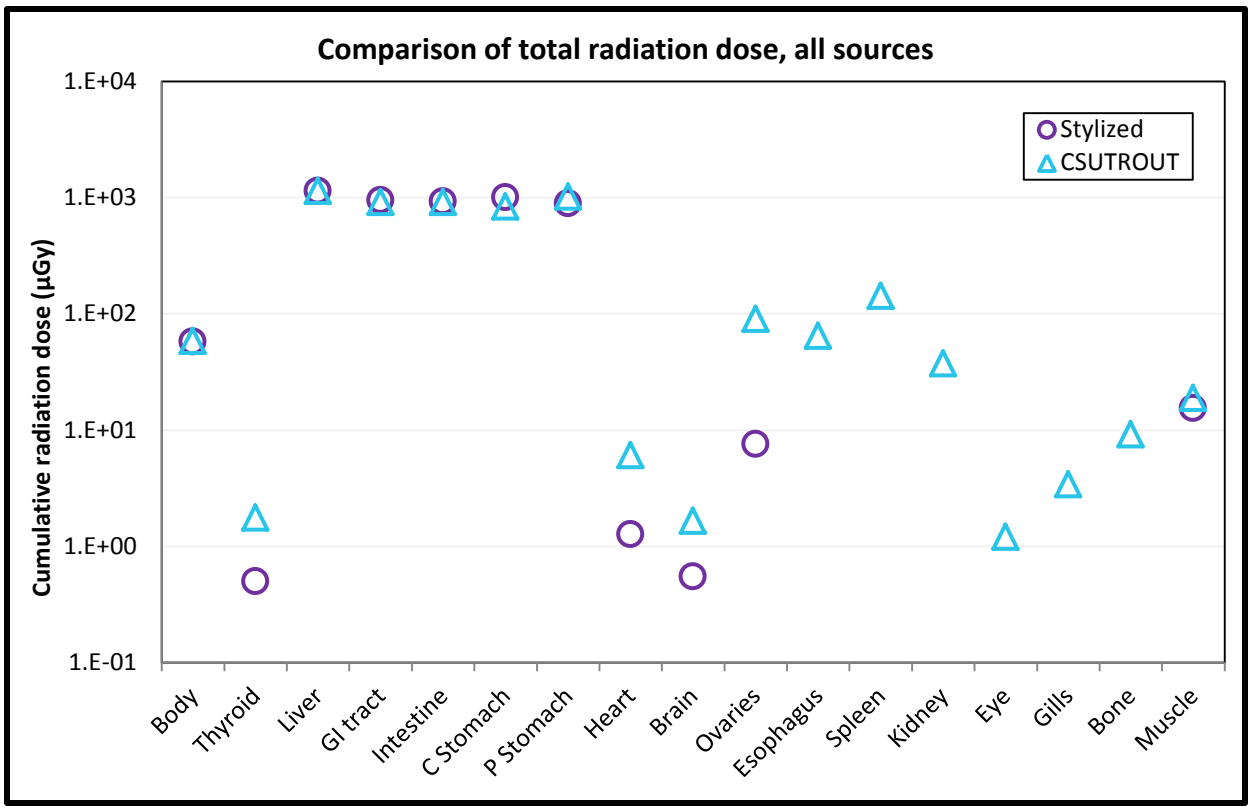

Figure 3.18: Comparison of cumulative 14 day radiation dose received by organs considered in the stylized model and in CSUTROUT from all internal sources of ^{99}Mo, including contribution from ^{99m}Tc.

The liver received the highest doses (1.14×10^{3} µGy, stylized and CSUTROUT), due to the preferential uptake of ^{99}Mo (Reid 2011), although uptake and doses to the GI tract were similar. The highest doses to organs not taking up ^{131}I were to the ovaries (7.58 and 90.4 µGy using the stylized model and CSUTROUT respectively) and the spleen (143 µGy, CSUTROUT), although these doses were much lower than doses to the source organs (between 800 and 1200 µGy).

4.2.1. Factor differences in using mass ratios to calculate organ specific DCF

In the absence of organ-specific data, a conservative estimate of organ specific DCF is to multiple the whole body DCF by the ratio of the mass of the whole body to the mass of the particular organ of interest. It should be noted that this approach is only valid for organs that are both the source and the target of radiation. The organ specific DCF was calculated directly from MCNP output and

calculated again using the mass ratio approach. The factor difference (ratio) between these two values is shown in Figure 3.19 and Figure 3.20 for ^{99}Mo and ^{99m}Tc respectively.

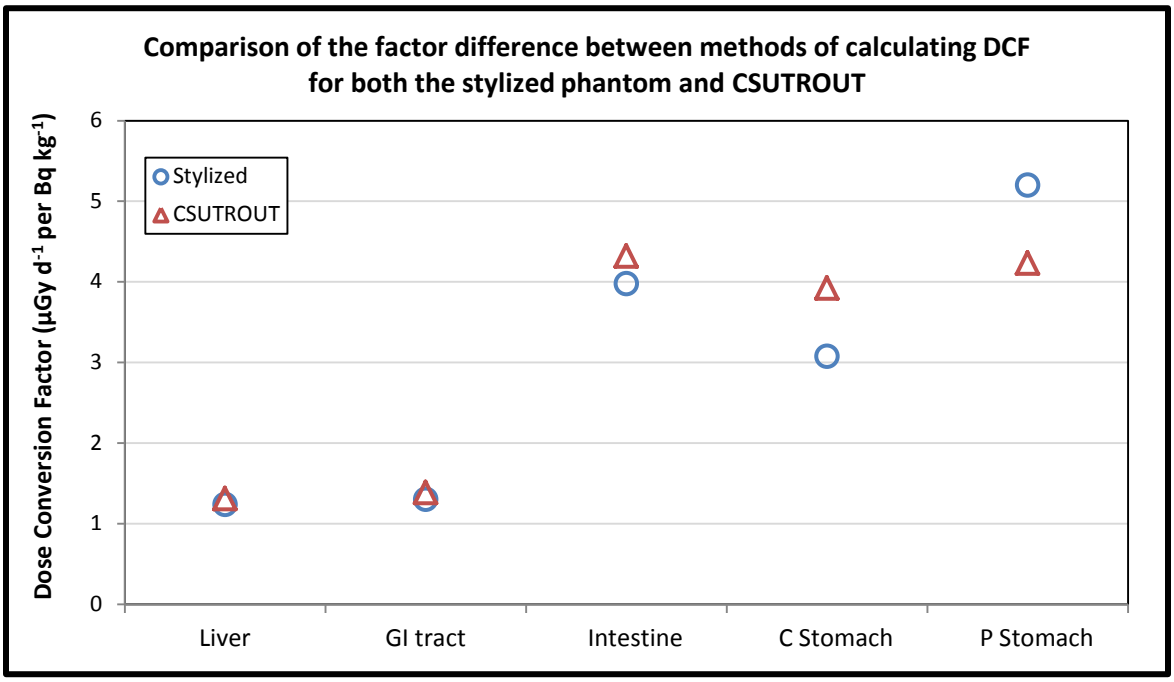

Figure 3.19: Factor difference between calculating organ-specific DCFs directly and by using the mass ratio approach for ^{99}Mo. This factor difference is shown for both the stylized phantom and CSUTROUT.

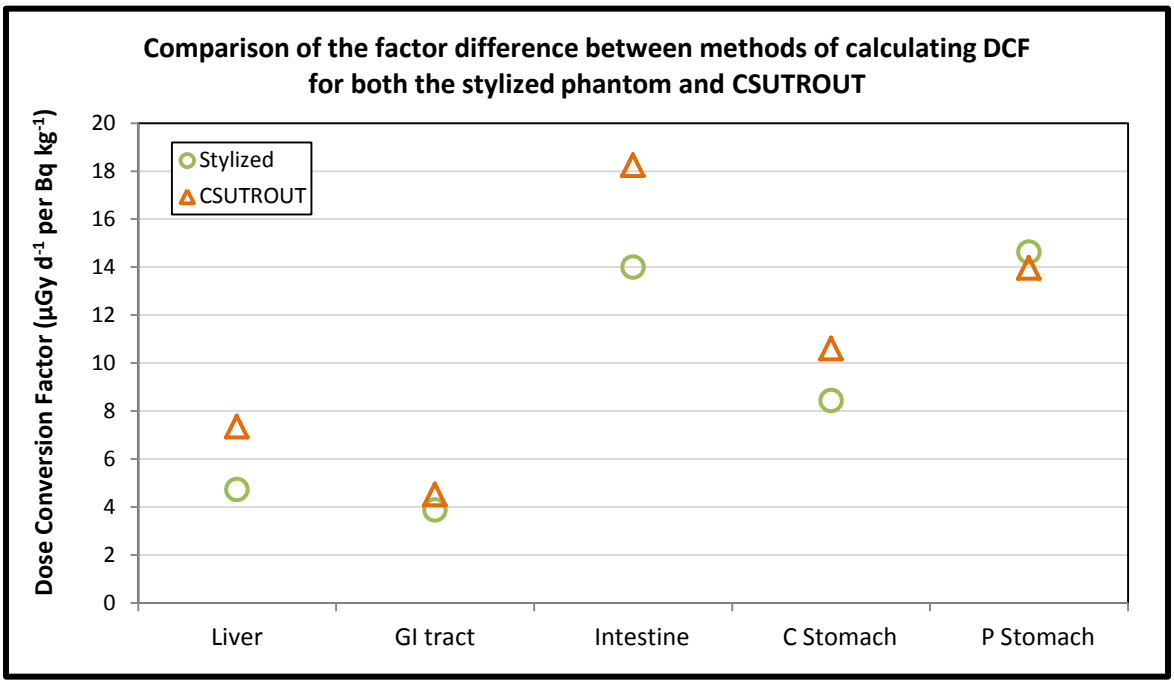

Figure 3.20: Factor difference between calculating organ-specific DCFs directly and by using the mass ratio approach for ^{99m}Tc. This factor difference is shown for both the stylized phantom and CSUTROUT.

All factor differences for ^{99}Mo, using either model, are less than 10 for all source-target organs. The differences between models are due to the slight difference in size and location of the particular organs, although these differences are small. These results are similar to the results for ^{131}I (Chapter 2), as both of these isotopes are beta emitters. Factor differences for ^{99m}Tc are less than 20 for all source-target organs, but larger than either ^{99}Mo or ^{131}I. Differences in model results are also more pronounced. ^{99m}Tc is a gamma emitter so its emissions will therefore deposit energy more evenly within the body than beta emitters; that is, a greater portion of energy will be deposited outside of the source organ compared to beta radiation. The mass ratio approach is therefore a reasonable approximation of organ dose, although more appropriate for beta emitters (or other low penetrating or low energy radiation) in agreement with Gómez-Ros et al. (2008).

4.3. Model considerations

Although the development of the voxel phantom was very time-consuming, once the model (along with the MCNP input files) was developed, implementing it for a different source radionuclide was straightforward, requiring no more time or effort than the stylized phantom (which was also previously developed).

5. Conclusions

5.1. Relative doses from ^{99}Mo and ^{99m}Tc

There was significantly less contribution to dose from ^{99m}Tc than ^{99}Mo, even though activity concentrations of the two radionuclides were similar. Although ^{99m}Tc has a strong gamma (140 keV; ICRP 2008a), the linear energy transfer is still well below that of the beta particles emitted from ^{99}Mo. From a radiological standpoint, beta emitters present more of an internal hazard than gamma emitters. However, if there was a release of fission products into the environment, there would be external radiation exposure in addition to internal exposure. Although gamma emitters do not contribute

significantly to internal radiation dose, they should not be discounted when performing a complete radiological evaluation.

5.2. Consideration of the mass ratio approach

Determining organ specific DCF using the mass ratio approach described by Gómez-Ros et al. (2008) was a reasonable approximation for calculating DCFs directly from MCNP output, although estimates were closer for beta emitters that gamma emitters. The mass ratio approach is also only valid for organs with preferential uptake of a radionuclide, so a significant benefit of both the stylized phantom and CSUTROUT is the ability to determine radiation dose due to "cross fire," i.e. the ability to calculate dose to organs from other organs.

5.3. Optimal phantom choice

Although CSUTROUT is the most realistic of the phantoms considered, the stylized phantom can be easily scaled, whereas the dimensions of CSUTROUT are fixed. There may be instances where a detailed phantom such as CSUTROUT is appropriate, especially if it is already available, as it will provide the most accurate radiation dose and dose rate information for the size, species, and gender it represents. Generally, the stylized phantom, scaled to the size of interest, will likely be the best choice for an ideal balance between accuracy and resource requirements.

5.4. Utility and implications of model development

The results of this study, as an extension of Chapter 1 and Chapter 2, support the eventual application and integration of this work into the regulatory paradigm of environmental protection of non-human biota by demonstrating the applicability of the models previously developed to an additional radionuclide.

REFERENCES

Bird GA, Motycka M, Rosentreter J, Schwartz WJ, and Vilks P. 1995a. Behavior of ^{125}I added to limnocorrals in two Canadian shield lakes of different trophic states. Science of the Total Environment, 166:161-177.

Bird GA, Schwartz WJ, and Rosentreter J. 1995b. Evolution of ^{131}I from freshwater and its partitioning in simple aquatic microcosms. Science of the Total Environment, 164:151-159.

Bird GA and Schwartz WJ. 1996. Distribution coefficients, K_ds, for iodine in Canadian shield lake sediments under oxic and anoxic conditions. Journal of Environmental Radioactivity, 35:261-279.

Bitar A, Lisbona A, Thedrez P, Maurel CS, Le Forestier D, Barbet J, and Bardies M. 2007. A voxel-based mouse for internal dose calculations using Monte Carlo simulations (MCNP). Physics in Medicine and Biology, 52:1013–1025.

Briesmeister JF. 2000. MCNP – A general Monte Carlo N- particle transport code. Version 4C. Los Alamos National Laboratory, Report LA-13709-M.

Caffrey EA and Higley KA. 2013. Creation of a voxel phantom of the ICRP reference crab. Journal of Environmental Radioactivity, 120:14-18.

Cember H and Johnson TE. 2009. Introduction to Health Physics. 4th Ed. McGraw-Hill: New York.

Chavin W and Bouman BN. 1965. Metabolism of iodine and thyroid hormone synthesis in the goldfish, *Carassius auratus* L. General and Comparative Endocrinology, 5:493-505.

Comans RNJ, Blust R, Carreiro MCV, Fernandez JA, Hakanson L, Sanone U, Smith JT, and Varskog P. 2001. Modelling fluxes and bioavailability of radiocesium in freshwaters in support of a theoretical basis for chemical/hydrological countermeasures. COPRAQ, Contract no. Fl4P-CT95-0018. In: European Commission, Radiation Protection. Fourth Framework Programme (1994-1998). Project Summaries. EUR 19792 EN.

Coughtrey PJ, Jackson D, and Thorne MC. 1983. Radionuclide distribution and transport in terrestrial and aquatic ecosystems. A critical review of data, vol. 3. Rotterdam.

Crick M J and Linsley GS. 1984. An assessment of the radiological impact of the Windscale reactor fire, October, 1957. International Journal of Radiation Biology and Related Studies in Physics Chemistry and Medicine, 46:479-506.

Diem K and Lentner C, eds. 1970. Scientific Tables. 7th Ed. GEIGY Pharmaceuticals: Ardsley. 810 pp.

Donaldson LR, Olson PR, and Dolandson JR. 1959. The Fern Lake trace mineral metabolism program. Transactions of the American Fisheries Society, 88:1-6.

Dogdas B, Stout D, Chatziioannou AF, and Leahy RM. 2007. Digimouse: A 3D whole body mouse atlas from CT and cryosection data. Physics in Medicine and Biology, 52:577–587.

Geven EJW, Nguyen NK, van den Boogaart M, Spanings FAT, Flik G, and Klaren PHM. 2007. Comparative thyroidology: Thyroid gland location and iodothyronine dynamics in Mozambique tilapia (*Oreochromis mossambicus* Peters) and common carp (*Cyprinus carpio* L.). Journal of Experimental Biology, 210:4005-4015.

Gilfedder BS, Petri M, and Biester H. 2009. Iodine speciation and cycling in fresh waters: A case study from a humic rich headwater lake (Mummelsee). Journal of Limnology, 68:396-408.

Gilfedder BS, Petri M, Wessels M, and Biester H. 2010. An iodine mass-balance for Lake Constance, Germany: Insights into iodine speciation changes and fluxes. Geochimica et Cosmochimica Acta, 74: 3090-3111.

Gomez-Guzman JM, Holm E, Enamorado-Baez SM, Abril JA, Pinto-Gomwz AR, Lopez-Gutierrez JM, and Garcia-Leon M. 2013. Pre- and post-Chernobyl accident levels of ^{129}I and ^{137}Cs in the southern Baltic Sea by brown seaweed *Fucus vesiculosus*. Journal of Environmental Radioactivity, 115:134-142.

Gómez-Ros JM, Prohl G, Ulanovsky A, and Lis M. 2008. Uncertainties of internal dose assessment for animals and plants due to non-homogeneously distributed radionuclides. Journal of Environmental Radioactivity, 99:1449-1455.

Hindorf C, Ljungberg M, and Strand SE. 2004. Evaluation of parameters influencing S values in mouse dosimetry. Journal of Nuclear Medicine, 45:1960–1965.

Hinton TG, Garnier-Laplace J, Vandenhove H, Dowdall M, Adam-Guillermin C. Alonzo F, Barnett C, Beaugelin-Seiller K, Beresford NA, Bradshaw C, Brown J, Eyrolle F, Fevrier L, Gariel JC, Gilbin R, Hertel-Aas T, Horemans N, Howard BJ, Ikäheimonen T, Mora JC, Oughton D, Real A, Salbu B, Simon-Cornu M, Steiner M, Sweek L, and Vives I Batlle J. 2013. An invitation to contribute to a strategic research agenda in radioecology. Journal of Environmental Radioactivity, 115:73-82.

Hunn JB and Fromm PO. 1966. *In vivo* uptake of radioiodine by rainbow trout. Journal of the Water Pollution Control Federation, 38:1981-1985.

ICRP. 2007. The 2007 Recommendations of the International Commission on Radiological Protection. ICRP Publication 103. Ann. ICRP 37(2-4).

ICRP. 2008a. Nuclear Decay Data for Dosimetric Calculations. ICRP Publication 107. Ann. ICRP 38(3).

ICRP. 2008b. Environmental Protection: the Concept and Use of Reference Animals and Plants. ICRP Publication 108. Ann. ICRP 38 (4-6).

ICRP. 2009. Environmental Protection: Transfer Parameters for Reference Animals and Plants. ICRP Publication 114. Ann. ICRP 39(6)

ICRU. 1989. Tissue Substitution in Radiation Dosimetry and Measurement. ICRU Report 44. Bethesda, MD.

Kinase S. 2008. Voxel-based frog phantom for internal dose evaluation. Journal of Nuclear Science and Technology, 45:1049–1052.

Kolehmainen S, Takatalo S and Miettinen JK. 1969. A tracer experiment in an oligotrophic lake, in: Nelson, D. J., Evans, F. C. (Eds.), Symposium on Radioecology, CONF-67050, Ann Arbor, Michigan.

Kramer GH, Capello K, Chiang A, Cardenas-Mendez E, and Sabourin T. 2010. Tools for creating and manipulating voxel phantoms. Health Physics, 98(3): 542–548.

Kramer GH, Capello K, Strocchi S, Bearrs B, Leung K, and Martinez N. 2012. The HML's new voxel phantoms: two human males, one human female, and two male canines. Health Physics, 103:802-807.

Kryshev I. 1995. Radioactive contamination of aquatic ecosystems following the Chernobyl accident. Journal of Environmental Radioactivity, 27:207-209.

Kuhne W, ed. 2012. Radioecology in the 21st centrury: National Center for Radioecology Workshop Summary. August 15-16, 2012; Aiken, SC.

La Roche G, Johnson CL, and Woodall AN. 1965. Thyroid function in the rainbow trout (*Salmo gairdneri*) I. Biochemical and histological evidence of radiothroidectomy. General and Comparative Endocrinology, 5:145-159.

La Roche G, Woodall AN, Johnson CL, and Halver JE. 1966. Thyroid function in the rainbow trout (*Salmo gairdneri*) II. Effects of thyroidectomy on the development of young fish. General and Comparative Endocrinology, 6:249-266.

Larsson CM. 2008. An overview of the ERICA Integrated Approach to the assessment and management of environmental risks from ionising contaminants. Journal of Environmental Radioactivity, 99:1364–1370.

Le VS. 2014. ^{99m}Tc generator development: up-to-date ^{99m}Tc recovery technologies for increasing the effectiveness of ^{99}Mo utilization. Science and Technology of Nuclear Installations, 2014:345252. http://dx.doi.org/10.1155/2014/345252

Martinez NE, Johnson TE, and Pinder JE 3rd. 2014. Influence of lake trophic structure on ^{131}I accumulation and subsequent cumulative radiaiton dose to trout thyroids. Journal of Envornmental Radioactivity, 131:62-71.

Mauxion T, Barbet J, Suhard J, Pouget JP, Poirot M, and Bardies M. Improved realism of hybrid mouse models may not be sufficient to generate reference dosimetric data. Medical Physics. http://dx.doi.org/10.1118/1.4800801

McDonnell RP. 1977. Toxicity of molybdenum to rainbow trout under laboratory conditions. In: Chappell WR, Peterson KK, eds. Molybdenum in the Environment Vol 2: The Geochemistry, Cycling, and Industrial Uses of Molybdenum. New York: Marcel Dekker Inc., 725-730.

Mohammadi A, Kinase S, and Saito K. 2011. Comparison of photon and electron absorbed fractions in voxel-based and simplified phantoms for small animals. Progress in Nuclear Science and Technology, 2:365-368.

Mohammadi A, Kinase S, and Saito K. 2012. Evaluation of absorbed doses in voxel-based and simplified models for small animals. Radiation Protection Dosimetry, 150:283-191.

Molinski VJ. 1982. A review of ^{99m}Tc generator technology. International Journal of Applied Radiation and Isotopes, 33: 811-819.

Monte L, Brittain JE, Hakanson L, Heling R, Smith JT, and Zheleznyak M. 2003. Review and assessment of models used to predict the fate of radionuclides in lakes. Journal of Environmental Radioactivity,69:177-205.

National Cancer Institute. 1999. Exposure of the American people to Iodine-131 from nuclear bomb tests. National Academy Press. Washington, DC.

Olsen S, Chakravarti D, and Olson PR. 1967. Water, bottom deposits, and zooplankton of Fern Lake, Washington. Limnology and Oceanography, 12:392-404.

Padilla L, Lee C, Milner R, Shahlaee A, and Bolch W. 2008. Canine anatomic phantom for preclinical dosimetry in internal emitter therapy. The Journal of Nuclear Medicine, 49:46-452.

Pinder JE III, Hinton TG, Whicker FW, and Smith JT. 2009. Cesium accumulation by fish following acute input to lakes: a comparison of experimental and Chernobyl-impacted systems. Journal of Environmental Radioactivity, 100:456-467.

Pinder JE III, Hinton TG, Taylor BT, and Whicker FW. 2011. Cesium accumulation by aquatic organisms at different trophic levels following an experimental release into a small reservoir. Journal of Environmental Radioactivity, 102:283-293.

Poston TM, and Klopfer DC. 1986. A literature review of the concentration ratios of selected radionuclides in freshwater and marine fish. PNL-5484. Batelle Pacific Northwest Laboratory. September.

Raine JC, Strelive U, and Leatherland JF. 2005. The thyroid tissue of juvenile *Oncorhynchus mykiss* is tubular, not follicular. Journal of Fish Biology, 67:823-833.

Rasmussen JB, Rowan DJ, Lean DRS, and Carey JH. 1990. Food chain structure determines PCB levels in lake trout (*Salvelinus namaycush*) and other pelagic fish. Canadian Journal of Fisheries and Aquatic Sciences, 47:2030-2038.

Regoli L, Tilborg WV, Heijerick D, Stubblefield W, and Carey S. 2012. The bioconcentration and bioaccumulation factors for molybdenum in the aquatic environment from natural environmental concentrations up to the toxicity boundary. Science of the Total Environment, 435:96-106.

Reid SD. 2002. Physiological impact of acute molybdenum exposure in juvenile Kokanee salmon (*Oncorhynchus nerka*). Comparative Biochemistry and Physiology, Part C, 133:355-367.

Reid SD. 2011. Molybdenum and Chromium In: Homeostasis and toxicology of essential metals. Fish Physiology, 31A: 375-415. http://dx.doi.org/10.1016/S1546-5098(11)31008-4

Robertson OH and Chaney AL. 1953. Thyroid hyperplasia and tissue iodine content in spawning rainbow trout: a comparative study of Lake Michigan and California sea-run trout. Physiological Zoology, 26: 328-340.

SAS Institute Inc. 1989. SAS/STAT User's Guide. Version 6, fourth ed. Vol. 2. SAS Institute. Cary, NC.

Segars WP, Tsui BM, Frey EC, Johnson GA, and Berr SS. 2004. Development of a 4-D digital mouse phantom for molecular imaging research. Molecular Imaging and Biology, 6:149–159.

Short ZF, Palumbo RF, Olson PR, and Donaldson JR. 1969. The uptake of ^{131}I by the biota of Fern Lake, Washington, in a laboratory and a field experiment. Ecology, 50:979-989.

Short ZF, Olson PR, Palumbo RF, Donaldson JR, and Lowman FG. 1971. Uptake of molybdenum, marked with ^{99}Mo, by the biota of Fern Lake, Washington, in a laboratory and a field experiment. In: Proceedings of the Third National Symposium on Radioecology Volume 1,May 1971. Oak Ridge, TN

Singh TP. 1968. Seasonal changes in radioiodine uptake and Pitkannokanlampi cell height of the thyroid gland in the freshwater teleosts *Esomus danricus* and *Mystus vittatus* under varying conditions of illumination. Zeitschrift fur Zellforschung Mikroskopische Anatomie, 87:422-428.

Smith JT, Belova NV, Bulgakov AA, Comans RNJ, Konoplev AV, Kudelsky AV, Madruga MJ, Voitsekhovitch OV, and Zibold G. 2005. The "AQUASCOPE" simplified model for predicting 89,90Cr, 131I, and 134,137Cs in surface waters after a large scale radioactive fallout. Health Physics, 89:628-644.

Smith JT, Kudelsky AV, Ryabov IN, Daire SE, Boyer L, Blust RJ, Fernandez JA, and Hadderingh RH. 2002. Uptake and elimination of radiocesium in fish and the "size effect". Journal of Environmental Radioactivity, 62:145-164.

Stabin MG and CQP da Luz L. 2002. Decay energy for internal and external dose assessment. Health Physics, 83:471-475.

Stabin MG, Peterson TE, Holburn GE, and Emmons MA. 2006. Voxel-based mouse and rat models for internal dose calculations. Journal of Nuclear Medicine, 47:655–659.

Suzuki S. 1985. Iodine distribution in the thyroid follicles of the hagfish, *Epatretus burger* and lamprey, *Lampetra japonica*: Electron-probe X-ray microanalysis. Cell and Tissue Research, 241:539-543.

Tang W, and Laodong G. 2012. Depositional fluxes and residence time of atmospheric radioiodine (^{131}I) from the Fukushima accident. Journal of Environmental Radioactivity, 113:32-36.

Tarrant RM Jr. 1971. Seasonal variation in the accumulation and loss of ^{131}I by tissues of adult female channel catfish, *Ictalurus punctatus* (Rafinesque). Transactions of the American Fisheries Society, 100:237-246.

Taschereau R, Chow PL, and Chatziioannou AF. 2006. Monte Carlo simulations of dose from microCT imaging procedures in a realistic mouse phantom. Medical Physics, 33:216–224.

Thomann RV. 1981. Equilibrium model of the fate of microcontaminants in diverse aquatic food chains. Canadian Journal of Fisheries and Aquatic Sciences, 38:280-296.

Tiffany MA, Winchester JW, and Loucks RH. 1969. Natural and pollution sources of iodine, bromine, and chlorine in the Great Lakes. Journal (Eastern Pollution Control Federation), 41:1319-1329.

Ulanovsky A, and Pröhl G. 2006. A practical method for assessment of dose conversion coefficients for aquatic biota. Radiatiation and Environmental Biophysics, 45:203–214.

Ulanovsky A, and Pröhl G. 2008. Tables of dose conversion coefficients for estimating internal and external radiation exposures to terrestrial and aquatic biota. Radiatiation and Environmental Biophysics, 47:195–203.

Vanderploeg HA, Parzyck DC, Wilcox WH, Kercher JR, and Kaye SV. 1975. Bioaccumulation factors for radionuclides in freshwater biota. Environmental Sciences DivisionPublication No. 783. Oak Rdge National Laboratory. Oak Ridge, TN.

Ward JV. 1973. Molybdenum concentrations in tissues of Rainbow Trout (*Salmo gairdneri*) and Kokanee Salmon (*Oncorhynchus nerka*) from waters differing widely in Molybdenum content. Journal of the Fisheries Research Board of Canada, 20:841-842.

Weinreb EL and Bilstad NM. 1955. Histology of the digestive tract and adjacent structures of the Rainbow Trout, *Salmo Gairdneri irideus*. Copeia, 3:194-204.

Whicker FW, and Schultz V. 1982a. Radioecology: Nuclear Energy and the Environment, vol. i. CRC Press Inc. Boca Raton, FL.

Whicker FW, and Schultz V. 1982b. Radioecology: Nuclear Energy and the Environment, vol. ii. CRC Press Inc. Boca Raton, FL.

Wu L, Zhang G, Luo Q, and Liu Q. 2008. An image-based rat model for Monte Carlo organ dose calculations. Medical Physics, 35:3759–3764.

X-5 Monte Carlo Team. 2003. MCNP – A General N-Particle Transportation Code, Version 5. Volume 1: Overview and Theory. Los Alamos National Laboratory Report LA-UR 31987. Los Alamos, NM

Xie T, Zhang G, Li Y, and Liu Q. 2010a. Comparison of absorbed fractions of electrons and photons using three kinds of computational phantoms of rat. Applied Physics Letters, 97:1-3.

Xie T, Han D, Liu Y, Sun W, and Liu Q. 2010b. Skeletal dosimetry in a voxel-based rat phantom for internal exposures to photons and electrons. Medical Physics, 37: 2167-2178.

Xu XG and Eckerman KF. Eds. 2010. Handbook of Anatomical Models for Radiation Dosimetry. Taylor and Francis Group: Boca Raton, FL.

Yankovich T, Beresford NA, Fesenko S, Fesenko J, Phaneuf M, Dagher E, Outola I, Andersson P, Thiessen K, Ryan J, Wood MD, Bollhofer A, Barnett CL, and Copplestone D. 2013. Establishing a database of radionuclide transfer parameters for freshwater wildlife. Journal of Environmental Radioactivity, 126:299-313.

Zaidi H and Tsui BMW. 2009. Review of computational anthropomorphic anatomical and physiological models. Proceedings of the IEEE, 97:1938-1953.

Zhang G, Xie T, Bosmans H, and Liu Q. 2009. Development of a rat computational phantom using boundary representation method for Monte Carlo simulation in radiological imaging. Proceedings of the IEEE, 97:2006-2014.

Zhang X, Ziangdong X, Cheng J, Ning J, Yuan Y, and Yang G. 2012. Organ dose conversion coefficients based on a voxel mouse model and MCNP code for external photon irradiation. Radiation Protection Doseimetry, 148:9-19.

Zolle I, ed. 2007. Technetium-99m Pharmaceuticals: Preparation and Quality Control in Nuclear Medicine. Springer: Berlin.

APPENDIX A1: DERIVATION OF ACTIVITY CONCENTRATION AND DOSE EQUATIONS

1. Activity concentration

$$\frac{dB(t)}{dt} = \mu \cdot W(t) - k \cdot B(t)$$

Substitute $W(t) = a \cdot e^{-bt} \Rightarrow \frac{dB(t)}{dt} = \mu \cdot a \cdot e^{-bt} - k \cdot B(t)$

Rearrange: $\frac{dB(t)}{dt} + k \cdot B(t) = \mu \cdot a \cdot e^{-bt}$

Multiply by an "integration factor," e^{kt}: $\frac{dB(t)}{dt} \cdot e^{kt} + k \cdot B(t) \cdot e^{kt} = \mu \cdot a \cdot e^{-bt} \cdot e^{kt}$

Make use of derivative rules: $\frac{de^{kt}}{dt} = ke^{kt} \Rightarrow \frac{dB(t)}{dt} \cdot e^{kt} + B(t) \cdot \frac{de^{kt}}{dt} = \mu \cdot a \cdot e^{(k-b)t}$

LHS of the equation is the power rule for derivatives: $\frac{d}{dt}\left(B(t)e^{kt}\right) = \mu \cdot a \cdot e^{(k-b)t}$

Rearrange: $d\left(B(t)e^{kt}\right) = \left(\mu \cdot a \cdot e^{(k-b)t}\right)dt$

Integrate:

$$\int d\left(B(t)e^{kt}\right) = \int\left(\mu \cdot a \cdot e^{(k-b)t}\right)dt$$

$$B(t)e^{kt}\Big|_0^t = \mu a \int\left(e^{(k-b)t}\right)dt$$

$$B(t)e^{kt} - B(0) = \mu a\left(\frac{1}{k-b}\right)\int\left(e^{u}\right)du$$

$$B(t)e^{kt} - B(0) = \mu a\left(\frac{1}{k-b}\right)e^{(k-b)t}\Big|_0^t$$

Solve for $B(t)$:

$$B(t)e^{kt} - B(0) = \mu a\left(\frac{1}{k-b}\right)\left[e^{(k-b)t} - 1\right]$$

$$B(t)e^{kt} = \mu a\left(\frac{1}{k-b}\right)e^{(k-b)t} - \mu a\left(\frac{1}{k-b}\right) + B(0)$$

$$B(t) = \mu a\left(\frac{1}{k-b}\right)e^{-bt} - \mu a\left(\frac{1}{k-b}\right)e^{-kt} + B(0)e^{-kt}$$

$$B(t) = \mu a\left(\frac{1}{k-b}\right)\left(e^{-bt} - e^{-kt}\right) + B(0)e^{-kt}$$

2. Dose and dose rate due to ^{99m}Tc

From Chapter 3 (Equation 3-4):

$$A_d(t) = A_p(t)\frac{\lambda_d(0.8773)\left(1-e^{(-\lambda_d+\lambda_p)t}\right)}{\left(\lambda_d-\lambda_p\right)} \Rightarrow B_d(t) = B_p(t)\frac{\lambda_d(0.8773)\left(1-e^{(-\lambda_d+\lambda_p)t}\right)}{\left(\lambda_d-\lambda_p\right)}$$

Substituting in for $B_p(t)$ (Equation 3-5):

$$B_d(t) = \left(\frac{\mu a}{k-b}\right)\left(e^{-bt}-e^{-kt}\right)\frac{\lambda_d(0.8773)\left(1-e^{(-\lambda_d+\lambda_p)t}\right)}{\left(\lambda_d-\lambda_p\right)}$$

$$B_d(t) = \left(\frac{\mu a\lambda_d(0.8773)}{(k-b)\left(\lambda_d-\lambda_p\right)}\right)\left(e^{-bt}-e^{-kt}\right)\left(1-e^{(-\lambda_d+\lambda_p)t}\right)$$

Therefore, dose rate becomes:

$$\dot{D}(t) = \text{DCF}(\text{mass ratio})B_d(t) = \text{DCF}(\text{mass ratio})\left(\frac{\mu a\lambda_d(0.8773)}{(k-b)\left(\lambda_d-\lambda_p\right)}\right)\left(e^{-bt}-e^{-kt}\right)\left(1-e^{(-\lambda_d+\lambda_p)t}\right)$$

Integrating:

$$\int dD(t) = \int \text{DCF}(\text{mass ratio})\left(\frac{\mu a\lambda_d(0.8773)}{(k-b)\left(\lambda_d-\lambda_p\right)}\right)\left(e^{-bt}-e^{-kt}\right)\left(1-e^{(-\lambda_d+\lambda_p)t}\right)dt$$

$$D(t) = \text{DCF}(\text{mass ratio})(0.8773)\left(\frac{\mu a\lambda_d}{(k-b)\left(\lambda_d-\lambda_p\right)}\right)\int\left(e^{-bt}-e^{-kt}\right)\left(1-e^{(-\lambda_d+\lambda_p)t}\right)dt$$

$$\int\left(e^{-bt}-e^{-kt}\right)\left(1-e^{(-\lambda_d+\lambda_p)t}\right)dt = \int\left(e^{-bt}-e^{(-b-\lambda_d+\lambda_p)t}-e^{-kt}+e^{(-k-\lambda_d+\lambda_p)t}\right)dt$$

$$\int e^{-bt}dt - \int e^{(-b-\lambda_d+\lambda_p)t}dt - \int e^{-kt}dt + \int e^{(-k-\lambda_d+\lambda_p)t}dt$$

$$\left[-\frac{1}{b}e^{-bt} - \frac{1}{\left(-b-\lambda_d+\lambda_p\right)}e^{(-b-\lambda_d+\lambda_p)t} + \frac{1}{k}e^{-kt} + \frac{1}{\left(-k-\lambda_d+\lambda_p\right)}e^{(-k-\lambda_d+\lambda_p)t}\right]\Bigg|_0^t$$

$$-\frac{1}{b}e^{-bt}-\frac{1}{\left(-b-\lambda_d+\lambda_p\right)}e^{\left(-b-\lambda_d+\lambda_p\right)t}+\frac{1}{k}e^{-kt}+\frac{1}{\left(-k-\lambda_d+\lambda_p\right)}e^{\left(-k-\lambda_d+\lambda_p\right)t}$$
$$-\left[-\frac{1}{b}-\frac{1}{\left(-b-\lambda_d+\lambda_p\right)}+\frac{1}{k}+\frac{1}{\left(-k-\lambda_d+\lambda_p\right)}\right]$$

$$-\frac{1}{b}e^{-bt}-\frac{1}{\left(-b-\lambda_d+\lambda_p\right)}e^{\left(-b-\lambda_d+\lambda_p\right)t}+\frac{1}{k}e^{-kt}+\frac{1}{\left(-k-\lambda_d+\lambda_p\right)}e^{\left(-k-\lambda_d+\lambda_p\right)t}$$
$$+\frac{1}{b}+\frac{1}{\left(-b-\lambda_d+\lambda_p\right)}-\frac{1}{k}-\frac{1}{\left(-k-\lambda_d+\lambda_p\right)}$$

$$\Rightarrow D(t)=\text{DCF}\cdot(\text{mass ratio})\cdot(0.8773)\cdot\left(\frac{\mu a\lambda_d}{(k-b)\left(\lambda_d-\lambda_p\right)}\right)\cdot$$
$$\left[\frac{1}{b}\left(1-e^{-bt}\right)+\frac{1}{\left(-b-\lambda_d+\lambda_p\right)}\left(1-e^{\left(-b-\lambda_d+\lambda_p\right)t}\right)+\frac{1}{k}\left(e^{-kt}-1\right)+\frac{1}{\left(-k-\lambda_d+\lambda_p\right)}\left(e^{\left(-k-\lambda_d+\lambda_p\right)t}-1\right)\right]$$

For the codes below, the first example in each section is the full version of the MCNP code (with the exception of the voxel code; the lattice structure runs upwards of 10,000 lines of code, most of which are omitted). The following versions within a section include just the portions of code that are different, as indicated in colored text.

1. Simple model

1.1. ^{131}I beta energy

```
c -------------------------------------------------------------------------------
c
c     __   __     |    __    .  _    __    __|     __          __   _|_   __   _|_   __
c    /     /  \   |   /  \   |/ \   __| /   |    /  \        /__     |    __|    |   /__\
c    \__   \__/   \_ \__/   |    |__| \__|    \__/        __/    \    |__|    \    \__,
c
c                  .  _     .              __   .  _    __   .   _|_
c              |   | |/ |   |   \    / /__\ |/ \ /__   |    |   |  |
c              \__| |   |   |    \/    \__, |     __/   |    \   \__|
c                                                          __|
c                        ~~~~~~~~~~~~~~~~~~~~~~~~~~
c                              NICOLE MARTINEZ
c                                JUNE 2013
c                        ~~~~~~~~~~~~~~~~~~~~~~~~~~
c                                    I-131
c                         BETA ENERGY DEPOSITION IN
c                    POUDRE RIVER (0.22 kg) RAINBOW TROUT THYROID
c                         L: 28.6 cm   W: 2.5 cm   H: 5.3 cm
c                    EXTRAPOLATED FROM JUVENILE RAINBOW TROUT
c                    MODELLED AS 18 CYLINDRICAL SHELL SOURCES
c
c
c -------------------------------------------------------------------------------
c                                 CELL CARDS
c -------------------------------------------------------------------------------
c
c        ______
c       |  38  |
c       | ____ |    Cell [odd] INNER PORTION THYROID TUBULE
c    74 ||    ||               LYMPH   P=1.0239 g/cm^3
c       || 37 ||    Cell [even]THYROID TUBULES
c       ||    ||               THYROID P=1.05 g/cm^3
c       ||____||    Cell 73    OUTSIDE THYROID TUBULES - FISH BODY
c       |      |               MUSCLE  P=1.05 g/cm^3
c       |______|    Cell 74    OUTSIDE FISH BODY
c
c         UPPER BUNDLE      LOWER BUNDLE  (OUTER CELLS)
c
c         __ __ __           __ __ __
c        /48\/44\/52\       /70\/66\/62\
c       _\__/\__/\__/       \__/\__/\__/_
c      /42\/38\/40\           /60\/56\/58\
c      \__/\__/\__/_          _\__/\__/\__/
```

```
c        /50\/46\/54\     /72\/68\/64\
c        \__/\__/\__/     \__/\__/\__/
c ---------------------------------------------------------------------------
c ------------------------------ CELLS ---------------------------------------
c --------------- Upper tubule bundle ---------------
37  1 -1.03  -2           imp:n=0 imp:p,e=1  $ Inner (colloid)
38  2 -1.05  -1   2       imp:n=0 imp:p,e=1  $ Outer shell (thyroid epithelial)
c ---------------
39  1 -1.03  -4           imp:n=0 imp:p,e=1
40  2 -1.05  -3   4       imp:n=0 imp:p,e=1
c ---------------
41  1 -1.03  -6           imp:n=0 imp:p,e=1
42  2 -1.05  -5   6       imp:n=0 imp:p,e=1
c ---------------
43  1 -1.03  -8           imp:n=0 imp:p,e=1
44  2 -1.05  -7   8       imp:n=0 imp:p,e=1
c ---------------
45  1 -1.03  -10          imp:n=0 imp:p,e=1
46  2 -1.05  -9   10      imp:n=0 imp:p,e=1
c ---------------
47  1 -1.03  -12          imp:n=0 imp:p,e=1
48  2 -1.05  -11   12     imp:n=0 imp:p,e=1
c ---------------
49  1 -1.03  -14          imp:n=0 imp:p,e=1
50  2 -1.05  -13   14     imp:n=0 imp:p,e=1
c ---------------
51  1 -1.03  -16          imp:n=0 imp:p,e=1
52  2 -1.05  -15   16     imp:n=0 imp:p,e=1
c ---------------
53  1 -1.03  -18          imp:n=0 imp:p,e=1
54  2 -1.05  -17   18     imp:n=0 imp:p,e=1
c --------------- Lower tubule bundle -------------
55  1 -1.03  -20          imp:n=0 imp:p,e=1
56  2 -1.05  -19   20     imp:n=0 imp:p,e=1
c ---------------
57  1 -1.03  -22          imp:n=0 imp:p,e=1
58  2 -1.05  -21   22     imp:n=0 imp:p,e=1
c ---------------
59  1 -1.03  -24          imp:n=0 imp:p,e=1
60  2 -1.05  -23   24     imp:n=0 imp:p,e=1
c ---------------
61  1 -1.03  -26          imp:n=0 imp:p,e=1
62  2 -1.05  -25   26     imp:n=0 imp:p,e=1
c ---------------
63  1 -1.03  -28          imp:n=0 imp:p,e=1
64  2 -1.05  -27   28     imp:n=0 imp:p,e=1
c ---------------
65  1 -1.03  -30          imp:n=0 imp:p,e=1
66  2 -1.05  -29   30     imp:n=0 imp:p,e=1
c ---------------
67  1 -1.03  -32          imp:n=0 imp:p,e=1
68  2 -1.05  -31   32     imp:n=0 imp:p,e=1
c ---------------
69  1 -1.03  -34          imp:n=0 imp:p,e=1
70  2 -1.05  -33   34     imp:n=0 imp:p,e=1
c ---------------
71  1 -1.03  -36          imp:n=0 imp:p,e=1
72  2 -1.05  -35   36     imp:n=0 imp:p,e=1
c ---------------- Body of fish ------------------
73  3 -1.05  -37   1 3 5 7 9 11 13 15 17 19
                   21 23 25 27 29 31 33 35   imp:n=0 imp:p,e=1
c -------------- Water around fish ---------------
c 74  4 -1    -999   37          imp:n=0 imp:p,e=1
```

```
c ---------------- Universe (void) ---------------
75  0              37         imp:n,p,e=0

c ------------------------------------------------------------------------------
c                            SURFACE CARDS                                     c
c ------------------------------------------------------------------------------
c  [odd] RCC: Outer right circular cylinder, // z-axis h=3.6 mm, r=0.30 mm
c [even] RCC: Inner right circular cylinder, // z-axis h=3.52 mm, r=0.26 mm
c        Base of even numbered RCC located such that it is centered within
c          within the prior odd numbered RCC
c
c  Radii of outer cylinders slightly less than 0.0239 cm to avoid surfaces
c    touching; i.e. "problem geometry" in source definition
c
c  For SQ: Ellipsoid centered at 0 2 -9 (to approximate thyroid location)
c            radius in z-direction = 16 cm (1/(16^2))=0.0030864 -> 36 cm length
c            radius in y-direction = 4 cm                       ->  8 cm height
c            radius in x-direction = 2 cm                       ->  4 cm width
c
c Raine et al. The thyroid tissue of juvenile Oncorhynchus mykiss is tubular,
c  not follicular. Journal of Fish Biology. 2005.
c
c ------------------------------------------------------------------------------
c          center of base          height       radius
c         x        y       z       // z-axis   normal to z axis
1   RCC   0        0       0         0 0 0.2862     0.0238
2   RCC   0        0      0.0032     0 0 0.2798     0.0207
3   RCC   0.0477   0      0.0080     0 0 0.2862     0.0238
4   RCC   0.0477   0      0.0111     0 0 0.2798     0.0207
5   RCC  -0.0477   0      0.0127     0 0 0.2862     0.0238
6   RCC  -0.0477   0      0.0159     0 0 0.2798     0.0207
7   RCC   0.0239  0.0413  0.0159     0 0 0.2862     0.0238
8   RCC   0.0239  0.0413  0.0191     0 0 0.2798     0.0207
9   RCC   0.0239 -0.0413 -0.0477     0 0 0.2862     0.0238
10  RCC   0.0239 -0.0413 -0.0445     0 0 0.2798     0.0207
11  RCC  -0.0239  0.0413  0.0636     0 0 0.2862     0.0238
12  RCC  -0.0239  0.0413  0.0668     0 0 0.2798     0.0207
13  RCC  -0.0239 -0.0413 -0.0159     0 0 0.2862     0.0238
14  RCC  -0.0239 -0.0413 -0.0127     0 0 0.2798     0.0207
15  RCC   0.0717  0.0413  0.1590     0 0 0.2862     0.0238
16  RCC   0.0717  0.0413  0.1622     0 0 0.2798     0.0207
17  RCC   0.0717 -0.0413  0.0239     0 0 0.2862     0.0238
18  RCC   0.0717 -0.0413  0.0270     0 0 0.2798     0.0207
19  RCC   0        0      -0.3816     0 0 0.2862     0.0238
20  RCC   0        0      -0.3784     0 0 0.2798     0.0207
21  RCC   0.0477   0      -0.3737     0 0 0.2862     0.0238
22  RCC   0.0477   0      -0.3705     0 0 0.2798     0.0207
23  RCC  -0.0477   0      -0.3689     0 0 0.2862     0.0238
24  RCC  -0.0477   0      -0.3657     0 0 0.2798     0.0207
25  RCC   0.0239  0.0413 -0.3657     0 0 0.2862     0.0238
26  RCC   0.0239  0.0413 -0.3625     0 0 0.2798     0.0207
27  RCC   0.0239 -0.0413 -0.4293     0 0 0.2862     0.0238
28  RCC   0.0239 -0.0413 -0.4261     0 0 0.2798     0.0207
29  RCC  -0.0239  0.0413 -0.3180     0 0 0.2862     0.0238
30  RCC  -0.0239  0.0413 -0.3148     0 0 0.2798     0.0207
31  RCC  -0.0239 -0.0413 -0.3975     0 0 0.2862     0.0238
32  RCC  -0.0239 -0.0413 -0.3943     0 0 0.2798     0.0207
33  RCC  -0.0717  0.0413 -0.2226     0 0 0.2862     0.0238
34  RCC  -0.0717  0.0413 -0.2194     0 0 0.2798     0.0207
35  RCC  -0.0717 -0.0413 -0.3578     0 0 0.2862     0.0238
36  RCC  -0.0717 -0.0413 -0.3546     0 0 0.2798     0.0207
c
37  SQ  0.64  0.12486 0.00488   0 0 0    -1     0 1.59 -10
```

```
c 999 SPH                                                0 1.59 -10.0   44
c ------------------------------------------------------
c 37 RCC 0 0 -0.4452    0 0 0.9063    0.1115
c Use above 37 RCC in exchange for SQ for graphical verification that
c   source definition geometry on data card is appropriate

c ------------------------------------------------------------------------------
c                              DATA CARDS
c ------------------------------------------------------------------------------
c ------------------------- SOURCE DEFININION ----------------------------------
c Particles started within the sampling boundary (cylinder) - any particle
c  that is started within the boundary but not within the specified source cells
c  (thyroid tubule 'shells') is rejected.  Sampling boundary MUST include all
c  source cells.
c
c  In source definition, "d1" is described by "si1" and "sp1" cards
c                                              where "i" info, "p" probability
c
c "L" list; "D" discrete; "A" indicates probablity distribution fuction defined
c Energy spectra references:
c  Stabin MG, and CQP da Luz, L. "Decay data for internal and external dose
c   assessment." Health Phys. 83:471-475; 2002. http://www.doseinfo-radar.com/
c  K. F. Eckerman, R. J. Westfall, J. C. Ryman, and M. Christy.
c   "Availability of Nuclear Decay Data in Electronic Form, Including Beta
c   Spectra not Previously Published," Health Phys. 67(4):338-345 (1994).
c ------------------------------------------------------------------------------
sdef cel=d5             $ Define source cells: which ones and what fraction
     axs=0 0 1          $ Define sampling boundary: cylinder along z-axis
     pos=0 0 -0.4452    $    Base centered at 0 0 -0.4452
     rad=d1             $    Define radius (in x and y direction)
     ext=d2             $    Define height (extend up z-axis)
     erg=d3             $ Define energy of source (beta spectra)
     par=3              $ par=3 --> electron
     eff=0.000001       $ Sampling efficiency (reduce because source is small)
c ----------------- Sampling boundary ----------------------
si1  0    0.1115       $ Radius of sampling cylinder that contains source
sp1 -21      1         $ -21 1 for radial sample (dependent on r)
si2  0    0.9063       $ Height of sampling cylinder that contains source
sp2 -21      0         $ Weighting for axial sample (not dependent on r)
c ----------------- Energy definition ----------------------
si3 A 2.02E-02  6.05E-02  1.01E-01  1.41E-01  1.82E-01    $ Iodine beta spectra
      2.22E-01  2.62E-01  3.03E-01  3.43E-01  3.83E-01
      4.24E-01  4.64E-01  5.04E-01  5.45E-01  5.85E-01
      6.25E-01  6.66E-01  7.06E-01  7.46E-01  7.87E-01
sp3   1.38E-01  1.31E-01  1.23E-01  1.13E-01  1.02E-01
      8.94E-02  7.70E-02  6.47E-02  5.30E-02  4.15E-02
      3.03E-02  2.00E-02  1.12E-02  4.55E-03  8.55E-04
      1.15E-04  6.94E-05  4.13E-05  1.73E-05  2.96E-06
c ------ Specific source cells with equal distribution -------
si5 L 38 40 42 44 46 48 50 52 54 56 58 60 62 64 66 68 70 72  $ Thyroid epithelial
sp5    1  1  1  1  1  1  1  1  1  1  1  1  1  1  1  1  1  1
c ------------------------------------------------------------------------------
c ---------------------------- TALLY -------------------------------------------
mode p e
nps 10000000                            $ Particle cutoff: 10^7
c *f18:p,e 38 40 42 44 46 48 50 52 54    $ Thyroid epithelial:
c        56 58 60 62 64 66 68 70 72 T    $   Individual tallies as well as total
*f28:p,e 73                             $ Fish body
*f38:p,e 37 39 41 43 45 47 49 51 53      $ Thyroid lumen:
         55 57 59 61 63 65 67 69 71 T    $   Individual tallies as well as total
*f48:p,e (37 39 41 43 45 47 49 51 53     $ Style to match above, total tally
          55 57 59 61 63 65 67 69 71     $   for lumen, epithelial, body
          38 40 42 44 46 48 50 52 54     $   for QA/QC
```

```
          56 58 60 62 64 66 68 70 72     $   --> Parenthesis indicate union only
          73)
E0 0 5.0
c  With combined line above will not get tally fluctuation
c  charts for each cell or individual statistical checks
PRINT 110
PRDMP 1E6
c ---------------------------------------------------------------------------
c ---------------------------- MATERIALS ------------------------------------
c McConn, Gesh, Pagh, Rucker, Williams. Radiation Portal Monitor Project:
c   Compendium of Material Composition Data for Radation Transport Modeling
c   Revision 1: March 4, 2011, Pacific Northwest National Laboratory
c   PIET-43541-TM-963 PNNL-15870 Rev. 1
c
c ICRU Report 44: Tissue Substitutes in Radiation Dosimetry and Measurement
c   International commission on Radiation Units and Measurements
c ---------------------------------------------------------------------------
c Lymph (ICRU) (by mass fraction), p = 1.0239 g/cm^3
m1    1000  -0.108   $ H
      6000  -0.041   $ C
      7000  -0.011   $ N
      8000  -0.832   $ O
     11000  -0.003   $ Na
     16000  -0.001   $ S
     17000  -0.004   $ Cl
c Thyroid (ICRU), p = 1.05 g/cm^3
m2    1000  -0.104   $ H
      6000  -0.119   $ C
      7000  -0.024   $ N
      8000  -0.745   $ O
     11000  -0.002   $ Na
     15000  -0.001   $ P
     16000  -0.001   $ S
     17000  -0.002   $ Cl
     19000  -0.001   $ K
     53000  -0.001   $ I
c Muscle, skeletal (ICRU) by mass fraction), p = 1.05 g/cm^3
m3    1000  -0.102   $ H
      6000  -0.143   $ C
      7000  -0.034   $ N
      8000  -0.710   $ O
     11000  -0.001   $ Na
     15000  -0.002   $ P
     16000  -0.003   $ S
     17000  -0.001   $ Cl
     19000  -0.004   $ K
c Water
m4   1000  -0.11190  $ H
     8000  -0.88810  $ O
```

1.2. ^{131}I gamma energy

```
c ---------------------------------------------------------------------------
c                                I-131
c                     GAMMA ENERGY DEPOSITION IN
c                  POUDRE RIVER (0.22 kg) RAINBOW TROUT
c                    L: 28.6 cm   W: 2.5 cm   H: 5.3 cm
c                          SOURCE - THYROID
c ---------------------------------------------------------------------------
c ---------------------------------------------------------------------------
sdef cel=d5            $ Define source cells: which ones and what fraction
     axs=0 0 1         $ Define sampling boundary: cylinder along z-axis
```

```
     pos=0 0 -0.4452   $    Base centered at 0 0 -0.4452
     rad=d1            $    Define radius (in x and y direction)
     ext=d2            $    Define height (extend up z-axis)
     erg=d3            $ Define energy of source (beta spectra)
     par=2             $ par=2 --> photon
     eff=0.000001      $ Sampling efficiency (reduce because source is small)
c ------------------ Sampling boundary ----------------------
si1  0    0.1115      $ Radius of sampling cylinder that contains source
sp1 -21      1        $ -21 1 for radial sample (dependent on r)
si2  0    0.9063      $ Height of sampling cylinder that contains source
sp2 -21      0        $ Weighting for axial sample (not dependent on r)
c ------------------ Energy definition -----------------------
si3 L 0.636989 0.364489   $ Gammas, in MeV; "L" = "list"
sp3 D 0.0717   0.817
c --------------------------------------------------------------------------------
```

2. Stylized model

2.1. ^{131}I beta energy, source organ thyroid

```
c --------------------------------------------------------------------------------
c
c    __   __      |    __   .  _   __    __|   __          __   _|_  __   _|_  __
c   /  \ /  \  |  |  /  \  |/ \  __| /  |  /  \       /__   |   __|  |  /__\
c   \__  \__/  \_ \__/  |    |__| \__|  \__/       __/   \  |__|  \  \__,
c
c                 .  _   .          __  .  _   __  .  _|_
c            |  | |/ |  |  \  / /__\ |/ \ /__  |   |  |  |
c            \__| |  |  |   \/  \__, |    __/  |   \  \__|
c                                                    __|
c                      ~~~~~~~~~~~~~~~~~~~~~~~~~~
c                            NICOLE MARTINEZ
c                             JANUARY 2014
c                      ~~~~~~~~~~~~~~~~~~~~~~~~~~
c                                I-131
c                       BETA ENERGY DEPOSITION IN
c
c                    POUDRE RIVER (0.22 kg) RAINBOW TROUT
c                      L: 28.6 cm   W: 2.5 cm   H: 5.3 cm
c
c  ORGANS:
c   Thyroid extrapolated from juvenile rainbow trout (Raine et al 2005) and
c      modeled as 18 cylindrical shells
c   Liver: Modeled as an ellipsoid
c   GI tract: Modeled as intestine (right circular cylinder, rotated 2 deg)
c      and cardiac/pyloric stomachs (right ellipsoidal cylinders)
c   Swim bladder: Modeled as an ellipsoid, rotated 2 deg from horizontal
c   Ovaries: Modeled as right circular cylinders, rotated 5 deg from horizontal
c
c                              SOURCE - THYROID
c
c
c --------------------------------------------------------------------------------
c                               CELL CARDS
c --------------------------------------------------------------------------------
c
c       ______
c      |  38  |
c      | ____ |    Cell [odd] INNER PORTION THYROID TUBULE
c   74 ||    ||               LYMPH   P=1.0239 g/cm^3
c      || 37 ||    Cell [even]THYROID TUBULES
c      ||    ||               THYROID P=1.05 g/cm^3
```

```
c      ||____||    Cell 73    OUTSIDE THYROID TUBULES - FISH BODY
c      |      |               MUSCLE  P=1.05 g/cm^3
c      |______|    Cell 74    OUTSIDE FISH BODY
c
c        UPPER BUNDLE     LOWER BUNDLE  (OUTER CELLS)
c          __  __  __       __  __  __
c        /48\/44\/52\     /70\/66\/62\
c       _\__/\__/\__/     \__/\__/\__/_
c      /42\/38\/40\         /60\/56\/58\
c      \__/\__/\__/_       _\__/\__/\__/
c        /50\/46\/54\     /72\/68\/64\
c        \__/\__/\__/     \__/\__/\__/
c ------------------------------------------------------------------------------
c ------------------------------- CELLS ----------------------------------------
c ++++++++++ Upper tubule bundle +++++++++++++
50  1 -1.03  -2            imp:n=0 imp:p,e=1  $ Inner (colloid)
51  2 -1.05  -1   2        imp:n=0 imp:p,e=1  $ Outer shell (thyroid epithelial)
c ---------------
52  1 -1.03  -4            imp:n=0 imp:p,e=1
53  2 -1.05  -3   4        imp:n=0 imp:p,e=1
c ---------------
54  1 -1.03  -6            imp:n=0 imp:p,e=1
55  2 -1.05  -5   6        imp:n=0 imp:p,e=1
c ---------------
56  1 -1.03  -8            imp:n=0 imp:p,e=1
57  2 -1.05  -7   8        imp:n=0 imp:p,e=1
c ---------------
58  1 -1.03  -10           imp:n=0 imp:p,e=1
59  2 -1.05  -9   10       imp:n=0 imp:p,e=1
c ---------------
60  1 -1.03  -12           imp:n=0 imp:p,e=1
61  2 -1.05  -11   12      imp:n=0 imp:p,e=1
c ---------------
62  1 -1.03  -14           imp:n=0 imp:p,e=1
63  2 -1.05  -13   14      imp:n=0 imp:p,e=1
c ---------------
64  1 -1.03  -16           imp:n=0 imp:p,e=1
65  2 -1.05  -15   16      imp:n=0 imp:p,e=1
c ---------------
66  1 -1.03  -18           imp:n=0 imp:p,e=1
67  2 -1.05  -17   18      imp:n=0 imp:p,e=1
c ++++++++++ Lower tubule bundle +++++++++++
68  1 -1.03  -20           imp:n=0 imp:p,e=1
69  2 -1.05  -19   20      imp:n=0 imp:p,e=1
c ---------------
70  1 -1.03  -22           imp:n=0 imp:p,e=1
71  2 -1.05  -21   22      imp:n=0 imp:p,e=1
c ---------------
72  1 -1.03  -24           imp:n=0 imp:p,e=1
73  2 -1.05  -23   24      imp:n=0 imp:p,e=1
c ---------------
74  1 -1.03  -26           imp:n=0 imp:p,e=1
75  2 -1.05  -25   26      imp:n=0 imp:p,e=1
c ---------------
76  1 -1.03  -28           imp:n=0 imp:p,e=1
77  2 -1.05  -27   28      imp:n=0 imp:p,e=1
c ---------------
78  1 -1.03  -30           imp:n=0 imp:p,e=1
79  2 -1.05  -29   30      imp:n=0 imp:p,e=1
c ---------------
80  1 -1.03  -32           imp:n=0 imp:p,e=1
81  2 -1.05  -31   32      imp:n=0 imp:p,e=1
c ---------------
```

```
82  1 -1.03  -34           imp:n=0 imp:p,e=1
83  2 -1.05  -33   34      imp:n=0 imp:p,e=1
c ---------------
84  1 -1.03  -36           imp:n=0 imp:p,e=1
85  2 -1.05  -35   36      imp:n=0 imp:p,e=1
c ++++++++++++++++++++++++++++++++++++++++++
86  5   -1.06  -37          imp:n=0 imp:p,e=1  $ Liver
c +++++++++++++++++ GI tract +++++++++++++++++
87  6   -1.03  -38          imp:n=0 imp:p,e=1  $ Intestine
88  6   -1.03  -39          imp:n=0 imp:p,e=1  $ Stomach
89  6   -1.03  -40          imp:n=0 imp:p,e=1  $ Pyloric stomach
90  6   -1.03  -41          imp:n=0 imp:p,e=1  $ Pyloric stomach
c ++++++++++++++++++++++++++++++++++++++++++
91  7   -1.05  -42          imp:n=0 imp:p,e=1  $ Ovary
92  7   -1.05  -43          imp:n=0 imp:p,e=1  $ Ovary
93  8   -0.001205 -44       imp:n=0 imp:p,e=1  $ Swim bladder
94  9   -1.06  -45          imp:n=0 imp:p,e=1  $ Heart
95  10  -1.04  -46          imp:n=0 imp:p,e=1  $ Brain
c ---------------- Body of fish ------------------
99  3 -1.05  -50   1 3 5 7  9  11 13 15 17 19 21 23 25 27 29
                   31 33 35 37 38 39 40 41 42 43 44 45 46    imp:n=0 imp:p,e=1
c -------------- Water around fish ---------------
c 101  4 -1   -999   50          imp:n=0 imp:p,e=1
c ---------------- Universe (void) ---------------
100  0             50         imp:n,p,e=0

c ------------------------------------------------------------------------------
c                            SURFACE CARDS                                     c
c ------------------------------------------------------------------------------
c  [odd] RCC: Outer right circular cylinder, // z-axis h=3.6 mm, r=0.30 mm
c [even] RCC: Inner right circular cylinder, // z-axis h=3.52 mm, r=0.26 mm
c        Base of even numbered RCC located such that it is centered within
c          within the prior odd numbered RCC
c
c  Radii of outer cylinders slightly less than 0.0239 cm to avoid surfaces
c    touching; i.e. "problem geometry" in source definition
c
c  For SQ: Ellipsoid centered at 0 1.59 -10 (to approximate thyroid location)
c       radius in z-direction = 14.3 cm (1/(14.3^2))= 0.00488 -> 28.6 cm length
c       radius in y-direction = 2.83 cm                       ->  5.66 cm height
c       radius in x-direction = 1.25 cm                       ->  2.5 cm width
c
c Raine et al. The thyroid tissue of juvenile Oncorhynchus mykiss is tubular,
c  not follicular. Journal of Fish Biology. 2005.
c
c ------------------------------------------------------------------------------
c          center of base             height        radius
c         x        y       z         // z-axis   normal to z axis
c ------------------------------------------------------------------------------
1   RCC   0       0       0          0 0 0.2862     0.0238
2   RCC   0       0       0.0032     0 0 0.2798     0.0207
3   RCC   0.0477  0       0.0080     0 0 0.2862     0.0238
4   RCC   0.0477  0       0.0111     0 0 0.2798     0.0207
5   RCC  -0.0477  0       0.0127     0 0 0.2862     0.0238
6   RCC  -0.0477  0       0.0159     0 0 0.2798     0.0207
7   RCC   0.0239  0.0413  0.0159     0 0 0.2862     0.0238
8   RCC   0.0239  0.0413  0.0191     0 0 0.2798     0.0207
9   RCC   0.0239 -0.0413 -0.0477     0 0 0.2862     0.0238
10  RCC   0.0239 -0.0413 -0.0445     0 0 0.2798     0.0207
11  RCC  -0.0239  0.0413  0.0636     0 0 0.2862     0.0238
12  RCC  -0.0239  0.0413  0.0668     0 0 0.2798     0.0207
13  RCC  -0.0239 -0.0413 -0.0159     0 0 0.2862     0.0238
14  RCC  -0.0239 -0.0413 -0.0127     0 0 0.2798     0.0207
```

```
15  RCC    0.0717  0.0413  0.1590      0 0 0.2862      0.0238
16  RCC    0.0717  0.0413  0.1622      0 0 0.2798      0.0207
17  RCC    0.0717 -0.0413  0.0239      0 0 0.2862      0.0238
18  RCC    0.0717 -0.0413  0.0270      0 0 0.2798      0.0207
19  RCC    0       0       -0.3816     0 0 0.2862      0.0238
20  RCC    0       0       -0.3784     0 0 0.2798      0.0207
21  RCC    0.0477  0       -0.3737     0 0 0.2862      0.0238
22  RCC    0.0477  0       -0.3705     0 0 0.2798      0.0207
23  RCC   -0.0477  0       -0.3689     0 0 0.2862      0.0238
24  RCC   -0.0477  0       -0.3657     0 0 0.2798      0.0207
25  RCC    0.0239  0.0413 -0.3657     0 0 0.2862      0.0238
26  RCC    0.0239  0.0413 -0.3625     0 0 0.2798      0.0207
27  RCC    0.0239 -0.0413 -0.4293     0 0 0.2862      0.0238
28  RCC    0.0239 -0.0413 -0.4261     0 0 0.2798      0.0207
29  RCC   -0.0239  0.0413 -0.3180     0 0 0.2862      0.0238
30  RCC   -0.0239  0.0413 -0.3148     0 0 0.2798      0.0207
31  RCC   -0.0239 -0.0413 -0.3975     0 0 0.2862      0.0238
32  RCC   -0.0239 -0.0413 -0.3943     0 0 0.2798      0.0207
33  RCC   -0.0717  0.0413 -0.2226     0 0 0.2862      0.0238
34  RCC   -0.0717  0.0413 -0.2194     0 0 0.2798      0.0207
35  RCC   -0.0717 -0.0413 -0.3578     0 0 0.2862      0.0238
36  RCC   -0.0717 -0.0413 -0.3546     0 0 0.2798      0.0207
c
c  ------------------ Surfaces for liver ------------------
37  SQ   9  1.8   1.8  0 0 0  -1   0.59 0.52 -3.9
c
c  ------------------ Surface for GI tract ----------------
c  TR     Center of base     Height    Radius2  Radius
c  ------------------------------------------------------
38  2 RCC  0   0.8 -19.5    0 0 15.5             0.25  $ Intestine
39    REC  0  -0.4 -11      0 0  7.2   0.4 0 0   0.4   $ C Stomach
40    REC  0.6 0.3 -10.8    0 0  5.5   0.2 0 0   0.35  $ P Stomach
41    REC -0.6 0.3 -10.8    0 0  5.5   0.2 0 0   0.35  $ P Stomach
c
c   ------------------ Surfaces for ovaries --------------- $ Shift with SB
42  1 RCC  0.52 1.9 -14     0 0  5             0.08
43  1 RCC -0.52 1.9 -14     0 0  5             0.08
c
c   ----------------- Surface for swim bladder ------------
44  2 SQ  3.3  4  0.04   0 0 0    -1    0 1.65 -14.0
c
c   ------------------ Surface for heart ------------------
45  SQ   9 4   4     0 0 0    -1    0 0.4 -1.5
c
c   ------------------- Surface for Brain -----------------
46  SPH  0 2.9 0     0.5
c
c   ---------------  Surface for fish body -----------------
50  SQ  0.64  0.12486 0.00488   0 0 0    -1     0 1.59 -10
c
c  ----- Surface for water body if desired ----------------
c 999 SPH                                       0 1.59 -10.0   44
c ------------------------------------------------------------
c 50 RCC 0 0 -0.4452    0 0 0.9063    0.1115
c Use above 50 RCC in exchange for SQ for graphical verification that
c   source definition geometry on data card is appropriate

c ---------------------------------------------------------------------------
c                              DATA CARDS
c ---------------------------------------------------------------------------
c ---------------------- COORDINATE TRANSFORMS ------------------------------
c '*'  indicates that values are in degrees vice cos(theta)
c
```

```
c  TR1 rotating ovaries 5 degrees in ZY-plane  (would shift origin up in TR, but
c    taken care of in surface description)
c  TR2 rotating swim bladder and intestine 2 degrees in ZY-plane
c
c      Origin   xx' xy' xz'  yx' yy' yz'  zx' zy' zz'   How origin defined
c ------------------------------------------------------------------------------
*TR1   0 0 0  0 90 90   90 5 95   90 85 5  1
*TR2   0 0 0  0 90 90   90 2 92   90 88 2  1
c ------------------------- SOURCE DEFININION ---------------------------------
c Particles started within the sampling boundary (cylinder) - any particle
c  that is started within the boundary but not within the specified source cells
c  (thyroid tubule 'shells') is rejected.  Sampling boundary MUST include all
c  source cells.
c
c  In source definition, "d1" is described by "si1" and "sp1" cards
c                                              where "i" info, "p" probability
c Source information definition
c  L-discrete source variable values
c  A-points where a probability density distribution is defined
c  S-distribution numbers  (allows sampling among distributions)
c  H—bin boundaries for a histogram distribution
c  * Note for "A" and "H" entries on SI card need to be monotonically increasing
c Source probability
c  D-bin probabilities for an H or L distribution on SI card. Default.
c  C-cumulative bin probabilities for an H or L distribution on SI card.
c  V-for cell distributions only. Probability is proportional to cell volume.
c
c Energy spectra references:
c  Stabin MG, and CQP da Luz, L. "Decay data for internal and external dose
c   assessment." Health Phys. 83:471-475; 2002. http://www.doseinfo-radar.com/
c  K. F. Eckerman, R. J. Westfall, J. C. Ryman, and M. Christy.
c   "Availability of Nuclear Decay Data in Electronic Form, Including Beta
c   Spectra not Previously Published," Health Phys. 67(4):338-345 (1994).
c ------------------------------------------------------------------------------
sdef cel=d5                $ Define source cells: which ones and what fraction
     axs=0 0 1             $ Define sampling boundary: cylinder along z-axis
     pos=0 0 -0.4452       $ Base centered at 0 0 -0.4452
     rad=d1                $    Define radius (in x and y direction)
     ext=d2                $    Define height (extend up z-axis)
     erg=d3                $ Define energy of source (beta spectra)
     par=3                 $ par=3 --> electron
     eff=0.000001          $ Sampling efficiency (reduce because source is small)
c ------------------ Sampling boundary ----------------------
si1  0    0.1115      $ Radius of sampling cylinder that contains source
sp1 -21      1        $ -21 1 for radial sample (dependent on r)
si2  0    0.9063      $ Height of sampling cylinder that contains source
sp2 -21      0        $ Weighting for axial sample (not dependent on r)
c ------------------ Energy definition ----------------------
si3 A 2.02E-02  6.05E-02  1.01E-01  1.41E-01  1.82E-01    $ I-131 beta spectra
      2.22E-01  2.62E-01  3.03E-01  3.43E-01  3.83E-01
      4.24E-01  4.64E-01  5.04E-01  5.45E-01  5.85E-01
      6.25E-01  6.66E-01  7.06E-01  7.46E-01  7.87E-01
sp3   1.38E-01  1.31E-01  1.23E-01  1.13E-01  1.02E-01
      8.94E-02  7.70E-02  6.47E-02  5.30E-02  4.15E-02
      3.03E-02  2.00E-02  1.12E-02  4.55E-03  8.55E-04
      1.15E-04  6.94E-05  4.13E-05  1.73E-05  2.96E-06
c ------ Specific source cells with equal distribution -------
si5 L 51 53 55 57 59 61 63 65 67 69 71 73 75 77 79 81 83 85
sp5    1  1  1  1  1  1  1  1  1  1  1  1  1  1  1  1  1  1
c ------------------------------------------------------------------------------
c ---------------------------- TALLY -------------------------------------------
mode p e
nps 10000000                          $ Particle cutoff: 10^7
```

```
*f18:p,e 51 53 55 57 59 61 63 65 67      $ Thyroid epithelial:
         69 71 73 75 77 79 81 83 85 T    $   Individual tallies as well as total
*f28:p,e 50 52 54 56 58 60 62 64 66      $ Thyroid lumen:
         68 70 72 74 76 78 80 82 84 T    $   Individual tallies as well as total
*f38:p,e 87 88 89 90 T                   $ GI tract
*f48:p,e 86 91 92 93 94 95               $ Liver, ovary, heart, brain
*f58:p,e 99                              $ Fish body
*f68:p,e (50 52 54 56 58 60 62 64 66     $ Style to match above, total tally
          68 70 72 74 76 78 80 82 84     $   for lumen, epithelial, body
          51 53 55 57 59 61 63 65 67     $   for QA/QC
          69 71 73 75 77 79 81 83 85     $   --> Parenthesis indicate union only
          86 87 88 89 90 91 92 93 94     $ Note that swim bladder and lumen
          95 99)                         $   doses not biologically relevant
e0  0  5.0
c  With combined line above will not get tally fluctuation
c  charts for each cell or individual statistical checks
PRINT 110
PRDMP 1E6
c ---------------------------------------------------------------------------
c ---------------------------- MATERIALS ------------------------------------
c McConn, Gesh, Pagh, Rucker, Williams. Radiation Portal Monitor Project:
c   Compendium of Material Composition Data for Radation Transport Modeling
c   Revision 1: March 4, 2011, Pacific Northwest National Laboratory
c   PIET-43541-TM-963 PNNL-15870 Rev. 1
c
c ICRU Report 44: Tissue Substitutes in Radiation Dosimetry and Measurement
c   International commission on Radiation Units and Measurements
c ---------------------------------------------------------------------------
c Lymph (ICRU) (by mass fraction), p = 1.0239 g/cm^3
m1    1000  -0.108   $ H
      6000  -0.041   $ C
      7000  -0.011   $ N
      8000  -0.832   $ O
     11000  -0.003   $ Na
     16000  -0.001   $ S
     17000  -0.004   $ Cl
c Thyroid (ICRU), p = 1.05 g/cm^3
m2    1000  -0.104   $ H
      6000  -0.119   $ C
      7000  -0.024   $ N
      8000  -0.745   $ O
     11000  -0.002   $ Na
     15000  -0.001   $ P
     16000  -0.001   $ S
     17000  -0.002   $ Cl
     19000  -0.001   $ K
     53000  -0.001   $ I
c Muscle, skeletal (ICRU) by mass fraction), p = 1.05 g/cm^3
m3    1000  -0.102   $ H
      6000  -0.143   $ C
      7000  -0.034   $ N
      8000  -0.710   $ O
     11000  -0.001   $ Na
     15000  -0.002   $ P
     16000  -0.003   $ S
     17000  -0.001   $ Cl
     19000  -0.004   $ K
c Water
m4   1000  -0.11190  $ H
     8000  -0.88810  $ O
c Liver (ICRU) (by mass fraction), p = 1.06 g/cm^3
m5    1000  -0.102   $ H
      6000  -0.139   $ C
```

```
       7000  -0.030   $ N
       8000  -0.716   $ O
      11000  -0.002   $ Na
      15000  -0.003   $ P
      16000  -0.003   $ S
      17000  -0.002   $ Cl
      19000  -0.003   $ K
c GI tract (ICRU) (by mass fraction), p = 1.03 g/cm^3
m6    1000  -0.106   $ H
       6000  -0.115   $ C
       7000  -0.022   $ N
       8000  -0.751   $ O
      11000  -0.001   $ Na
      15000  -0.001   $ P
      16000  -0.001   $ S
      17000  -0.002   $ Cl
      19000  -0.001   $ K
c Ovary (ICRU) (by mass fraction), p = 1.05 g/cm^3
m7    1000  -0.105   $ H
       6000  -0.093   $ C
       7000  -0.024   $ N
       8000  -0.768   $ O
      11000  -0.002   $ Na
      15000  -0.002   $ P
      16000  -0.002   $ S
      17000  -0.002   $ Cl
      19000  -0.002   $ K
c SwimBladder - air
m8    7000  -0.755
       8000  -0.232
      18000  -0.013
c Heart - ICRU p = 1.06 g/cm^3
m9    1000  -0.103  $ H
       6000  -0.121  $ C
       7000  -0.032  $ N
       8000  -0.734  $ O
      11000  -0.001  $ Na
      15000  -0.001  $ P
      16000  -0.002  $ S
      17000  -0.003  $ Cl
      19000  -0.002  $ K
      26000  -0.001  $ Fe
c Brain - ICRU p = 1.04 g/cm^3
m10   1000  -0.107  $ H
       6000  -0.145  $ C
       7000  -0.022  $ N
       8000  -0.712  $ O
      11000  -0.002  $ Na
      15000  -0.004  $ P
      16000  -0.002  $ S
      17000  -0.003  $ Cl
      19000  -0.003  $ K
```

2.2. ^{131}I gamma energy, source organ liver

```
c ---------------------------------------------------------------------------
c                                I-131
c                     GAMMA ENERGY DEPOSITION IN
c                   POUDRE RIVER (0.22 kg) RAINBOW TROUT
c                     L: 28.6 cm   W: 2.5 cm   H: 5.3 cm
c                           SOURCE - LIVER
c ---------------------------------------------------------------------------
```

```
c 50 SPH 0.65 0.52 -3.9    0.72
c Use above 50 SPH in exchange for SQ for graphical verification that
c   source definition geometry on data card is appropriate

c ------------------------------------------------------------------------------
sdef cel=d5               $ Define source cells: which ones and what fraction
     pos=0.65 0.52 -3.9   $ Sampling boundary: sphere centered at 0.65 0.52 -3.9
     rad=d1               $    Define radius (in x, y, and z direction)
     erg=d3               $ Define energy of source (gamma)
     par=2                $ par=2 --> photon
     eff=0.000001         $ Sampling efficiency (reduce because source is small)
c ------------------ Sampling boundary ----------------------
si1  0       0.72     $ Radius of sphere containing source
sp1 -21      2        $ -21 2 for radial sample (dependent on r^2)
c ------------------ Energy definition ----------------------
si3 L 0.636989 0.364489   $ I-131 gammas, in MeV; "L" = "list"
sp3 D 0.0717   0.817
c ------ Specific source cells with equal distribution -------
si5 L 86
sp5    1
c ------------------------------------------------------------------------------
```

2.3. ^{131}I beta energy, source organ liver

```
c ------------------------------------------------------------------------------
c                                I-131
c                        BETA ENERGY DEPOSITION IN
c                    POUDRE RIVER (0.22 kg) RAINBOW TROUT
c                      L: 28.6 cm   W: 2.5 cm   H: 5.3 cm
c                            SOURCE - LIVER
c ------------------------------------------------------------------------------
c 50 SPH 0.65 0.52 -3.9    0.72
c Use above in exchange for SQ for graphical verification that
c   source definition geometry on data card is appropriate

c ------------------------------------------------------------------------------
sdef cel=d5               $ Define source cells: which ones and what fraction
     pos=0.65 0.52 -3.9   $ Sampling boundary: sphere centered at 0.65 0.52 -3.9
     rad=d1               $    Define radius
     erg=d3               $ Define energy of source (beta spectra)
     par=3                $ par=3 --> electron
     eff=0.000001           $ Sampling efficiency (reduce because source is small)
c ------------------ Sampling boundary ----------------------
si1  0       0.72     $ Radius of sphere containing source
sp1 -21      2        $ -21 2 for radial sample (dependent on r^2)
c ------------------ Energy definition ----------------------
si3 A 2.02E-02  6.05E-02  1.01E-01  1.41E-01  1.82E-01    $ Iodine beta spectra
      2.22E-01  2.62E-01  3.03E-01  3.43E-01  3.83E-01
      4.24E-01  4.64E-01  5.04E-01  5.45E-01  5.85E-01
      6.25E-01  6.66E-01  7.06E-01  7.46E-01  7.87E-01
sp3   1.38E-01  1.31E-01  1.23E-01  1.13E-01  1.02E-01
      8.94E-02  7.70E-02  6.47E-02  5.30E-02  4.15E-02
      3.03E-02  2.00E-02  1.12E-02  4.55E-03  8.55E-04
      1.15E-04  6.94E-05  4.13E-05  1.73E-05  2.96E-06
c ------ Specific source cells with equal distribution -------
si5 L 86
sp5    1
c ------------------------------------------------------------------------------
```

2.4. ^{131}I gamma energy, source organ thyroid

```
c ------------------------------------------------------------------------------
```

```
c                                I-131
c                        GAMMA ENERGY DEPOSITION IN
c                     POUDRE RIVER (0.22 kg) RAINBOW TROUT
c                       L: 28.6 cm   W: 2.5 cm   H: 5.3 cm
c                            SOURCE - THYROID
c ---------------------------------------------------------------------------
c 50 RCC 0 0 -0.4452    0 0 0.9063    0.1115
c Use above 50 RCC in exchange for SQ for graphical verification that
c   source definition geometry on data card is appropriate

c ---------------------------------------------------------------------------
c                               DATA CARDS
c ---------------------------------------------------------------------------
sdef cel=d5             $ Define source cells: which ones and what fraction
     axs=0 0 1          $ Define sampling boundary: cylinder along z-axis
     pos=0 0 -0.4452    $ Base centered at 0 0 -0.4452
     rad=d1             $    Define radius (in x and y direction)
     ext=d2             $    Define height (extend up z-axis)
     erg=d3             $ Define energy of source (gamma spectra)
     par=2              $ par=2 --> photon
     eff=0.000001       $ Sampling efficiency (reduce because source is small)
c ------------------ Sampling boundary ----------------------
si1  0    0.1115       $ Radius of sampling cylinder that contains source
sp1 -21      1         $ -21 1 for radial sample (dependent on r)
si2  0    0.9063       $ Height of sampling cylinder that contains source
sp2 -21      0         $ Weighting for axial sample (not dependent on r)
c ------------------ Energy definition -----------------------
si3 L 0.636989 0.364489   $ I-131 gammas, in MeV; "L" = "list"
sp3 D 0.0717   0.817
c ------ Specific source cells with equal distribution -------
si5 L 51 53 55 57 59 61 63 65 67 69 71 73 75 77 79 81 83 85
sp5    1  1  1  1  1  1  1  1  1  1  1  1  1  1  1  1  1  1
c ---------------------------------------------------------------------------
```

2.5. ^{131}I gamma energy, source organ GI tract

```
c ---------------------------------------------------------------------------
c                                I-131
c                        GAMMA ENERGY DEPOSITION IN
c                     POUDRE RIVER (0.22 kg) RAINBOW TROUT
c                       L: 28.6 cm   W: 2.5 cm   H: 5.3 cm
c                            SOURCE - GI TRACT
c ---------------------------------------------------------------------------
c 50 RCC 0 0.06 -20.75    0 0 17.5   1
c Use above in exchange for SQ for graphical verification that
c   source definition geometry on data card is appropriate

c ---------------------------------------------------------------------------
sdef cel=d5               $ Define source cells: which ones and what fraction
     axs=0 0 1            $ Define sampling boundary: cylinder along z-axis
     pos=0 0.06 -20.75    $    Base centered at 0 0.06 -20.75
     rad=d1               $    Define radius (in x and y direction)
     ext=d2               $    Define height (extend up z-axis)
     erg=d3               $ Define energy of source (gamma)
     par=2                $ par=2 --> photon
     eff=0.000001         $ Sampling efficiency (reduce because source is small)
c ------------------ Sampling boundary ----------------------
si1  0       1            $ Radius of sampling cylinder that contains source
sp1 -21      1            $ -21 1 for radial sample (dependent on r)
si2  0      17.5          $ Height of sampling cylinder that contains source
sp2 -21      0            $ Weighting for axial sample (not dependent on r)
c ------------------ Energy definition -----------------------
```

```
si3 L 0.636989 0.364489   $ Iodine-131 gammas, in MeV; "L" = "list"
sp3 D 0.0717   0.817
c ------ Specific source cells with equal probability -------
si5 L 87 88 89 90
sp5   0.34 0.40 0.13 0.13  $ Evenly distribute source across GI tract
c ---------------------------------------------------------------------------
```

2.6. ^{131}I beta energy, source organ GI tract

```
c ---------------------------------------------------------------------------
c                                I-131
c                      BETA ENERGY DEPOSITION IN
c                   POUDRE RIVER (0.22 kg) RAINBOW TROUT
c                     L: 28.6 cm   W: 2.5 cm   H: 5.3 cm
c                           SOURCE - GI TRACT
c ---------------------------------------------------------------------------
c 50 RCC 0 0.06 -20.75    0 0 17.5   1
c Use above 50 RCC in exchange for SQ for graphical verification that
c   source definition geometry on data card is appropriate

c ---------------------------------------------------------------------------
sdef cel=d5               $ Define source cells: which ones and what fraction
     axs=0 0 1            $ Define sampling boundary: cylinder along z-axis
     pos=0 0.06 -20.75    $    Base centered at 0 0.06 -20.75
     rad=d1               $    Define radius (in x and y direction)
     ext=d2               $    Define height (extend up z-axis)
     erg=d3               $ Define energy of source (beta spectra)
     par=3                $ par=3 --> electron
     eff=0.000001         $ Sampling efficiency (reduce because source is small)
c ------------------ Sampling boundary ----------------------
si1  0       1        $ Radius of sampling cylinder that contains source
sp1 -21      1        $ -21 1 for radial sample (dependent on r)
si2  0      17.5      $ Height of sampling cylinder that contains source
sp2 -21      0        $ Weighting for axial sample (not dependent on r)
c ------------------ Energy definition ------------------------
si3 A 2.02E-02  6.05E-02  1.01E-01  1.41E-01  1.82E-01    $ Iodine beta spectra
      2.22E-01  2.62E-01  3.03E-01  3.43E-01  3.83E-01
      4.24E-01  4.64E-01  5.04E-01  5.45E-01  5.85E-01
      6.25E-01  6.66E-01  7.06E-01  7.46E-01  7.87E-01
sp3   1.38E-01  1.31E-01  1.23E-01  1.13E-01  1.02E-01
      8.94E-02  7.70E-02  6.47E-02  5.30E-02  4.15E-02
      3.03E-02  2.00E-02  1.12E-02  4.55E-03  8.55E-04
      1.15E-04  6.94E-05  4.13E-05  1.73E-05  2.96E-06
c ------ Specific source cells with equal distribution -------
si5 L 87 88 89 90
sp5    0.34 0.40 0.13 0.13 $ Evenly distribute source across the GI tract
c ---------------------------------------------------------------------------
```

2.7. ^{99}Mo beta energy, source organ liver

```
c ---------------------------------------------------------------------------
c                                Mo-99
c                      BETA ENERGY DEPOSITION IN
c                   POUDRE RIVER (0.22 kg) RAINBOW TROUT
c                     L: 28.6 cm   W: 2.5 cm   H: 5.3 cm
c                           SOURCE - LIVER
c ---------------------------------------------------------------------------
c 50 SPH 0.65 0.52 -3.9    0.72
c Use above in exchange for SQ for graphical verification that
c   source definition geometry on data card is appropriate

c ---------------------------------------------------------------------------
```

```
sdef cel=d5               $ Define source cells: which ones and what fraction
     pos=0.65 0.52 -3.9   $ Sampling boundary: sphere centered at 0.65 0.52 -3.9
     rad=d1               $    Define radius
     erg=d3               $ Define energy of source (beta spectra)
     par=3                $ par=3 --> electron
     eff=0.000001         $ Sampling efficiency (reduce because source is small)
c ------------------ Sampling boundary ----------------------
si1  0       0.72     $ Radius of sphere containing source
sp1 -21      2        $ -21 1 for radial sample (dependent on r^2)
c ------------------ Energy definition -----------------------
si3 A 3.04E-02 9.11E-02 1.52E-01 2.12E-01 2.73E-01   $ Mo-99 Energy
      3.34E-01 3.95E-01 4.55E-01 5.16E-01 5.77E-01
      6.37E-01 6.98E-01 7.59E-01 8.19E-01 8.80E-01
      9.41E-01 1.00E+00 1.06E+00 1.12E+00 1.18E+00
sp3   9.51E-02 9.48E-02 9.22E-02 8.71E-02 8.02E-02  $ Abundance
      7.29E-02 6.69E-02 6.36E-02 6.05E-02 5.63E-02  $   i.e. probability
      5.11E-02 4.51E-02 3.85E-02 3.16E-02 2.47E-02
      1.79E-02 1.17E-02 6.41E-03 2.66E-03 4.11E-04
c ------ Specific source cells with equal distribution -------
si5 L 86
sp5    1
c ------------------------------------------------------------------------------
```

2.8. ^{99}Mo gamma energy, source organ liver

```
c ------------------------------------------------------------------------------
c                                Mo-99
c                        GAMMA ENERGY DEPOSITION IN
c                    POUDRE RIVER (0.22 kg) RAINBOW TROUT
c                      L: 28.6 cm   W: 2.5 cm   H: 5.3 cm
c                            SOURCE - LIVER
c ------------------------------------------------------------------------------
c 50 SPH 0.65 0.52 -3.9    0.72
c Use above in exchange for SQ for graphical verification that
c   source definition geometry on data card is appropriate

c ------------------------------------------------------------------------------
sdef cel=d5               $ Define source cells: which ones and what fraction
     pos=0.65 0.52 -3.9   $ Sampling boundary: sphere centered at 0.65 0.52 -3.9
     rad=d1               $    Define radius
     erg=d4               $ Define energy of source (gamma spectra)
     par=2                $ par=2 --> photon
     eff=0.000001         $ Sampling efficiency (reduce because source is small)
c ------------------ Sampling boundary ----------------------
si1  0       0.72     $ Radius of sphere containing source
sp1 -21      2        $ -21 1 for radial sample (dependent on r^2)
c ------------------ Energy definition -----------------------
si4 L  0.77792  0.7395  0.1811  0.1405  $ Mo-99 gammas in MeV
sp4 D  0.0426   0.1213  0.0599  0.0452  $  Probability
c ------ Specific source cells with equal distribution -------
si5 L 86
sp5    1
c ------------------------------------------------------------------------------
```

2.9. ^{99m}Tc gamma energy, source organ liver

```
c ------------------------------------------------------------------------------
c                               Tc-99m
c                        GAMMA ENERGY DEPOSITION IN
c                    POUDRE RIVER (0.22 kg) RAINBOW TROUT
c                      L: 28.6 cm   W: 2.5 cm   H: 5.3 cm
c                            SOURCE - LIVER
```

```
c ---------------------------------------------------------------------------
c 50 SPH 0.65 0.52 -3.9    0.72
c Use above in exchange for SQ for graphical verification that
c   source definition geometry on data card is appropriate

c ---------------------------------------------------------------------------
sdef cel=d5               $ Define source cells: which ones and what fraction
     pos=0.65 0.52 -3.9   $ Sampling boundary: sphere centered at 0.65 0.52 -3.9
     rad=d1               $    Define radius
     erg=d3               $ Define energy of source (beta spectra)
     par=2                $ par=2 --> photon
     eff=0.000001         $ Sampling efficiency (reduce because source is small)
c ------------------ Sampling boundary ----------------------
si1  0       0.72     $ Radius of sphere containing source
sp1 -21      2        $ -21 1 for radial sample (dependent on r^2)
c ------------------ Energy definition ----------------------
si3 L  0.1405  $ Tc-99m gamma in MeV
sp3 D  0.8906  $  Probability
c ------ Specific source cells with equal distribution -------
si5 L 86
sp5    1
c ---------------------------------------------------------------------------
```

2.10. ^{99}Mo beta energy, source organ GI tract

```
c ---------------------------------------------------------------------------
c                               Mo-99
c                        BETA ENERGY DEPOSITION IN
c                    POUDRE RIVER (0.22 kg) RAINBOW TROUT
c                      L: 28.6 cm   W: 2.5 cm   H: 5.3 cm
c                            SOURCE - GI TRACT
c ---------------------------------------------------------------------------
c 50 RCC 0 0.06 -20.75    0 0 17.5   1
c Use above in exchange for SQ for graphical verification that
c   source definition geometry on data card is appropriate
c ---------------------------------------------------------------------------
sdef cel=d5               $ Define source cells: which ones and what fraction
     axs=0 0 1            $ Define sampling boundary: cylinder along z-axis
     pos=0 0.06 -20.75    $    Base centered at 0 0.06 -20.75
     rad=d1               $    Define radius (in x and y direction)
     ext=d2               $    Define height (extend up z-axis)
     erg=d3               $ Define energy of source (beta spectra)
     par=3                $ par=3 --> electron
     eff=0.000001         $ Sampling efficiency (reduce because source is small)
c ------------------ Sampling boundary ----------------------
si1  0       1        $ Radius of sampling cylinder that contains source
sp1 -21      1        $ -21 1 for radial sample (dependent on r)
si2  0      17.5      $ Height of sampling cylinder that contains source
sp2 -21      0        $ Weighting for axial sample (not dependent on r)
c ------------------ Energy definition ----------------------
si3 A 3.04E-02 9.11E-02 1.52E-01 2.12E-01 2.73E-01  $ Mo-99 Beta spectra
      3.34E-01 3.95E-01 4.55E-01 5.16E-01 5.77E-01
      6.37E-01 6.98E-01 7.59E-01 8.19E-01 8.80E-01
      9.41E-01 1.00E+00 1.06E+00 1.12E+00 1.18E+00
sp3   9.51E-02 9.48E-02 9.22E-02 8.71E-02 8.02E-02  $ Abundance
      7.29E-02 6.69E-02 6.36E-02 6.05E-02 5.63E-02  $   i.e. probability
      5.11E-02 4.51E-02 3.85E-02 3.16E-02 2.47E-02
      1.79E-02 1.17E-02 6.41E-03 2.66E-03 4.11E-04
c ------ Specific source cells with equal distribution -------
si5 L 87 88 89 90
sp5    0.34 0.40 0.13 0.13 $ Evenly distribute source across GI tract
c ---------------------------------------------------------------------------
```

2.11. ^{99}Mo gamma energy, source organ GI tract

```
c ------------------------------------------------------------------------------
c                                Mo-99
c                       GAMMA ENERGY DEPOSITION IN
c                    POUDRE RIVER (0.22 kg) RAINBOW TROUT
c                      L: 28.6 cm   W: 2.5 cm   H: 5.3 cm
c                            SOURCE - GI TRACT
c ------------------------------------------------------------------------------
c 50 RCC 0 0.06 -20.75    0 0 17.5   1
c Use above in exchange for SQ for graphical verification that
c   source definition geometry on data card is appropriate

c ------------------------------------------------------------------------------
sdef cel=d5             $ Define source cells: which ones and what fraction
     axs=0 0 1          $ Define sampling boundary: cylinder along z-axis
     pos=0 0.06 -20.75  $    Base centered at 0 0.06 -20.75
     rad=d1             $    Define radius (in x and y direction)
     ext=d2             $    Define height (extend up z-axis)
     erg=d3             $ Define energy of source (gamma)
     par=2              $ par=2 --> photon
     eff=0.000001       $ Sampling efficiency (reduce because source is small)
c ------------------ Sampling boundary ----------------------
si1  0       1        $ Radius of sampling cylinder that contains source
sp1 -21      1        $ -21 1 for radial sample (dependent on r)
si2  0      17.5      $ Height of sampling cylinder that contains source
sp2 -21      0        $ Weighting for axial sample (not dependent on r)
c ------------------ Energy definition ----------------------
si3 L  0.77792  0.7395  0.1811  0.1405  $ Mo-99 Gammas in MeV
sp3 D  0.0426   0.1213  0.0599  0.0452  $  Probability
c ------ Specific source cells with equal distribution -------
si5 L 87 88 89 90
sp5    0.34 0.40 0.13 0.13  $ Evenly distribute source across GI tract
c ------------------------------------------------------------------------------
```

2.12. ^{99m}Tc gamma energy, source organ GI tract

```
c ------------------------------------------------------------------------------
c                                Tc-99m
c                       GAMMA ENERGY DEPOSITION IN
c                    POUDRE RIVER (0.22 kg) RAINBOW TROUT
c                      L: 28.6 cm   W: 2.5 cm   H: 5.3 cm
c                            SOURCE - GI TRACT
c ------------------------------------------------------------------------------
c 50 RCC 0 0.06 -20.75    0 0 17.5   1
c Use above in exchange for SQ for graphical verification that
c   source definition geometry on data card is appropriate

c ------------------------------------------------------------------------------
sdef cel=d5               $ Define source cells: which ones and what fraction
     axs=0 0 1            $ Define sampling boundary: cylinder along z-axis
     pos=0 0.06 -20.75    $    Base centered at 0 0.06 -20.75
     rad=d1               $    Define radius (in x and y direction)
     ext=d2               $    Define height (extend up z-axis)
     erg=d3               $ Define energy of source (gamma spectra)
     par=2                $ par=2 --> photon
     eff=0.000001         $ Sampling efficiency (reduce because source is small)
c ------------------ Sampling boundary ----------------------
si1  0       1       $ Radius of sampling cylinder that contains source
sp1 -21      1       $ -21 1 for radial sample (dependent on r)
si2  0     17.5      $ Height of sampling cylinder that contains source
sp2 -21      0       $ Weighting for axial sample (not dependent on r)
```

```
c ------------------ Energy definition -----------------------
si3 L  0.1405  $ Tc-99m Gamma in MeV
sp3 D  0.8906  $  Probability
c ------ Specific source cells with equal distribution -------
si5 L  87 88 89 90
sp5    0.34 0.40 0.13 0.13 $ Evenly distribute source across GI tract
c ------------------------------------------------------------------------------
```

3. Voxel model

3.1. ^{131}I beta energy, source organ thyroid

```
c ------------------------------------------------------------------------------
c
c    __   __    |   __   . _   __    __|   __          __  _|_  __   _|_  __
c   /    /  \   |  /  \  |/ \  __| /   |  /  \        /__   |   __|  |  /__\
c   \__  \__/   \_ \__/  |    |__| \__|  \__/        __/   \  |__|  \  \__,
c
c                . _   .          __  . _   __  .  _|_
c             |  | |/ |  |  \  / /__\ |/ \ /__  |   |  |  |
c             \__| |  |  |   \/  \__, |    __/  |   \  \__|
c                                                    __|
c                      ~~~~~~~~~~~~~~~~~~~~~~~~~~
c                            NICOLE MARTINEZ
c                             JANUARY 2014
c                      ~~~~~~~~~~~~~~~~~~~~~~~~~~
c                                I-131
c                      BETA ENERGY DEPOSITION IN
c                       VOXELIZED RAINBOW TROUT
c                       SOURCE ORGAN - THYROID
c                      ~~~~~~~~~~~~~~~~~~~~~~~~~~
c
c  to run:
c    C:\MCNP\mcnp5> mcnp5 tasks 8 i=input.i
c    C:\MCNP\mcnp5> mcpnx i=input.i
c ------------------------------------------------------------------------------
c                              CELL CARDS
c ------------------------------------------------------------------------------
c This input file was made with the MCNP Lattice Tool
c originally created by Erick Daniel Cardenas-Mendez (a.k.a. Ace Wave)
c for the Human Monitoring Laboratory of Health Canada
c
c Input file originally created on:
c Tue Jan 28 2014
c
c Empty space universe: 22
c compression factor: 4
c
c ---------------------------------------------------------
c                        Cells
c ---------------------------------------------------------
c _____________________________________________________________
c  ID#  | Material# |Density|Definition:   |Importance
c       |(0 if void)| N/A if| Surface      |
c       |           |  void | relationships|
c ---------------------------------------------------------
   999    0                    999           imp:p,e=0         $ Outside
   998   22          -1.0    -999  1 #997    imp:p,e=1         $ Water
c
c ---------------- Filling Universes --------------------
c _____________________________________________________________
c Cell#|Mat#|Density|Defn:   | Define |Importance
```

```
c      |    |       |in void |Universe|
c      |    |       |"mortar"|        |
c ------------------------------------------------------
   1    1   -1.03       -2     u = 1    imp:p,e=1 $ Gut contents CS
   2    2   -0.001205   -2     u = 2    imp:p,e=1 $ SwimBladder
   3    3   -1.92       -2     u = 3    imp:p,e=1 $ Bone
   4    4   -1.06       -2     u = 4    imp:p,e=1 $ Liver
   5    5   -1.06       -2     u = 5    imp:p,e=1 $ Heart
   6    6   -1.04       -2     u = 6    imp:p,e=1 $ Brain
   7    7   -1.07       -2     u = 7    imp:p,e=1 $ Eye
   8    8   -1.03       -2     u = 8    imp:p,e=1 $ CStomach
   9    9   -1.03       -2     u = 9    imp:p,e=1 $ PStomach
   10   10  -1.03       -2     u = 10   imp:p,e=1 $ Intestine
   11   11  -1.05       -2     u = 11   imp:p,e=1 $ Gonad
   12   12  -1.05       -2     u = 12   imp:p,e=1 $ Kidney
   13   13  -1.00       -2     u = 13   imp:p,e=1 $ Gills
   14   14  -1.06       -2     u = 14   imp:p,e=1 $ Spleen
   15   15  -1.03       -2     u = 15   imp:p,e=1 $ Esophagus
   16   16  -1.07       -2     u = 16   imp:p,e=1 $ LensofEye
   17   17  -1.05       -2     u = 17   imp:p,e=1 $ Muscle/Soft Tissue
   18   18  -1.05       -2     u = 18   imp:p,e=1 $ "Thyroid"
   19   19  -1.03       -2     u = 19   imp:p,e=1 $ Gut contents PS
   20   20  -1.03       -2     u = 20   imp:p,e=1 $ Gut contents Int
   21   21  -1.03       -2     u = 21   imp:p,e=1 $ Lymph
   22   22  -1.00       -2     u = 22   imp:p,e=1 $ Surrounding water
c
c ---------------- Lattice Unit Cell -------------------
c ____________________________________________________________________________
c ID#|Mat#|Density|Defn:  |Lattice|Define  |Importance|Fill: long list of
c    |    |       | in    | Type  |Universe|          | universes in specified
c    |    |       |"house"|       |        |          | x,y,z grid
c ----------------------------------------------------------------------------
    996   0         -2     lat=1  u=996  imp:p,e=1  fill = 0:255  0:255 0:285
     22 167583r 17 2r 22 251r 17 1r 22 65279r 17 2r 22 250r 17 3r 22
     249r 17 2r 22 252r 17 22 1739r 17 22 254r 17 2r 22 253r 17 2r 22
     62516r 17 2r 22 249r 17 3r 22 250r 17 2r 22 250r 17 2r 22 252r 17
     . . .

     251r 17 4r 22 249r 17 6r 22 246r 17 8r 22 246r 17 8r 22 246r 17
     8r 22 246r 17 8r 22 247r 17 7r 22 248r 17 5r 22 250r 17 4r 22
     27507r
c
c ------------- Cell Containing Lattice -----------------
c ____________________________________________________
c ID#|Mat#|Density|Defn:  |Fill with|Importance
c    |    |       | in    | lattice |
c    |    |       |"house"|i.e. 996 |
c ----------------------------------------------------
  997  0             -1   fill = 996   imp:p,e=1
c

c ----------------------------------------------------
c     Surfaces
c ----------------------------------------------------
c Universe boundary: RPP just larger than the “house”
c
  999  RPP      -1.000     16          -1.000    16           -1.000    30
c
c Box for Filling Universes
c   RPP 1: Range of x, y, z; from fill in lattice structure above and RPP2
c      0.0585936(x + 1) = 14.9999616
c      0.0585936(y + 1) = 14.9999616
c            0.1(z + 1) = 0.1(285+1) = 28.6
```

```
c
c This information comes from Image-->Image Information in 3D doctor
c   namely: # columns, # rows, # planes, pixel width, and slice thickness
c   Note that pixel width and slice thickness are given in mm in 3D doctor
c     but need to be in cm for Voxelizer and MCNP
c
c  In our case, # columns = 1024, # rows = 1024, planes (slices) = 286
c   Pixel width = 0.0146484 cm, slice thickness = 0.1 cm
c   For compression factor = 4, then # columns = # rows = 1024/4 = 256
c    0.0146484(4)=0.0585936; 256(0.0146484)(4)=14.9999616
c
c
c  RPP 1: Dimensions of "house" in which to build the lattice
c  RPP 2: Dimensions for "brick" in which each voxel is placed
c
  1  RPP        0.000     14.9999616    0.000   14.9999616     0.000    28.6
  2  RPP        0.000     0.0585936     0.000     0.0585936    0.000     0.1
c
c


c ---------------------------------------------------------------------------
c                               DATA CARDS
c ---------------------------------------------------------------------------
c ------------------------ SOURCE DEFININION ---------------------------------
c Particles started within the sampling boundary (cylinder) - any particle
c  that is started within the boundary but not within the specified source cells
c  (thyroid tubule 'shells') is rejected.  Sampling boundary MUST include all
c  source cells.
c
c  In source definition, "d1" is described by "si1" and "sp1" cards
c                                              where "i" info, "p" probability
c Source information definition
c  L-discrete source variable values
c  A-points where a probability density distribution is defined
c  S-distribution numbers
c  H-bin boundaries for a histogram distribution
c Source probability
c  D-bin probabilities for an H or L distribution on SI card. Default.
c  C-cumulative bin probabilities for an H or L distribution on SI card.
c  V-for cell distributions only. Probability is proportional to cell volume.
c
c Energy spectra references:
c  Stabin MG, and CQP da Luz, L. "Decay data for internal and external dose
c   assessment." Health Phys. 83:471-475; 2002. http://www.doseinfo-radar.com/
c  K. F. Eckerman, R. J. Westfall, J. C. Ryman, and M. Christy.
c   "Availability of Nuclear Decay Data in Electronic Form, Including Beta
c   Spectra not Previously Published," Health Phys. 67(4):338-345 (1994).
c
c Note on sampling efficiency:  Thyroid is tiny, so when the thyroid is the
c  source organ, sampling efficiency needs to be 0.0000001.  Other source
c  organs aren't as small so can have larger sampling efficiency.  Specifically,
c  liver eff=0.000001 and GI tract eff=0.000001
c ---------------------------------------------------------------------------
sdef cel=d5            $ Define source cells: which ones and what fraction
     X=d1              $ Sampling boundary by X, Y, Z
     Y=d2              $
     Z=d3              $
     erg=d4            $ Define energy of source (beta spectra)
     par=3             $ par=3 --> electron
     eff=0.0000001       $ Sampling efficiency (reduce because source is small)
c ------------------ Sampling boundary from RPP above ----------------------
si1 h 0.0    0.059      $ range of X
sp1 d 0      1          $
```

```
si2 h 0.0     0.059       $ range of Y
sp2 d 0       1           $
si3 h 0.0     0.1         $ range of Z
sp3 d 0       1
c ------------------ Energy definition -----------------------
si4 A 2.02E-02  6.05E-02  1.01E-01  1.41E-01  1.82E-01  $ I-131 beta spectra
      2.22E-01  2.62E-01  3.03E-01  3.43E-01  3.83E-01
      4.24E-01  4.64E-01  5.04E-01  5.45E-01  5.85E-01
      6.25E-01  6.66E-01  7.06E-01  7.46E-01  7.87E-01
sp4   1.38E-01  1.31E-01  1.23E-01  1.13E-01  1.02E-01  $ Abundance
      8.94E-02  7.70E-02  6.47E-02  5.30E-02  4.15E-02
      3.03E-02  2.00E-02  1.12E-02  4.55E-03  8.55E-04
      1.15E-04  6.94E-05  4.13E-05  1.73E-05  2.96E-06
c ------ Specific source cells with equal distribution -------
c  L = List, equal probability (1) each cell (organ) listed
c  source cell < lattice universe < universe box that contains lattice
c  Use sdef "helper" (calculates the exact voxel array coordinates)
c     because the thyroid is so small (code will run MUCH faster)
si5 L
    (18<996[109 142 248]<997)
     (18<996[108 143 248]<997)
     (18<996[109 143 248]<997)
     (18<996[108 144 248]<997)
     (18<996[109 144 248]<997)
     (18<996[108 143 249]<997)
     (18<996[109 142 250]<997)
     (18<996[108 143 250]<997)
     (18<996[108 143 251]<997)
     (18<996[108 143 252]<997)
     (18<996[108 143 253]<997)
     (18<996[108 143 254]<997)
     (18<996[108 143 255]<997)
sp5  1 12r
c ------------------------------------------------------------------------------
c ----------------------------- TALLY ------------------------------------------
mode p e
nps 10000000                              $ Particle cutoff: 10^7
dbcn 12J 5444034                          $ more random #'s
 *f8:p,e   u=(1 2 3 4 5 6 7 8 9 10 11 12 13 14 15 16 17 18 19 20 21)
 *f18:p,e  u=(1)
 *f28:p,e  u=(2)
 *f38:p,e  u=(3)
 *f48:p,e  u=(4)
 *f58:p,e  u=(5)
 *f68:p,e  u=(6)
 *f78:p,e  u=(7)
 *f88:p,e  u=(8)
 *f98:p,e  u=(9)
 *f108:p,e u=(10)
 *f118:p,e u=(11)
 *f128:p,e u=(12)
 *f138:p,e u=(13)
 *f148:p,e u=(14)
 *f158:p,e u=(15)
 *f168:p,e u=(16)
 *f178:p,e u=(17)
 *f188:p,e u=(18)
 *f198:p,e u=(19)
 *f208:p,e u=(20)
 *f218:p,e u=(21)
 *f228:p,e u=(22)
E0 0 5.0      $ Energy bins; 0 catchs "negative" energy from knowck-on electrons
c
```

```
PRINT 110     $ Print table to ensure source origination correct
PRDMP 1E6
c
c ---------------------------------------------------------------------------
c ---------------------------- MATERIALS ------------------------------------
c McConn, Gesh, Pagh, Rucker, Williams. Radiation Portal Monitor Project:
c   Compendium of Material Composition Data for Radation Transport Modeling
c   Revision 1: March 4, 2011, Pacific Northwest National Laboratory
c   PIET-43541-TM-963 PNNL-15870 Rev. 1
c
c ICRU Report 44: Tissue Substitutes in Radiation Dosimetry and Measurement
c   International commission on Radiation Units and Measurements
c ---------------------------------------------------------------------------
c
c Gut contents CS - ICRU GI tract p = 1.03 g/cm^3
m1
      1000  -0.106  $ H
      6000  -0.115  $ C
      7000  -0.022  $ N
      8000  -0.751  $ O
     11000  -0.001  $ Na
     15000  -0.001  $ P
     16000  -0.001  $ S
     17000  -0.002  $ Cl
     19000  -0.001  $ K
c
c SwimBladder - air
m2
      7000  -0.755
      8000  -0.232
     18000  -0.013
c
c Bone - ICRU Cortical Bone p = 1.92 g/cm^3
m3
      1000  -0.034  $ H
      6000  -0.155  $ C
      7000  -0.042  $ N
      8000  -0.435  $ O
     11000  -0.001  $ Na
     12000  -0.002  $ Mg
     15000  -0.103  $ P
     16000  -0.003  $ S
     20000  -0.225  $ Ca
c
c Liver - ICRU p = 1.06 g/cm^3
m4
      1000  -0.102  $ H
      6000  -0.139  $ C
      7000  -0.030  $ N
      8000  -0.716  $ O
     11000  -0.002  $ Na
     15000  -0.003  $ P
     16000  -0.003  $ S
     17000  -0.002  $ Cl
     19000  -0.003  $ K
c
c Heart - ICRU p = 1.06 g/cm^3
m5
      1000  -0.103  $ H
      6000  -0.121  $ C
      7000  -0.032  $ N
      8000  -0.734  $ O
     11000  -0.001  $ Na
```

```
     15000  -0.001  $ P
     16000  -0.002  $ S
     17000  -0.003  $ Cl
     19000  -0.002  $ K
     26000  -0.001  $ Fe
c
c Brain - ICRU p = 1.04 g/cm^3
m6
      1000  -0.107  $ H
      6000  -0.145  $ C
      7000  -0.022  $ N
      8000  -0.712  $ O
     11000  -0.002  $ Na
     15000  -0.004  $ P
     16000  -0.002  $ S
     17000  -0.003  $ Cl
     19000  -0.003  $ K
c
c Eye - ICRU p = 1.07 g/cm^3
m7
      1000  -0.096  $ H
      6000  -0.195  $ C
      7000  -0.057  $ N
      8000  -0.646  $ O
     11000  -0.001  $ Na
     15000  -0.001  $ P
     16000  -0.003  $ S
     17000  -0.001  $ Cl
c
c CStomach - ICRU GI tract p = 1.03 g/cm^3
m8
      1000  -0.106  $ H
      6000  -0.115  $ C
      7000  -0.022  $ N
      8000  -0.751  $ O
     11000  -0.001  $ Na
     15000  -0.001  $ P
     16000  -0.001  $ S
     17000  -0.002  $ Cl
     19000  -0.001  $ K
c
c PStomach - ICRU GI tract p = 1.03 g/cm^3
m9
      1000  -0.106  $ H
      6000  -0.115  $ C
      7000  -0.022  $ N
      8000  -0.751  $ O
     11000  -0.001  $ Na
     15000  -0.001  $ P
     16000  -0.001  $ S
     17000  -0.002  $ Cl
     19000  -0.001  $ K
c
c Intestine - ICRU GI tract p = 1.03 g/cm^3
m10
      1000  -0.106  $ H
      6000  -0.115  $ C
      7000  -0.022  $ N
      8000  -0.751  $ O
     11000  -0.001  $ Na
     15000  -0.001  $ P
     16000  -0.001  $ S
     17000  -0.002  $ Cl
```

```
     19000  -0.001  $ K
c
c Gonad  - ICRU ovary p = 1.05 g/cm^3
m11
      1000  -0.105  $ H
      6000  -0.093  $ C
      7000  -0.024  $ N
      8000  -0.768  $ O
     11000  -0.002  $ Na
     15000  -0.002  $ P
     16000  -0.002  $ S
     17000  -0.002  $ Cl
     19000  -0.002  $ K
c
c Kidney - ICRU p = 1.05 g/cm^3
m12
      1000  -0.103  $ H
      6000  -0.132  $ C
      7000  -0.030  $ N
      8000  -0.724  $ O
     11000  -0.002  $ Na
     15000  -0.002  $ P
     16000  -0.002  $ S
     17000  -0.002  $ Cl
     19000  -0.002  $ K
     20000  -0.001  $ Ca
c
c Gills - soft tissue
m13
     1000  -0.101
     6000  -0.111
     7000  -0.026
     8000  -0.762
c
c Spleen - ICRU p = 1.06 g/cm^3
m14
      1000  -0.103  $ H
      6000  -0.113  $ C
      7000  -0.032  $ N
      8000  -0.741  $ O
     11000  -0.001  $ Na
     15000  -0.003  $ P
     16000  -0.002  $ S
     17000  -0.002  $ Cl
     19000  -0.003  $ K
c
c Esophagus - ICRU GI tract p = 1.03 g/cm^3
m15
      1000  -0.106  $ H
      6000  -0.115  $ C
      7000  -0.022  $ N
      8000  -0.751  $ O
     11000  -0.001  $ Na
     15000  -0.001  $ P
     16000  -0.001  $ S
     17000  -0.002  $ Cl
     19000  -0.001  $ K
c
c LensofEye - ICRU Eye lens p = 1.07 g/cm^3
m16
      1000  -0.096  $ H
      6000  -0.195  $ C
      7000  -0.057  $ N
```

```
       8000  -0.646  $ O
      11000  -0.001  $ Na
      15000  -0.001  $ P
      16000  -0.003  $ S
      17000  -0.001  $ Cl
c
c Muscle/soft tissue, skeletal (ICRU) by mass fraction), p = 1.05 g/cm^3
m17   1000  -0.102   $ H
       6000  -0.143   $ C
       7000  -0.034   $ N
       8000  -0.710   $ O
      11000  -0.001   $ Na
      15000  -0.002   $ P
      16000  -0.003   $ S
      17000  -0.001   $ Cl
      19000  -0.004   $ K
c
c Thyroid (ICRU), p = 1.05 g/cm^3
m18   1000  -0.104   $ H
       6000  -0.119   $ C
       7000  -0.024   $ N
       8000  -0.745   $ O
      11000  -0.002   $ Na
      15000  -0.001   $ P
      16000  -0.001   $ S
      17000  -0.002   $ Cl
      19000  -0.001   $ K
      53000  -0.001   $ I
c
c Gut contents Pyloric Stomach - ICRU GI tract p = 1.03 g/cm^3
m19
       1000  -0.106  $ H
       6000  -0.115  $ C
       7000  -0.022  $ N
       8000  -0.751  $ O
      11000  -0.001  $ Na
      15000  -0.001  $ P
      16000  -0.001  $ S
      17000  -0.002  $ Cl
      19000  -0.001  $ K
c
c Gut contents Intestine - ICRU GI tract p = 1.03 g/cm^3
m20
       1000  -0.106  $ H
       6000  -0.115  $ C
       7000  -0.022  $ N
       8000  -0.751  $ O
      11000  -0.001  $ Na
      15000  -0.001  $ P
      16000  -0.001  $ S
      17000  -0.002  $ Cl
      19000  -0.001  $ K
c
c Lymph (ICRU) (by mass fraction), p = 1.03 g/cm^3
m21   1000  -0.108   $ H
       6000  -0.041   $ C
       7000  -0.011   $ N
       8000  -0.832   $ O
      11000  -0.003   $ Na
      16000  -0.001   $ S
      17000  -0.004   $ Cl
c
c Default Surrounding Water
```

```
m22  1000  -0.11190  $ H
     8000  -0.88810  $ O
```

3.2. ^{131}I beta energy, source organ GI tract

```
c ------------------------------------------------------------------------------
c                                I-131
c                      BETA ENERGY DEPOSITION IN
c                       VOXELIZED RAINBOW TROUT
c                       SOURCE ORGAN - GI TRACT
c ------------------------------------------------------------------------------
sdef cel=d5            $ Define source cells: which ones and what fraction
     X=d1              $ Sampling boundary by X, Y, Z
     Y=d2              $
     Z=d3
     erg=d4            $ Define energy of source (beta spectra)
     par=3             $ par=3 --> electron
     eff=0.000001      $ Sampling efficiency (reduce because source is small)
c ------------------ Sampling boundary from RPP above ----------------------
si1 h 0.0    0.059       $ range of X
sp1 d 0      1           $
si2 h 0.0    0.059       $ range of Y
sp2 d 0      1           $
si3 h 0.0    0.1         $ range of Z
sp3 d 0      1
c ------------------ Energy definition -----------------------
si4 A 2.02E-02  6.05E-02  1.01E-01  1.41E-01  1.82E-01  $ I-131 beta spectra
      2.22E-01  2.62E-01  3.03E-01  3.43E-01  3.83E-01
      4.24E-01  4.64E-01  5.04E-01  5.45E-01  5.85E-01
      6.25E-01  6.66E-01  7.06E-01  7.46E-01  7.87E-01
sp4   1.38E-01  1.31E-01  1.23E-01  1.13E-01  1.02E-01  $ Abundance
      8.94E-02  7.70E-02  6.47E-02  5.30E-02  4.15E-02
      3.03E-02  2.00E-02  1.12E-02  4.55E-03  8.55E-04
      1.15E-04  6.94E-05  4.13E-05  1.73E-05  2.96E-06
c ------ Specific source cells with equal distribution -------
c  L = List, equal probability (1) each cell (organ) listed
c  source cell < lattice universe < universe box that contains lattice
si5 L (1<996<997) $ Source definition for GI tract
      (8<996<997)     $   Intestine + contents (10,20)
      (9<996<997)     $   Pyloric stomach + contents (9,19)
      (10<996<997)    $   Cardiac stomach + contents (1,8)
      (19<996<997)
      (20<996<997)
sp5  1
     1
     1
     1
     1
     1
c ------------------------------------------------------------------------------
```

3.3. ^{131}I gamma energy, source organ thyroid

```
c ------------------------------------------------------------------------------
c                                I-131
c                      GAMMA ENERGY DEPOSITION IN
c                       VOXELIZED RAINBOW TROUT
c                         SOURCE ORGAN – THYROID
c ------------------------------------------------------------------------------
sdef cel=d5            $ Define source cells: which ones and what fraction
     X=d1              $ Sampling boundary by X, Y, Z
     Y=d2
     Z=d3
```

```
     erg=d4            $ Define energy of source (gamma)
     par=2             $ par=2 --> photon
     eff=0.0000001     $ Sampling efficiency (reduce because source is small)
c ------------------ Sampling boundary from RPP above ----------------------
si1 h 0.0    0.059       $ range of X
sp1 d 0      1           $
si2 h 0.0    0.059       $ range of Y
sp2 d 0      1           $
si3 h 0.0    0.1         $ range of Z
sp3 d 0      1
c ------------------ Energy definition -----------------------
si4 L 0.636989 0.364489   $ I-131 gammas, in MeV; "L" = "list"
sp4 D 0.0717   0.817

c ------ Specific source cells with equal distribution -------
c  L = List, equal probability (1) each cell (organ) listed
c  source cell < lattice universe < universe box that contains lattice
c  Use sdef "helper" (calculates the exact voxel array coordinates)
c     because the thyroid is so small (code will run MUCH faster)
si5 L
     (18<996[109 142 248]<997)
     (18<996[108 143 248]<997)
     (18<996[109 143 248]<997)
     (18<996[108 144 248]<997)
     (18<996[109 144 248]<997)
     (18<996[108 143 249]<997)
     (18<996[109 142 250]<997)
     (18<996[108 143 250]<997)
     (18<996[108 143 251]<997)
     (18<996[108 143 252]<997)
     (18<996[108 143 253]<997)
     (18<996[108 143 254]<997)
     (18<996[108 143 255]<997)
sp5  1 12r
c ------------------------------------------------------------------------------
```

3.4. ^{131}I gamma energy, source organ GI tract

```
c ------------------------------------------------------------------------------
c                                 I-131
c                      GAMMA ENERGY DEPOSITION IN
c                       VOXELIZED RAINBOW TROUT
c                         SOURCE ORGAN - GI TRACT
c ------------------------------------------------------------------------------
sdef cel=d5            $ Define source cells: which ones and what fraction
     X=d1              $ Sampling boundary by X, Y, Z
     Y=d2              $
     Z=d3
     erg=d4            $ Define energy of source (gamma)
     par=2             $ par=2 --> photon
     eff=0.000001       $ Sampling efficiency (reduce because source is small)
c ------------------ Sampling boundary from RPP above ----------------------
si1 h 0.0    0.059       $ range of X
sp1 d 0      1           $
si2 h 0.0    0.059       $ range of Y
sp2 d 0      1           $
si3 h 0.0    0.1         $ range of Z
sp3 d 0      1
c ------------------ Energy definition -----------------------
si4 L 0.636989 0.364489   $ I-131 gammas, in MeV; "L" = "list"
sp4 D 0.0717   0.817
c ------------------------------------------------------------------------------
```

3.5. ^{131}I beta energy, source organ liver

```
c ------------------------------------------------------------------------------
c                                I-131
c                      BETA ENERGY DEPOSITION IN
c                       VOXELIZED RAINBOW TROUT
c                         SOURCE ORGAN - LIVER
c ------------------------------------------------------------------------------
sdef cel=d5            $ Define source cells: which ones and what fraction
     X=d1              $ Sampling boundary by X, Y, Z
     Y=d2              $
     Z=d3
     erg=d4            $ Define energy of source (beta spectra)
     par=3             $ par=3 --> electron
     eff=0.000001       $ Sampling efficiency (reduce because source is small)
c ------------------ Sampling boundary from RPP above ----------------------
si1 h 0.0    0.059       $ range of X
sp1 d 0      1           $
si2 h 0.0    0.059       $ range of Y
sp2 d 0      1           $
si3 h 0.0    0.1         $ range of Z
sp3 d 0      1
c ------------------ Energy definition ------------------------
si4 A 2.02E-02  6.05E-02  1.01E-01  1.41E-01  1.82E-01  $ I-131 Energy
      2.22E-01  2.62E-01  3.03E-01  3.43E-01  3.83E-01
      4.24E-01  4.64E-01  5.04E-01  5.45E-01  5.85E-01
      6.25E-01  6.66E-01  7.06E-01  7.46E-01  7.87E-01
sp4   1.38E-01  1.31E-01  1.23E-01  1.13E-01  1.02E-01  $ Abundance
      8.94E-02  7.70E-02  6.47E-02  5.30E-02  4.15E-02
      3.03E-02  2.00E-02  1.12E-02  4.55E-03  8.55E-04
      1.15E-04  6.94E-05  4.13E-05  1.73E-05  2.96E-06
c ------ Specific source cells with equal distribution -------
c  L = List, equal probability (1) each cell (organ) listed
c  source cell < lattice universe < universe box that contains lattice
si5 L (4<996<997)
sp5  1
c ------------------------------------------------------------------------------
```

3.6. ^{131}I gamma energy, source organ liver

```
c ------------------------------------------------------------------------------
c                                I-131
c                      GAMMA ENERGY DEPOSITION IN
c                       VOXELIZED RAINBOW TROUT
c                         SOURCE ORGAN - LIVER
c ------------------------------------------------------------------------------
sdef cel=d5            $ Define source cells: which ones and what fraction
     X=d1              $ Sampling boundary by X, Y, Z
     Y=d2              $
     Z=d3
     erg=d4            $ Define energy of source (gamma)
     par=2             $ par=2 --> photon
     eff=0.000001        $ Sampling efficiency (reduce because source is small)
c ------------------ Sampling boundary from RPP above ----------------------
si1 h 0.0    0.059       $ range of X
sp1 d 0      1           $
si2 h 0.0    0.059       $ range of Y
sp2 d 0      1           $
si3 h 0.0    0.1         $ range of Z
sp3 d 0      1
```

```
c ------------------ Energy definition -----------------------
si4 L 0.636989 0.364489   $ I-131 Gammas, in MeV; "L" = "list"
sp4 D 0.0717   0.817
c ------ Specific source cells with equal distribution -------
c  L = List, equal probability (1) each cell (organ) listed
c  source cell < lattice universe < universe box that contains lattice
si5 L (4<996<997)
sp5  1
c ---------------------------------------------------------------------------
```

3.7. ^{99}Mo beta energy, source organ liver

```
c ---------------------------------------------------------------------------
c                                Mo-99
c                       BETA ENERGY DEPOSITION IN
c                        VOXELIZED RAINBOW TROUT
c                          SOURCE ORGAN - LIVER
c ---------------------------------------------------------------------------
sdef cel=d5            $ Define source cells: which ones and what fraction
     X=d1              $ Sampling boundary by X, Y, Z
     Y=d2              $
     Z=d3
     erg=d4            $ Define energy of source (beta spectra)
     par=3             $ par=3 --> electron
     eff=0.000001       $ Sampling efficiency (reduce because source is small)
c ------------------ Sampling boundary from RPP above ----------------------
si1 h 0.0    0.059       $ range of X
sp1 d 0      1           $
si2 h 0.0    0.059       $ range of Y
sp2 d 0      1           $
si3 h 0.0    0.1         $ range of Z
sp3 d 0      1
c ------------------ Energy definition -----------------------
si4 A 3.04E-02 9.11E-02 1.52E-01 2.12E-01 2.73E-01  $ Mo-99 Beta spectra
      3.34E-01 3.95E-01 4.55E-01 5.16E-01 5.77E-01
      6.37E-01 6.98E-01 7.59E-01 8.19E-01 8.80E-01
      9.41E-01 1.00E+00 1.06E+00 1.12E+00 1.18E+00
sp4   9.51E-02 9.48E-02 9.22E-02 8.71E-02 8.02E-02  $ Abundance
      7.29E-02 6.69E-02 6.36E-02 6.05E-02 5.63E-02  $   i.e. probability
      5.11E-02 4.51E-02 3.85E-02 3.16E-02 2.47E-02
      1.79E-02 1.17E-02 6.41E-03 2.66E-03 4.11E-04
c ------ Specific source cells with equal distribution -------
c  L = List, equal probability (1) each cell (organ) listed
c  source cell < lattice universe < universe box that contains lattice
si5 L (4<996<997)
sp5  1
c ---------------------------------------------------------------------------
```

3.8. ^{99}Mo gamma energy, source organ liver

```
c ---------------------------------------------------------------------------
c                                Mo-99
c                       GAMMA ENERGY DEPOSITION IN
c                        VOXELIZED RAINBOW TROUT
c                          SOURCE ORGAN - LIVER
c ---------------------------------------------------------------------------
sdef cel=d5            $ Define source cells: which ones and what fraction
     X=d1              $ Sampling boundary by X, Y, Z
     Y=d2              $
     Z=d3
     erg=d4            $ Define energy of source (gamma)
     par=2             $ par=2 --> photon
```

```
     eff=0.000001        $ Sampling efficiency (reduce because source is small)
c ------------------ Sampling boundary from RPP above ----------------------
si1 h 0.0    0.059       $ range of X
sp1 d 0      1           $
si2 h 0.0    0.059       $ range of Y
sp2 d 0      1           $
si3 h 0.0    0.1         $ range of Z
sp3 d 0      1
c ------------------ Energy definition -----------------------
si4 L  0.77792  0.7395  0.1811  0.1405  $ Mo-99 Gammas in MeV
sp4 D  0.0426   0.1213  0.0599  0.0452  $  Probability
c ------ Specific source cells with equal distribution -------
c  L = List, equal probability (1) each cell (organ) listed
c  source cell < lattice universe < universe box that contains lattice
si5 L (4<996<997)
sp5  1
c ------------------------------------------------------------------------------
```

3.9. ^{99m}Tc gamma energy, source organ liver

```
c ------------------------------------------------------------------------------
c                                Tc-99m
c                       GAMMA ENERGY DEPOSITION IN
c                        VOXELIZED RAINBOW TROUT
c                          SOURCE ORGAN - LIVER
c ------------------------------------------------------------------------------
sdef cel=d5            $ Define source cells: which ones and what fraction
     X=d1              $ Sampling boundary by X, Y, Z
     Y=d2              $
     Z=d3
     erg=d4            $ Define energy of source (gamma)
     par=2             $ par=2 --> photon
     eff=0.000001        $ Sampling efficiency (reduce because source is small)
c ------------------ Sampling boundary from RPP above ----------------------
si1 h 0.0    0.059       $ range of X
sp1 d 0      1           $
si2 h 0.0    0.059       $ range of Y
sp2 d 0      1           $
si3 h 0.0    0.1         $ range of Z
sp3 d 0      1
c ------------------ Energy definition -----------------------
si4 L  0.1405  $ Tc-99m gamma in MeV
sp4 D  0.8906  $  Probability
c ------ Specific source cells with equal distribution -------
c  L = List, equal probability (1) each cell (organ) listed
c  source cell < lattice universe < universe box that contains lattice
si5 L (4<996<997)
sp5  1
c ------------------------------------------------------------------------------
```

3.10. ^{99}Mo beta energy, source organ GI tract

```
c ------------------------------------------------------------------------------
c                                Mo-99
c                       BETA ENERGY DEPOSITION IN
c                        VOXELIZED RAINBOW TROUT
c                          SOURCE ORGAN - GI TRACT
c ------------------------------------------------------------------------------
sdef cel=d5            $ Define source cells: which ones and what fraction
     X=d1              $ Sampling boundary by X, Y, Z
     Y=d2              $
     Z=d3
```

```
     erg=d4            $ Define energy of source (beta spectra)
     par=3             $ par=3 --> electron
     eff=0.000001      $ Sampling efficiency (reduce because source is small)
c ------------------ Sampling boundary from RPP above ----------------------
si1 h 0.0    0.059       $ range of X
sp1 d 0      1           $
si2 h 0.0    0.059       $ range of Y
sp2 d 0      1           $
si3 h 0.0    0.1         $ range of Z
sp3 d 0      1
c ------------------ Energy definition -----------------------
si4 A 3.04E-02 9.11E-02 1.52E-01 2.12E-01 2.73E-01  $ Mo-99 Beta spectra
      3.34E-01 3.95E-01 4.55E-01 5.16E-01 5.77E-01
      6.37E-01 6.98E-01 7.59E-01 8.19E-01 8.80E-01
      9.41E-01 1.00E+00 1.06E+00 1.12E+00 1.18E+00
sp4   9.51E-02 9.48E-02 9.22E-02 8.71E-02 8.02E-02  $ Abundance
      7.29E-02 6.69E-02 6.36E-02 6.05E-02 5.63E-02  $   i.e. probability
      5.11E-02 4.51E-02 3.85E-02 3.16E-02 2.47E-02
      1.79E-02 1.17E-02 6.41E-03 2.66E-03 4.11E-04
c ------ Specific source cells with equal distribution -------
c  L = List, equal probability (1) each cell (organ) listed
c  source cell < lattice universe < universe box that contains lattice
si5 L (1<996<997) $ Source definition for GI tract
      (8<996<997)     $   Intestine + contents (10,20)
      (9<996<997)     $   Pyloric stomach + contents (9,19)
      (10<996<997)    $   Cardiac stomach + contents (1,8)
      (19<996<997)
      (20<996<997)
sp5  1
     1
     1
     1
     1
     1
c ------------------------------------------------------------------------------
```

3.11. ^{99}Mo gamma energy, source organ GI tract

```
c ------------------------------------------------------------------------------
c                                Mo-99
c                      GAMMA ENERGY DEPOSITION IN
c                       VOXELIZED RAINBOW TROUT
c                         SOURCE ORGAN - GI TRACT
c ------------------------------------------------------------------------------
c ------------------------------------------------------------------------------
sdef cel=d5            $ Define source cells: which ones and what fraction
     X=d1              $ Sampling boundary by X, Y, Z
     Y=d2              $
     Z=d3
     erg=d4            $ Define energy of source (gamma)
     par=2             $ par=2 --> photon
     eff=0.000001       $ Sampling efficiency (reduce because source is small)
c ------------------ Sampling boundary from RPP above ----------------------
si1 h 0.0    0.059       $ range of X
sp1 d 0      1           $
si2 h 0.0    0.059       $ range of Y
sp2 d 0      1           $
si3 h 0.0    0.1         $ range of Z
sp3 d 0      1
c ------------------ Energy definition -----------------------
si4 L  0.77792  0.7395  0.1811  0.1405  $ Mo-99 Gammas in MeV
sp4 D  0.0426   0.1213  0.0599  0.0452  $  Probability
c ------ Specific source cells with equal distribution -------
```

```
c  L = List, equal probability (1) each cell (organ) listed
c  source cell < lattice universe < universe box that contains lattice
si5 L (1<996<997)  $ Source definition for GI tract
      (8<996<997)     $   Intestine + contents (10,20)
      (9<996<997)     $   Pyloric stomach + contents (9,19)
      (10<996<997)    $   Cardiac stomach + contents (1,8)
      (19<996<997)
      (20<996<997)
sp5  1
     1
     1
     1
     1
     1
c ---------------------------------------------------------------------------
```

3.12. ^{99m}Tc gamma energy, source organ GI tract

```
c ---------------------------------------------------------------------------
c                               Mo-99
c                      GAMMA ENERGY DEPOSITION IN
c                       VOXELIZED RAINBOW TROUT
c                         SOURCE ORGAN - GI TRACT
c ---------------------------------------------------------------------------
c ---------------------------------------------------------------------------
sdef cel=d5            $ Define source cells: which ones and what fraction
     X=d1              $ Sampling boundary by X, Y, Z
     Y=d2              $
     Z=d3
     erg=d4            $ Define energy of source (gamma)
     par=2             $ par=2 --> photon
     eff=0.000001       $ Sampling efficiency (reduce because source is small)
c ------------------ Sampling boundary from RPP above ----------------------
si1 h 0.0    0.059       $ range of X
sp1 d 0      1           $
si2 h 0.0    0.059       $ range of Y
sp2 d 0      1           $
si3 h 0.0    0.1         $ range of Z
sp3 d 0      1
c ------------------ Energy definition -----------------------
si4 L  0.1405  $ Tc-99m gamma in MeV
sp4 D  0.8906  $  Probability
c ------ Specific source cells with equal distribution -------
c  L = List, equal probability (1) each cell (organ) listed
c  source cell < lattice universe < universe box that contains lattice
si5 L (1<996<997)  $ Source definition for GI tract
      (8<996<997)     $   Intestine + contents (10,20)
      (9<996<997)     $   Pyloric stomach + contents (9,19)
      (10<996<997)    $   Cardiac stomach + contents (1,8)
      (19<996<997)
      (20<996<997)
sp5  1
     1
     1
     1
     1
     1
c ---------------------------------------------------------------------------
```

APPENDIX A3: DETAILED RESULTS

1. Mass ratios

1.1. Stylized model

Table A3.1: Masses and mass ratios for organs considered in the stylized model

Organ	Mass (g)	Mass ratio			
		WB:organ	Thyroid:organ	Liver:organ	GI:organ
Body	2.23E+02	1.00E+00	4.26E-05	3.69E-03	4.20E-02
Thyroid	2.51E-03	8.88E+04	3.79E+00	3.28E+02	3.73E+03
Thryoid (whole)	9.49E-03	2.35E+04	1.00E+00	8.66E+01	9.86E+02
Liver	8.22E-01	2.71E+02	1.15E-02	1.00E+00	1.14E+01
GI tract	9.35E+00	2.38E+01	1.01E-03	8.79E-02	1.00E+00
Intestine	3.13E+00	7.11E+01	3.03E-03	2.62E-01	2.98E+00
C Stomach	3.73E+00	5.97E+01	2.55E-03	2.21E-01	2.51E+00
P Stomach	2.49E+00	8.94E+01	3.81E-03	3.30E-01	3.75E+00
Swim bladder	6.95E-03	3.21E+04	1.37E+00	1.18E+02	1.35E+03
Heart	3.70E-01	6.02E+02	2.56E-02	2.22E+00	2.53E+01
Brain	5.45E-01	4.09E+02	1.74E-02	1.51E+00	1.72E+01
Ovaries	2.11E-01	1.05E+03	4.50E-02	3.89E+00	4.43E+01
Muscle	1.96E+02	1.14E+00	4.85E-05	4.21E-03	4.78E-02

1.2. Voxel model

Table A3.2: Masses and mass ratios for organs considered in CSUTROUT

Organ	Mass (g)	Mass ratio			
		WB:organ	Thyroid:organ	Liver:organ	GI:organ
Body	2.19E+02	1.00E+00	5.14E-05	4.30E-03	4.06E-02
Thyroid	6.19E-03	3.54E+04	1.82E+00	1.52E+02	1.43E+03
Thryoid (whole)	1.13E-02	1.95E+04	1.00E+00	8.37E+01	7.89E+02
Liver	9.42E-01	2.32E+02	1.20E-02	1.00E+00	9.43E+00
GI tract	8.88E+00	2.47E+01	1.27E-03	1.06E-01	1.00E+00
Intestine	2.82E+00	7.76E+01	3.99E-03	3.34E-01	3.15E+00
C Stomach	3.44E+00	6.37E+01	3.27E-03	2.74E-01	2.58E+00
P Stomach	2.62E+00	8.36E+01	4.30E-03	3.59E-01	3.39E+00
Swim bladder	6.66E-03	3.29E+04	1.69E+00	1.41E+02	1.33E+03
Heart	4.52E-01	4.84E+02	2.49E-02	2.08E+00	1.96E+01
Brain	6.34E-01	3.45E+02	1.78E-02	1.49E+00	1.40E+01
Ovaries	2.03E-01	1.08E+03	5.55E-02	4.64E+00	4.38E+01
Esophagus	9.80E-02	2.23E+03	1.15E-01	9.61E+00	9.06E+01
Spleen	7.85E-02	2.79E+03	1.43E-01	1.20E+01	1.13E+02
Kidney	5.70E-01	3.84E+02	1.97E-02	1.65E+00	1.56E+01
Eye (whole)	2.24E+00	9.77E+01	5.02E-03	4.20E-01	3.96E+00
Eye Lens	1.12E-01	1.96E+03	1.01E-01	8.44E+00	7.96E+01
Gills	3.52E+00	6.22E+01	3.20E-03	2.68E-01	2.52E+00
Bone	2.22E+01	9.84E+00	5.06E-04	4.24E-02	3.99E-01
Muscle	1.74E+02	1.26E+00	6.47E-05	5.41E-03	5.10E-02

2. Detailed results for ^{131}I

2.1. Stylized model

2.1.1. MeV per disintegration

Table A3.3: MCNP output, i.e. MeV per disintegration, listed by source organ and radiation type

Organ	MeV per disintegration								
	Thyroid			Liver			GI Tract		
	I-131 β	I-131 γ	Total	I-131 β	I-131 γ	Total	I-131 β	I-131 γ	Total
Body	1.95E-01	1.80E-02	2.13E-01	1.01E-02	2.51E-02	3.51E-02	1.95E-01	2.59E-02	2.21E-01
Thyroid	3.90E-02	1.78E-04	3.92E-02	1.58E-19	9.58E-08	9.58E-08	0.00E+00	1.45E-08	1.59E-08
Thryoid (whole)	1.06E-01	6.69E-04	1.07E-01	2.32E-19	4.46E-07	4.46E-07	0.00E+00	1.15E-07	1.09E-07
Liver	3.86E-08	4.47E-05	4.47E-05	1.85E-01	5.20E-03	1.90E-01	3.15E-06	1.19E-04	1.02E-04
GI tract	5.32E-08	1.12E-04	1.12E-04	3.12E-05	1.37E-03	1.40E-03	1.81E-01	6.58E-03	1.87E-01
Intestine	6.58E-09	2.52E-05	2.52E-05	2.94E-05	4.26E-04	4.55E-04	6.10E-02	1.81E-03	4.65E-02
C Stomach	1.75E-08	6.04E-05	6.04E-05	1.52E-06	7.40E-04	7.42E-04	7.39E-02	3.04E-03	4.86E-02
P Stomach	2.92E-08	2.63E-05	2.63E-05	2.40E-07	2.58E-04	2.58E-04	4.66E-02	1.74E-03	9.20E-02
Swim bladder	7.69E-21	9.06E-09	9.06E-09	2.13E-19	3.88E-08	3.88E-08	1.83E-08	7.27E-07	6.55E-07
Heart	2.74E-07	1.68E-04	1.68E-04	5.16E-08	5.85E-05	5.85E-05	8.22E-09	8.83E-06	8.05E-06
Brain	4.06E-08	5.98E-05	5.98E-05	5.20E-09	2.04E-05	2.04E-05	1.38E-09	4.87E-06	4.80E-06
Ovaries	0.00E+00	6.76E-07	6.76E-07	5.56E-20	2.79E-06	2.79E-06	5.79E-08	3.69E-05	3.87E-05
Muscle	8.93E-02	1.70E-02	1.06E-01	1.01E-02	1.84E-02	2.85E-02	1.37E-02	1.92E-02	3.28E-02

2.1.2. Dose conversion factors

Table A3.4: Dose conversion factors as determined by MCNP and as determined by using mass ratios

Organ	DCF by source organ (µGy d-1 per Bq kg-1)			Ratio of WB:organ DCFs (by source organ)		
	Thyroid	Liver	GI	Thyroid	Liver	GI
Body	2.95E-03	3.04E-03	3.06E-03	--	--	--
Thyroid	5.41E-04	1.32E-09	2.01E-10	5.44	--	--
Thryoid (whole)	1.47E-03	6.17E-09	1.59E-09	2.00	--	--
Liver	6.18E-07	2.63E-03	1.69E-06	--	1.16	--
GI tract	1.55E-06	1.94E-05	2.60E-03	--	--	1.18
Intestine	3.48E-07	6.29E-06	8.69E-04	--	--	3.52
C Stomach	8.35E-07	1.03E-05	1.06E-03	--	--	2.87
P Stomach	3.64E-07	3.57E-06	6.68E-04	--	--	4.58
Swim bladder	1.25E-10	5.36E-10	1.03E-08	--	--	--
Heart	2.32E-06	8.09E-07	1.22E-07	--	--	--
Brain	8.27E-07	2.82E-07	6.73E-08	--	--	--
Ovaries	9.35E-09	3.85E-08	5.11E-07	--	--	--
Muscle	1.47E-03	3.93E-04	4.54E-04	--	--	--

2.1.3. Cumulative dose and maximum dose rate

Table A3.5: Cumulative 32 day doses and maximum dose rates listed by source organ

Organ	Cumulative dose (µGy) by source organ				Maximum dose rate (µGy d^{-1}) by source organ			
	Thyroid	Liver	GI	Total	Thyroid	Liver	GI	Overall
Body	7.55E-01	1.30E+00	1.29E+02	1.37E+02	2.89E-02	3.15E-01	5.01E+00	5.35E+00
Thyroid	1.23E+04	3.15E-01	7.50E-01	1.23E+04	4.72E+02	1.22E-02	2.92E-02	4.72E+02
Thyroid (whole)	8.87E+03	3.87E-01	1.57E+00	8.87E+03	3.40E+02	1.50E-02	6.12E-02	3.40E+02
Liver	4.29E-02	1.90E+03	1.92E+01	1.92E+03	1.64E-03	7.37E+01	7.49E-01	7.44E+01
GI tract	9.44E-03	1.24E+00	2.60E+03	2.60E+03	3.61E-04	4.78E-02	1.01E+02	1.01E+02
Intestine	6.33E-03	1.20E+00	2.59E+03	2.60E+03	2.42E-04	4.63E-02	1.01E+02	1.01E+02
C Stomach	1.28E-02	1.64E+00	2.67E+03	2.67E+03	4.90E-04	6.34E-02	1.04E+02	1.04E+02
P Stomach	8.33E-03	8.53E-01	2.51E+03	2.51E+03	3.19E-04	3.30E-02	9.78E+01	9.78E+01
Swim bladder	1.03E-03	4.60E-02	1.39E+01	1.39E+01	3.94E-05	1.78E-03	5.41E-01	5.43E-01
Heart	3.59E-01	1.30E+00	3.09E+00	4.75E+00	1.37E-02	5.04E-02	1.20E-01	1.85E-01
Brain	8.67E-02	3.08E-01	1.16E+00	1.55E+00	3.32E-03	1.19E-02	4.51E-02	6.03E-02
Ovaries	2.53E-03	1.09E-01	2.27E+01	2.28E+01	9.68E-05	4.20E-03	8.83E-01	8.87E-01
Muscle	4.29E-01	1.20E+00	2.17E+01	2.34E+01	1.64E-02	4.63E-02	8.47E-01	9.10E-01

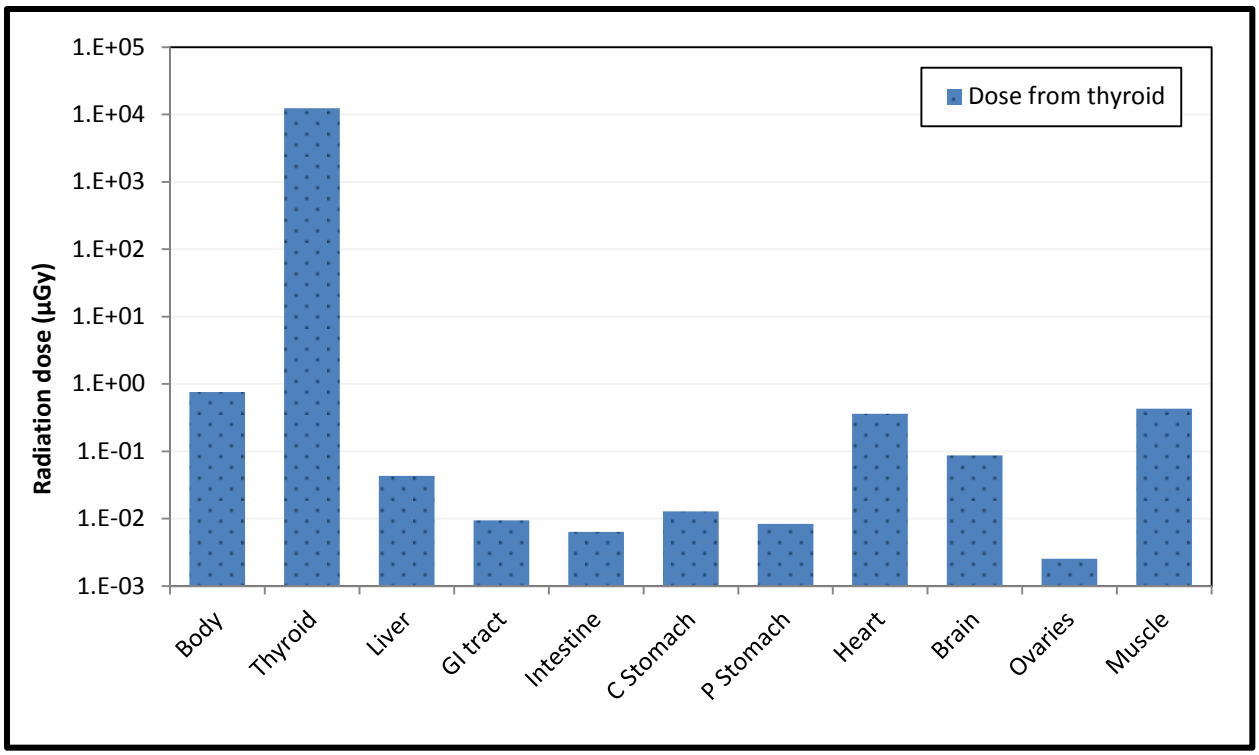

Figure A3.1: Cumulative 32 day dose received from ^{131}I in the thyroid, radiation dose shown on a log scale.

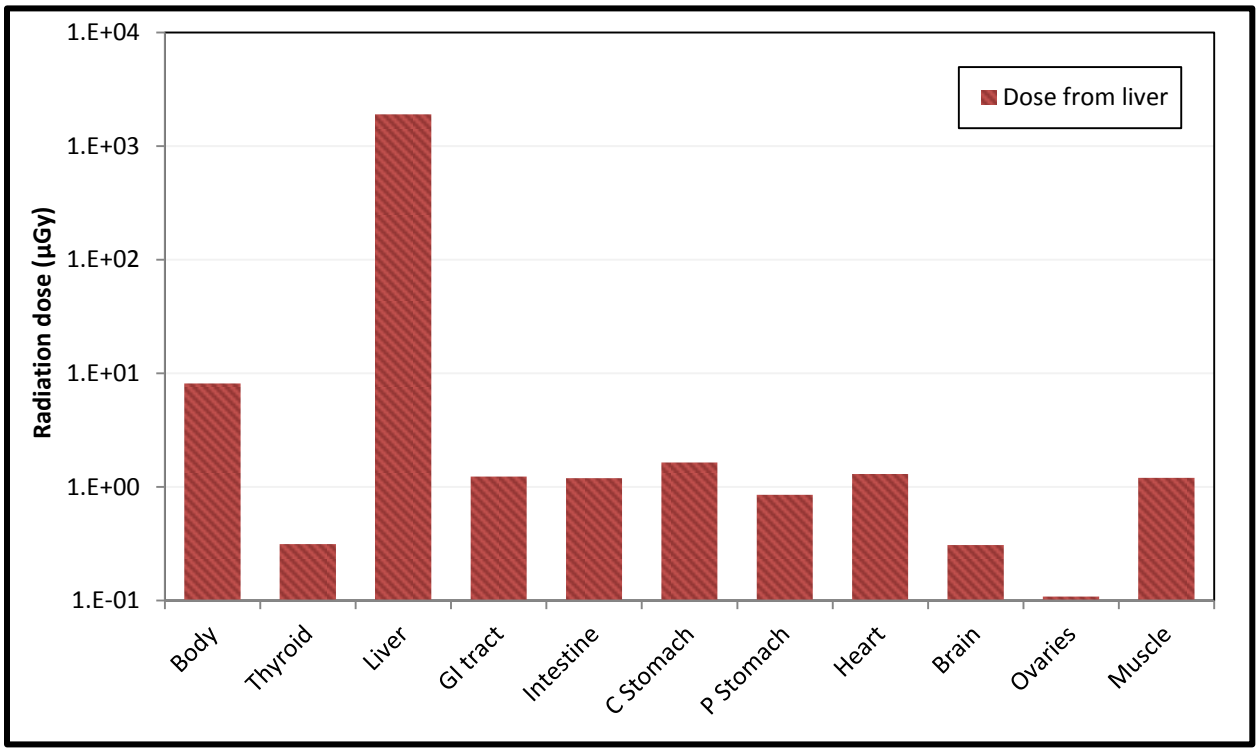

Figure A3.2: Cumulative 32 day dose received from ^{131}I in the thyroid, radiation dose shown on a log scale.

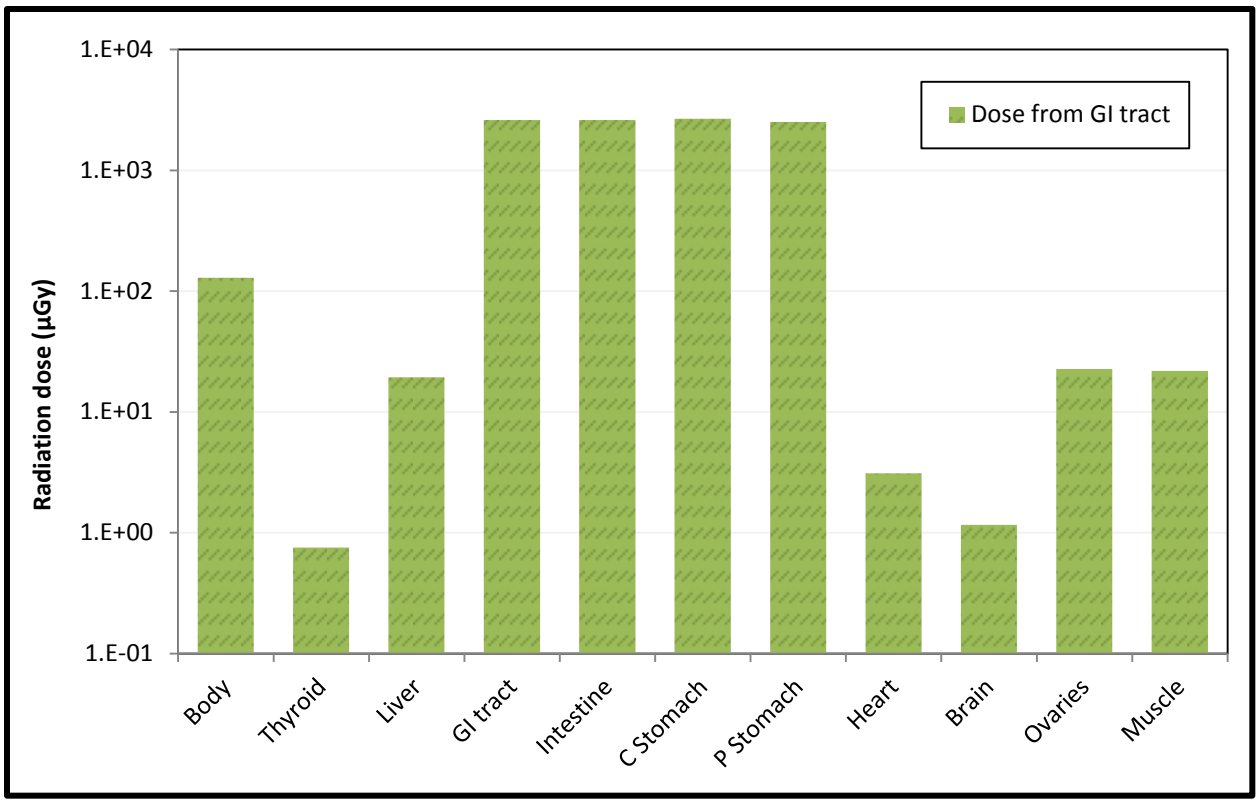

Figure A3.3: Cumulative 32 day dose received from ^{131}I in the thyroid, radiation dose shown on a log scale.

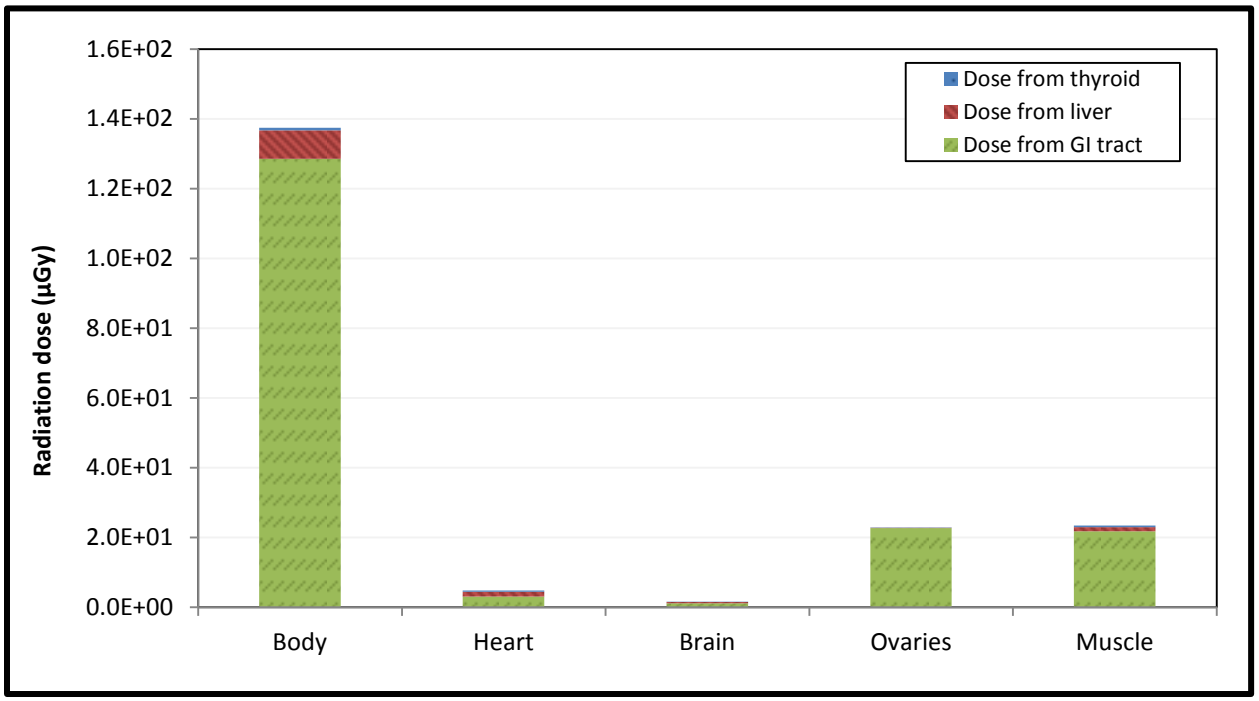

Figure A3.4: Cumulative 32 day dose received from ^{131}I to all non-source organs, radiation dose shown on a linear scale.

2.2. Voxel model

2.2.1. MeV per disintegration

Table A3.6: MCNP output, i.e. MeV per disintegration, listed by source organ and radiation type

Organ	MeV per disintegration by source organ and decay isotope/type								
	Thyroid			Liver			GI Tract		
	I-131 β	I-131 γ	Total	I-131 β	I-131 γ	Total	I-131 β	I-131 γ	Total
Body	1.95E-01	2.90E-02	2.24E-01	1.95E-01	3.45E-02	2.30E-01	1.95E-01	3.22E-02	2.27E-01
Thyroid (epi)	1.07E-01	4.81E-04	1.08E-01	1.09E-19	7.12E-07	7.12E-07	1.94E-20	2.70E-07	2.70E-07
Thryoid (whl)	1.35E-01	8.81E-04	1.36E-01	4.48E-19	1.94E-06	1.94E-06	1.69E-19	7.59E-07	7.59E-07
Liver	1.44E-07	1.45E-04	1.45E-04	1.81E-01	5.33E-03	1.87E-01	1.22E-04	3.32E-04	4.54E-04
GI tract	4.48E-07	4.99E-04	4.99E-04	1.24E-03	3.24E-03	4.48E-03	1.71E-01	7.95E-03	1.79E-01
Intestine	7.11E-08	8.42E-05	8.42E-05	5.85E-07	4.19E-04	4.19E-04	5.67E-02	1.96E-03	5.87E-02
C Stomach	9.72E-08	1.50E-04	1.50E-04	5.09E-05	9.96E-04	1.05E-03	5.80E-02	3.40E-03	6.14E-02
P Stomach	2.34E-07	2.35E-04	2.35E-04	9.28E-04	1.70E-03	2.62E-03	5.64E-02	2.57E-03	5.90E-02
Swim bladder	1.56E-17	8.94E-08	8.94E-08	4.54E-17	2.38E-07	2.38E-07	1.61E-05	1.56E-06	1.76E-05
Heart	7.87E-06	5.61E-04	5.69E-04	3.28E-07	1.88E-04	1.88E-04	4.68E-08	4.59E-05	4.60E-05
Brain	4.86E-08	8.89E-05	8.90E-05	3.96E-08	4.99E-05	4.99E-05	2.67E-09	2.00E-05	2.00E-05
Ovaries	3.50E-10	3.29E-06	3.29E-06	3.19E-09	9.89E-06	9.89E-06	1.24E-04	6.05E-05	1.85E-04
Esophagus	4.58E-08	2.89E-05	2.89E-05	2.63E-04	1.30E-04	3.93E-04	5.64E-06	1.94E-05	2.50E-05
Spleen	5.43E-19	1.44E-06	1.44E-06	4.01E-09	4.05E-06	4.05E-06	7.69E-05	3.67E-05	1.14E-04
Kidney	1.03E-08	1.10E-05	1.10E-05	2.71E-08	2.80E-05	2.80E-05	7.09E-05	1.09E-04	1.80E-04
Eye (whole)	1.86E-07	3.51E-04	3.51E-04	9.27E-08	1.23E-04	1.23E-04	2.32E-08	5.23E-05	5.24E-05
Eye Lens	4.53E-09	1.66E-05	1.67E-05	3.16E-09	5.88E-06	5.88E-06	5.92E-10	2.85E-06	2.85E-06
Gills	3.06E-06	2.19E-03	2.19E-03	5.77E-07	6.94E-04	6.95E-04	1.60E-07	2.10E-04	2.10E-04
Bone	6.84E-03	6.11E-03	1.30E-02	1.68E-05	3.33E-03	3.35E-03	2.45E-04	2.48E-03	2.73E-03
Muscle	5.34E-02	1.81E-02	7.16E-02	1.25E-02	2.15E-02	3.41E-02	2.35E-02	2.09E-02	4.43E-02

2.2.2. Dose conversion factors

Table A3.7: Dose conversion factors as determined by MCNP and by using mass ratios

Organ	DCF by source organ (μGy d^{-1} per Bq kg^{-1})			Ratio of WB:organ DCF by source organ		
	Thyroid	Liver	GI	Thyroid	Liver	GI
Body	3.10E-03	3.18E-03	3.14E-03	--	--	--
Thyroid	1.49E-03	9.85E-09	3.74E-09	2.08	--	--
Thryoid (whl)	1.88E-03	2.68E-08	1.05E-08	1.65	--	--
Liver	2.01E-06	2.58E-03	6.28E-06	--	1.23	--
GI tract	6.90E-06	6.20E-05	2.48E-03	--	--	1.27
Intestine	1.16E-06	5.80E-06	8.11E-04	--	--	3.88
C Stomach	2.08E-06	1.45E-05	8.49E-04	--	--	3.70
P Stomach	3.25E-06	3.63E-05	8.16E-04	--	--	3.85
Swim bladder	1.24E-09	3.29E-09	2.44E-07	--	--	--
Heart	7.87E-06	2.60E-06	6.36E-07	--	--	--
Brain	1.23E-06	6.90E-07	2.76E-07	--	--	--
Ovaries	4.54E-08	1.37E-07	2.56E-06	--	--	--
Espophagus	4.00E-07	5.43E-06	3.46E-07	--	--	
Spleen	1.99E-08	5.60E-08	1.57E-06	--	--	--
Kidney	1.53E-07	3.87E-07	2.49E-06	--	--	--
Eye (whole)	4.86E-06	1.70E-06	7.24E-07	--	--	--
Eye Lens	2.30E-07	8.13E-08	3.93E-08	--	--	--
Gills	3.03E-05	9.60E-06	2.91E-06	--	--	--
Bone	1.79E-04	4.62E-05	3.77E-05	--	--	--
Muscle	9.89E-04	4.71E-04	6.13E-04	--	--	--

2.2.3. Cumulative dose and maximum dose rate

Table A3.8: Cumulative 32 day doses and maximum dose rates listed by source organ

Organ	Cumulative dose (µGy), by source organ				Maximum dose rate (µGy d^{-1}), by source organ			
	Thyroid	Liver	GI	Total	Thyroid	Liver	GI	Total
Body	9.58E-01	9.90E+00	1.28E+02	1.39E+02	3.67E-02	3.83E-01	4.97E+00	5.39E+00
Thyroid	1.63E+04	1.08E+00	5.37E+00	1.63E+04	6.23E+02	4.20E-02	2.09E-01	6.23E+02
Thyroid (whole)	1.13E+04	1.62E+00	8.29E+00	1.13E+04	4.32E+02	6.28E-02	3.23E-01	4.33E+02
Liver	1.44E-01	1.87E+03	5.93E+01	1.93E+03	5.53E-03	7.23E+01	2.31E+00	7.46E+01
GI tract	5.26E-02	4.76E+00	2.48E+03	2.48E+03	2.01E-03	1.84E-01	9.66E+01	9.67E+01
Intestine	2.79E-02	1.40E+00	2.55E+03	2.56E+03	1.07E-03	5.42E-02	9.95E+01	9.96E+01
C Stomach	4.10E-02	2.87E+00	2.19E+03	2.20E+03	1.57E-03	1.11E-01	8.55E+01	8.56E+01
P Stomach	8.41E-02	9.45E+00	2.77E+03	2.78E+03	3.22E-03	3.65E-01	1.08E+02	1.08E+02
Swim bladder	1.26E-02	3.37E-01	3.25E+02	3.26E+02	4.81E-04	1.30E-02	1.27E+01	1.27E+01
Heart	1.18E+00	3.92E+00	1.25E+01	1.76E+01	4.51E-02	1.52E-01	4.87E-01	6.83E-01
Brain	1.31E-01	7.42E-01	3.88E+00	4.75E+00	5.03E-03	2.87E-02	1.51E-01	1.85E-01
Ovaries	1.52E-02	4.60E-01	1.12E+02	1.13E+02	5.81E-04	1.78E-02	4.36E+00	4.38E+00
Esophagus	2.76E-01	3.78E+01	3.14E+01	6.94E+01	1.06E-02	1.46E+00	1.22E+00	2.69E+00
Spleen	1.72E-02	4.87E-01	1.78E+02	1.79E+02	6.59E-04	1.88E-02	6.93E+00	6.95E+00
Kidney	1.81E-02	4.63E-01	3.88E+01	3.93E+01	6.95E-04	1.79E-02	1.51E+00	1.53E+00
Eye (whole)	1.47E-01	5.17E-01	2.87E+00	3.54E+00	5.61E-03	2.00E-02	1.12E-01	1.37E-01
Eye Lens	1.40E-01	4.97E-01	3.13E+00	3.77E+00	5.35E-03	1.92E-02	1.22E-01	1.47E-01
Gills	5.83E-01	1.86E+00	7.35E+00	9.80E+00	2.23E-02	7.20E-02	2.86E-01	3.81E-01
Bone	5.45E-01	1.42E+00	1.51E+01	1.70E+01	2.09E-02	5.49E-02	5.87E-01	6.63E-01
Muscle	3.85E-01	1.85E+00	3.13E+01	3.35E+01	1.47E-02	7.14E-02	1.22E+00	1.31E+00

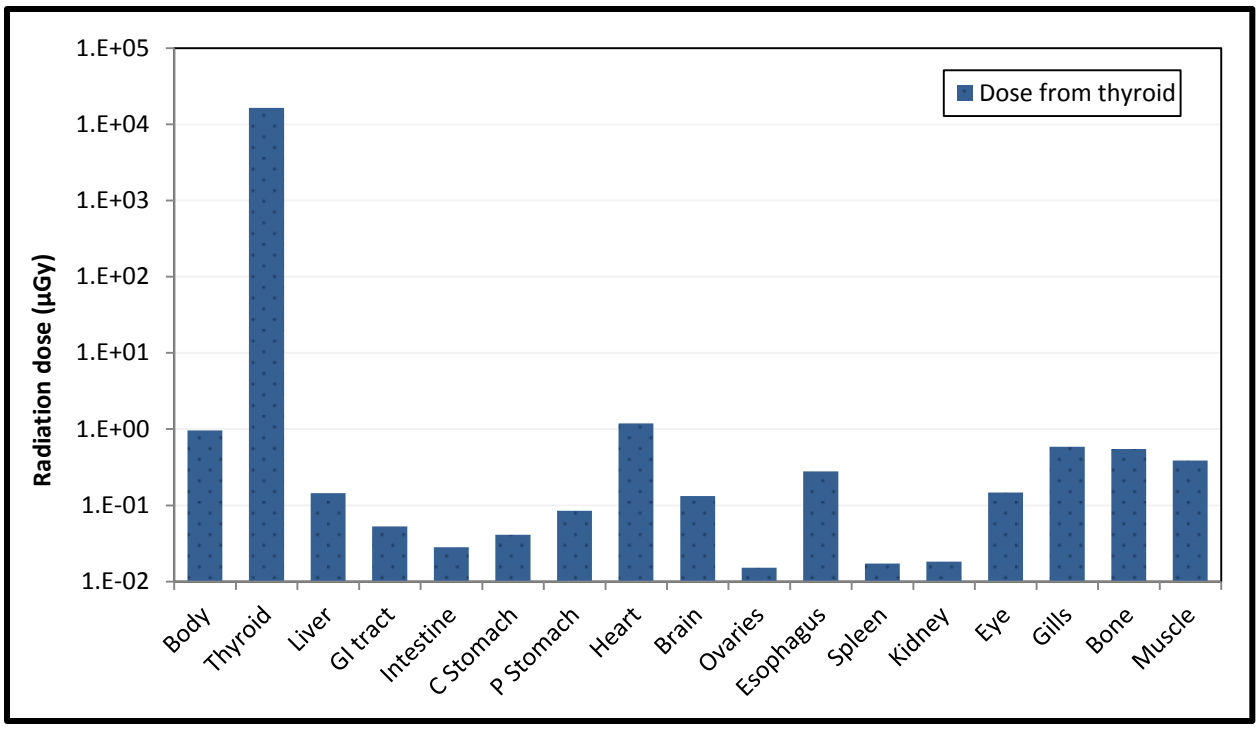

Figure A3.5: Cumulative 32 day dose received from ^{131}I in the thyroid, radiation dose shown on a log scale.

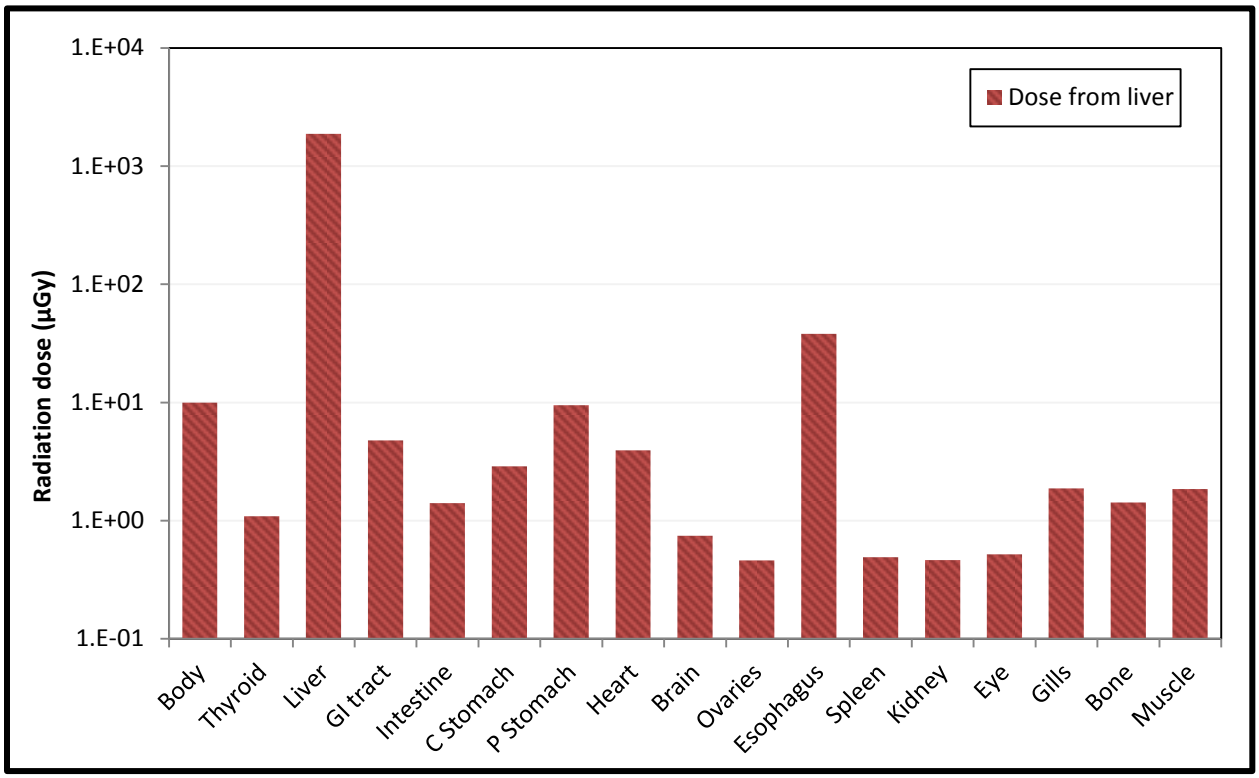

Figure A3.6: Cumulative 32 day dose received from ^{131}I in the liver, radiation dose shown on a log scale.

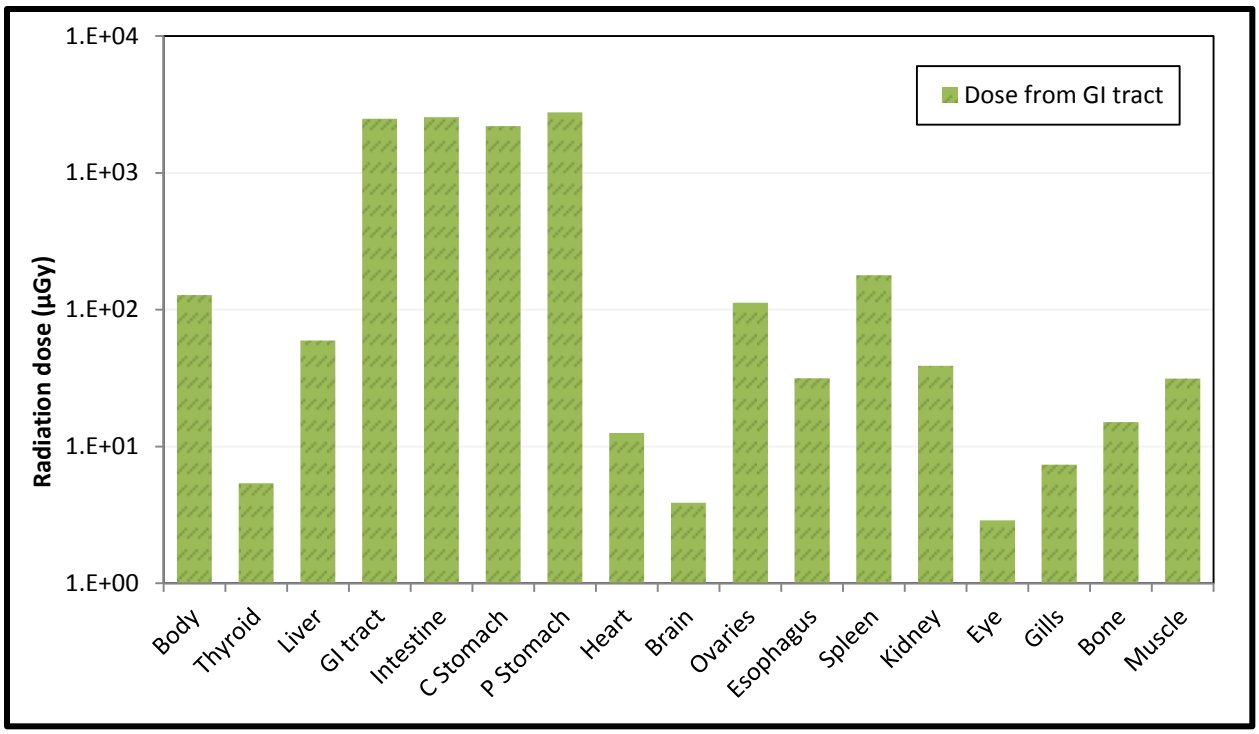

Figure A3.7: Cumulative 32 day dose received from ^{131}I in the GI tract, radiation dose shown on a log scale.

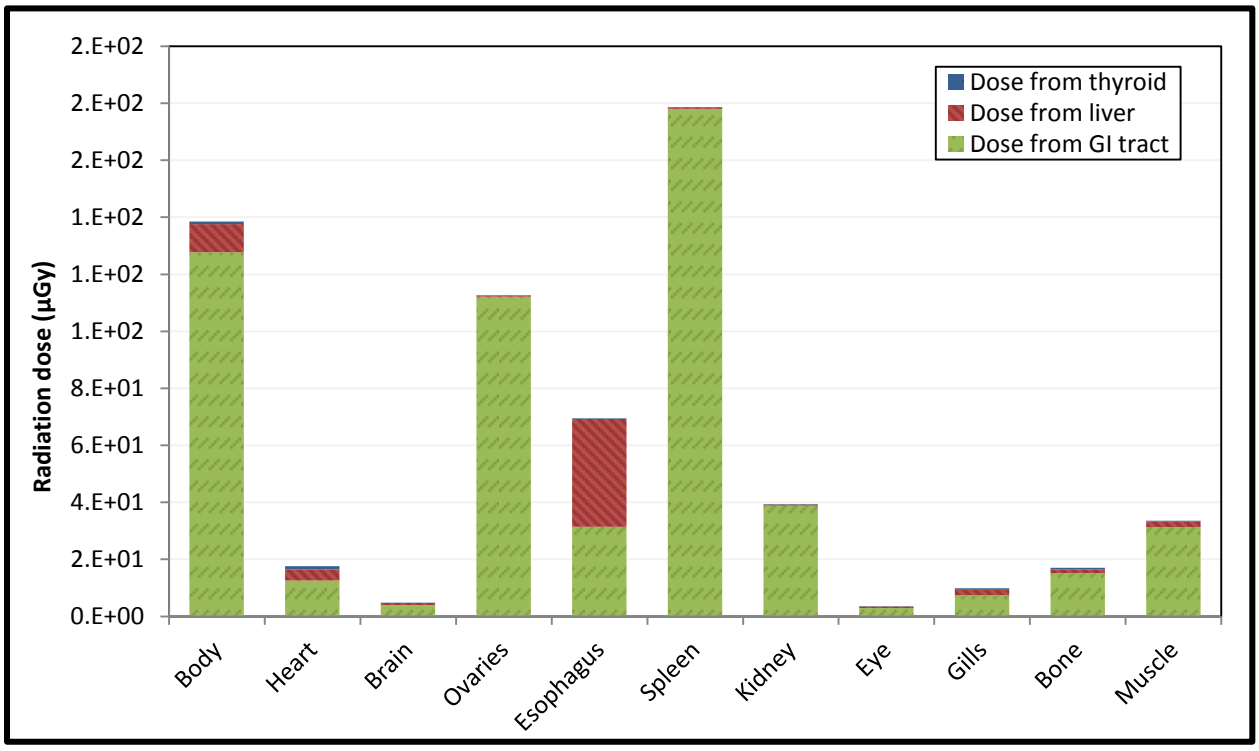

Figure A3.8: Cumulative 32 day dose received from ^{131}I to all non-source organs, radiation dose shown on a linear scale.

2.3. Comparison of stylized and voxel model results

2.3.1. Dose conversion factors

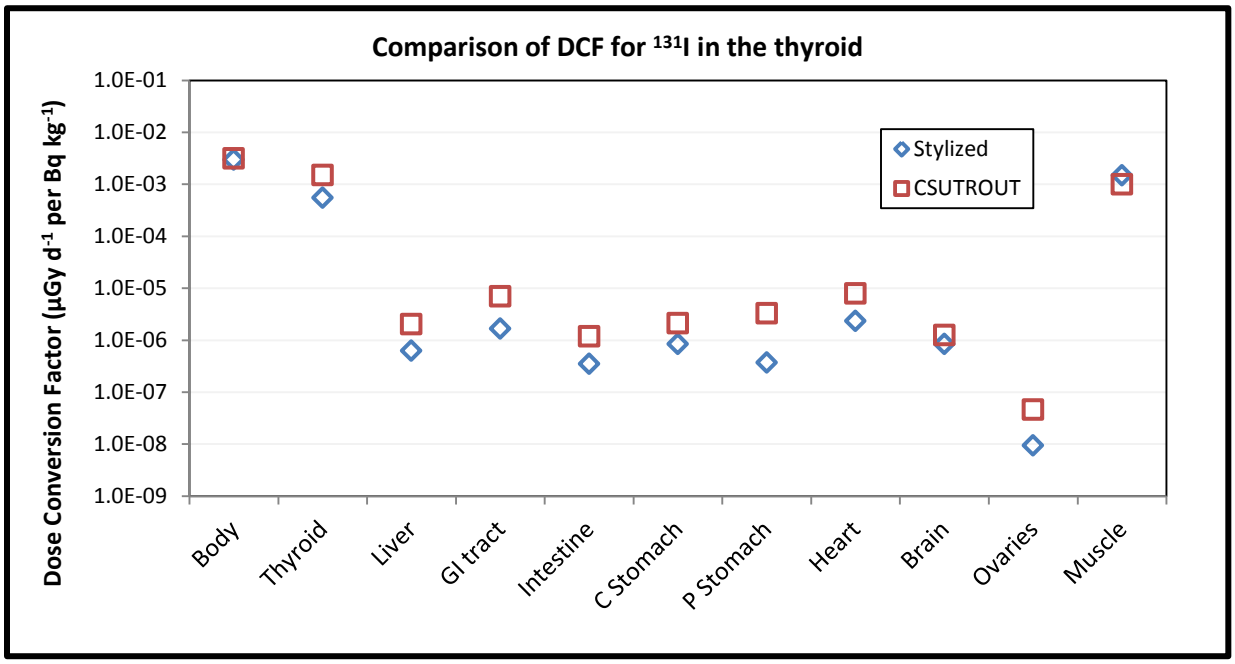

Figure A3.9: Comparison of DCF for ^{131}I in the thyroid, determined by the stylized model and CSUTROUT; DCF is shown on a log scale.

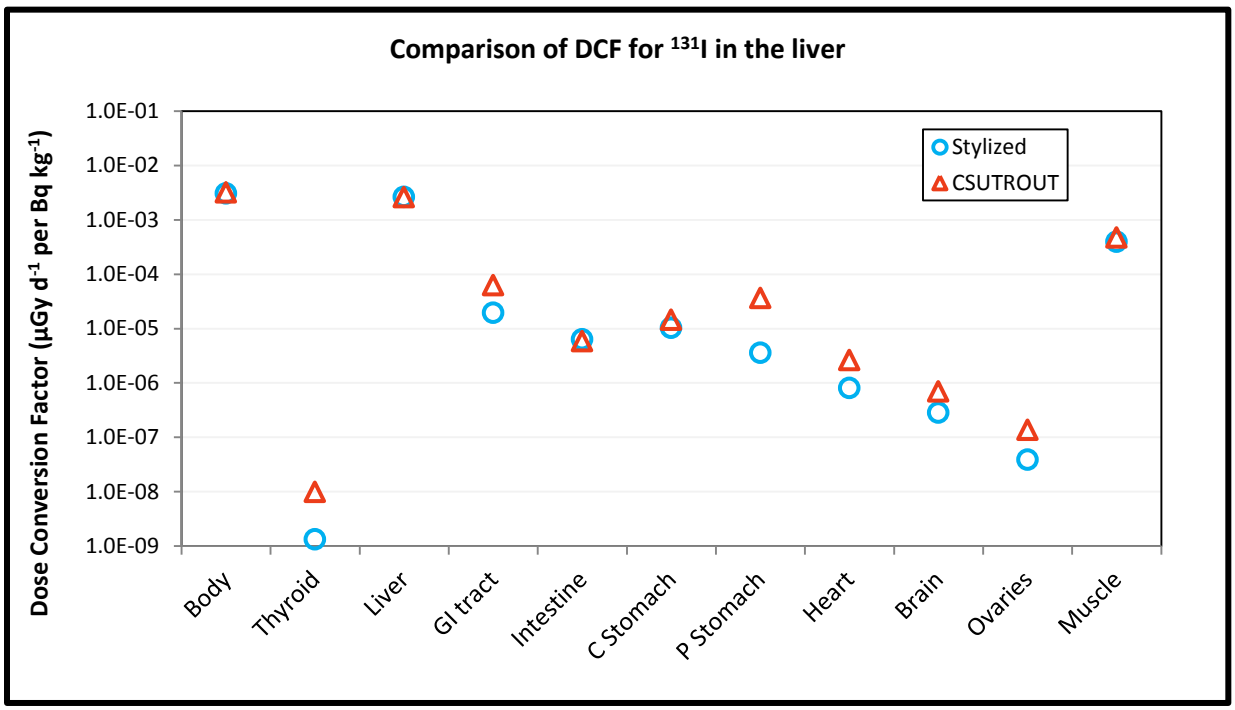

Figure A3.10: Comparison of DCF for ^{131}I in the liver, determined by the stylized model and CSUTROUT; DCF is shown on a log scale.

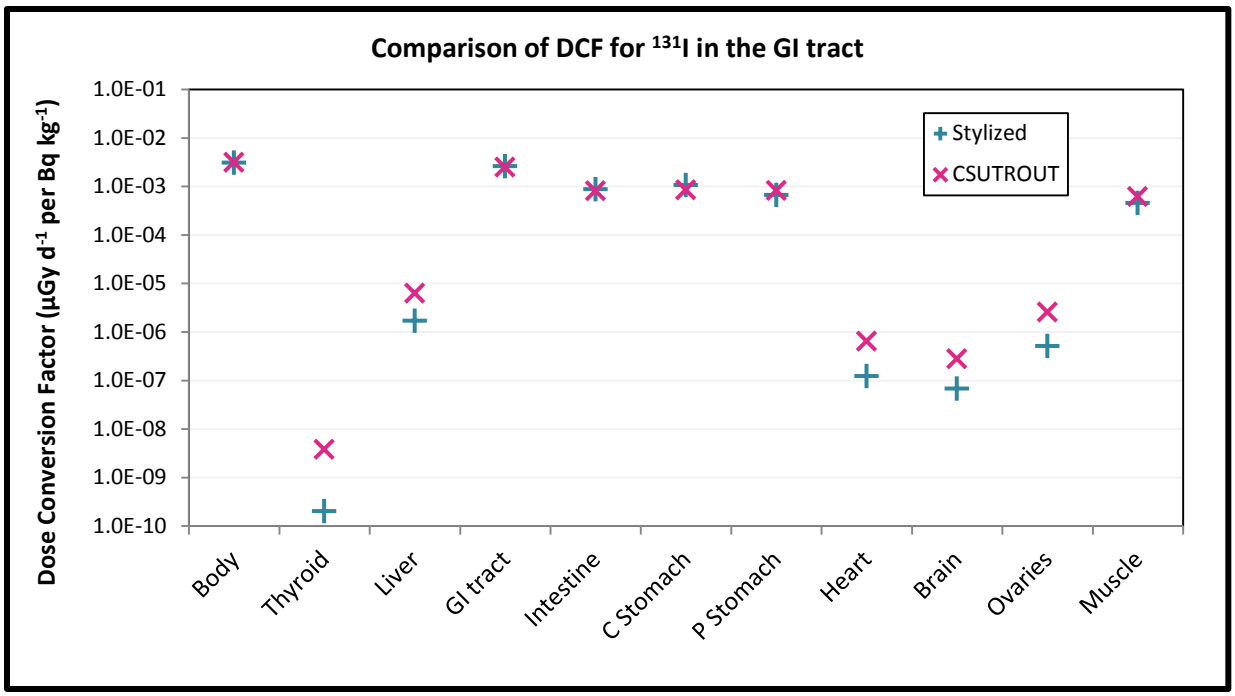

Figure A3.11: Comparison of DCF for ^{131}I in the GI tract, determined by the stylized model and CSUTROUT; DCF is shown on a log scale.

2.3.1. Cumulative 32 day dose

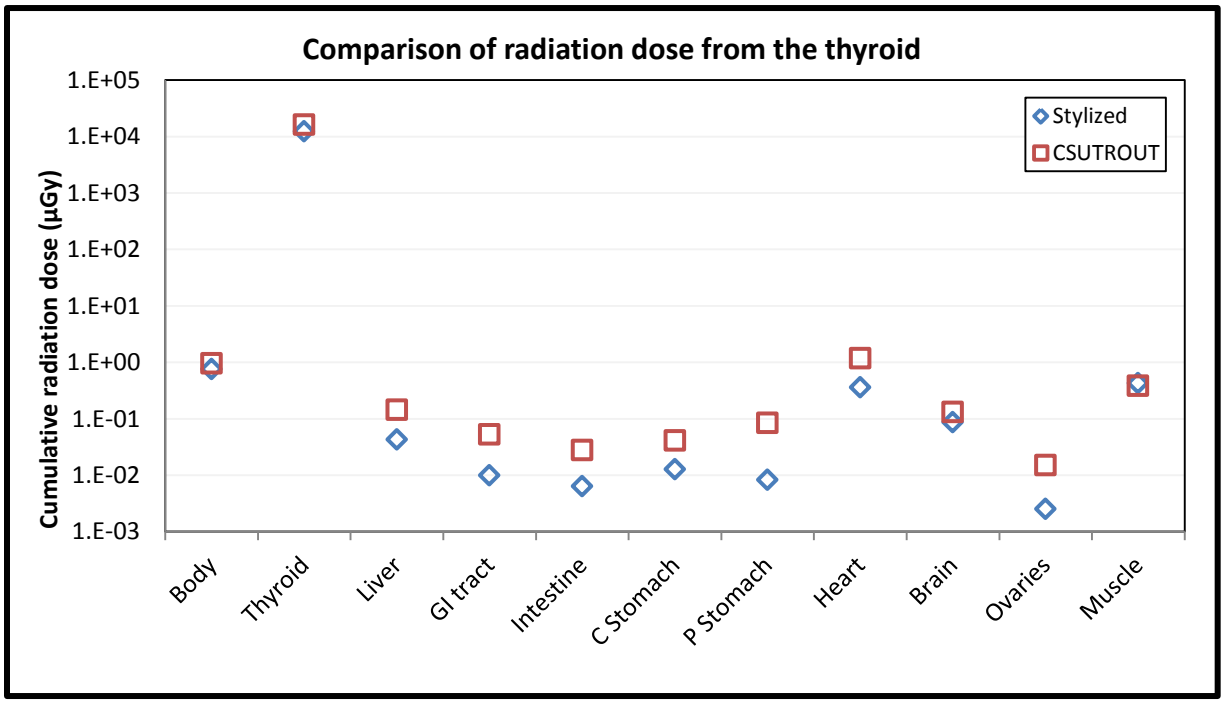

Figure A3.12: Comparison of cumulative 32 day radiation dose received from the thyroid, determined by the stylized model and CSUTROUT; radiation dose is shown on a log scale.

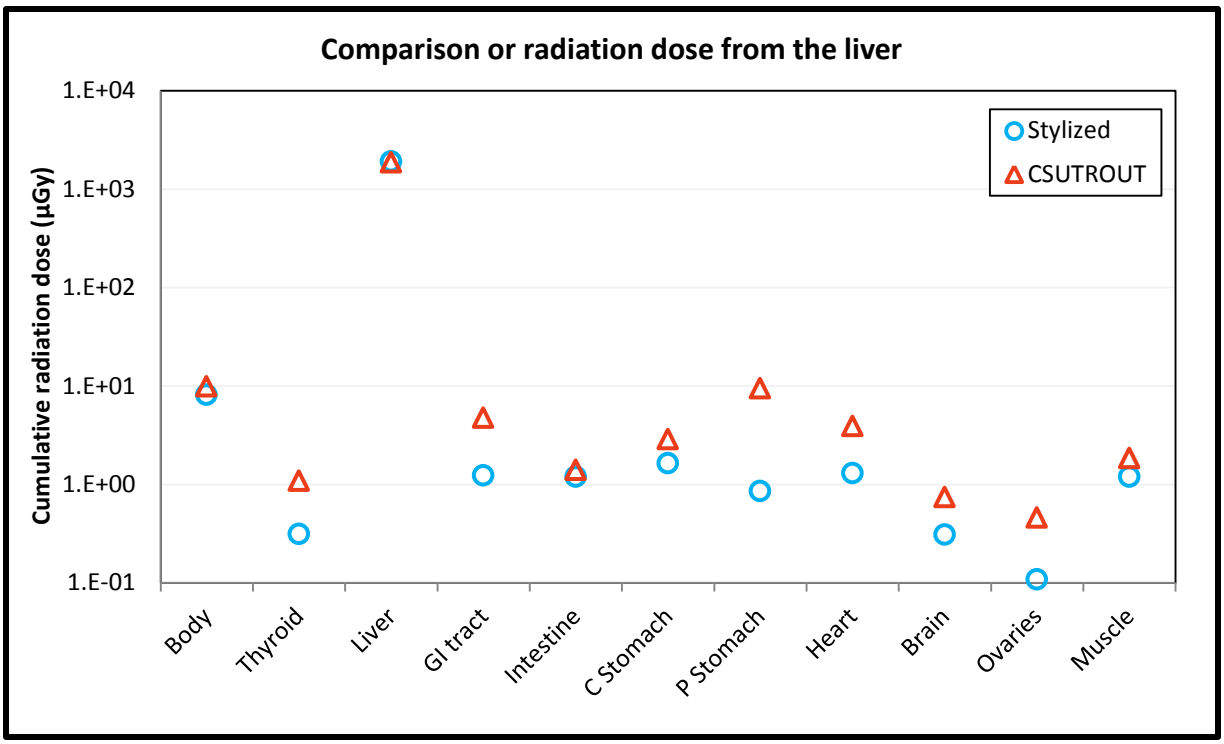

Figure A3.13: Comparison of radiation dose received from the thyroid, determined by the stylized model and CSUTROUT; radiation dose is shown on a log scale.

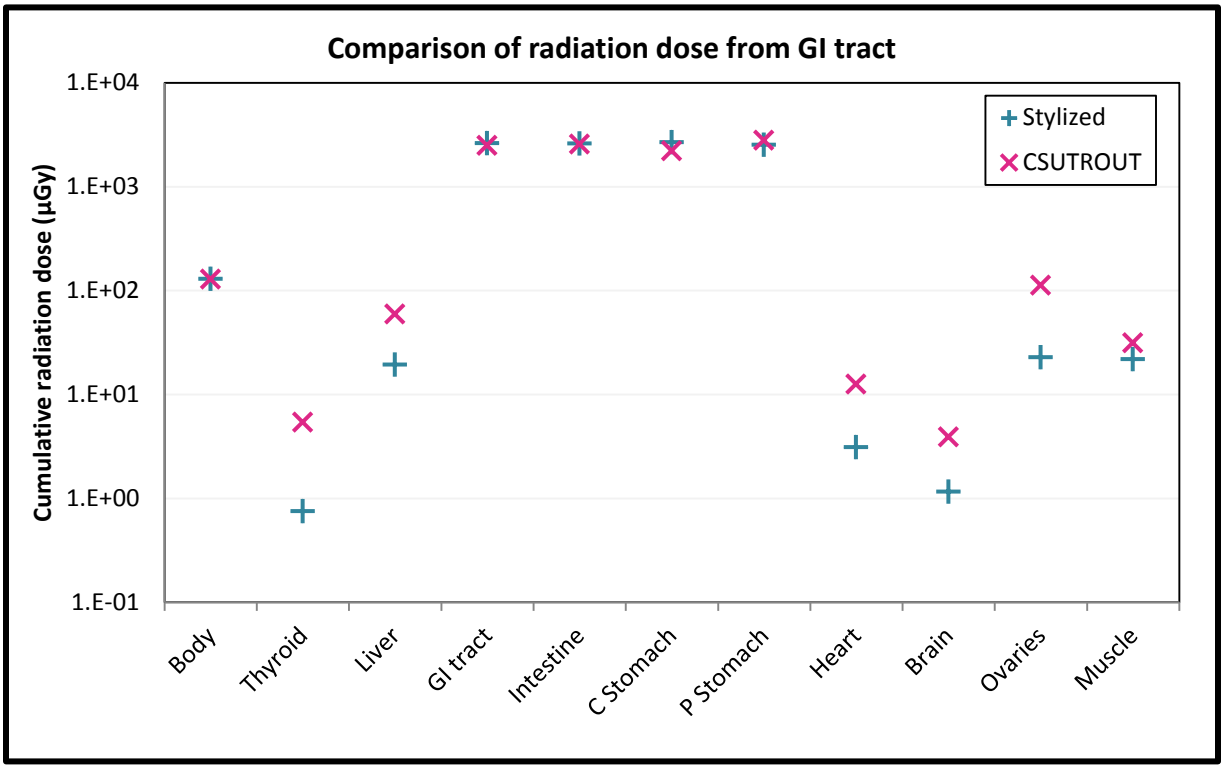

Figure A3.14: Comparison of radiation dose received from the GI tract, determined by the stylized model and CSUTROUT; radiation dose is shown on a log scale.

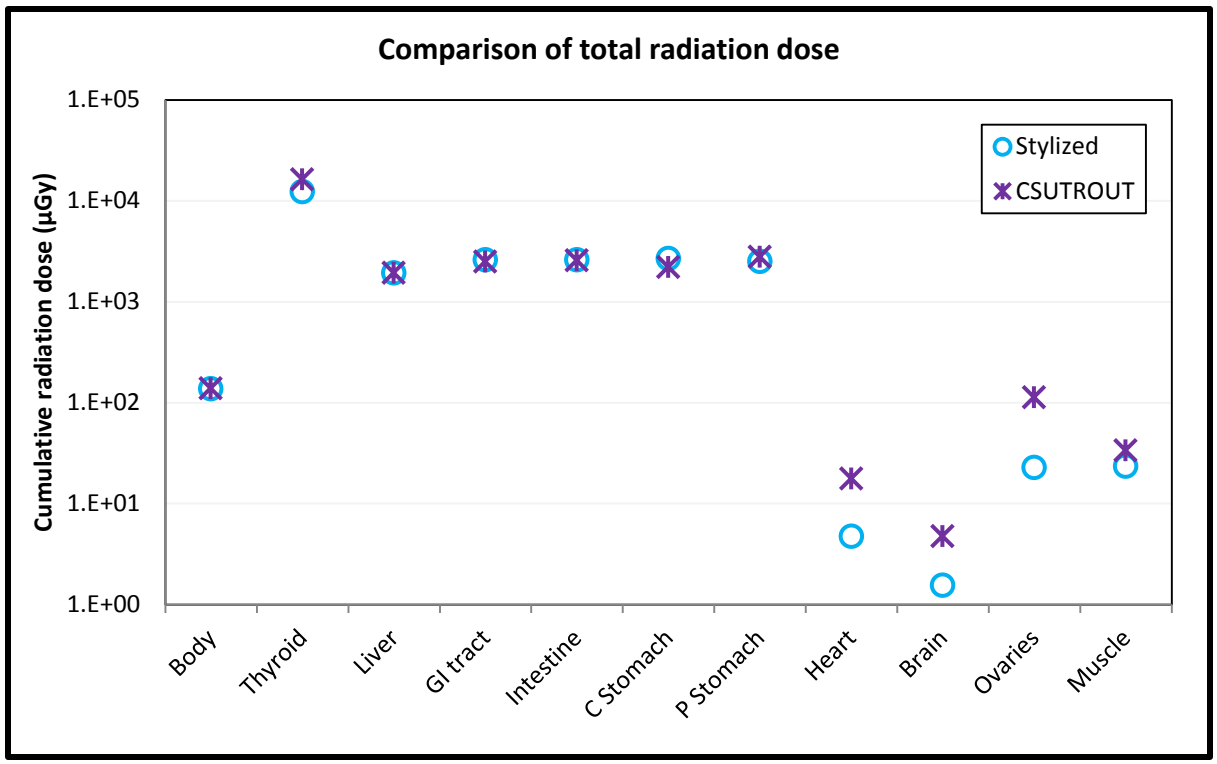

Figure A3.15: Comparison of radiation dose received from all sources, determined by the stylized model and CSUTROUT; radiation dose is shown on a log scale.

3. Detailed results for ^{99}Mo and ^{99m}Tc

3.1. Stylized model

3.1.1. MeV per disintegration

Table A3.9: MCNP output, i.e. MeV per disintegration, listed by source organ and radiation type

Organ	MeV per disintegration by source organ and decay isotope/type							
	Liver				GI Tract			
	^{99}Mo β	^{99}Mo γ	Total ^{99}Mo	^{99m}Tc γ	^{99}Mo β	^{99}Mo γ	Total ^{99}Mo	^{99m}Tc γ
Body	4.04E-01	3.25E-02	4.36E-01	7.85E-03	4.07E-01	3.36E-02	4.40E-01	8.13E-03
Thyroid	3.13E-19	1.28E-07	1.28E-07	2.77E-08	1.01E-19	2.60E-08	2.60E-08	6.96E-09
Thryoid (whole)	4.61E-19	5.46E-07	5.46E-07	1.28E-07	1.38E-19	1.32E-07	1.32E-07	2.05E-08
Liver	3.46E-01	6.29E-03	3.52E-01	1.66E-03	7.64E-05	1.61E-04	2.37E-04	3.76E-05
GI tract	8.91E-04	1.82E-03	2.71E-03	4.29E-04	3.31E-01	8.14E-03	3.39E-01	2.10E-03
Intestine	7.07E-04	5.57E-04	1.26E-03	1.34E-04	1.09E-01	2.20E-03	1.11E-01	5.81E-04
C Stomach	1.84E-04	9.86E-04	1.17E-03	2.30E-04	1.40E-01	3.77E-03	1.43E-01	9.63E-04
P Stomach	6.73E-07	2.79E-04	2.80E-04	6.50E-05	8.26E-02	2.17E-03	8.47E-02	5.56E-04
Swim bladder	8.76E-19	7.63E-08	7.63E-08	8.46E-09	1.93E-06	1.04E-06	2.97E-06	2.39E-07
Heart	1.83E-07	1.76E-05	1.78E-05	1.84E-05	1.88E-08	1.20E-05	1.20E-05	2.57E-06
Brain	4.34E-08	2.79E-05	2.79E-05	6.09E-06	6.98E-09	6.84E-06	6.85E-06	1.28E-06
Ovaries	9.12E-09	3.21E-06	3.22E-06	6.98E-07	1.00E-06	4.86E-05	4.96E-05	1.20E-05
Muscle	5.69E-02	2.43E-02	8.12E-02	5.74E-03	7.61E-02	2.52E-02	1.01E-01	5.98E-03

3.1.2. Dose conversion factors

Table A3.10: Dose conversion factors as determined by MCNP and by using mass ratios

Organ	DCF by source organ (µGy d^{-1} per Bq kg^{-1})				Ratio of WB:organ DCFs (by source organ)			
	^{99}Mo		^{99m}Tc		^{99}Mo		^{99m}Tc	
	Liver	GI	Liver	GI	Liver	GI	Liver	GI
Body	6.03E-03	6.09E-03	1.09E-04	1.12E-04	--	--	--	--
Thyroid (epi)	1.77E-09	3.59E-10	3.83E-10	9.62E-11	--	--	--	--
Thryoid (whl)	7.54E-09	1.82E-09	1.77E-09	2.83E-10	--	--	--	--
Liver	4.87E-03	3.28E-06	2.30E-05	5.19E-07	1.24	--	4.72	--
GI tract	3.75E-05	4.68E-03	5.93E-06	2.90E-05	--	1.30	--	3.87
Intestine	1.75E-05	1.53E-03	1.85E-06	8.03E-06	--	3.98	--	14.0
C Stomach	2.55E-06	1.98E-03	3.18E-06	1.33E-05	--	3.07	--	8.44
P Stomach	3.87E-06	1.17E-03	8.99E-07	7.68E-06	--	5.20	--	14.6
Swim bladder	1.06E-09	4.10E-08	1.17E-10	3.30E-09	--	--	--	--
Heart	2.46E-07	1.66E-07	2.55E-07	3.55E-08	--	--	--	--
Brain	3.86E-07	9.47E-08	8.42E-08	1.76E-08	--	--	--	--
Ovaries	4.45E-08	6.85E-07	9.65E-09	1.66E-07	--	--	--	--
Muscle	1.12E-03	1.40E-03	7.93E-05	8.26E-05	--	--	--	--

3.1.3. Cumulative 14 day radiation doses

Table A3.11: Cumulative 14 day doses listed by source organ radionuclide

Organ	Cumulative 14 day radiation dose (μGy)								
	^{99}Mo			^{99m}Tc			Total		
	Liver	GI tract	^{99}Mo Total	Liver	GI tract	^{99m}Tc Total	Liver	GI	Overall
Body	5.14E+00	5.15E+01	5.66E+01	8.83E-02	9.06E-01	9.95E-01	5.23E+00	5.24E+01	5.76E+01
Thyroid	1.34E-01	2.70E-01	4.04E-01	2.77E-02	6.90E-02	9.66E-02	1.62E-01	3.39E-01	5.00E-01
Thryoid (whole)	1.51E-01	3.61E-01	5.12E-01	3.38E-02	5.36E-02	8.74E-02	1.85E-01	4.15E-01	6.00E-01
Liver	1.12E+03	7.50E+00	1.13E+03	5.06E+00	1.13E+00	6.20E+00	1.13E+03	8.64E+00	1.14E+03
GI tract	7.61E-01	9.43E+02	9.44E+02	1.15E-01	5.57E+00	5.69E+00	8.76E-01	9.49E+02	9.49E+02
Intestine	1.06E+00	9.20E+02	9.21E+02	1.07E-01	4.60E+00	4.71E+00	1.16E+00	9.25E+02	9.26E+02
C Stomach	1.30E-01	1.00E+03	1.00E+03	1.54E-01	6.42E+00	6.57E+00	2.84E-01	1.01E+03	1.01E+03
P Stomach	2.95E-01	8.85E+02	8.86E+02	6.54E-02	5.54E+00	5.61E+00	3.60E-01	8.91E+02	8.91E+02
Swim bladder	2.88E-02	1.11E+01	1.12E+01	3.05E-03	8.54E-01	8.57E-01	3.19E-02	1.20E+01	1.20E+01
Heart	1.26E-01	8.46E-01	9.72E-01	1.25E-01	1.73E-01	2.97E-01	2.51E-01	1.02E+00	1.27E+00
Brain	1.34E-01	3.27E-01	4.62E-01	2.80E-02	5.82E-02	8.62E-02	1.62E-01	3.86E-01	5.48E-01
Ovaries	4.00E-02	6.11E+00	6.15E+00	8.27E-03	1.42E+00	1.42E+00	4.83E-02	7.53E+00	7.58E+00
Muscle	1.09E+00	1.35E+01	1.46E+01	7.34E-02	7.59E-01	8.33E-01	1.16E+00	1.42E+01	1.54E+01

3.1.4. Maximum dose rates

Table A3.12: Maximum dose rates, listed by source organ and radionuclide

Organ/tissue	Maximum dose rate (µGy d-1)						
	^{99}Mo		^{99m}Tc		Liver Total	GI Total	Overall
	Liver	GI	Liver	GI			
Body	3.91E-01	3.99E+00	6.79E-03	7.11E-02	3.98E-01	4.06E+00	4.46E+00
Thyroid	1.02E-02	2.09E-02	2.13E-03	5.41E-03	1.23E-02	2.63E-02	3.86E-02
Thryoid (whole)	1.15E-02	2.80E-02	2.60E-03	4.20E-03	1.41E-02	3.22E-02	4.63E-02
Liver	8.55E+01	5.81E-01	3.90E-01	8.89E-02	8.59E+01	6.70E-01	8.66E+01
GI tract	5.79E-02	7.31E+01	8.84E-03	4.37E-01	6.67E-02	7.35E+01	7.36E+01
Intestine	8.05E-02	7.13E+01	8.24E-03	3.61E-01	8.87E-02	7.16E+01	7.17E+01
C Stomach	9.88E-03	7.75E+01	1.19E-02	5.03E-01	2.18E-02	7.80E+01	7.81E+01
P Stomach	2.24E-02	6.86E+01	5.03E-03	4.34E-01	2.75E-02	6.90E+01	6.91E+01
Swim bladder	2.19E-03	8.62E-01	2.35E-04	6.70E-02	2.43E-03	9.29E-01	9.31E-01
Heart	9.61E-03	6.56E-02	9.59E-03	1.35E-02	1.92E-02	7.91E-02	9.83E-02
Brain	1.02E-02	2.54E-02	2.15E-03	4.56E-03	1.24E-02	2.99E-02	4.23E-02
Ovaries	3.04E-03	4.74E-01	6.37E-04	1.11E-01	3.68E-03	5.85E-01	5.88E-01
Muscle	8.29E-02	9.19E-02	5.65E-03	5.95E-02	8.85E-02	1.51E-01	2.40E-01

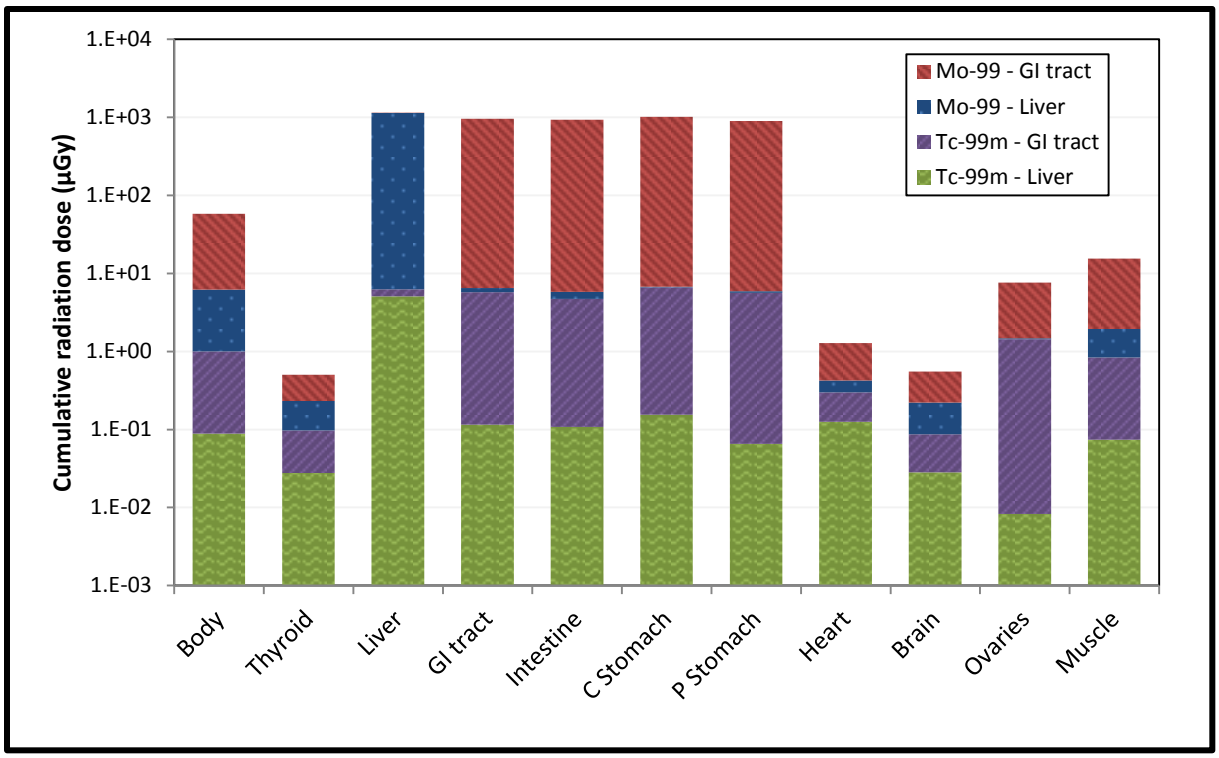

Figure A3.16: Cumulative 14 day radiation dose calculated by the stylized phantom; radiation dose shown on a log scale, with ^{99}Mo and ^{99m}Tc reordered compared to Figure 3.8.

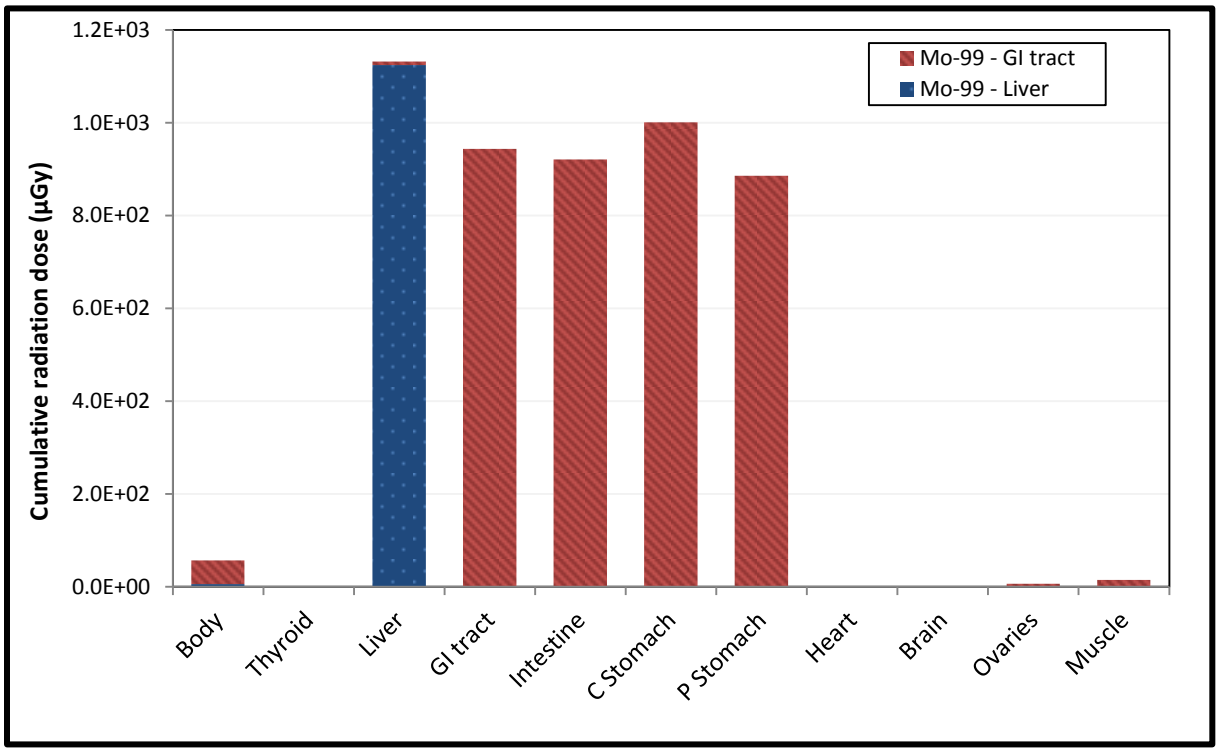

Figure A3.17: Cumulative 14 day radiation dose calculated by the stylized phantom; radiation dose shown on a linear scale for ^{99}Mo only.

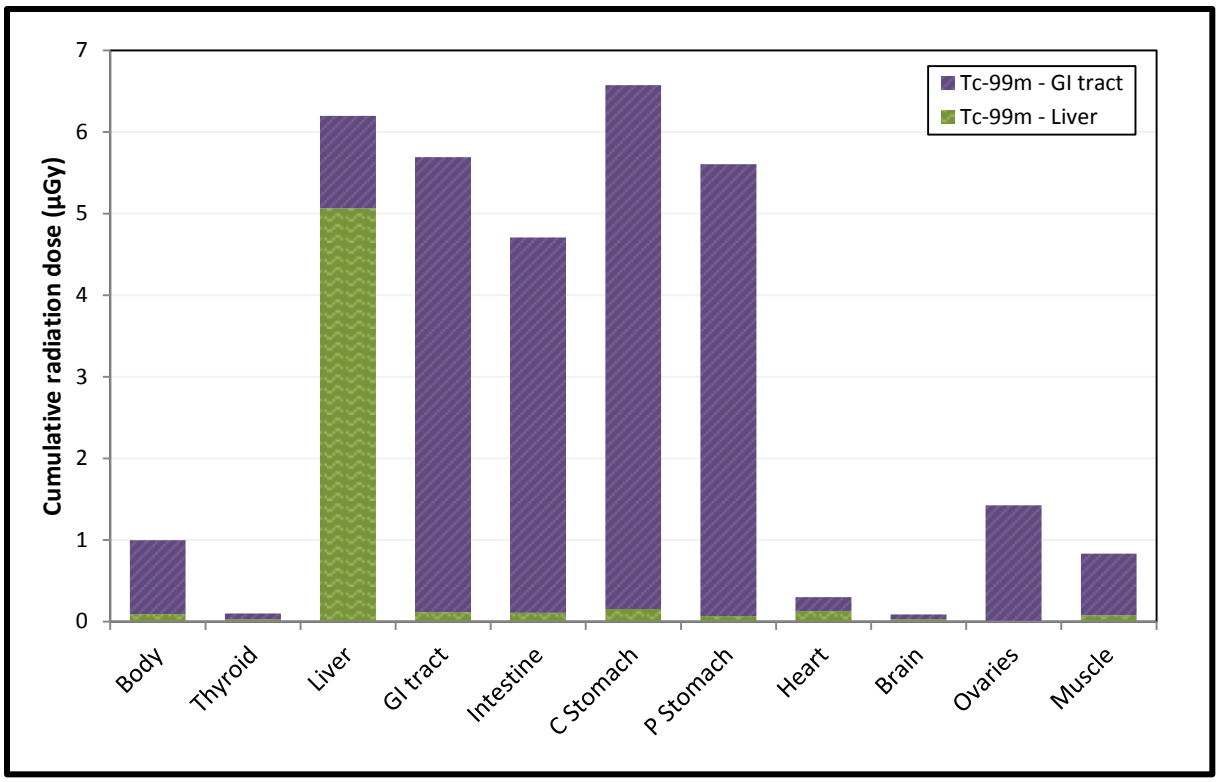

Figure A3.18: Cumulative 14 day radiation dose calculated by the stylized phantom; radiation dose shown on a linear scale for ^{99m}Tc only.

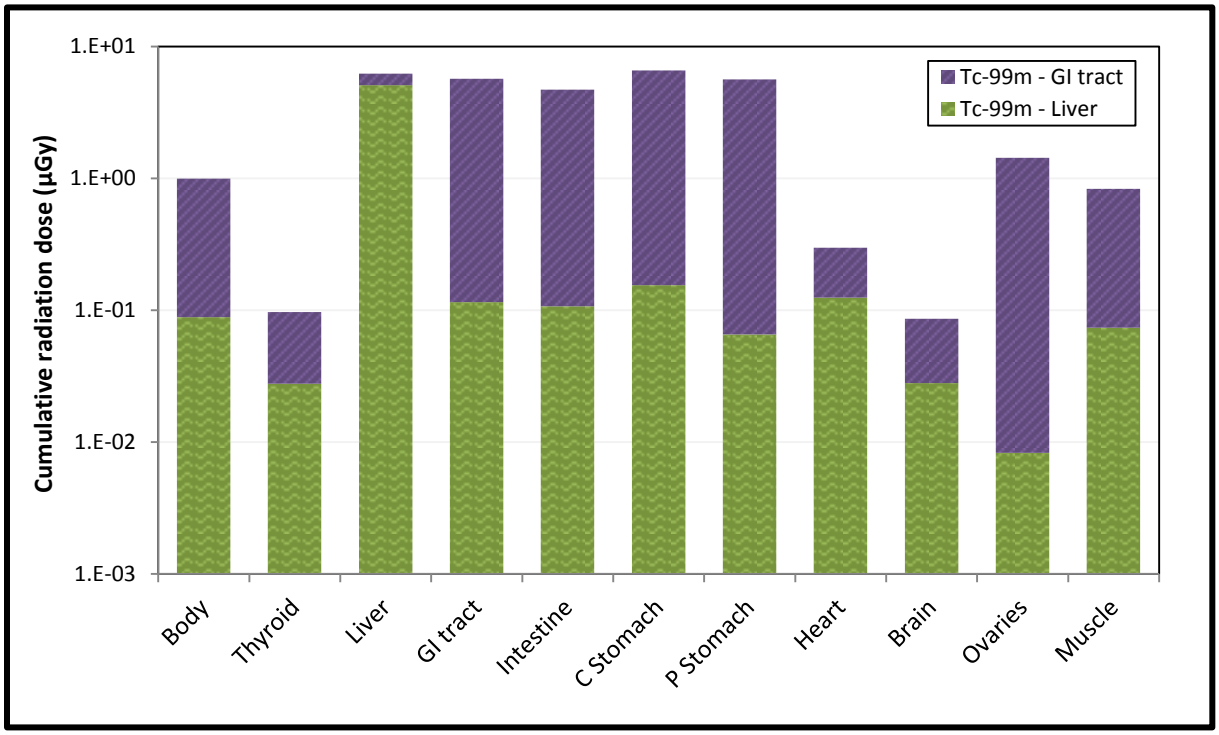

Figure A3.19: Cumulative 14 day radiation dose calculated by the stylized phantom; radiation dose shown on a log scale for ^{99m}Tc only.

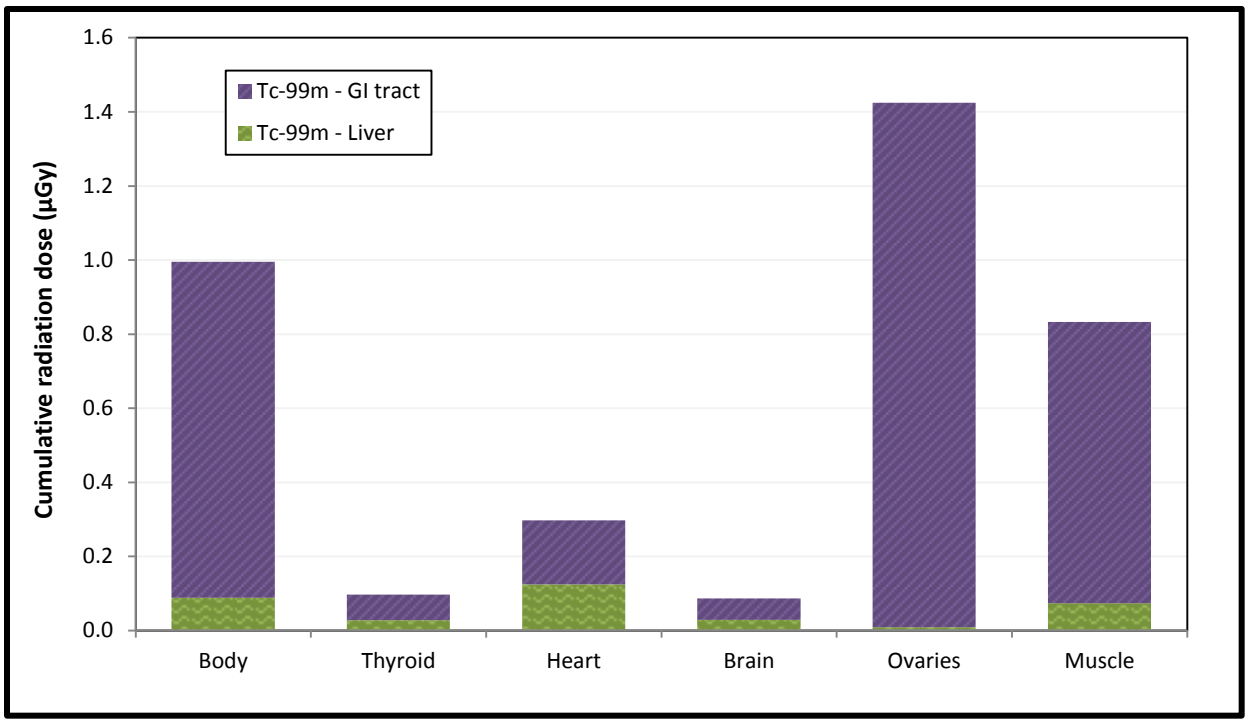

Figure A3.20: Cumulative 14 day radiation dose calculated by the stylized model; radiation dose shown on a linear scale for ^{99m}Tc only, excluding major source organs.

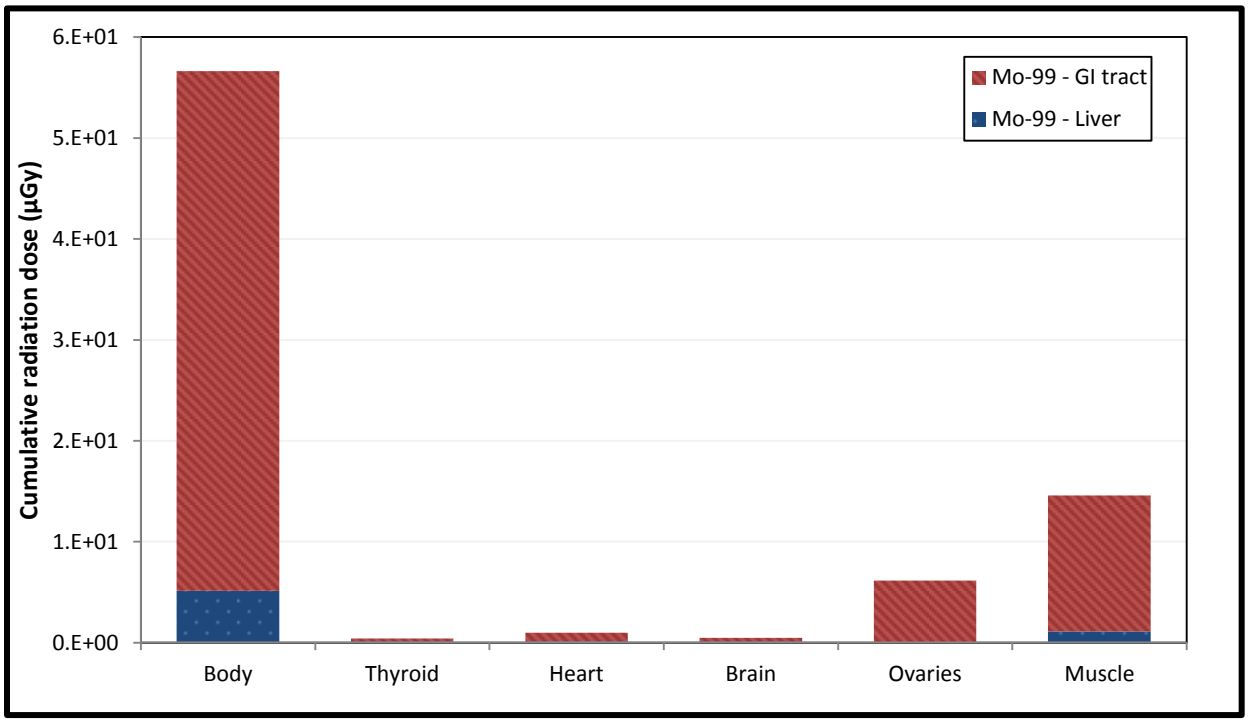

Figure A3.21: Cumulative 14 day radiation dose calculated by stylized phantom; radiation dose shown on a linear scale for ^{99}Mo only, excluding major source organs.

3.2. Voxel model

3.2.1. MeV per disintegration

Table A3.13: MCNP output, i.e. MeV per disintegration, listed by source organ and radiation type

Organ	MeV per disintegration by source organ and decay isotope/type							
	Liver				GI tract			
	^{99}Mo β	^{99}Mo γ	Total ^{99}Mo	^{99m}Tc γ	^{99}Mo β	^{99}Mo γ	Total ^{99}Mo	^{99m}Tc γ
Body	4.07E-01	4.43E-02	4.51E-01	1.27E-02	4.07E-01	4.11E-02	4.48E-01	1.18E-02
Thyroid (epi)	2.40E-10	8.70E-07	8.71E-07	2.70E-07	1.62E-10	2.17E-07	2.17E-07	9.04E-08
Thryoid (whl)	6.33E-09	2.40E-06	2.41E-06	6.81E-07	1.77E-09	7.65E-07	7.67E-07	2.83E-07
Liver	3.39E-01	6.51E-03	3.45E-01	1.72E-03	8.25E-04	4.31E-04	1.26E-03	1.12E-04
GI tract	8.16E-03	4.20E-03	1.24E-02	1.09E-03	3.14E-01	9.92E-03	3.24E-01	2.60E-03
Intestine	1.40E-05	5.38E-04	5.52E-04	1.47E-04	1.01E-01	2.41E-03	1.04E-01	6.45E-04
C Stomach	9.39E-04	1.29E-03	2.23E-03	3.40E-04	1.10E-01	4.28E-03	1.14E-01	1.11E-03
P Stomach	5.78E-03	2.20E-03	7.98E-03	5.62E-04	1.03E-01	3.19E-03	1.06E-01	8.42E-04
Swim bladder	2.19E-16	2.89E-07	2.89E-07	8.87E-08	3.99E-05	2.04E-06	4.19E-05	5.17E-07
Heart	8.38E-07	2.44E-04	2.44E-04	6.50E-05	1.23E-07	5.79E-05	5.80E-05	1.70E-05
Brain	1.01E-07	6.48E-05	6.49E-05	1.85E-05	2.36E-08	2.48E-05	2.48E-05	7.95E-06
Ovaries	2.99E-08	1.26E-05	1.27E-05	3.82E-06	6.42E-04	7.76E-05	7.20E-04	2.01E-05
Espophagus	1.43E-03	1.68E-04	1.59E-03	4.11E-05	2.49E-05	2.54E-05	5.03E-05	6.80E-06
Spleen	6.65E-09	5.04E-06	5.05E-06	1.63E-06	3.93E-04	4.85E-05	4.42E-04	1.19E-05
Kidney	1.13E-07	3.63E-05	3.64E-05	1.06E-05	6.79E-04	1.43E-04	8.21E-04	3.76E-05
Eye (whole)	3.10E-07	1.55E-04	1.55E-04	4.70E-05	1.16E-07	6.48E-05	6.49E-05	2.08E-05
Eye Lens	1.47E-08	7.63E-06	7.64E-06	2.41E-06	4.69E-09	3.29E-06	3.29E-06	1.01E-06
Gills	2.50E-06	8.99E-04	9.01E-04	2.46E-04	5.59E-07	2.71E-04	2.71E-04	7.87E-05
Bone	2.79E-04	4.30E-03	4.57E-03	1.92E-03	2.89E-03	3.19E-03	6.08E-03	1.48E-03
Muscle	5.99E-02	2.79E-02	8.77E-02	7.54E-03	8.75E-02	2.69E-02	1.14E-01	7.37E-03

3.2.2. Dose conversion factors

Table A3.14: Dose conversion factors as determined by MCNP and by using mass ratios

Organ	DCF by source organ (μGy d^{-1} per Bq kg^{-1})				Ratio of WB:organ DCF by source organ			
	Liver		GI tract		Mo-99		GI tract	
	Mo-99	Tc-99m	Mo-99	Tc-99m	Liver	GI Tract	Liver	GI Tract
Body	6.24E-03	1.75E-04	6.20E-03	1.63E-04	--	--	--	--
Thyroid (epi)	1.20E-08	3.73E-09	3.00E-09	1.25E-09	--	--	--	--
Thryoid (whl)	3.33E-08	9.41E-09	1.06E-08	3.91E-09	--	--	--	--
Liver	4.77E-03	2.38E-05	1.74E-05	1.55E-06	1.31	--	7.35	--
GI tract	1.71E-04	1.51E-05	4.48E-03	3.60E-05	--	1.38	--	4.52
Intestine	7.63E-06	2.03E-06	1.44E-03	8.91E-06	--	4.32	--	18.24
C Stomach	9.29E-05	4.70E-06	1.58E-03	1.53E-05	--	3.92	--	10.60
P Stomach	1.10E-04	7.76E-06	1.46E-03	1.16E-05	--	4.23	--	13.96
Swim bladder	4.00E-09	1.23E-09	5.80E-07	7.14E-09	--	--	--	--
Heart	3.38E-06	8.98E-07	8.02E-07	2.35E-07	--	--	--	--
Brain	8.97E-07	2.56E-07	3.43E-07	1.10E-07	--	--	--	--
Ovaries	1.75E-07	5.28E-08	9.95E-06	2.77E-07	--	--	--	--
Espophagus	2.20E-05	5.68E-07	6.95E-07	9.39E-08	--	--	--	--
Spleen	6.98E-08	2.26E-08	6.11E-06	1.65E-07	--	--	--	--
Kidney	5.03E-07	1.47E-07	1.14E-05	5.20E-07	--	--	--	--
Eye (whole)	2.14E-06	6.49E-07	8.97E-07	2.88E-07	--	--	--	--
Eye Lens	1.06E-07	3.33E-08	4.55E-08	1.39E-08	--	--	--	--
Gills	1.25E-05	3.40E-06	3.75E-06	1.09E-06	--	--	--	--
Bone	6.32E-05	2.66E-05	8.41E-05	2.04E-05	--	--	--	--
Muscle	1.21E-03	1.04E-04	1.58E-03	1.02E-04	--	--	--	--

3.2.3. Cumulative 14 day radiation doses

Table A3.15: Cumulative 14 day doses listed by source organ radionuclide

Organ	Cumulative 14 day dose (µGy), by source organ								
	^{99}Mo			^{99m}Tc			Total		
	Liver	GI	Total ^{99}Mo	Liver	GI	Total ^{99m}Tc	Liver	GI	Overall
Body	6.19E+00	5.06E+01	5.68E+01	1.66E-01	1.27E+00	1.43E+00	6.36E+00	5.19E+01	5.82E+01
Thyroid (epi)	4.22E-01	8.67E-01	1.29E+00	1.25E-01	3.44E-01	4.69E-01	5.47E-01	1.21E+00	1.76E+00
Thryoid (whl)	6.42E-01	1.68E+00	2.33E+00	1.73E-01	5.93E-01	7.66E-01	8.16E-01	2.28E+00	3.09E+00
Liver	1.10E+03	3.30E+01	1.13E+03	5.25E+00	2.80E+00	8.05E+00	1.11E+03	3.58E+01	1.14E+03
GI tract	4.18E+00	9.02E+02	9.07E+02	3.52E-01	6.91E+00	7.26E+00	4.54E+00	9.09E+02	9.14E+02
Intestine	5.88E-01	9.10E+02	9.10E+02	1.49E-01	5.39E+00	5.54E+00	7.37E-01	9.15E+02	9.16E+02
C Stomach	5.87E+00	8.22E+02	8.28E+02	2.83E-01	7.61E+00	7.89E+00	6.16E+00	8.30E+02	8.36E+02
P Stomach	9.16E+00	1.00E+03	1.01E+03	6.15E-01	7.58E+00	8.20E+00	9.77E+00	1.01E+03	1.02E+03
Swim bladder	1.30E-01	1.55E+02	1.56E+02	3.82E-02	1.83E+00	1.87E+00	1.68E-01	1.57E+02	1.57E+02
Heart	1.62E+00	3.17E+00	4.79E+00	4.12E-01	8.85E-01	1.30E+00	2.04E+00	4.05E+00	6.09E+00
Brain	3.08E-01	9.66E-01	1.27E+00	8.38E-02	2.96E-01	3.80E-01	3.91E-01	1.26E+00	1.65E+00
Ovaries	1.88E-01	8.78E+01	8.79E+01	5.40E-02	2.33E+00	2.39E+00	2.42E-01	9.01E+01	9.03E+01
Esophagus	4.89E+01	1.27E+01	6.15E+01	1.20E+00	1.63E+00	2.84E+00	5.01E+01	1.43E+01	6.44E+01
Spleen	1.93E-01	1.39E+02	1.39E+02	5.96E-02	3.59E+00	3.65E+00	2.53E-01	1.43E+02	1.43E+02
Kidney	1.92E-01	3.56E+01	3.58E+01	5.35E-02	1.56E+00	1.61E+00	2.45E-01	3.72E+01	3.74E+01
Eye (whole)	2.08E-01	7.15E-01	9.23E-01	6.01E-02	2.19E-01	2.79E-01	2.68E-01	9.34E-01	1.20E+00
Eye Lens	2.06E-01	7.29E-01	9.35E-01	6.18E-02	2.12E-01	2.74E-01	2.68E-01	9.42E-01	1.21E+00
Gills	7.70E-01	1.91E+00	2.68E+00	2.00E-01	5.28E-01	7.28E-01	9.70E-01	2.43E+00	3.41E+00
Bone	6.18E-01	6.76E+00	7.38E+00	2.48E-01	1.57E+00	1.82E+00	8.66E-01	8.33E+00	9.19E+00
Muscle	1.52E+00	1.62E+01	1.78E+01	1.24E-01	9.99E-01	1.12E+00	1.64E+00	1.72E+01	1.89E+01

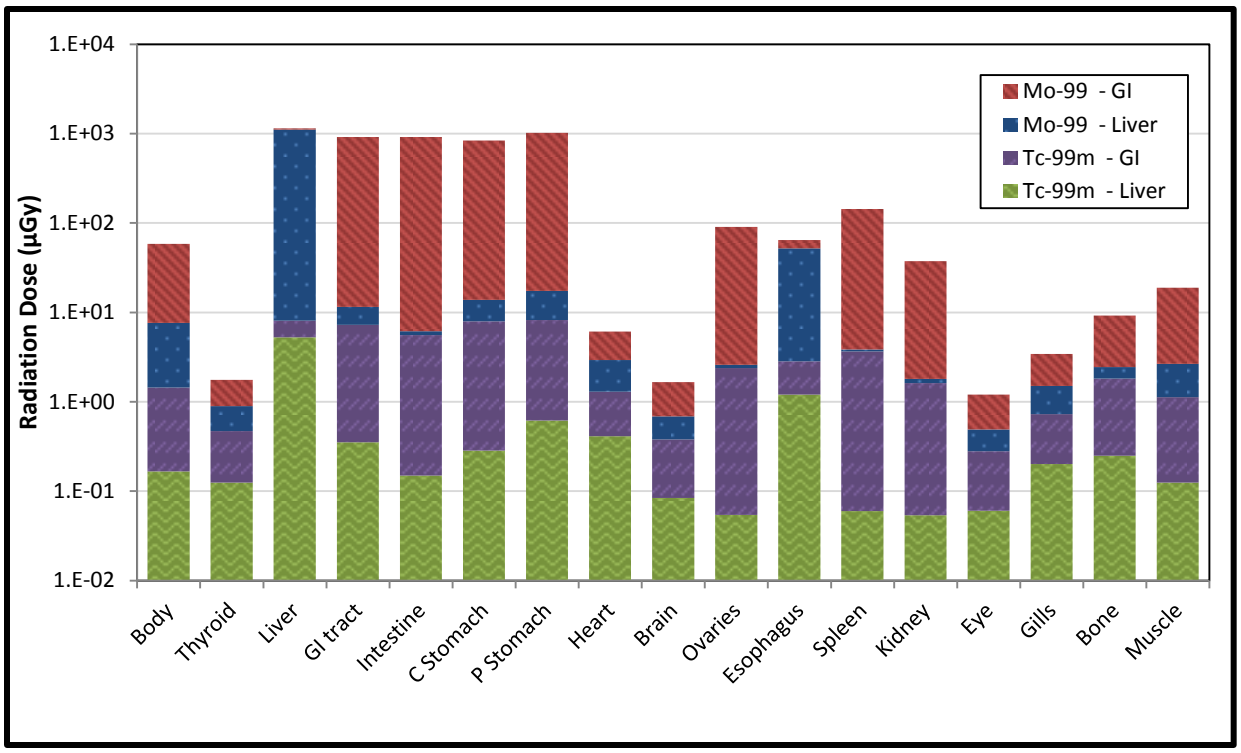

Figure A3.22: Cumulative 14 day radiation dose calculated by CSUTROUT; radiation dose shown on a log scale, with ^{99}Mo and ^{99m}Tc reordered compared to Figure 3.11 in text.

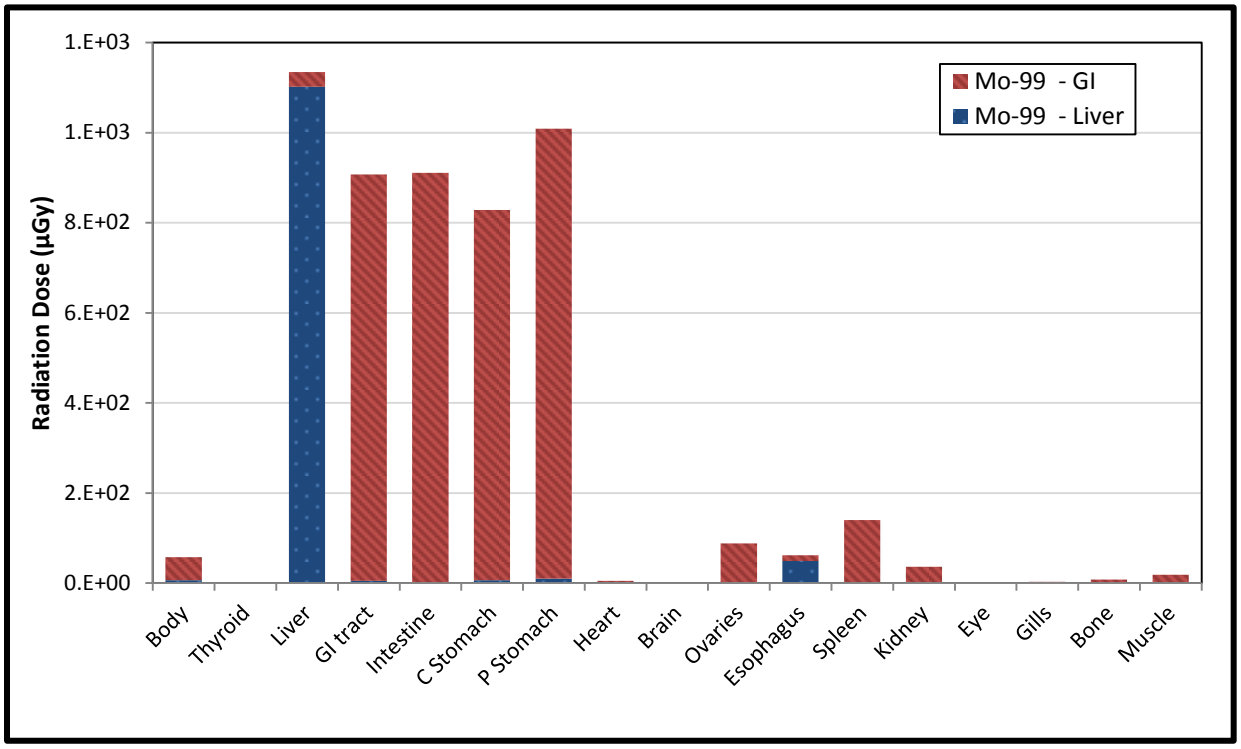

Figure A3.23: Cumulative 14 day radiation dose calculated by CSUTROUT; radiation dose shown on a linear scale for ^{99}Mo only.

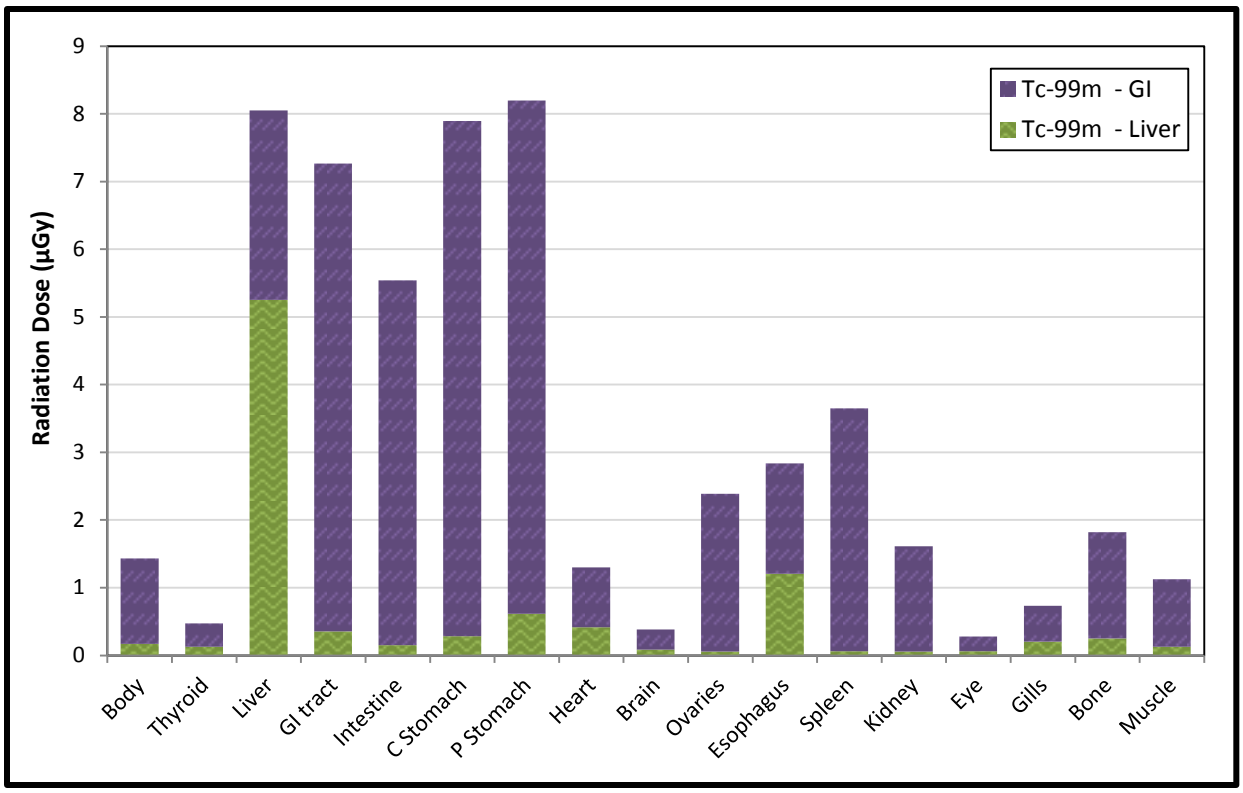

Figure A3.24: Cumulative 14 day radiation dose calculated by CSUTROUT; radiation dose shown on a linear scale for ^{99m}Tc only.

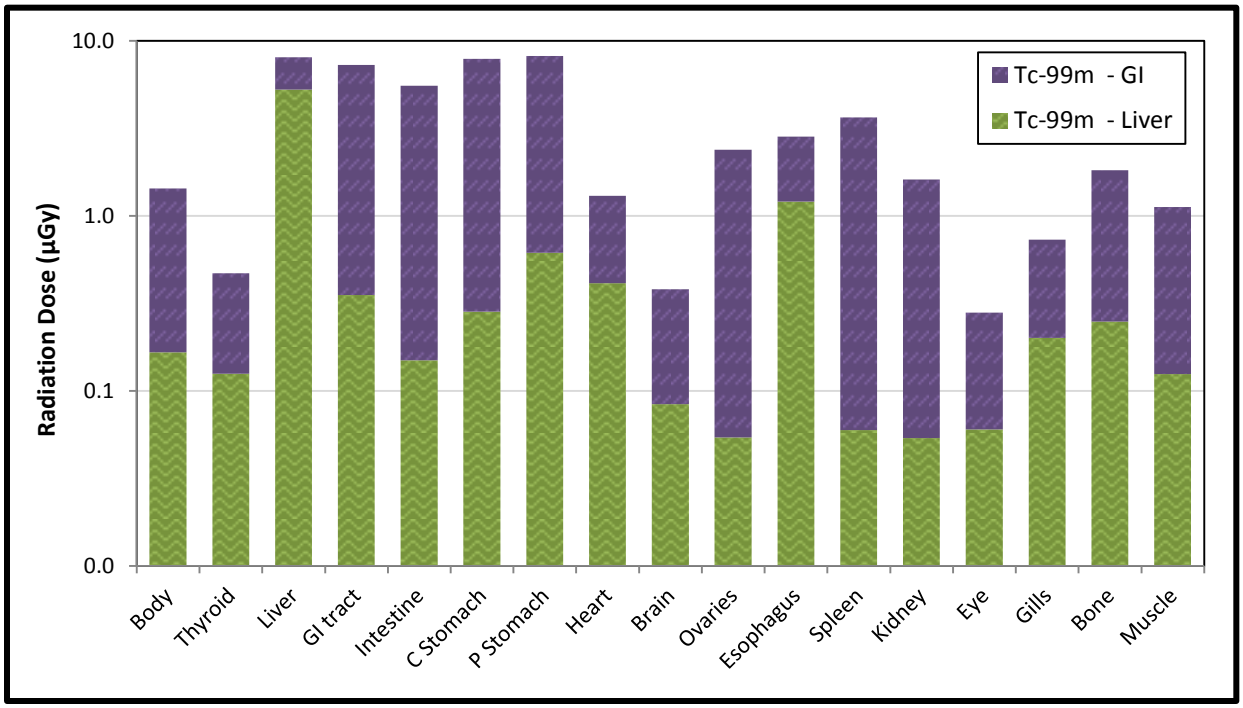

Figure A3.25: Cumulative 14 day radiation dose calculated by CSUTROUT; radiation dose shown on a log scale for ^{99m}Tc only.

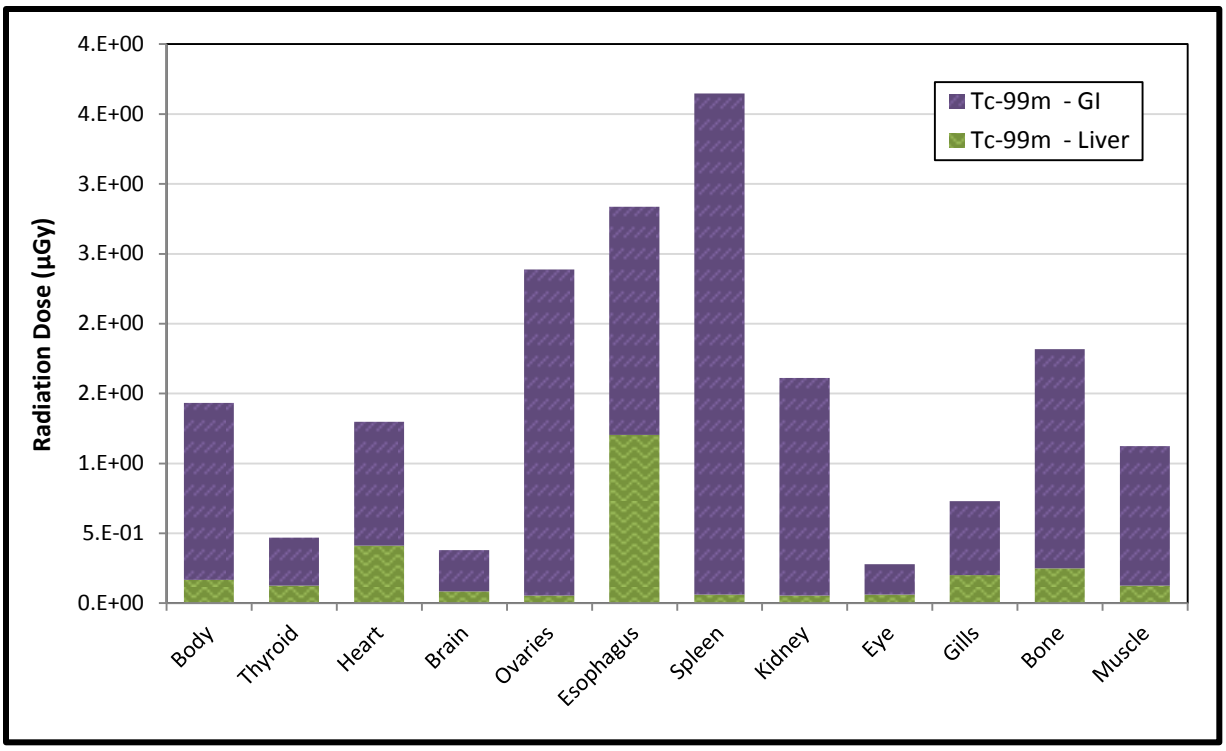

Figure A3.26: Cumulative 14 day radiation dose calculated by CSUTROUT; radiation dose shown on a linear scale for ^{99m}Tc only, excluding major source organs.

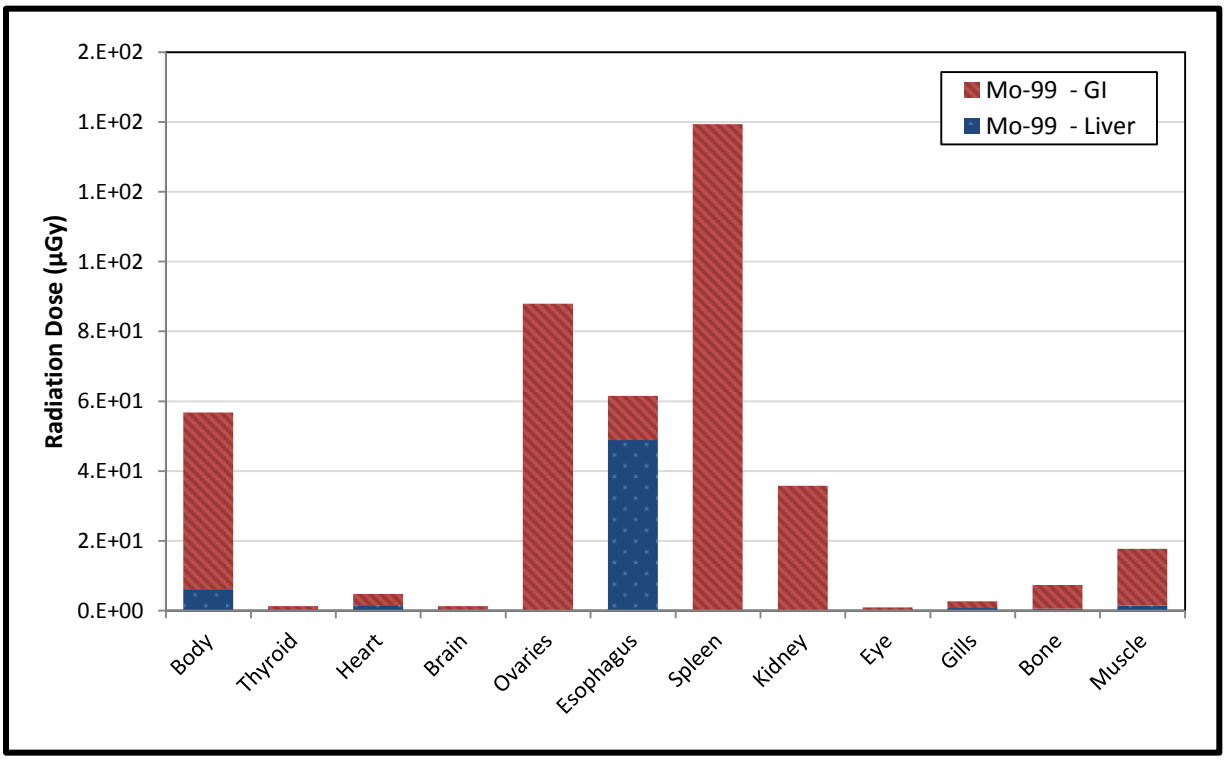

Figure A3.27: Cumulative 14 day radiation dose calculated by CSUTROUT; radiation dose shown on a linear scale for ^{99}Mo only, excluding major source organs.

3.2.4. Maximum dose rates

Table A3.16: Maximum dose rates, listed by source organ and radionuclide

Organ	Maximum dose rate (μGy d^{-1}), by source organ								
	^{99}Mo			^{99m}Tc			Liver Total	GI Total	Overall
	Liver	GI	Total ^{99}Mo	Liver	GI	Total ^{99m}Tc			
Body	4.71E-01	3.92E+00	4.39E+00	1.28E-02	9.93E-02	1.12E-01	4.84E-01	4.02E+00	4.50E+00
Thyroid (epi)	3.21E-02	6.72E-02	9.93E-02	9.60E-03	2.70E-02	3.66E-02	4.17E-02	9.42E-02	1.36E-01
Thryoid (whl)	4.89E-02	1.30E-01	1.79E-01	1.33E-02	4.65E-02	5.98E-02	6.22E-02	1.77E-01	2.39E-01
Liver	8.38E+01	2.55E+00	8.63E+01	4.04E-01	2.19E-01	6.23E-01	8.42E+01	2.77E+00	8.70E+01
GI tract	3.18E-01	6.99E+01	7.02E+01	2.71E-02	5.42E-01	5.69E-01	3.45E-01	7.05E+01	7.08E+01
Intestine	4.47E-02	7.05E+01	7.05E+01	1.15E-02	4.22E-01	4.34E-01	5.62E-02	7.09E+01	7.09E+01
C Stomach	4.47E-01	6.37E+01	6.41E+01	2.18E-02	5.96E-01	6.18E-01	4.69E-01	6.43E+01	6.47E+01
P Stomach	6.97E-01	7.74E+01	7.81E+01	4.73E-02	5.94E-01	6.42E-01	7.44E-01	7.80E+01	7.88E+01
Swim bladder	9.91E-03	1.20E+01	1.21E+01	2.94E-03	1.43E-01	1.46E-01	1.29E-02	1.22E+01	1.22E+01
Heart	1.23E-01	2.45E-01	3.69E-01	3.17E-02	6.94E-02	1.01E-01	1.55E-01	3.15E-01	4.70E-01
Brain	2.34E-02	7.49E-02	9.83E-02	6.45E-03	2.32E-02	2.96E-02	2.98E-02	9.81E-02	1.28E-01
Ovaries	1.43E-02	6.80E+00	6.81E+00	4.16E-03	1.83E-01	1.87E-01	1.84E-02	6.98E+00	7.00E+00
Esophagus	3.72E+00	9.82E-01	4.70E+00	9.25E-02	1.28E-01	2.21E-01	3.81E+00	1.11E+00	4.92E+00
Spleen	1.47E-02	1.08E+01	1.08E+01	4.59E-03	2.81E-01	2.86E-01	1.93E-02	1.11E+01	1.11E+01
Kidney	1.46E-02	2.76E+00	2.77E+00	4.12E-03	1.22E-01	1.26E-01	1.87E-02	2.88E+00	2.90E+00
Eye (whole)	1.58E-02	5.54E-02	7.12E-02	4.62E-03	1.72E-02	2.18E-02	2.04E-02	7.26E-02	9.30E-02
Eye Lens	1.57E-02	5.65E-02	7.22E-02	4.76E-03	1.66E-02	2.14E-02	2.04E-02	7.32E-02	9.36E-02
Gills	5.86E-02	1.48E-01	2.06E-01	1.54E-02	4.14E-02	5.68E-02	7.40E-02	1.89E-01	2.63E-01
Bone	4.70E-02	5.24E-01	5.71E-01	1.91E-02	1.23E-01	1.42E-01	6.61E-02	6.47E-01	7.13E-01
Muscle	1.15E-01	3.16E-04	1.16E-01	9.56E-03	7.83E-02	8.79E-02	1.25E-01	7.86E-02	2.03E-01

3.3. Comparison of stylized and voxel model results

3.3.1. Dose conversion factors

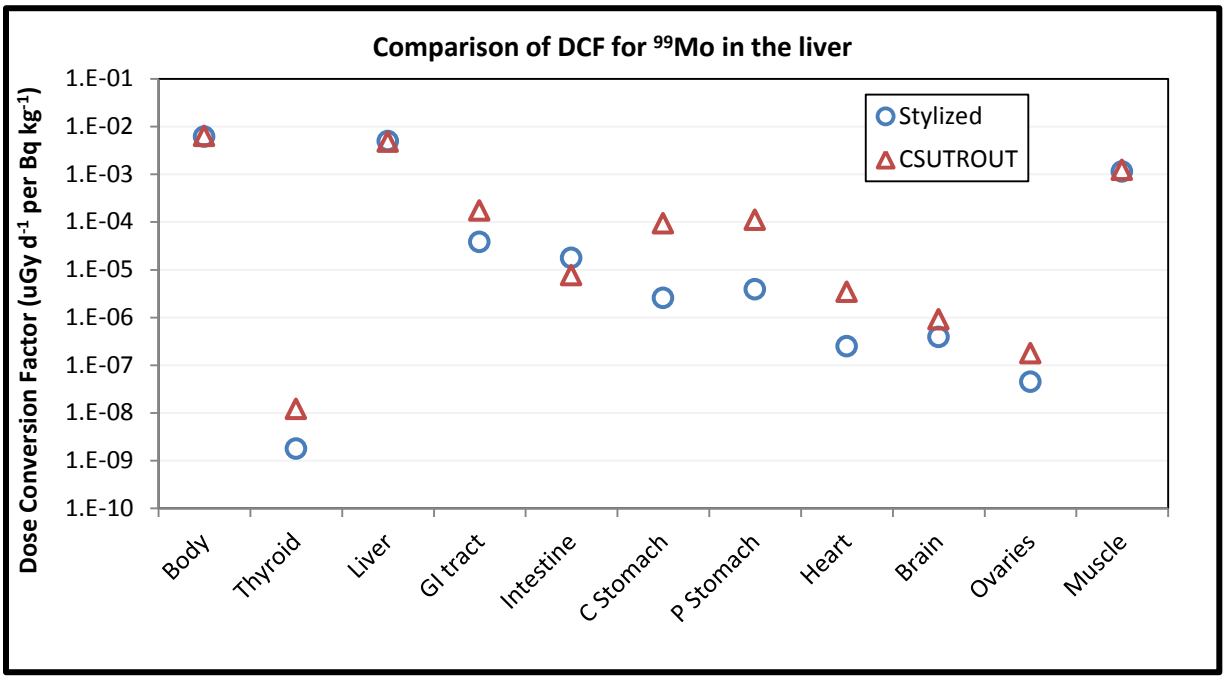

Figure A3.28: Comparison of DCF for ^{99}Mo in the liver, determined by the stylized model and CSUTROUT; DCF is shown on a log scale.

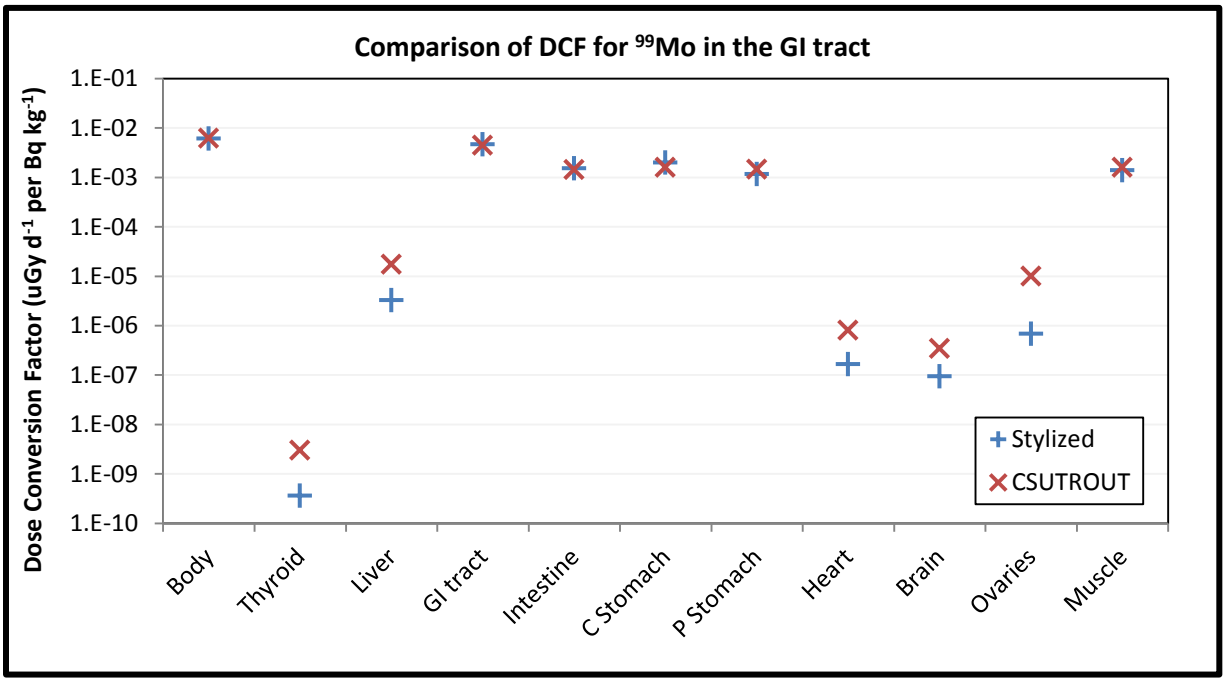

Figure A3.29: Comparison of DCF for ^{99}Mo in the GI tract, determined by the stylized model and CSUTROUT; DCF is shown on a log scale.

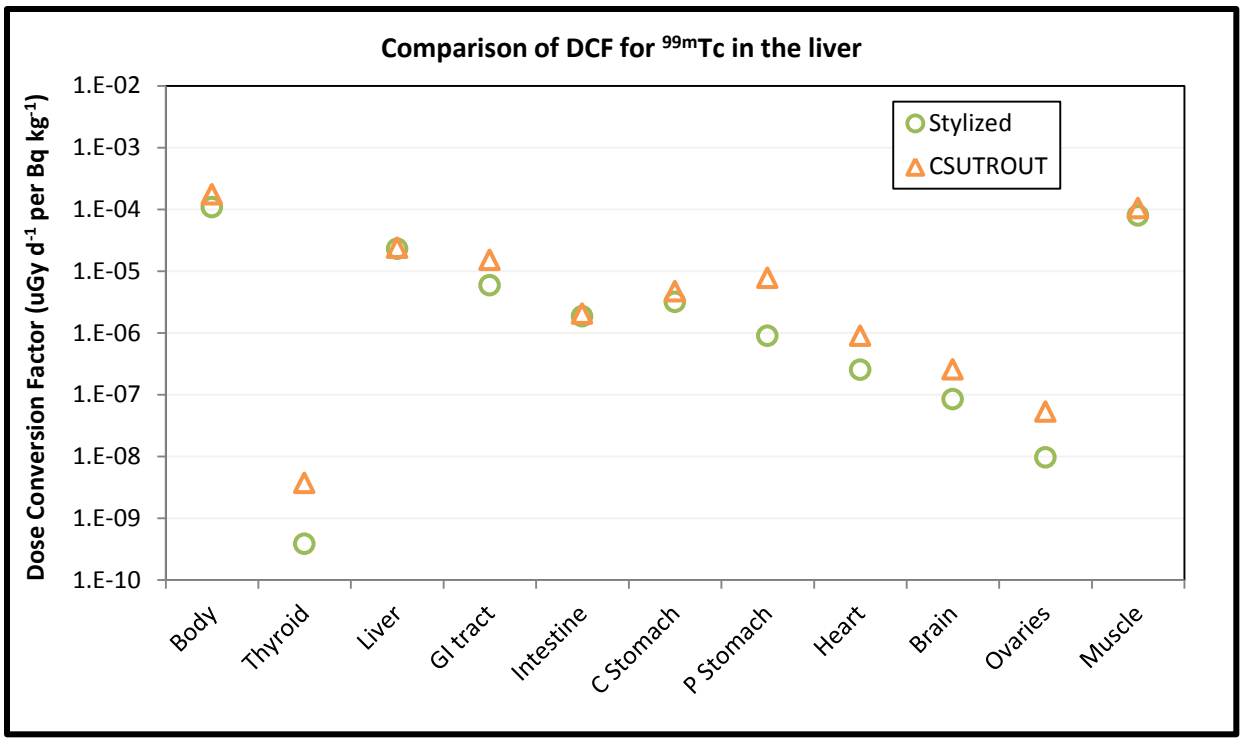

Figure A3.30: Comparison of DCF for ^{99m}Tc in the liver, determined by the stylized model and CSUTROUT; DCF is shown on a log scale.

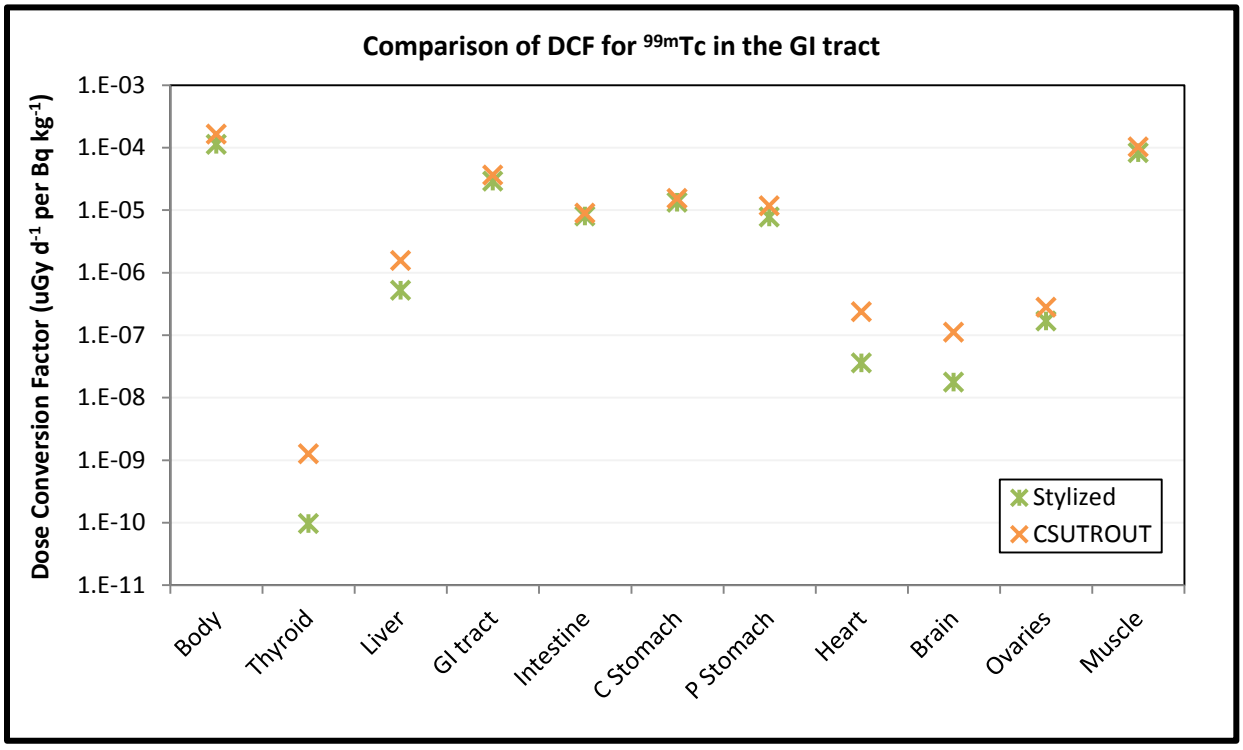

Figure A3.31: Comparison of DCF for ^{99m}Tc in the GI tract, determined by the stylized model and CSUTROUT; DCF is shown on a log scale.

3.3.2. Cumulative 14 day doses

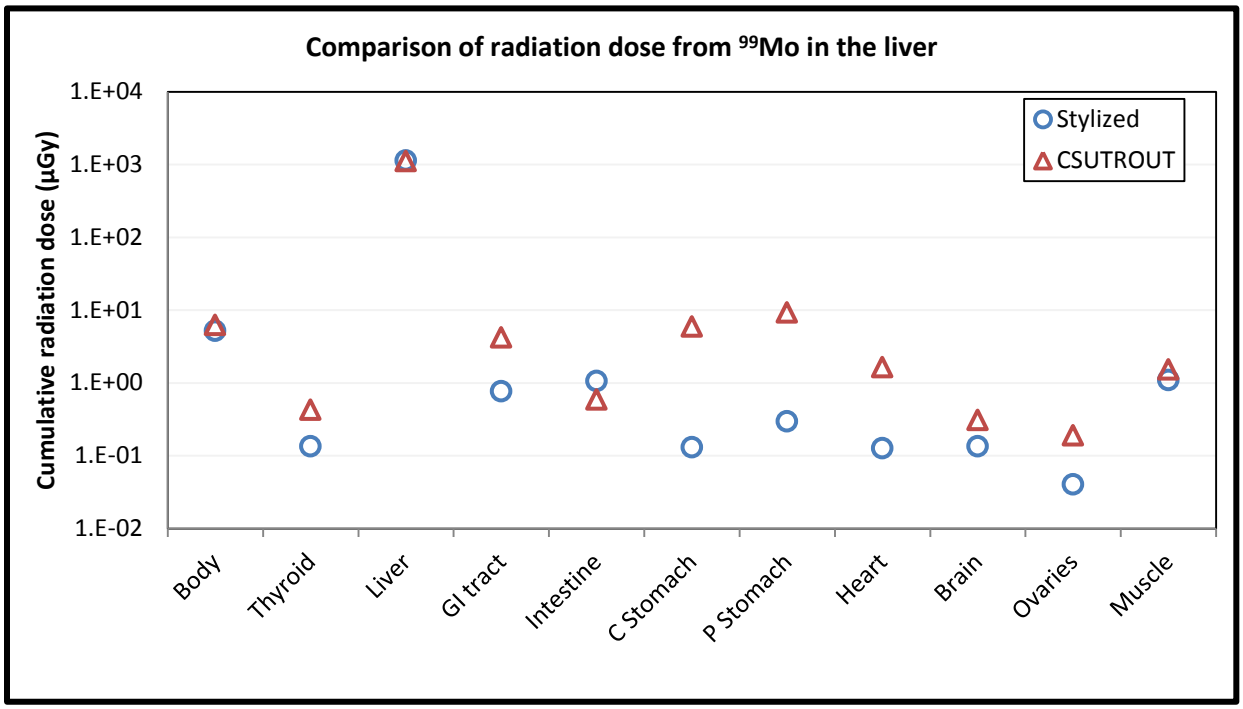

Figure A3.32: Comparison of cumulative 14 day radiation dose received from ^{99}Mo in the liver, determined by the stylized model and CSUTROUT; radiation dose is shown on a log scale.

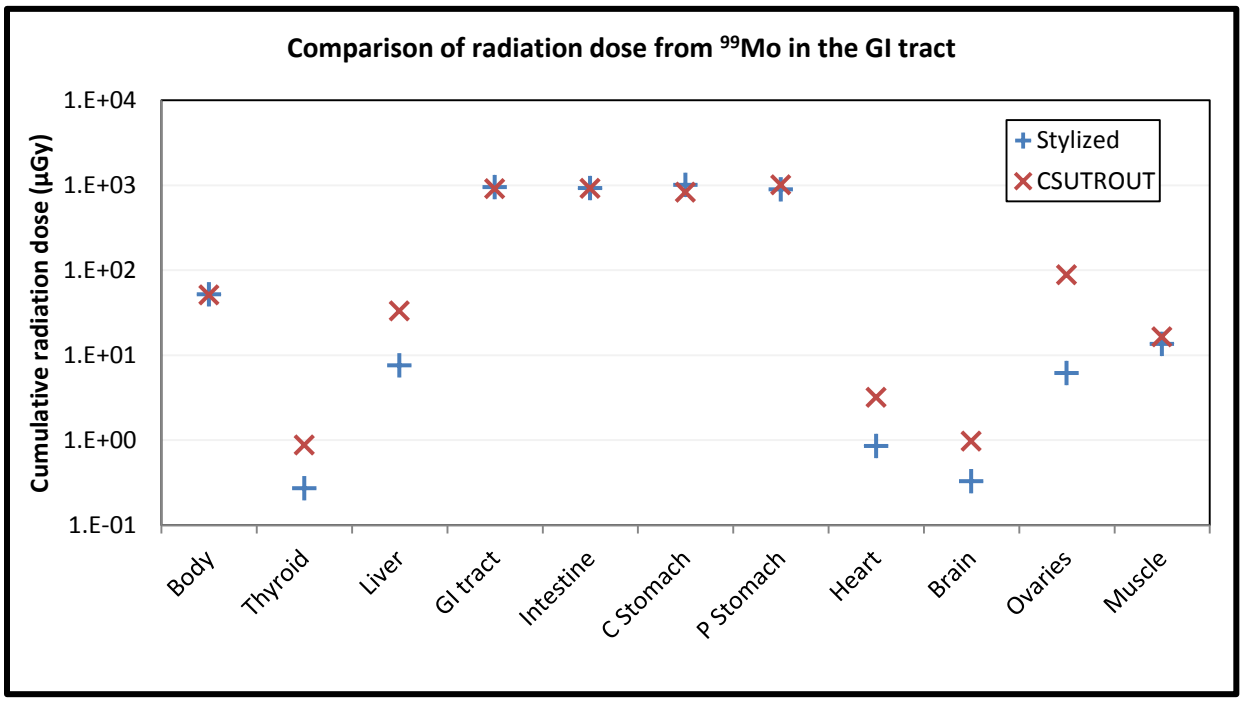

Figure A3.33: Comparison of cumulative 14 day radiation dose received from ^{99}Mo in the GI tract, determined by the stylized model and CSUTROUT; radiation dose is shown on a log scale.

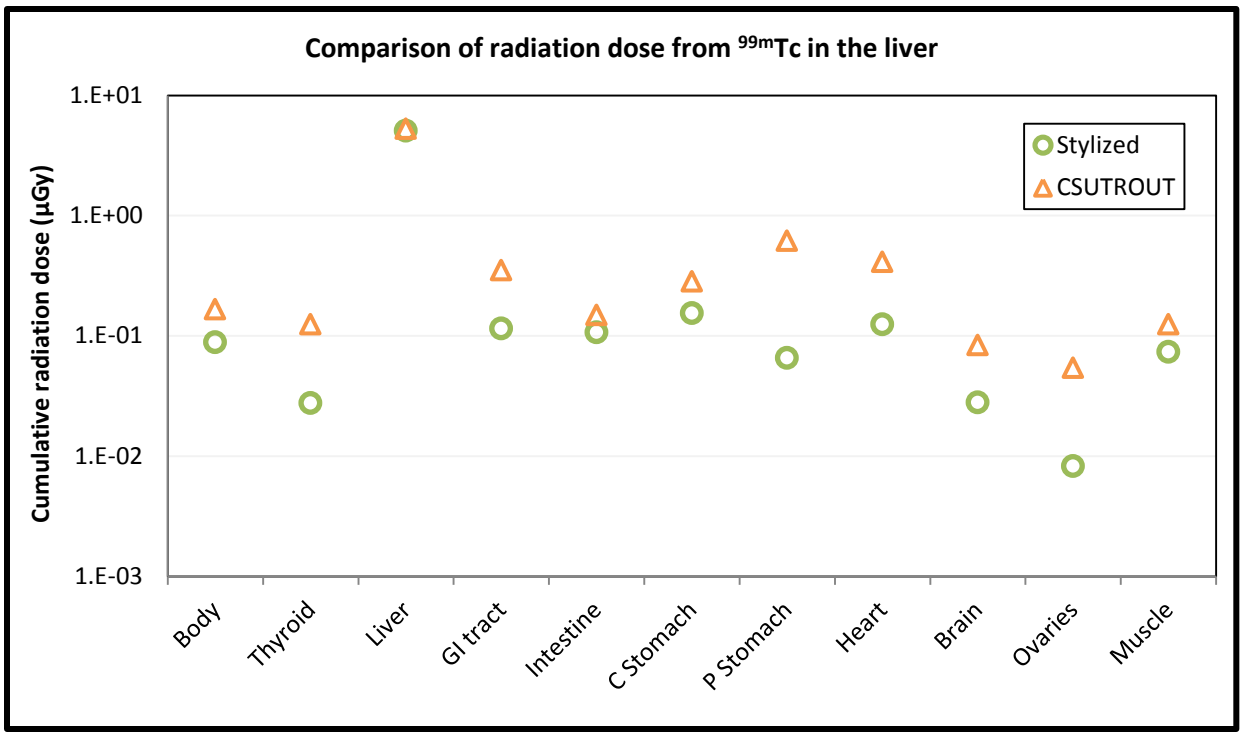

Figure A3.34: Comparison of cumulative 14 day radiation dose received from ^{99m}Tc in the liver, determined by the stylized model and CSUTROUT; radiation dose is shown on a log scale

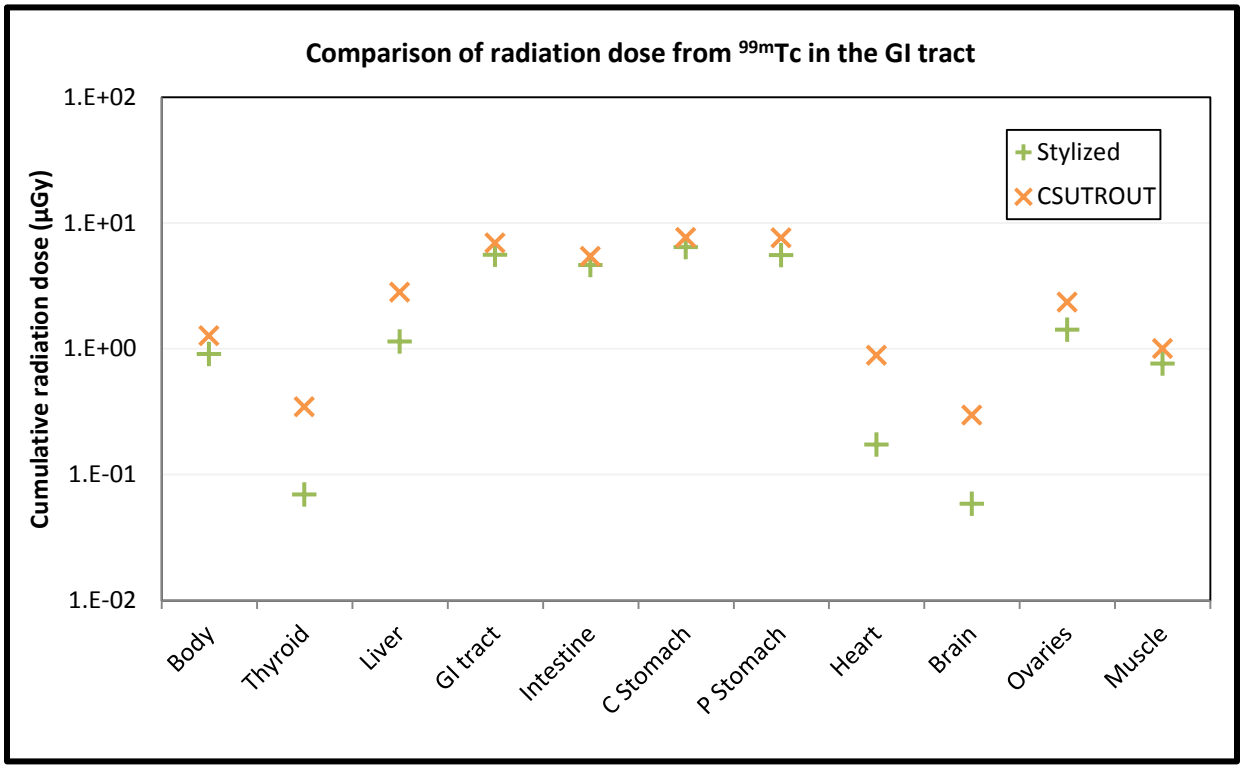

Figure A3.35: Comparison of cumulative 14 day radiation dose received from ^{99m}Tc in the GI tract, determined by the stylized model and CSUTROUT; radiation dose is shown on a log scale

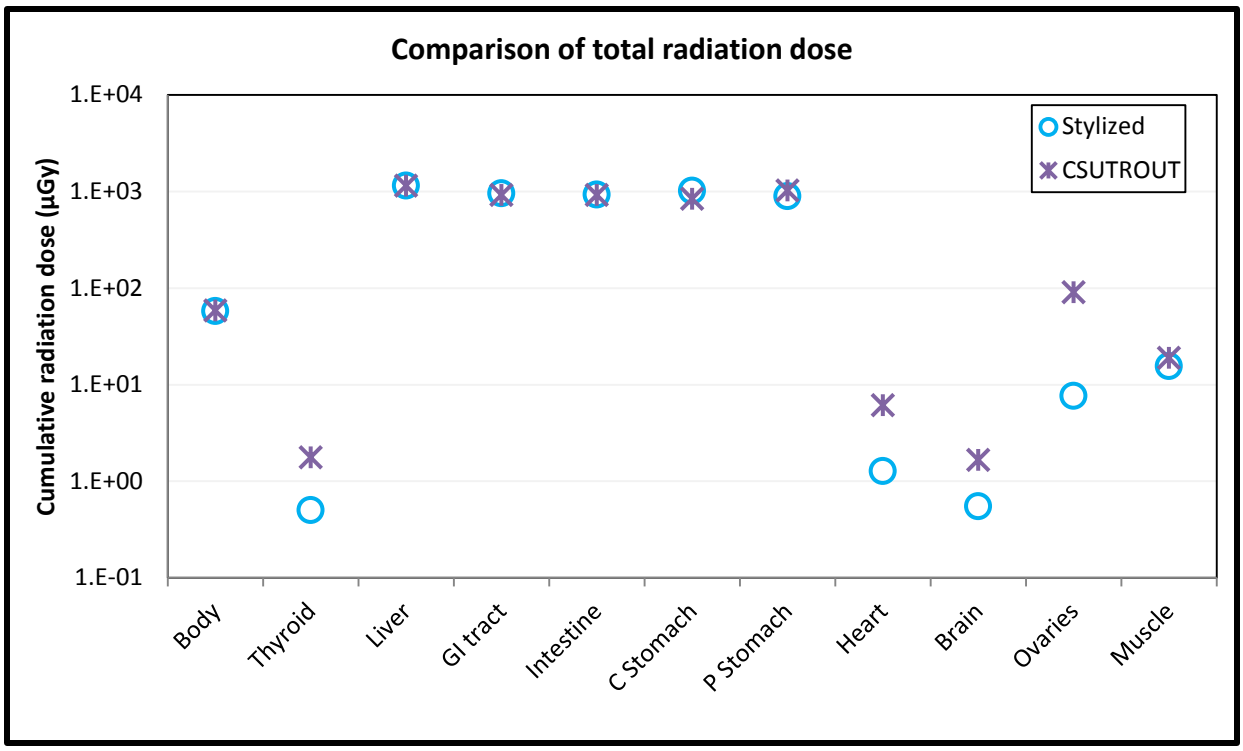

Figure A3.36: Comparison of cumulative 14 day radiation dose received from all sources, determined by the stylized model and CSUTROUT; radiation dose is shown on a log scale.

PART 2: ASSESSING THE USE OF REFLECTANCE SPECTROSCOPY IN DETERMINING CESIUM CHLORIDE STRESS IN THE MODEL SPECIES *ARABIDOPSIS THALIANA* AND LITHIUM CHLORIDE STRESS ACROSS THREE ADDITIONAL PLANT SPECIES

EXECUTIVE SUMMARY

Reflectance spectroscopy is a rapid and non-destructive analytical technique that may be used for assessing plant stress and has potential applications for use in remediation. Changes in reflectance such as that due to metal stress may occur before damage is visible, and existing studies have shown that metal stress does cause changes in plant reflectance. The studies herein further investigate the potential use of reflectance spectroscopy as a method for assessing metal stress in plants.

In the first study, *Arabidopsis thaliana* plants were treated twice weekly in a laboratory setting with varying levels (0 mM, 0.5 mM, or 5 mM) of cesium chloride (CsCl) solution, and reflectance spectra were collected every week for three weeks using an ASD FieldSpec Pro Spectroradiometer with a contact probe and a field of view probe at 36.8 and 66.7 cm above the plant. As metal stress is known to mimic drought stress, plants were harvested each week after spectra collection for determination of relative water content and chlorophyll content. A visual assessment of the plants was also conducted using point observations on a uniform grid of 81 points. Two-way ANOVAs were performed on selected vegetation indices (VI) to determine the significance of the effects of treatment level and length of treatment. Linear regression was used to relate the most appropriate vegetation indices to the aforementioned endpoints and to compare results provided by the three different spectra collection techniques. One-way ANOVAs were performed on selected VI at each time point to determine which, if any, indices offered a significant prediction of the overall extent of Cs toxicity.

Of the 14 vegetation indices considered, the two most significant were the slope at the red edge position (SREP) and the ratio of reflectance at 950 nm to the reflectance at 750 nm (R_{950}/R_{750}). Contact probe readings and field of view readings differed significantly, although field of view measurements were generally consistent at each height.

The purpose of the second study was to determine whether a quantifiable relationship exists between lithium (Li) contamination and reflectance spectra in each species of plant considered, and if such a relationship exists similarly across species. The species considered were *Arabidopsis thaliana, Helianthus annuus, Brassica rapa,* and *Zea mays.* Reflectance spectra were collected every week for three weeks using an ASD FieldSpec Pro Spectroradiometer with a contact probe and a field of view probe (set at 66.7 cm above the plant) for plants treated twice weekly in a laboratory setting with 0 mM or 15 mM of lithium chloride (LiCl) solution. Plants were harvested each week immediately after spectra collection for determination of relative water content and chlorophyll content, as in the first study. Linear regression was used to relate the most appropriate vegetation indices (determined by the Pearson correlation coefficient) to the aforementioned endpoints and to compare results provided by the different spectra collection techniques. Two-way ANOVAs were performed on 12 selected vegetation indices (VI) for each species individually to determine the significance of the effects of treatment level and length of treatment on a species basis. Balanced ANOVAs were conducted across all species to determine significance of treatment, time, and species.

LiCl effects and corresponding reflectance shifts were significant for *A. thaliana,* but *Z. mays* and *H. annuus* showed little response to LiCl at the treatment level considered in this study, with no significant differences in relative water content or chlorophyll content by treatment level. *B. rapa* reflectance spectra responded similarly to Li exposure as *Z. mays,* but *B. rapa* did have significant differences in relative water content by treatment level. All species demonstrated a potential stimulatory effect of LiCl, with at least one week of increased reflectance in the near-IR. Different VI proved to be the best predictor of endpoint values for each species, with only SIPI and the ratio of reflectance at 1390 nm to the reflectance at 1454 nm (R_{1390}/R_{1454}) common between species. The most significant VI considering all species together was SIPI, although *A. thaliana* effects dominate this result. VI determined separately by CP and FOV were occasionally well-related, but this relationship was

inconsistent between species, further supporting the conclusion in the previous study that CP and FOV are not interchangeable. These techniques should either be used as compliments or independently, depending on the application.

CHAPTER 4: ASSESSING THE USE OF REFLECTANCE SPECTROSCOPY IN DETERMINING CESIUM CHLORIDE STRESS IN THE MODEL SPECIES *ARABIDOPSIS THALIANA*[*]

1. Introduction

1.1. Background

When light interacts with a material, some may be reflected back depending on the wavelength of light and the properties of the material. Reflectance spectroscopy, the collection and analysis of reflectance spectra, provides a quick, non-destructive analytical technique that has found use in numerous fields (Burns, ed. 2001; Pasquini 2003). Fresh plant reflectance in the visible region (400 to 700 nm) of the electromagnetic spectrum is associated with composition, amount, and distribution of pigments. Plant reflectance in the near infrared region (700 to 1300 nm) is associated with leaf structure, and within the mid-infrared region (1300 to 2500 nm) reflectance is associated with water content (Gates et al. 1965; Knipling 1970; Van der Meer and de Jong 2006). Figure 4.1 shows typical green plant reflectance spectra from 400 nm to 2500 nm, with dominant features and regions of the electromagnetic spectrum labelled.

[*] Martinez, N.E., T.E. Johnson, W.W. Kuhne, C.T. Stafford, M.C. Duff. 2014. Assessing the use of reflectance spectroscopy in determining CsCl stress in the model species *Arabidopsis thaliana.* International Journal of Remote Sensing. Submitted: 21Dec13. Accepted with revisions.

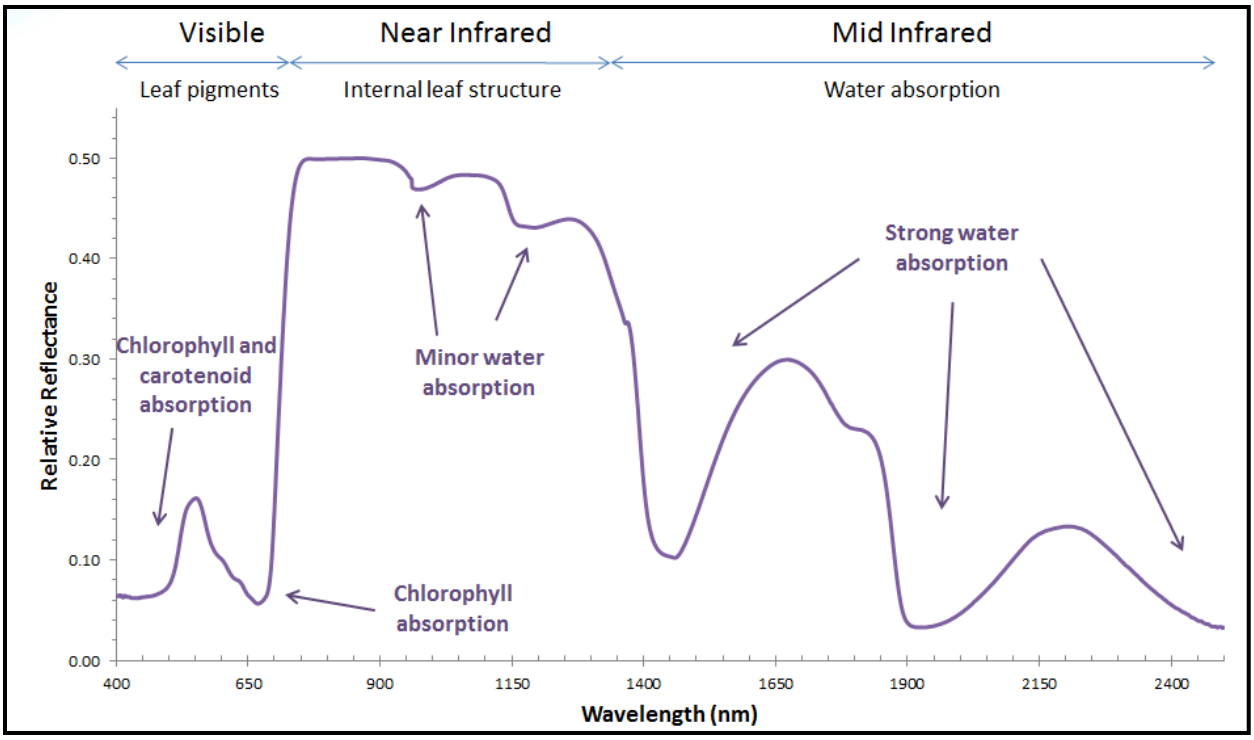

Figure 4.1: Spectral regions and corresponding dominant feature (adapted from Knipling 1970).

Shifts in infrared reflectance of leaves in response to disease, senescence, or stress can vary; at times reflectance will decrease and other times increase, depending on the situation (Van der Meer and de Jong, eds. 2006). Numerous studies have been conducted to qualitatively and/or quantitatively relate reflectance intensity at the leaf, whole plant, or canopy scale to various plant characteristics and conditions (Card et al. 1988; Carter 1993; Carter and Knapp 2001; Curran et al. 1992; Horler et al. 1983; Knapp and Carter 1998; Knipling 1970; Gamon et al. 1992; Gates et al. 1965; Gausman et al. 1970; Gitelson et al. 2009; Grzesiak et al. 2010; Ourcival et al. 1999; Peng and Gitelson 2012; Pinder and McLeod 1999; Serbin et al. 2012; Serrano 2008; Shull 1929; Sims and Gamon 2002; Slaton et al. 2001; Viña et al. 2011; Wang and Pingheng 2012; Woodhouse et al. 1994; Yoder and Pettigrew-Crosby 1995; among others), and among the applications of remote sensing is the early detection of plant stress (Peñuelas and Filella 1998). Changes in reflectance due to stress have already been demonstrated to occur before damage is visible (e.g. Chaerle and Van Der Stragen 2000; Milton et al. 1989). Although imaging is a powerful technique for visualizing, diagnosing, and quantifying plant stresses, many

different stressors have similar intermediate responses that may be indistinguishable (Jones and Schofield 2008).

The purpose of this study was to determine whether a quantifiable relationship exists between caesium (Cs) contamination in *Arabidopsis thaliana* and reflectance spectra through the utilization of vegetation indices (VI). VI are mathematical combinations of different reflectance spectral bands that attempt to provide semi-analytical measures of vegetation activity. Reflectance spectra were collected at multiple time points because VI may provide better indication of temporal trends in plant status than precise conditions of a plant at a single arbitrary point in time (Berger et al. 2010; Lichtenthaler et al. 1998; Viña et al. 2011; Van der Meer and de Jong 2006; Wang and Pingheng 2012). VI may be related to one or more properties of a set of samples (e.g. relative water content or chlorophyll content). Therefore, treatment response variables that can be related back to the reflectance spectra need to be utilized (Agelet and Hurburgh 2010).

1.2. Related Studies

Numerous studies have shown that there are shifts in plant reflectance spectra due to metal stress (or simulated metal stress) (Bandaru 2010; Collins et al. 1983; Davids and Tyler 2003; Dunaganet al. 2007; Horler et al. 1980; Kooistra et al. 2004; Maruthi-Sridar et al. 2007a, 2007b, 2011; Milton et al. 1989, 1991; Schwaller et al. 1981; Su et al. 2007; Woodhouse et al. 1994).

Schwaller et al. (1981) investigated the reflectance of greenhouse grown sugar maple leaves when treated with anomalous amounts of heavy metals (copper (Cu) and manganese (Mn) in the rooting medium and saw an general increased reflectance in treated plants over 475 to 1650 nm (entire range considered).

Milton et al. (1989) demonstrated the possibility of identifying spectral reflectance changes in individual plants growing in high concentrations of arsenic (As) or selenium (Se). However, changes in spectral reflectance seem to correlate well with soil metal concentrations, but not with plant metal

concentrations, so a follow-up experiment was conducted with phosphorus (P) deficiency (Milton et al. 1991). This was to assess the hypothesis of an indirect effect of metals (related to nutrient status) on plant reflectance, and in fact, P deficiency was found to produce spectral and morphological changes similar to those observed in metal-dosed plants.

Woodhouse et al. (1994) briefly considered reflectance spectroscopy to detect various stresses (Cu and zinc (Zn) treatments, nutrient deficiencies, and water stress) in hydroponically grown lettuce and wheat (Controlled Ecological Life Support System type crops) and concluded that this technique has potential for the assessment of plant health.

Maruthi-Sridhar et al. (2007a) investigated As and chromium (Cr) accumulation in potted Chinese brake fern in a laboratory setting and found that there were significant structural and spectral changes in Cr treated plants, but only minimal changes in As treated plants, although Bandaru (2010) did see a strong correlation between leaf As concentration and leaf structural changes in hydroponically grown spinach plants. Maruthi-Sridhar et al. (2007b) considered the effect of Zn and cadmium (Cd) on potted barley plants in order to look for spectral signatures that indicate the impact and content of heavy metals in the leaves and canopies of living plants during the process of phytoremediation. There were morphological and spectral changes for both treatments, although more significant changes in Zn treated plants.

Dunagan et al. (2007) found some correlations between spectral characteristics of mustard spinach plant leaves and foliar mercury (Hg) content.

Collins et al. (1983), Maruthi-Sridhar et al. (2011), and Kooistra et al. (2004) used remote sensing reflectance spectroscopy to assess vegetation effects as indirect indicators of soil chemical characteristics. Collins et al. (1983) utilized an airborne spectroradiometer to collect spectra from a known forest-covered Cu soil anomaly, which revealed spectral changes that were repeatable in a laboratory setting. Maruthi-Sridhar et al. (2011) used both airborne (field study) and handheld

(greenhouse study) spectroradiometers to assess the accumulation of various heavy metals in soybeans, as related to biosolid surface amended soils. Kooistra et al. (2004) investigated the relation between vegetation reflectance and elevated concentrations of Ni, Cd, Cu, Zn, and lead (Pb) in river floodplain soils. The results of these studies indicate the potential of remote sensing to contribute to the survey of elevated metal concentrations using the spectral response of vegetation as an indicator.

Two reflectance spectroscopy studies consider Cs contaminated plants. Davids and Tyler (2003) reported that Cs and strontium (Sr) contamination within the Chernobyl exclusion zone has a measurable effect on the spectral characteristics of silver birch (*Betula pendula*) and Scots pine (*Pinus sylvestris L.*), and demonstrated the potential of remote reflectance spectroscopy to assess the ecological impact of radionuclide contamination. Su et al. (2007) also evaluated accumulation of Cs and Sr, by Indian mustard (*Brassica juncea*), and found morphological changes for Cs treated plants was associated with a shift in the reflectance spectra.

1.3. Cs toxicity in *Arabidopsis thaliana*

Arabidopsis thaliana is a member of the mustard family that is closely related to various crop plants. It has been the subject of intense study over the past several decades and is considered to be a model organism and ideal for use in the laboratory setting for biological research (NSF 2013).

Cs is a group I element that exists in nature as a +1 charged cation, and its behavior in soils resembles that of potassium (K) (White et al. 2003; Zhu and Smolders 2000; White and Broadley 2000). Whereas K is an essential macronutrient (Hampton et al. 2004), Cs has no known nutritional role in plant physiology (White and Broadley 2000; White et al. 2003) and at excessive levels can become an abiotic oxidative stress factor (Hampton et al. 2004; Sahr et al. 2005; White and Broadley 2000; White et al. 2003). Cs^+ competes with K^+ for binding sites in proteins, and will also inhibit the potassium-induced cellular activities associated with plant nutrition (Hampton et al. 2004). The most notable effects of Cs toxicity include reduced growth and photosynthesis (Hampton et al. 2004; Sahr et al. 2005), and at

higher concentrations, necrotic leaf areas have been seen (Sahr et al. 2005). Understanding the behavior and effects of Cs on plants is important for determination of potential remediation strategies for radiocaesium contamination. Cs enters the terrestrial food chain through plants (Broadly and Willey 1997; Hampton et al. 2004), and can become a concern from a human health standpoint regarding at least two radioisotopes: ^{134}Cs and ^{137}Cs as they emit beta and strong gamma radiation (ICRP 2008). These isotopes have been released to the environment through the manufacturing and testing of nuclear weapons as well as purposeful or accidental releases from nuclear power plants (Hampton et al. 2004; White and Broadley 2000). Cesium-133 will behave identically to radiocesium chemically, and we consider stable cesium here to avoid unnecessary radiation dose to persons involved in the study, as recommended by the ICRP (ICRP 2007).

Reflectance spectra was collected weekly for three weeks in a laboratory setting of twice-weekly CsCl treated (0 mM, 0.5 mM, and 5 mM) *A. thaliana*. Fourteen VI were considered for this data set, and two-way ANOVAs were conducted for each based on treatment level, week, and the interaction between the two. Two-way ANOVAs were conducted similarly for available endpoints: relative water content (RWC), chlorophyll content, and three factors based on visual assessment. Boxplots are also presented for selected endpoints. One-way ANOVAs were performed on selected VI at each time point to determine which, if any, indices offered a significant prediction of the overall extent of Cs toxicity. Additionally, correlation coefficients and regression were used to relate appropriate indices to available endpoints as well as to compare the same VI by collection method (contact probe [CP] as well as high and low field of view [FOV]).

1.4. Consideration of chloride effects

CsCl has been used previously to consider Cs uptake and stress (Broadley et al. 2001; Kanter et al. 2010; Le Lay et al. 2006; Qi et al. 2008), and although chlorine (Cl) is an essential micronutrient for higher plants, at high plant tissue concentrations Cl can be toxic (White and Broadley 2001). However,

three weeks after germination on media supplemented with different concentrations of sodium chloride (NaCl), Boyko et al. (2010) only saw phenotypic differences in *A. thaliana* plants at concentrations >75 mM NaCl. Effects were attributed primarily to Cl, as experiments were repeated with different salts (NaCl, $MgCl_2$, Na_2SO_4, and $MgSO_4$) to control for the effect of each element. Additionally, Suter and Widmer (2013) saw no major effects on plant fitness below 25 mM NaCl for four different genotypes of *A. thaliana* plants grown in soil and watered once a week with varying concentrations of NaCl. Because the concentrations used in this study are an order of magnitude below concentrations shown to have phenotypic effects on *A. thaliana,* the contribution of Cl to the effects seen here is considered negligible.

2. Materials and methods

2.1. Plant growth and treatment

The soil mix used was four parts PGX (Promix PGX, Premier Horticulture Inc., Quakertown, PA) and 1 part Perlite (Hoffman Horticultural Perlite, Good Earth, Lancaster, NY). Soil was mixed and placed in square plastic grow pots (10.8 × 10.8 × 12.7 cm, Kordlok SQL0450 from ITML Horticultural Products, Myers Industries Inc., Akron, OH) with perforated bottoms to allow water seepage; soil was hydrated by placing pots by multiples of twelve in a Nalgene tray (Thermo Scientific, Wilmington, DE) with 3-5 cm deep deionized water. Water level was maintained for at least three days to allow the soil to absorb sufficient moisture for planting.

A. thaliana seeds (*Arabidopsis thaliana*, WT-02-41-01 Columbia [alias Col-0] Wildtype, LEHLE Seeds, Round Rock, TX) were removed from 4°C storage, soaked in 1/32 strength hydroponic (HP) media solution, and exposed to red light for 30 minutes to synchronize germination. Hydroponic media was made with DI water, 1/32 strength Murashige and Skoog basal medium (137.5 mg L^{-1}) (Sigma-Aldrich Cat No M5519, St. Louis MO), and 250 mg L^{-1} MES hydrate (Sigma-Aldrich Cat No M2933), using KOH to pH balance to 5.7. Seeds were subsequently pipetted into a 96 well tray (five seeds per well) to verify number of seeds planted. Seeds were then pipetted from the tray onto potted soil as three sets of five

seeds per pot, i.e. 15 seeds per pot, to ensure adequate germination. Following the sowing of the seeds, the 1/32 HP media was further diluted to 1/64 strength for subsequent treatment.

After planting, arbitrary sets of 6 pots each were transferred to Sterlite tubs (40 × 31.75 × 15.24 cm, Target Corp., Minneapolis, MN). Tubs were placed in rows of up to four on growth shelves, 42 cm beneath growth lights (Four Philips F32T8 TL741 700 series 32W ALTO II Fluorescent bulbs, cat. No. 0002904, Philips North America Corporation, Andover, MA). Plants were on a nine hour light : 15 hour dark cycle under ambient laboratory environmental conditions.

The bottoms of the pots were submerged in approximately 3 cm distilled water until the plants reached a previously determined treatment date (i.e. day 37 post-planting, rosettes ~30 mm in diameter). *A. thaliana* the seedling stage, plants were culled to three per pot, based on size and appearance of health, such that one plant per group remained.

Immediately prior to CsCl treatment, pots were rearranged between nine tubs (6 pots each, no longer submerged in DI water) such that each tub, now serving as a treatment group, had similar size and quality plants. Spike solution was evenly applied to the top of each pot as 100 mL (25 mL delivered to each quadrant) of the appropriate concentration of CsCl (0.5 mM CsCl or 5 mM CsCl) in 1/64 strength HP media twice weekly, with control plants receiving 100 mL 1/64 HP media only. Two pots were randomly selected from each treatment group for weekly spectra collection and harvest. After each application of hydroponic media, the plants were rotated within the tubs and the tubs were rearranged among the growth shelves to account for potential variation in lighting or other environmental conditions. Figure 4.2 shows an example of a growth shelf.

Figure 4.2: Example growth shelf; A. thaliana plants in treatment (here in three red tubs on the left hand side) or control (here in the single black tub on the far right) tubs prior to week 3 spectra collection.

2.2. Equipment, setup, and collection of spectra

Reflectance spectra were collected using a FieldSpec Pro (FSP 350-2500P; Analytical Spectral Devices (ASD), Boulder, CO) which is a full range (350 nm – 2500 nm) portable spectroradiometer (with sampling intervals/spectral resolutions of 1.4 nm/3 nm and 2 nm/10 nm for 350-1000 nm and 1000-2500 nm respectively) (ASD 2002). CP spectra were collected using a leaf clip attachment (Figure 4.3) on individual leaves.

Figure 4.3: Contact probe with leaf clip, demonstrating both white and black backgrounds.

The CP provides light (3.825 V, 4.05 W low intensity bulb) and collects reflectance spectra. The leaf clip attachment has both a white (for white reference) and black (to minimize back scatter)

background. Triplicate CP spectra were collected on one leaf from each of typically three separate plants per pot.

FOV spectra were collected using an 8° probe (i.e. a viewing angle of 8°) at two height settings (referred to as "high" and "low"). Incident light was provided by two halogen lamps (Pro Lamp, 14.5 V, 50W, P/N 145378, ASD, Boulder, CO) angled at 30 degrees from horizontal. The lights were 180° apart at 30.5 cm from the center of pot on the horizontal and 76.2 cm (high) or 59 cm (low) above the table surface. The fore optics probe was centered between the lights at 66.7 cm (high) or 36.8 cm (low) above the plane of the pot surface (Figure 4.4 and Figure 4.5).

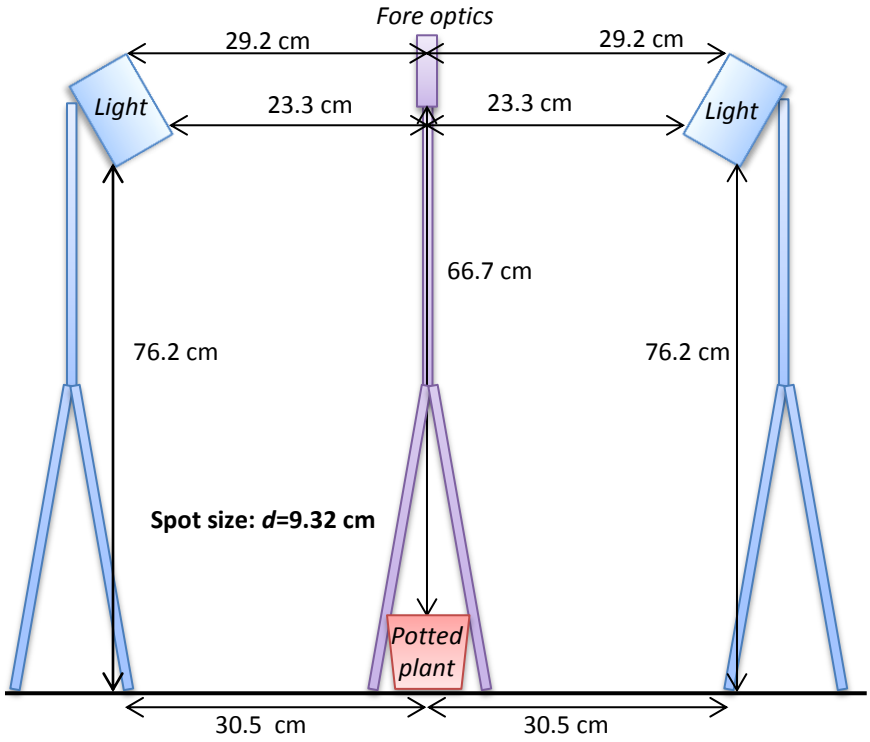

Figure 4.4: Equipment set up: "high" field of view.

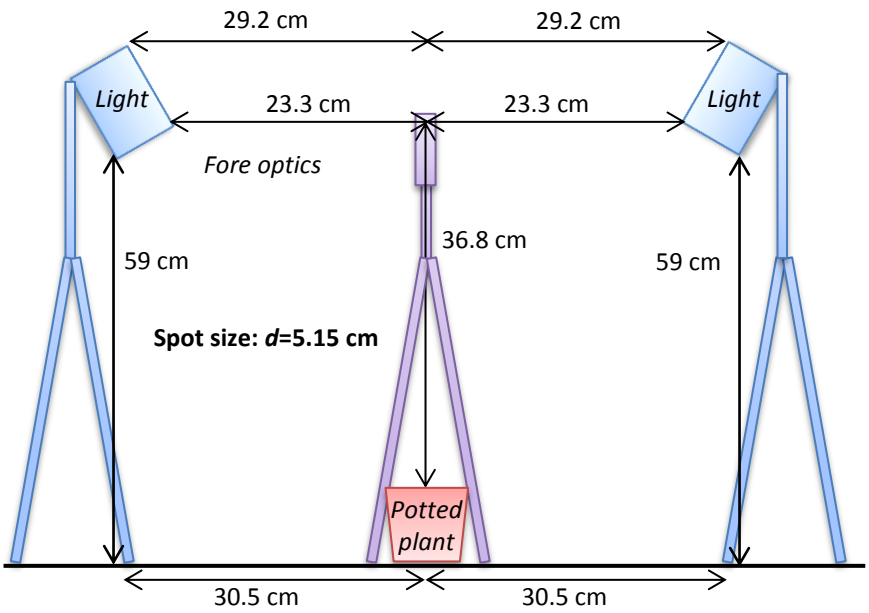

Figure 4.5: Equipment set up: "low" field of view.

The high (HFOV) and low (LFOV) set ups had spot size diameters of 9.32 cm and 5.15 cm respectively. Reflective surfaces were covered with absorbent material to minimize noise and thus variability in spectra, and dark room conditions were approximated by surrounding the lights and fore optics with a black felt canopy (Figure 4.6).

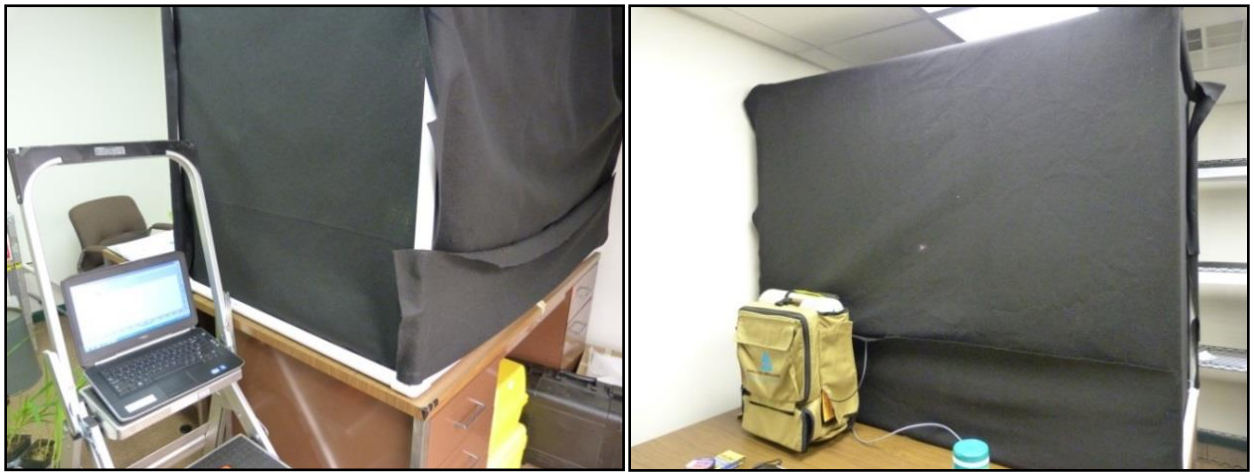

Figure 4.6: Front and rear of "dark room" set up.

Tripod surfaces were also wrapped in black felt. The white reference was a calibrated Spectralon (25.4 × 25.4 cm, LabSphere, North Sutton, NH) panel of 99% reflectance that was elevated to

a height equivalent to a grow pot. Grow pots were placed on black paper plates when collecting spectra and the table top was lined with a light-absorbent black rubber. Four spectra, each collected at a different arbitrary rotation of the pot to get an overall assessment of the reflectance of the sample, were saved for each FOV session. FOV spectra were always acquired prior to CP because it is possible for the CP to injure the plant and therefore affect subsequent FOV readings.

2.3. Collection of physical measures

2.3.1. Relative water content

As metal stress is known to mimic drought stress (Thenkabail et al. 2012), plants were harvested after spectra collection each week to determine relative water content and chlorophyll content. To determine relative water content, sufficient leaves were removed to obtain between 1000 and 2000 mg of fresh mass for each replicate (i.e. pot). Samples were placed in weigh boats, fresh mass was obtained, samples were dried to a constant mass, and dry mass was obtained. A sample's relative water content was then expressed as Equation 4-1:

$$\mathrm{RWC} = 1 - \frac{\text{dry mass}}{\text{fresh mass}} \tag{4-1}$$

2.3.2. Chlorophyll content

The concentrations of chlorophyll *a* (Chl *a*) and chlorophyll *b* (Chl *b*) were determined for each replicate (i.e. pot) (Knudson et al. 1977; Li et al. 2009; Papista et al. 2002). Four circular leaf subsamples were collected from representative leaves of the plants in a pot using a #3 cork borer (Fisher Scientific, Pittsburgh, PA). Leaf samples were stored in the dark at 4°C in capped 20 mL vials (KG-33 borosilicate glass; Kimble Chase, Vineland, New Jersey) containing 2 mL 100% ethanol for three days (at which point disks were white) before absorbance (*A*) at 665 nm, 649 nm, 629 nm, and 696 nm, with an offset at 750 nm, was determined for 1.5 mL subsamples for each vial using a NanoDrop 2000c UV-Vis spectrophotometer (Thermo Scientific, Wilmington, DE). Disposable methacrylate cuvettes with

transmission from 300 to 800 nm > 80% were used with the 1.5 mL subsample (Cole Palmer, Vernon Hills, Illinois). Chlorophyll content was determined using appropriate, previously published equations (Ritchie 2006; Equation 4-2 and Equation 4-3):

$$\text{Chl } a \ (\mu\text{g/mL}) = -5.2007 \cdot A_{649} + 13.5275 \cdot A_{665} \tag{4-2}$$

$$\text{Chl } b \ (\mu\text{g/mL}) = 22.4327 \cdot A_{649} - 7.0741 \cdot A_{665} \tag{4-3}$$

2.3.3. Visual assessment

A visual assessment of the proportion of a plot covered by any plant material and any existing chlorotic plant material was performed by overlaying an 8 × 8 (13.5 × 13.5 mm) grid on a computer display of top-down photos of each treatment group at each of three time points, forming 64 squares with 81 evenly-spaced points (grid intersections). Photographs were taken immediately prior to spectra collection, directly above each six-pot treatment group in the same manner each week. However, to account for any potential change in magnification or alignment, gridlines were laid based on pot dimensions, which were definitively consistent. Using the grid intersections, three additional endpoints were defined:

- Coarse Leaf Area Index (CLAI) provides an approximate indication of how much of the pot surface is covered by plant material.

$$\text{CLAI} = \frac{\text{Number of points on leaf material}}{\text{Total number of points}} \tag{4-4}$$

- Green Factor (GF) provides an approximate indication of the proportion of pot surface that is covered with green plant material.

$$\text{GF} = \frac{\left(\text{Number of points on leaf material}\right) - \left(\text{Number of points on leaf with visible chlorosis}\right)}{\text{Total number of points}} \tag{4-5}$$

- Chlorosis Factor (CF) provides an approximate indication of the proportion of plant material that has visible chlorosis.

$$CF = \frac{\text{Number of points on leaf with visible chlorosis}}{\text{Total number of points}} \quad (4\text{-}6)$$

2.4. Data analysis

Fourteen VI (Table 4.1) are considered for applicable spectra acquisition technique(s) (i.e. FOV and/or CP), including indices from the literature as well as indices selected by the authors through scientific judgment and visual consideration of spectra.

Table 4.1: List of vegetation indices considered, including name and abbreviation if applicable, the relevant acquisition technique(s), formulation, and either potential predictive characteristics along with the corresponding reference or indication that the listed index is newly considered by the authors.

Abbreviation/Name		Relevant acquisition technique	Formulation	Potential indicator of:	Reference
NORMALIZED DIFFERENCES					
NDVI	Non-destructive vegetation index	FOV	$\frac{R_{800}-R_{670}}{R_{800}+R_{670}}$	Green biomass; leaf area	Rouse et al. (1974)
PRI	Photochemical reflective index	FOV CP	$\frac{R_{531}-R_{570}}{R_{531}+R_{570}}$	Photosynthetic radiation-use efficiency	Gamon, Peñuelas, and Field (1992)
SIPI	Structural independent pigment index	FOV CP	$\frac{R_{800}-R_{445}}{R_{800}-R_{680}}$	Carotenoid to chlorophyll a ratio	Peñuelas, Baret, and Filella (1995)
PSND	Pigment specific normalized difference	FOV CP	$\frac{R_{800}-R_{680}}{R_{800}+R_{680}}$	Chlorophyll content	Serrano (2008)
SIMPLE RATIOS					
WI	Water index	FOV CP	$\frac{R_{900}}{R_{970}}$	Plant water content	Peñuelas et al. (1997)
--	--	FOV CP	$\frac{R_{750}}{R_{550}}$	Some correlation with metal content	Davids and Tyler (2003)
--	--	FOV CP	$\frac{R_{1110}}{R_{810}}$	Metal stress	Maruthi-Sridhar et al. (2007a)
--	--	FOV CP	$\frac{R_{725}}{R_{675}}$	Some correlation with chlorophyll content; appeared independent of soil moisture	Davids and Tyler (2003)
--	--	FOV CP	$\frac{R_{950}}{R_{750}}$	*Selected by author*	--
--	--	FOV CP	$\frac{R_{1390}}{R_{1454}}$	*Selected by author*	--
--	--	FOV CP	$\frac{R_{1676}}{R_{1933}}$	*Selected by author*	--

DERIVATIVE ANALYSIS					
YI	Yellowness index	FOV CP	$-0.1*\left(\frac{R_{580}-2R_{624}+R_{668}}{\Delta\lambda^2}\right)$	Chlorosis	Adams, Philpot, and Norvell (1999)
REP	Red edge position	FOV CP	Wavelength of inflection point from red to NIR	Chlorophyll content	Horler, Dockray, and Barber (1983)
SREP	Slope at red edge position	FOV CP	First derivative value at the red edge position	Chlorophyll content; leaf area index	Filella and Peñuelas (1994)

First, two-way ANOVAs were utilized to test whether means were significantly different by treatment level or week or interaction was present between the treatment level and week. Box plots by time and treatment level for relative water content, chlorophyll content, and visual assessment factors were generated. One-way ANOVAs on treatment level for each time point were used to determine how much variability was accounted for (R^2) by the selected VI at each week. Pearson correlation coefficients were calculated for each VI (calculated separately at each view) and the aforementioned endpoints. The highest (absolute value) correlation coefficients were used to determine VI for which to perform a linear regression. Linear regression was used to determine the applicability of the selected VI in predicting the corresponding endpoint, and was also used to compare spectra collection methods. Statistics were performed using Minitab version 16 (Minitab Inc., State College, PA).

3. Results

Photographs of each treatment group of plants are shown for each week in Figure 4.7, and reflectance spectra for each treatment group is are shown for each week in Figure 4.8.

Treatment group	Week		
	1	2	3
Control			
0.5 mM CsCl			
5 mM CsCl			

Figure 4.7: Pictures of samples by week and treatment group.

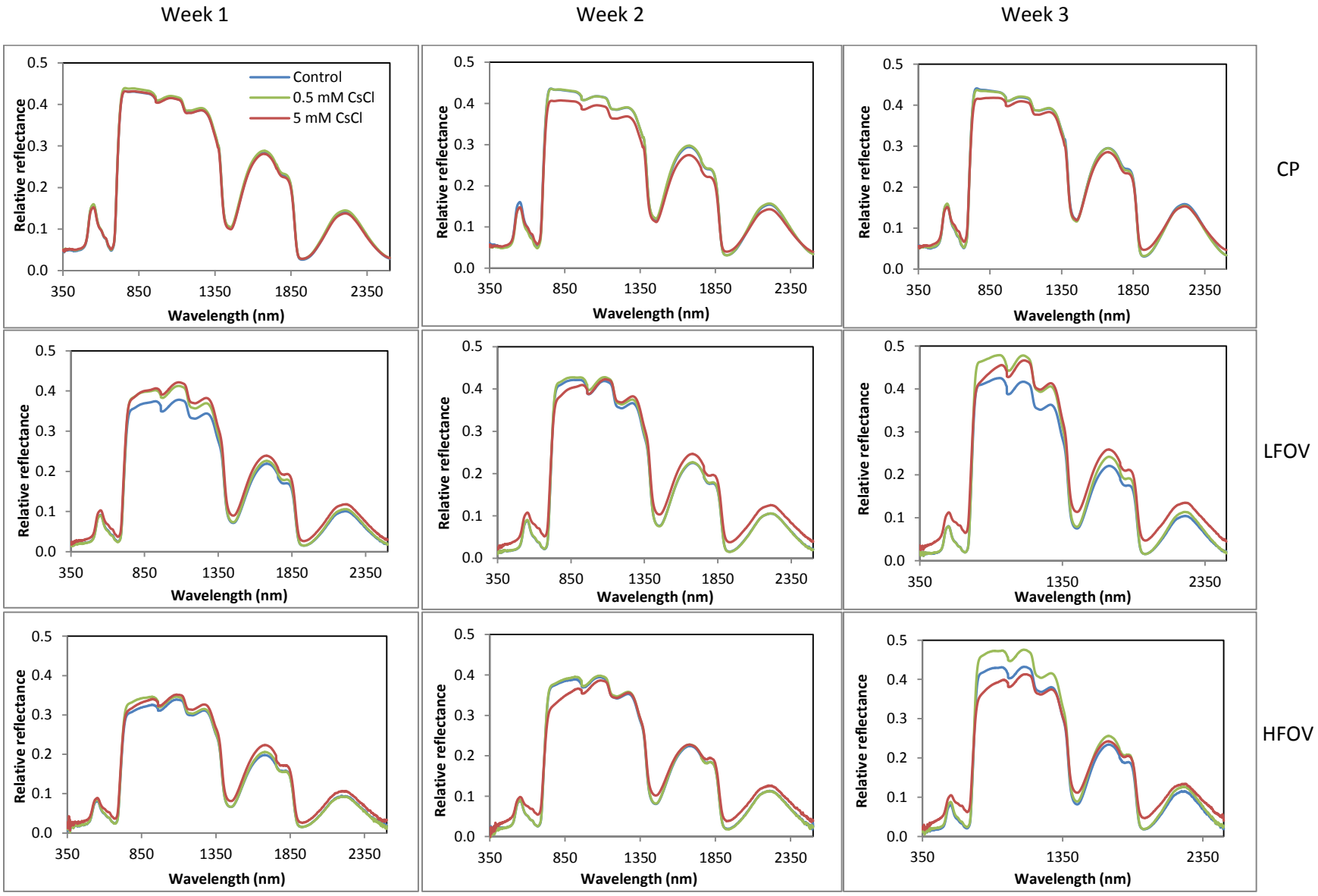

Figure 4.8: Reflectance spectra for Arabidopsis CsCl treatments, where red is 5 mM CsCl, green is 0.5 mM CsCl, and blue is the control.

Mean reflectance spectra relative to the control for weeks 1 and 3 are shown for each view in Figure 4.9 to visually demonstrate the temporal shift in reflectance by treatment level.

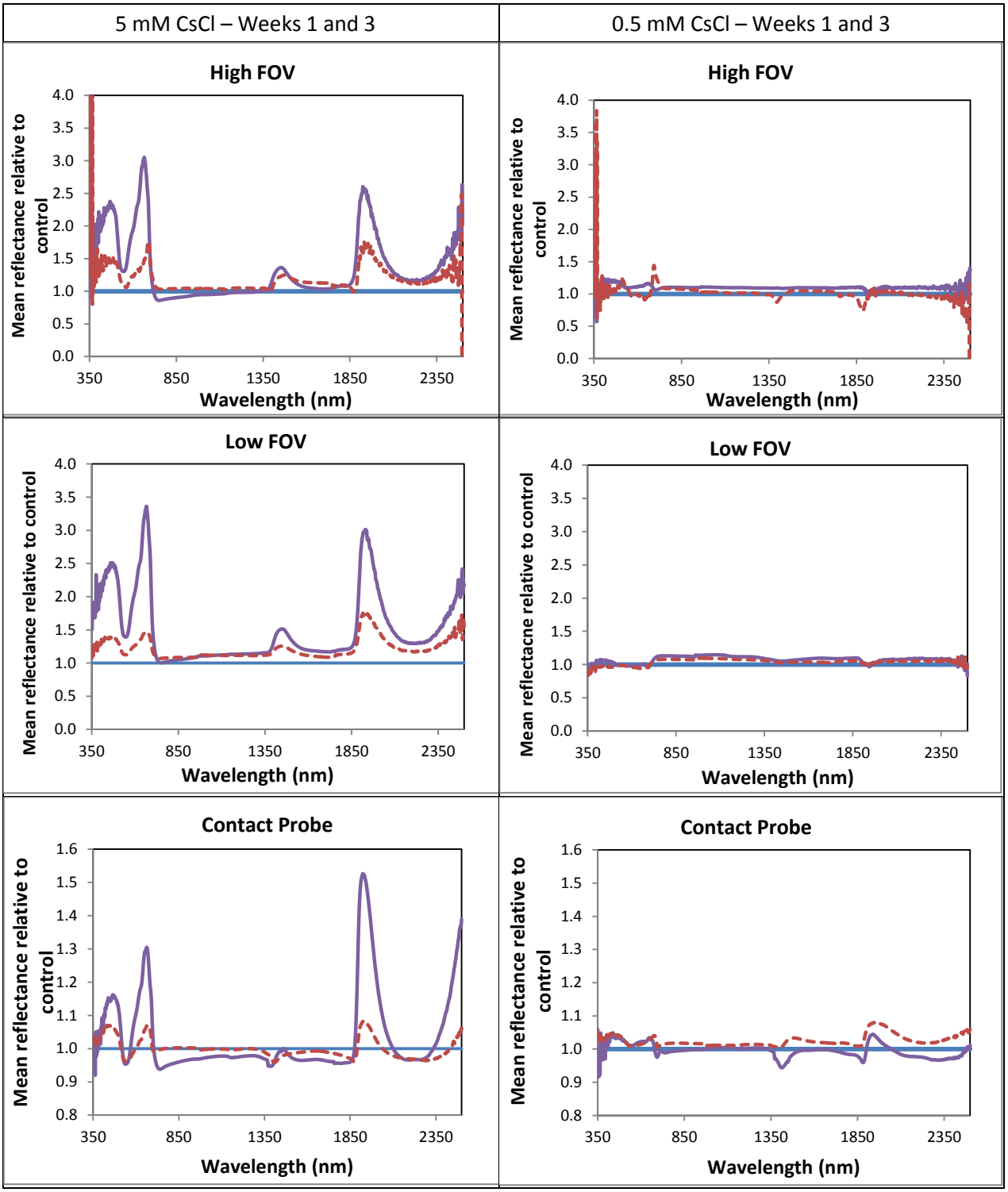

Figure 4.9: Mean reflectance spectra relative to control for 5 mM CsCl and 0.5 mM CsCl. Solid blue line represents the control, dashed red line represents week one, and solid purple line represents week 3.

Shifts are much more pronounced and consistent for the higher treatment level, indicating that the lower treatment level has little effect.

Table 4.2 contains P-values from the two-way ANOVAs conducted on fourteen different vegetation indices, which consider Cs toxicity in general rather than the specific symptoms.

Table 4.2: P-Values for Vegetation Index ANOVAs

	NDVI			PRI			WI		
	HFOV	LFOV	CP	HFOV	LFOV	CP	HFOV	LFOV	CP
Tmt Level	**<0.001**	**<0.001**	--	**<0.001**	**<0.001**	**<0.001**	**0.001**	**<0.001**	0.513
Week	0.403	0.844	--	**<0.001**	**0.049**	0.125	0.178	**0.003**	0.250
Interaction	**0.006**	**0.001**	--	**<0.001**	**<0.001**	**<0.001**	0.069	0.953	0.355

	SIPI			PSND			YI		
	HFOV	LFOV	CP	HFOV	LFOV	CP	HFOV	LFOV	CP
Tmt Level	**<0.001**	**<0.001**	**<0.001**	**<0.001**	**<0.001**	**<0.001**	**<0.001**	**<0.001**	**<0.001**
Week	0.455	0.085	**0.049**	0.286	**0.035**	**0.005**	**<0.001**	0.378	0.263
Interaction	0.095	**0.001**	**0.030**	**0.023**	**0.022**	0.111	**0.005**	**<0.001**	0.231

	R_{1110}/R_{810}			R_{950}/R_{750}			R_{750}/R_{550}		
	HFOV	LFOV	CP	HFOV	LFOV	CP	HFOV	LFOV	CP
Tmt Level	**<0.001**	**<0.001**	**<0.001**	**<0.001**	**<0.001**	**<0.001**	**<0.001**	**<0.001**	0.732
Week	0.108	0.213	**<0.001**	0.067	0.240	**0.003**	**<0.001**	**0.001**	0.597
Interaction	0.052	0.250	**0.001**	**0.023**	**0.036**	**<0.001**	**0.011**	**0.042**	0.345

	R_{1390}/R_{1454}			R_{1676}/R_{1933}			R_{725}/R_{675}		
	HFOV	LFOV	CP	HFOV	LFOV	CP	HFOV	LFOV	CP
Tmt Level	**<0.001**	**<0.001**	0.284	**<0.001**	**<0.001**	**<0.001**	**<0.001**	**<0.001**	**<0.001**
Week	**<0.001**	**0.001**	**<0.001**	**0.027**	**0.019**	**<0.001**	**0.002**	**0.038**	**0.001**
Interaction	**0.001**	0.060	0.790	**0.027**	**0.002**	0.067	**<0.001**	**<0.001**	0.076

	REP			Slope at REP		
	HFOV	LFOV	CP	HFOV	LFOV	CP
Tmt Level	**<0.001**	**0.001**	0.293	**<0.001**	**0.001**	**<0.001**
Week	**0.001**	**0.001**	0.436	**<0.001**	0.081	**<0.001**
Interaction	0.077	0.541	0.757	**0.036**	**0.036**	**0.015**

For those P-values less than our chosen confidence level (0.05), shown underlined and in bold, we reject the null hypothesis and conclude that there is a statistically significant difference between the

particular means (or that there is a statistically significant interaction between the factors considered). From these P-values we see that methods of spectra acquisition are not always consistent, especially between CP and FOV, and that all VIs have a least one element of significance, although the extent of significant differences vary between them.

R^2 values (listed as percentages) for one-way ANOVAs were plotted by week to determine if there was increase in explanation in variability in the particular vegetation index. In this manner a "critical index" indicative of the overall effect of Cs was determined, vice individual symptoms of Cs stress (e.g. reduction in water content), which can also be indicators of other stressors. Selected plots from this analysis are shown in Figure 4.10 through Figure 4.14.

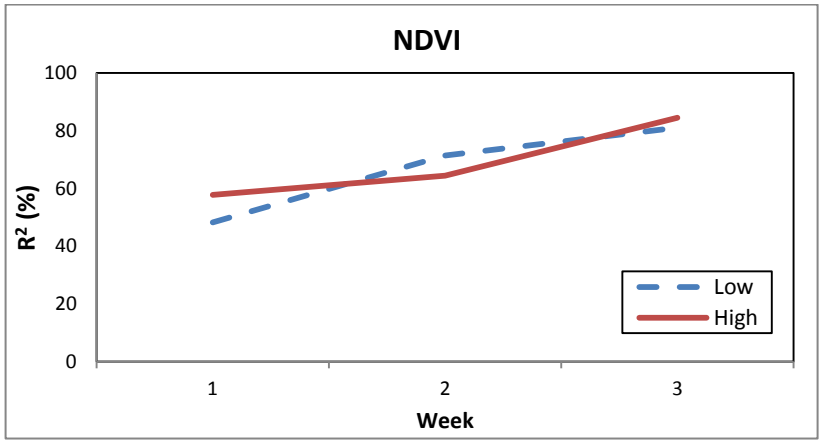

Figure 4.10: R^2 Values by week for NDVI one-way ANOVA.

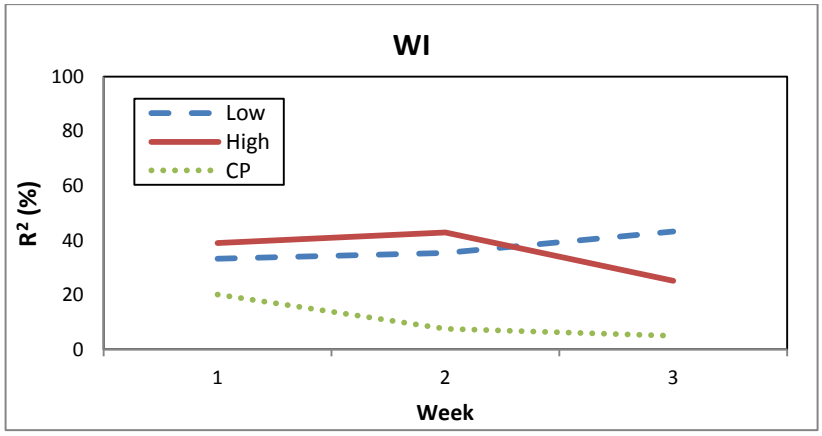

Figure 4.11: R^2 Values by week for NDVI one-way ANOVA.

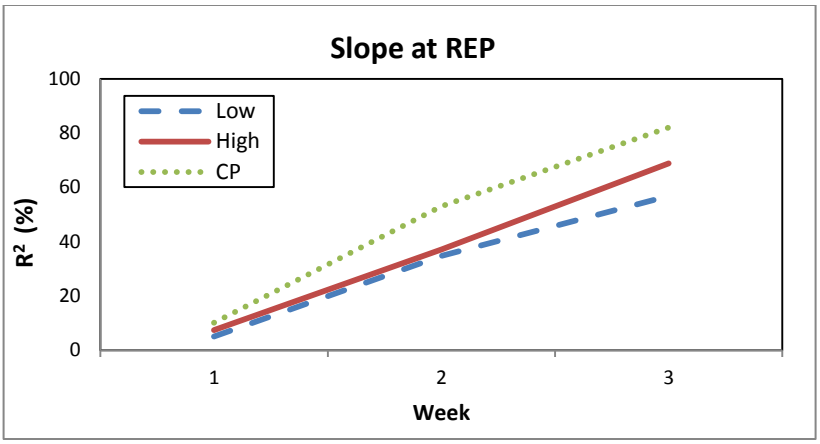

Figure 4.12: R^2 Values by week for NDVI one-way ANOVA.

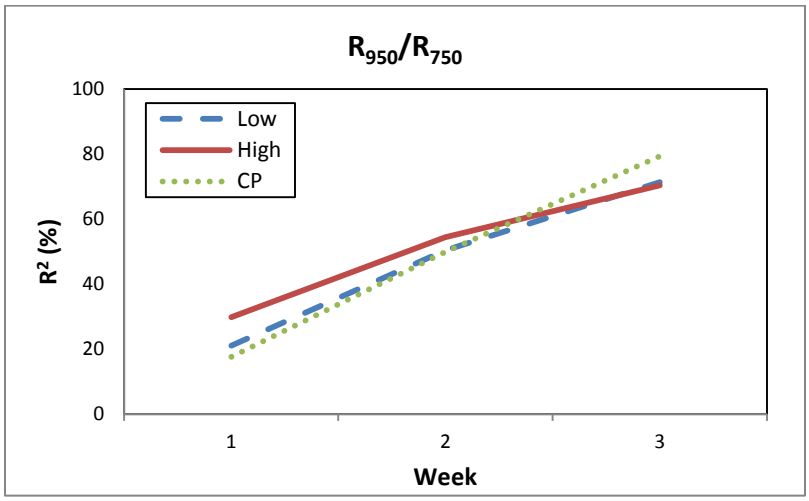

Figure 4.13: R^2 Values by week for NDVI one-way ANOVA.

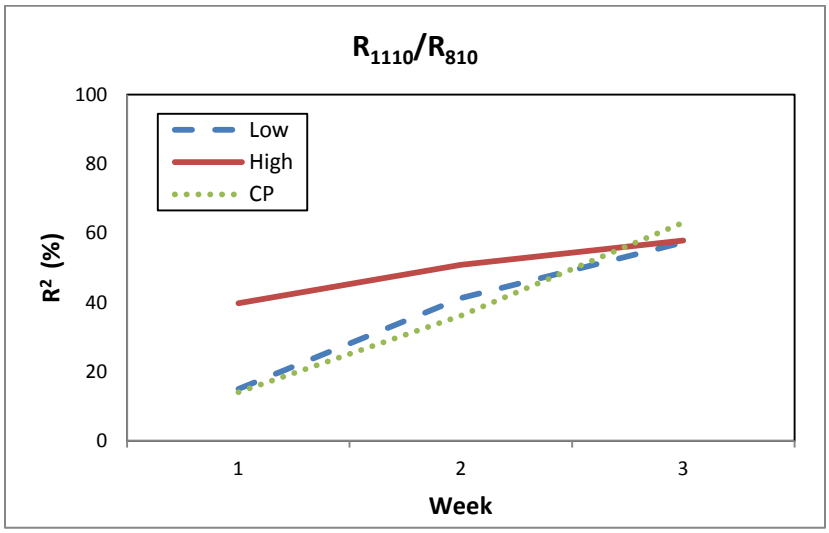

Figure 4.14: R^2 Values by week for NDVI one-way ANOVA.

NDVI, one of the most common VI (Thenkabail et al. 2012), is only slightly affected by an increase in Cs treatment. WI, another common VI, is not affected, even though relative water content does decrease by time and treatment (Figure 4.15).

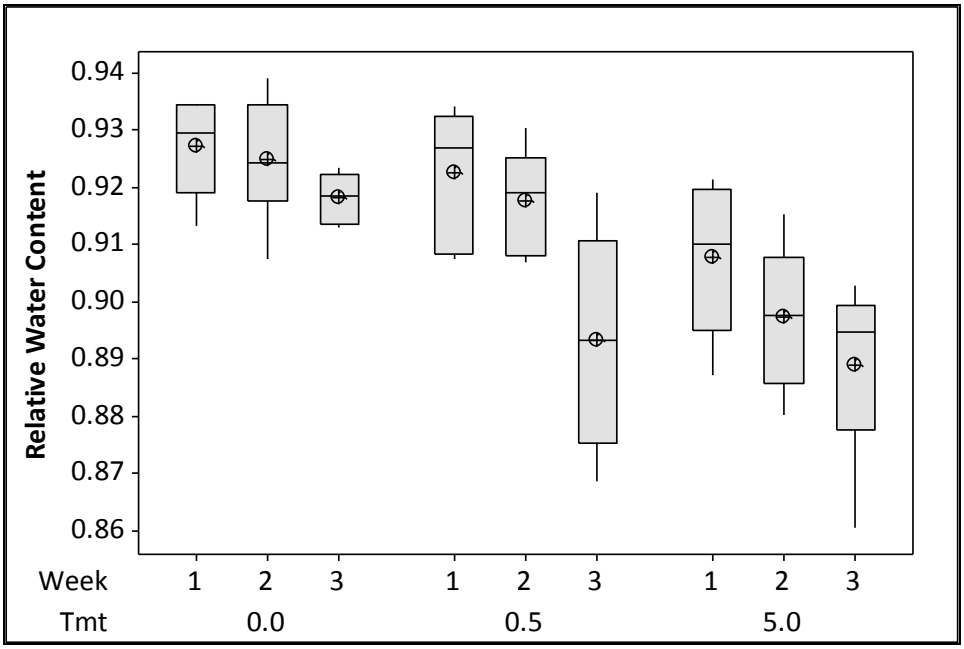

Figure 4.15: Boxplot of relative water content by week and treatment level.

SREP has a linear increase in R^2 values by week, and collection methods (i.e. CP and FOV) are consistent, with similar results for R_{950}/R_{750}, indicating that these indices may be good predictors of Cs toxicity. R_{1110}/R_{810}, which has previously shown to be metal sensitive, appears to not be as sensitive for Cs as it was for As (Maruthi-Sridhar et al. 2007a).

Boxplots of endpoints by treatment level and time are shown in Figure 4.15 (above) through Figure 4.19, and results (P-values) of two-way ANOVA for Cs symptom assessment are listed in Table 4.3 along with the relevant VI, determined by the largest Pearson correlation coefficient.

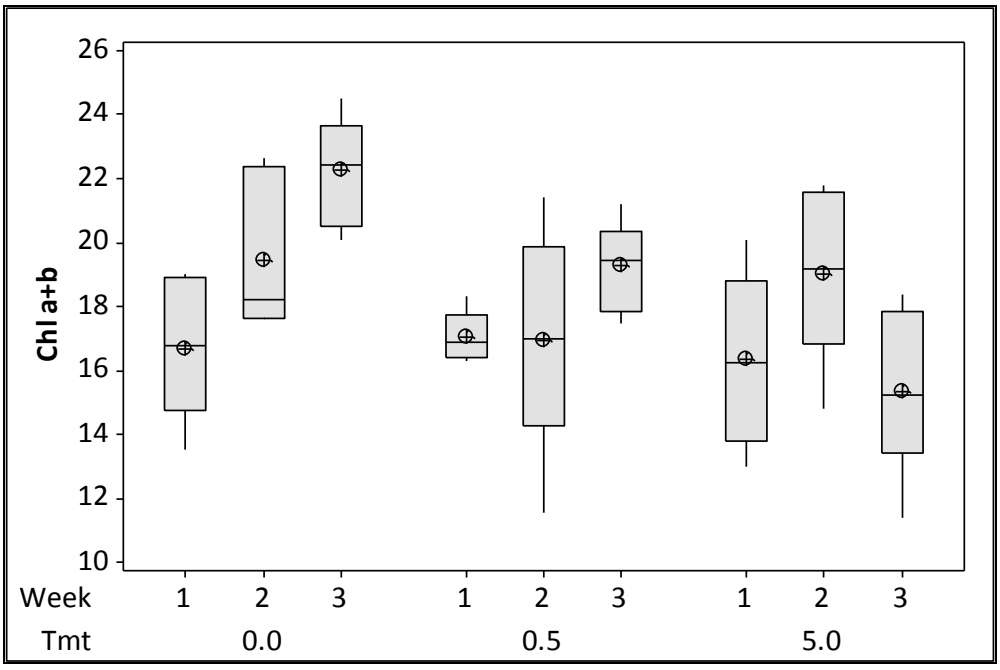

Figure 4.16: Boxplot of chlorophyll content by week and treatment level.

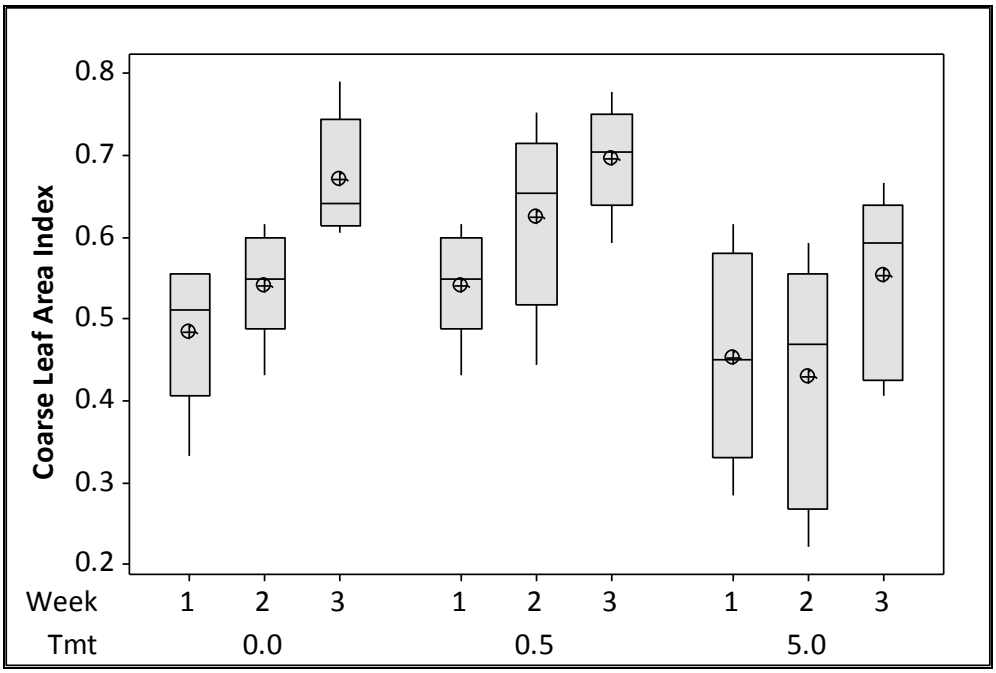

Figure 4.17: Boxplot of CLAI by week and treatment level.

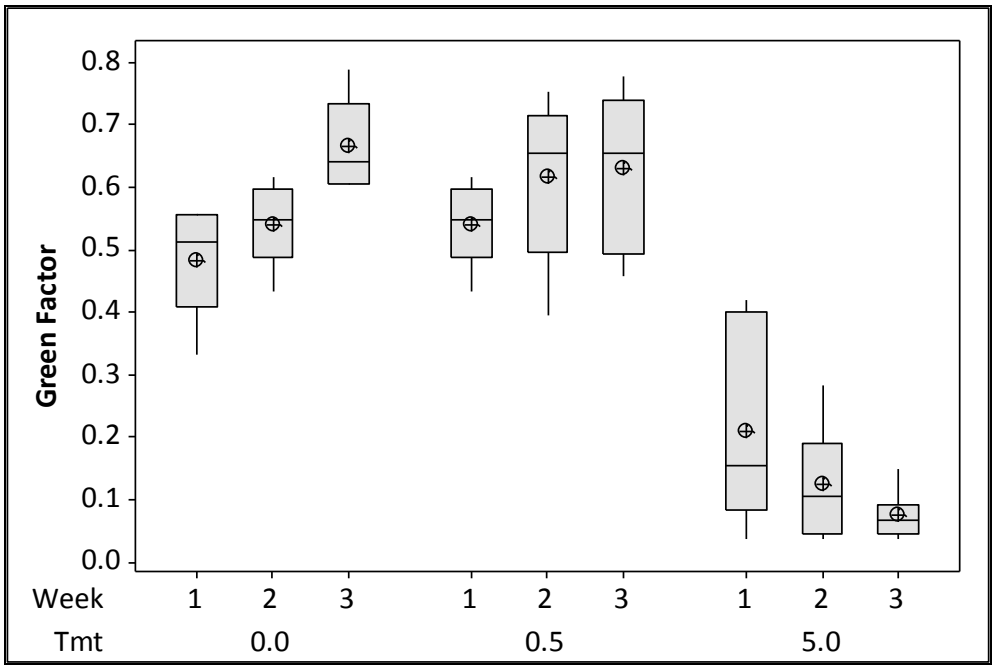

Figure 4.18: Boxplot of GF by week and treatment level.

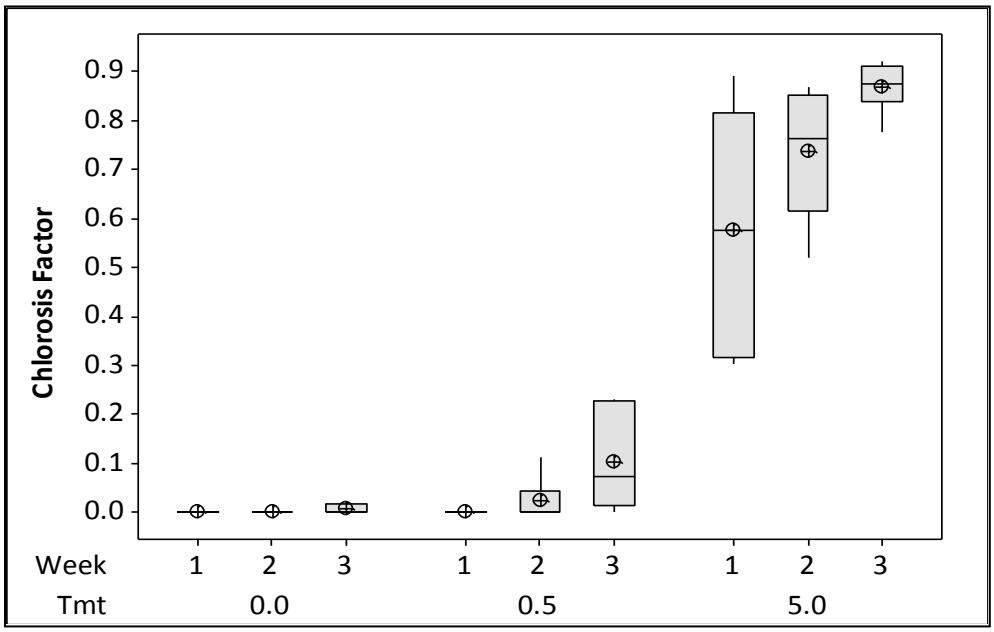

Figure 4.19: Boxplot of CF by week and treatment level.

Table 4.3: Results of endpoint analysis for CsCl exposure including (1) P-values from the two-way ANOVA, with significant values (<0.05) shown underlined and in bold and (2) relevant VI as determined by the largest Pearson correlation coefficient between the particular assessment factor and the VI listed in Table 1, considering all modes of spectra acquisition.

	RWC	Chl a+b	CLAI	GF	CF
Tmt Level	**<0.001**	**0.006**	**<0.001**	**<0.001**	**<0.001**
Week	**<0.001**	**0.014**	**<0.001**	0.403	**0.001**
Interaction	0.240	**0.002**	0.653	**0.006**	**0.020**
Relevant VI	R_{950}/R_{750}	REP	SREP	R_{1676}/R_{1933}	R_{1676}/R_{1933}

Details of the regressions results shown in Table 4.3 are presented in Appendix B1. Scatterplots of the linear regression of endpoint and relevant VI are shown in Figure 4.20 through Figure 4.24.

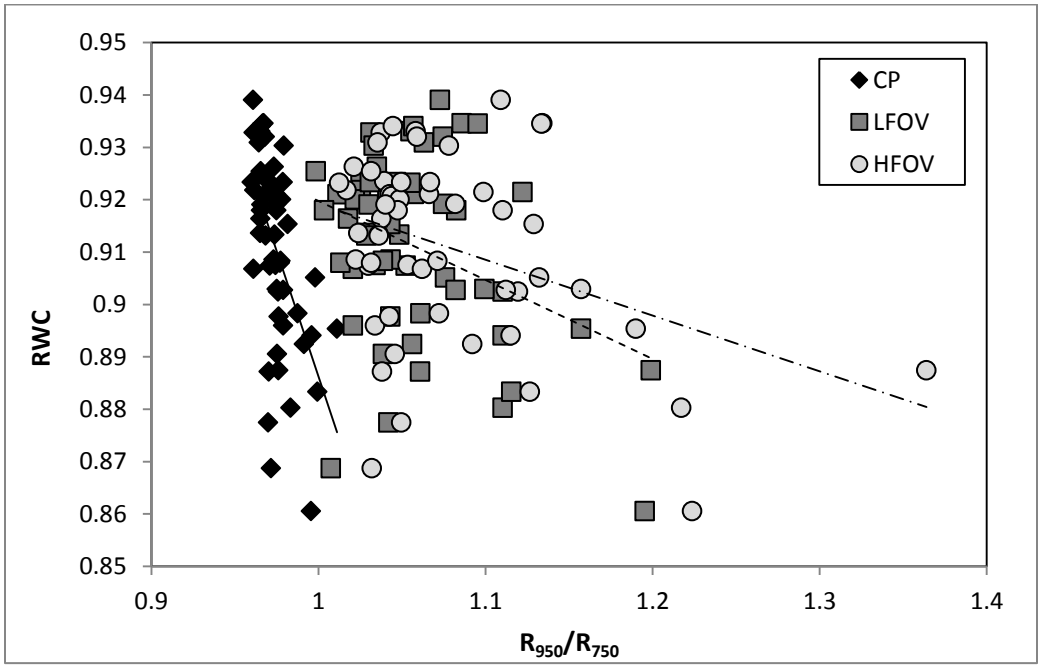

Figure 4.20: Scatterplot of RWC vs R_{950}/R_{750}.

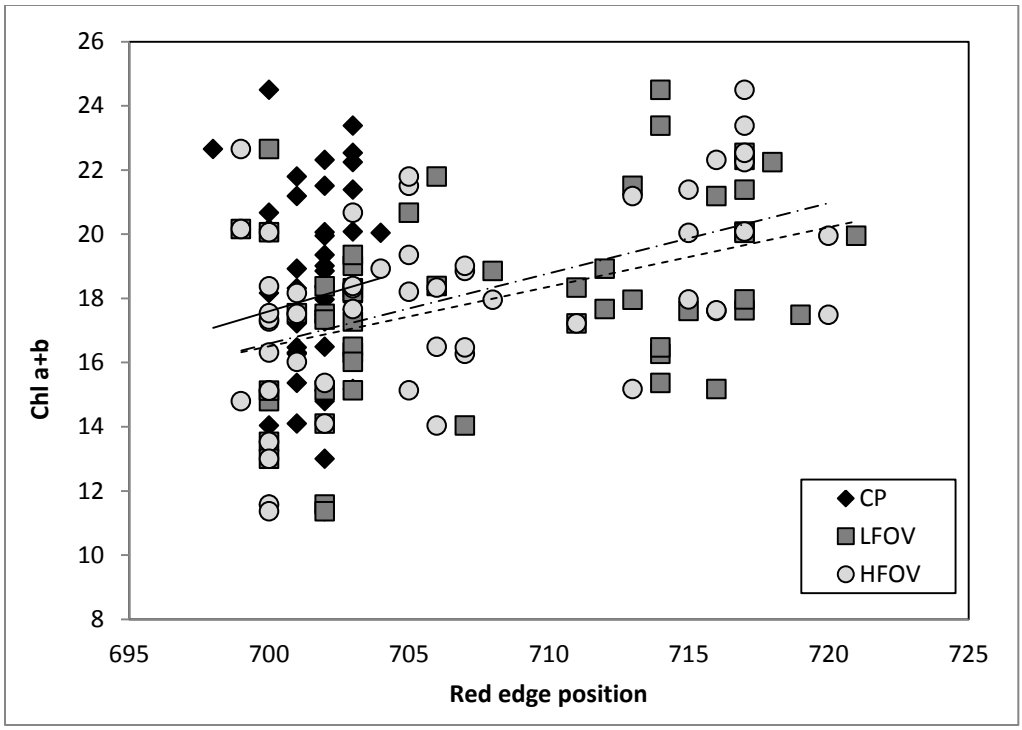

Figure 4.21: Scatterplot of Chlorophyll Content vs REP.

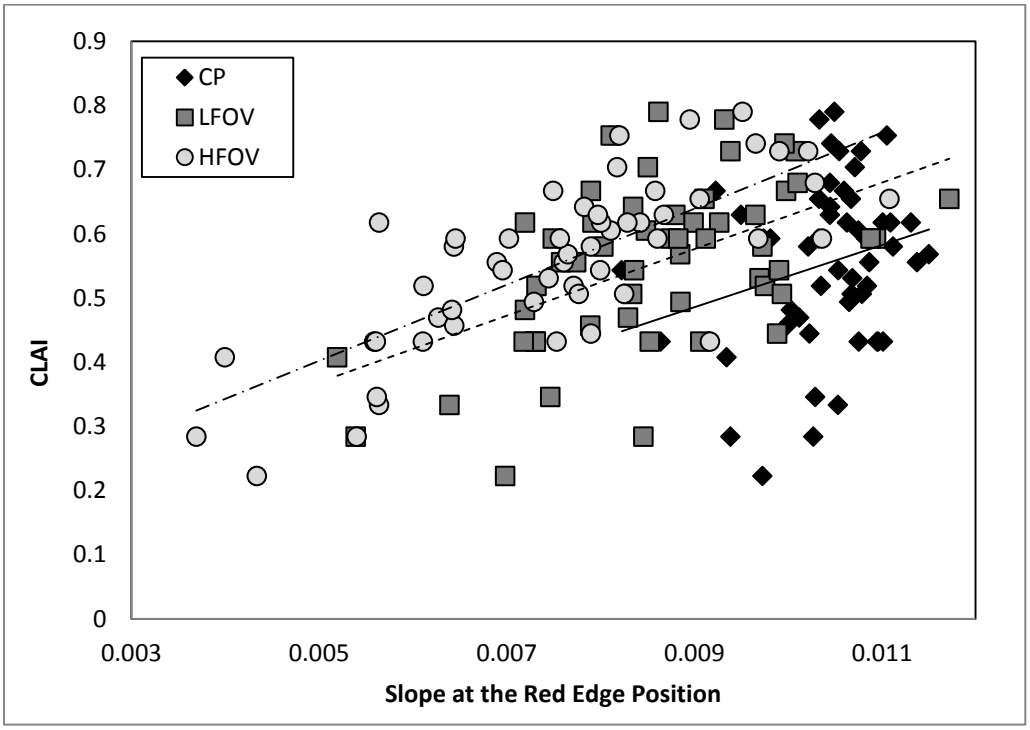

Figure 4.22: Scatterplot of Coarse Leaf Area Index vs SREP.

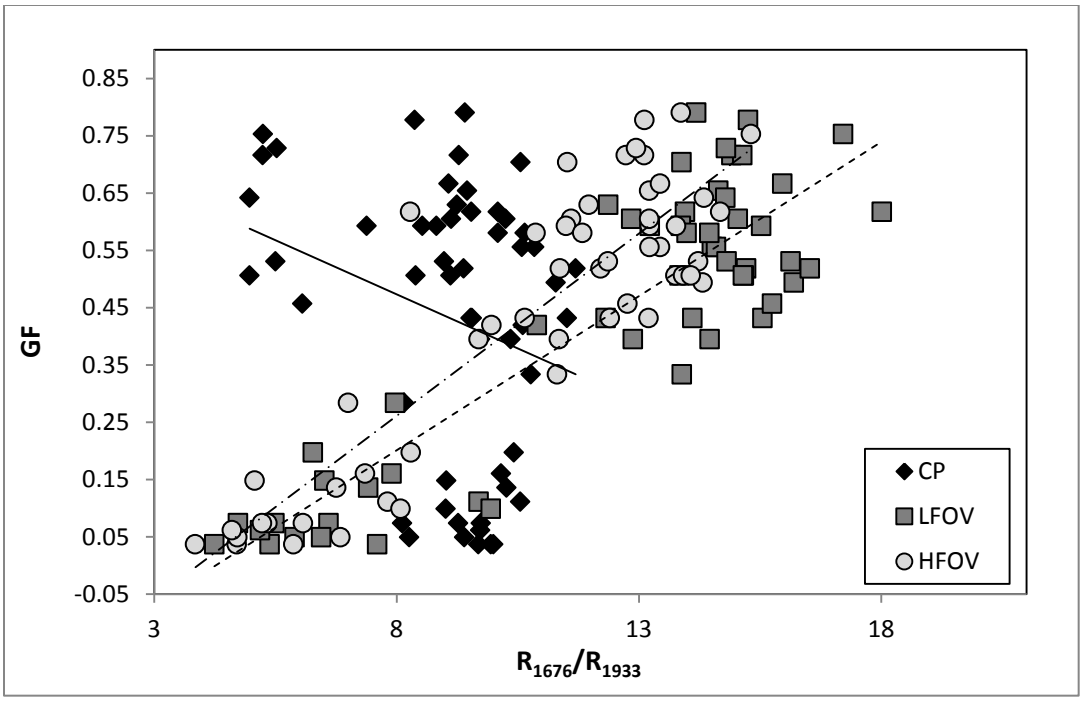

Figure 4.23: Scatterplot of Green Factor vs R_{1676}/R_{1933}.

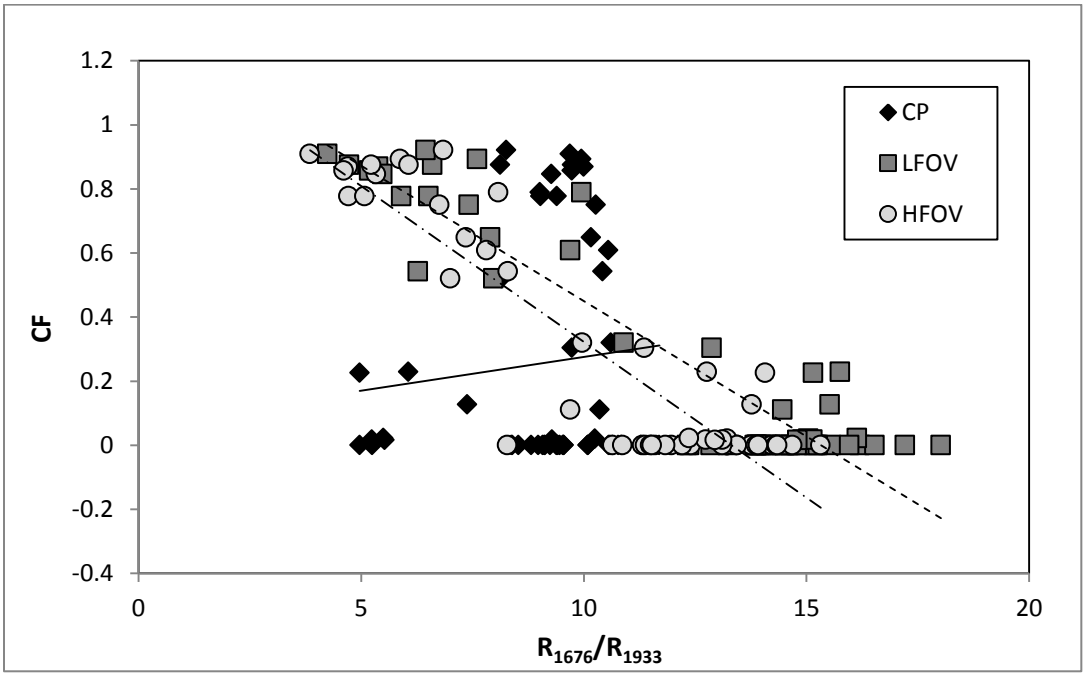

Figure 4.24: Scatterplot of Chlorosis Factor vs R_{1676}/R_{1933}.

Of particular interest are R_{950}/R_{750} and SREP, which correspond to RWC and CLAI respectively, as those indices were determined previously to be the most likely indicators of overall Cs stress.

4. Discussion

In this experiment a model species of plant *A. thaliana* was treated with a contaminant of interest at two concentrations, in conjunction with a lifetime control. A lifetime control is important, because it has been shown that as plants mature, their reflectance spectra will shift (Horler et al. 1980; Milton et al. 1991); a lifetime control helps ensure that one can relate spectral changes to the contaminant exposure, without confounding from plant growth stage.

4.1. Vegetation Indices and Endpoints

4.1.1. Relative water content

Some vegetation indices proved useful for the assessment of plant characteristics. Of the vegetation indices considered, R_{950}/R_{750} as determined using the CP proved to be the best indicator of relative water content. The water index did not prove to be a statistically significant predictor of RWC for any of the spectral views, which is contrary to the findings of other studies (Peñuelas and Inoue 1999). However, the 950-970 nm reflectance band is associated with water absorption and is common between the chosen index and the water index; the selection of a different reference band (750 nm as opposed to 900 nm) may provide a more appropriate indicator of stress in some circumstances. Additionally, the ratio WI/NDVI has been used to correct WI for the effect of NDVI (Peñuelas et al. 1997). In considering this corrected WI, as well as an adjusted R_{950}/R_{750}, for low and high FOV (NDVI is only appropriate for remote sensing), correlations to RWC were much higher.

4.1.2. Chlorophyll content

Of the vegetation indices considered, the red edge position determined by the HFOV set up proved to be the best indicator of total chlorophyll content. However, at the leaf level, REP was not well correlated (-0.128) with chlorophyll content. The latter is inconsistent with findings in the literature; generally REP has been shown to correlate well with total chlorophyll content at the leaf, whole plant, and canopy scales (e.g. Horler et al. 1980; Curran et al. 1990; Filella and Peñuelas 1994; Lichtenthaler et

al. 1996; Wong and He 2013). We hypothesize that because of the variability within samples of the same treatment group, acquiring a greater number of representative samples per plant (e.g. acquiring CP spectra and chlorophyll content for all available leaves) would result in a more remarkable relationship between CP spectra and chlorophyll content.

4.1.3. Visual assessment factors

As summarized in Table 4.4, SREP as determined from reflectance spectra acquired by HFOV proved to be the best indicator of CLAI.

Table 4.4: R^2 values (%) for endpoints and most appropriate VI predictor, listed by acquisition technique.

	RWC vs R_{950}/R_{750}	RWC vs WI/NDVI	Chl a+b vs REP	CLAI vs SREP	GF vs R_{1676}/R_{1933}	CF vs R_{1676}/R_{1933}
CP	33.0	--	1.00	5.9	7.2	1.0
LFOV	13.3	24.1	18.3	27.5	78.3	86.7
HFOV	14.3	25.4	24.9	57.3	78.5	82.5

R_{1676}/R_{1933} proved to be the best indicator for both GF and CF, although HFOV was more fitting for GF and LFOV more fitting for CF. Because the visual assessment factors were determined using whole-plant photographs, it follows that VI calculated from reflectance spectra acquired by FOV would be more appropriate statistical predictors for these factors than would VI determined from CP acquired spectra; CP only considers individual leaves whereas FOV considers areas of the whole plant. The R^2 values for the visual assessment factors were generally high (Table 4.4), serving as a "proof of principle" that FOV does provide indication of plant status. Details of the regression results shown in Table 4.4 are contained in Appendix B1.

Whether or not FOV indication of plant appearance is useful is debatable; on the scale of a few individual plants, a visual assessment is likely less time consuming than acquiring and analysing spectra. However, when applied to a canopy or landscape scale, using vegetation indices would prove more convenient.

It should be also be noted that although the selected vegetation indices were statistically significant predictors of the corresponding endpoints, the occasionally low R^2 values (summarized in Table 4.4) indicate that these predictors might not necessarily be useful, especially when time, effort, and other resources required for data acquisition are taken into consideration. The expense of and information gained through data collection by the different types of probes should be considered when developing experiments in the future. This may depend on desired endpoint; the CP provided the best indication of plant water status, whereas the FOV probe provided the best indicator of other endpoints.

4.2. Comparison of spectra collection techniques

Biochemistry may be highly variable within single plants (Bock et al. 2010). The distribution of chemical constituents is not uniform because of the organization of cells and organelles; non-uniformity results in micro-differential absorbance and reflectance across a leaf surface. Optical properties of leaves are determined by (1) external leaf structure, (e.g. surface roughness) which controls the reflectance from the upper surface of the leaf, (2) composition, amount and distribution of pigments, which determine the absorption of radiation in the ultraviolet and visible ranges, (3) internal leaf structure, which affects the scattering of incident radiation within the leaf, and (4) water content, which affects the absorption infrared radiation (Knipling 1970; Van der Meer and de Jong 2006; Peng and Gitelson 2012). While these factors still contribute to reflectance spectra of an entire plant, or multiple plants, trends may be perceived to indicate wilting or decreased vegetative growth. Considering the whole plant may also give indication of leaf properties/orientation in addition to soil properties.

The CP acquires reflectance spectra for individual leaves, whereas the FOV probe considers the entire plant, or portion of a plant; reflectance spectra acquired by FOV is a combination of plant and soil reflectance. In theory, FOV is more convenient and can be performed remotely, and although the CP gives cleaner, more consistent spectra, FOV was more likely to discern plant stress conditions in this experiment than the CP. As mentioned above, differences between collection techniques in predictive

ability may be due to the need for additional samples with the CP resulting from the inherent biological variability between plants.

LFOV and HFOV were well related (Table 4.5), implying that vegetation indices may be similarly applied for these spectral acquisition techniques.

Table 4.5: Example relationship comparison between spectra acquisition techniques. Using the relevant VI previously established, linear regression was conducted comparing VI calculated from different techniques. Results (R^2 values (%)) are shown below.

	R_{950}/R_{750}		REP		SREP		R_{1676}/R_{1933}	
	HFOV	LFOV	HFOV	LFOV	HFOV	LFOV	HFOV	LFOV
CP	21.4	23.4	44.1	42.2	11.1	6.9	7.5	4.8
LFOV	74.5	--	74.1	--	73.1	--	88.6	--

Neither of the FOV heights considered proved better than the other, so although there are slight differences between them, the general consistency indicates that acquiring spectra at one height, either high or low, will prove sufficiently equivalent. This result is convenient, as if this equipment is taken into the field, holding the FOV probe "waist high" will have significant variation, depending on the operator. The vegetation indices acquired by CP did not correlate well with the same indices determined by FOV (R^2 values shown in Table 4.5; details contained in Appendix B1), although the overall predictive ability for some VI was consistent between modes of acquisition (i.e. R_{950}/R_{750} and SREP, Figure 4.20 and Figure 4.22). Care should be given applying VI across views as CP and FOV may provide different results, depending on the endpoint of concern. Different VI should be developed and applied for CP than FOV when utilizing a single reflectance spectra acquisition technique. It is possible that the combination of spectra collection techniques could provide the overall best approximation of plant stress status by accounting for both whole plant and leaf optical properties; multi-index use should be given future consideration in studies utilizing both CP and FOV.

5. Conclusions

From this study, certain vegetation indices seem promising for selected endpoints (Table 4.4), but as discussed above, are not always consistent with the typical findings in the literature. R_{950}/R_{750} and SREP were the best indicators of overall Cs toxicity, although SREP has also been shown to generally indicate chlorophyll content and leaf area index (Filella and Peñuelas 1994). Although limited positive results were seen in the laboratory, environmental and sampling conditions were controlled; therefore, care should be given if the intent is to extrapolate to field studies. Measurements taken in the field may not be as consistent or informative as measurements taken in the laboratory due to extraneous and potentially unknown environmental factors.

CHAPTER 5: FEASIBILITY ASSESSMENT OF REFLECTANCE SPECTROSCOPY TO DETECT EFFECTS OF LITHIUM CHLORIDE EXPOSURE IN FOUR PLANT SPECIES[*]

1. Introduction

As discussed in Chapter 4, reflectance spectroscopy has potential applications for use in phytoremediation as non-destructive analytical technique for assessing plant stress, specifically metal stress. To further investigate the potential use of reflectance spectroscopy as a method for assessing metal stress across different species of plants, reflectance spectra were collected for four different species of plants which were treated twice weekly in a laboratory setting with 0 mM or 15 mM of lithium chloride (LiCl) solution.

1.1. Species considered

The four species considered here are *Arabidopsis thaliana (*the model species considered in Chapter 4)*, Helianthus annuus, Brassica rapa,* and *Zea mays.* Several species of the *Brassica* family, which are vegetable and oilseed crops (Li et al. 2009; Wang et al. 2011), are known to be heavy metal tolerant and have been considered potential phytoremediation candidates (Li et al. 2009). Here phytoremediation is defined as the use of green plants for environmental clean-up, or the use of plants to remove or neutralize pollutants (Salt et al. 1995, 1998). Dunagan et al. (2007) even found some correlations between spectral characteristics of mustard spinach plant (*B. rapa*) leaves and foliar mercury (Hg) content. Sunflower (*H. annuus)* is an ornamental flower as well as an important environmental crop, primarily as an oilseed crop (Vanaja et al. 2011), and it has been shown to be an effective phytoremediation crop (Prasad 2007; Wuana and Okieimen 2010). Corn (*Z. mays*) has also been shown to have heavy metal phytoremediation potential (Wuana and Okieimen 2010). Corn is the major feed grain (90%) in the United States and is also processed into a broad assortment of food stuffs,

[*] Martinez et al. 2014. Feasibility assessment of reflectance spectroscopy to detect effects of LiCl exposure in four plant species. Journal of Near Infrared Spectroscopy. In preparation.

from cereals to sweeteners. Corn even has industrial utility as a component in the fabrication of fuel ethanol. As the world's largest corn producer, the United States exports about one-fifth of the yearly corn crop (Capehart 2013). Several studies have considered the reflectance spectra of corn and sunflower, from assessing pigment concentrations to nutrient/water status and photosynthetic efficiency at both leaf and canopy scales (e.g. Al-Abbas et al. 1974; Ercoli et al. 1993; Blackmer et al. 1994; Peñuelas et al. 1994; Masoni et al. 1994, 1997; Peñuelas et al. 1995; Mariotta et al. 1996; Daughtry et al. 2000; Reddy et al. 2001; Zhao et al. 2003; Grzesiak et al. 2010; Peng and Gitelson 2012; Schlemmer et al. 2013).

1.2. Lithium toxicity in plants

Lithium (Li) is widely used in the US, which is the leading producer and consumer of Li materials, finding utility in ceramics and glass, aluminum production, the medical industry, certain batteries and greases, nuclear reactor coolant, radiation dosimeters (e.g. Cameron et al. 1961), and historically, in thermonuclear weapon development (Hawrylak-Nowak et al. 2012; Kszos and Stewart 2003; Aral and Vecchio-Sadus 2008). Although Li is not a radioactive concern, it is an anthropogenic contaminant related to the nuclear fuel cycle and to legacy waste and contamination from nuclear weapons development (Crowley and Ahearne 2002; Kszos and Stewart 2003; IAEA 2004). For example, historical waste-disposal activities at the Department of Energy's Oak Ridge Y-12 plant resulted in the release of Li to groundwater (Kszos and Stewart 2003). Lithium becomes an ancillary concern when assessing the overall environmental impact of and remediation strategies surrounding nuclear power and waste management.

Lithium is the lightest metal, although as it is highly reactive, it does not occur naturally in its elemental form. Li occurs in various minerals and salts, and typically enters the environment through weathering processes (Hawrkyak-Nowak et al. 2012; Kszos and Stewart 2003). Once in the environment,

Li is easily transported to above-ground plant parts because it shares the potassium transport carrier; all plants will take up Li (Hawrylak-Nowak et al. 2012; Aral and Vecchio-Sadus 2008).

Lithium uptake, tolerance, and toxicity symptoms are all species specific (Hawrylak-Nowak et al. 2012; Aral and Vecchio-Sadus 2008; Schrauzer 2002; McStay et al. 1980), although stimulatory effects are commonly seen at low levels of lithium (Hawrylak-Nowak et al. 2012; Aral and Vecchio-Sadus 2008; Schrauzer 2002; McStay et al. 1980). Although symptoms of Li toxicity are not distinct among species (Bingham et al. 1964), general symptoms include chlorosis, necrotic spot development, leaf curling, and reduced biomass (Bingham et al. 1964; Hawrylak-Nowak et al. 2012; Naranjo et al. 2003), and these are all symptoms exhibited in pathogen defense. There is preferential concentration of Li in older leaves, and effects may be more pronounced on older rather than newer growth (Hawrylak-Nowak et al. 2012, Naranjo et al. 2003; Kent 1941; McStay et al. 1980).

As for the mechanism of Li toxicity, plants have the enzymes inositol monophosphatase and HAL2 nucleotidase that have been shown to be Li sensitive in animals, but which of these is the major target of Li action is unknown (Bueso et al. 2007). Generally, at high concentrations, Li increases the production of ethylene, which is known to inhibit plant growth. The mechanism is not wholly understood, although the "inositol depletion hypothesis" is generally accepted (Gillaspy et al. 1995; Berridge 1993). This theory holds that Li inhibits inositol monophosphatase, which ultimately triggers ACC (aminocyclopropane carboxylic acid) synthase, resulting in an increase in ethylene biosynthesis (Bueso et al. 2007; Mulkey 2005**;** Naranjo et al. 2003; Hawrylak-Nowak et al. 2012).

Bingham et al. (1964) considered the effects of lithium sulfate on 11 different species of plants, including corn, and found a marked difference between species uptake and symptoms of toxicity; corn was seen to be fairly lithium tolerant. Hawrylak-Nowak et al. (2012) exposed both sunflower and corn to varying levels of LiCl and saw a reduction in biomass in species, necrotic spots and leaf area reduction in sunflower, and reduction in chlorophyll content in corn. Sunflower accumulated greater amounts of

Li than did corn, and also showed an increase in biomass at lower Li concentrations. Li et al. (2009) showed that *Brassica carinata* seedlings were able to accumulate and survive at reasonably high concentrations of LiCl (media concentrations >150 mM) and concluded that this species has potential for phytoremediation of Li. Additional studies on Li toxicity in plants include Kent 1941a, 1941b; Sneva 1979; Mulkey 2005; Bartolo and Carter 1992, Bueso et al. 2007; McStay et al. 1980; and Naranjo et al. 2003.

1.3. Consideration of chloride effects

LiCl has been used previously to consider Li uptake and stress (Mulkey 2005; Kent 1941a, 1941b; Sneva 1979; Bueso 2007; Hawrylak-Nowak et al. 2012; Li et al. 2009), and although chlorine (Cl) is an essential micronutrient for higher plants, at high plant tissue concentrations Cl can be toxic (White and Broadley 2001). However, the concentrations of LiCl that will be used here are considered below levels of which Cl might be toxic, and the contribution of Cl to the stress expected here are considered to be negligible.

1.4. Study summary and objective

Reflectance spectra were collected every week for three weeks using an ASD FieldSpec Pro Spectroradiometer with a contact probe and a field of view probe. Time points after the third week were not considered because beyond week three as twice weekly 100 mL treatments no longer provided adequate hydration, and in addition, both corn and sunflower plants became root bound.

The study was designed to compare the effects of increasing levels of LiCl on levels of plant stress for *A. thaliana, H. annuus, B. rapa,* and *Z. mays*. An absence of stress symptoms for *A. thaliana* where stress symptoms where symptoms were observed for *B. rapa*, *H. annuus*, and *Z. mays* would suggest that *A. thaliana*, like these three other species, was Li tolerant and a potential candidate for phytoremediation. Greater stress symptoms for *A. thaliana* would suggest otherwise. Detection of symptoms of possible stress were made by measures of reflected spectra which have previously been

demonstrated to indicate stress when other visual or more complex physical or chemical procedures do not yet indicate stress. To enhance the ability to detect stress in reflected spectra, reflected spectra were measured at the leaf surface and at 66.7 cm above the plant surface.

Plants were harvested each week immediately after spectra collection for determination of relative water content and chlorophyll content. The final purpose of this study was to determine whether a quantifiable relationship exists between Li contamination in four species of plants, and if that relationship exists similarly across these species.

2. Materials and methods

2.1. Plant growth and treatment

The soil mix used was four parts PGX (Promix PGX, Premier Horticulture Inc., Quakertown, PA) and 1 part Perlite (Hoffman Horticultural Perlite, Good Earth, Lancaster, NY). Soil was mixed and placed in square plastic grow pots (10.8 × 10.8 × 12.7 cm, Kordlok SQL0450 from ITML Horticultural Products, Myers Industries Inc., Akron, OH) with perforated bottoms to allow water seepage; soil was hydrated by placing pots by multiples of twelve in a Nalgene tray (Thermo Scientific, Wilmington, DE) with 3-5 cm deep deionized water. Water level was maintained for at least three days to allow the soil to absorb sufficient moisture for planting.

A. thaliana seeds (*Arabidopsis thaliana*, WT-02-41-01 Columbia [alias Col-0] Wildtype, LEHLE Seeds, Round Rock, TX) were removed from 4°C storage, soaked in 1/32 strength hydroponic (HP) media solution, and exposed to red light for 30 minutes to synchronize germination. Hydroponic media was made with DI water, 1/32 strength Murashige and Skoog basal medium (137.5 mg L^{-1}) (Sigma-Aldrich Cat No M5519, St. Louis MO), and 250 mg L^{-1} MES hydrate (Sigma-Aldrich Cat No M2933), using KOH to pH balance to 5.7. Seeds were subsequently pipetted into a 96 well tray (five seeds per well) to verify number of seeds planted. Seeds were then pipetted from the tray onto potted soil as three sets of five

seeds per pot, i.e. 15 seeds per pot, to ensure adequate germination. Following the sowing of the seeds, the 1/32 HP media was further diluted to 1/64 strength for subsequent treatments for all plant species.

Z. mays seeds (*Zea mays*, Burpee Sweet Corn Bi-Licious Hybrid, Burpee Garden Products Co, Warminster, PA) *H. annuus* seeds (*Helianthus annus*, Snow Country Black Oil Sunflowers, Ridley Inc, Mankato, MN), and *B. rapa* seeds (*Brassica rapa*, Winfred Brassica Rape, outsidepride.com, lot: M31-9-2WIN, Independence, OR) were stored at room temperature. *B. rapa* were planted as three sets of five seeds; three equally spaced ~3 cm deep divots were made in the soil, into which five seeds were dropped into each divot and lightly covered in soil. *Z. mays* and *H. annuus* seeds were planted similarly with four divots, one seed per divot.

After planting, arbitrary sets of 6 pots each were transferred to Sterlite tubs (40 × 31.75 × 15.24 cm, Target Corp., Minneapolis, MN). Tubs were placed in rows of up to four on growth shelves, 42 cm beneath growth lights (Four Philips F32T8 TL741 700 series 32W ALTO II Fluorescent bulbs, cat. No. 0002904, Philips North America Corporation, Andover, MA). Plants were on a nine hour light : 15 hour dark cycle under ambient laboratory environmental conditions.

The bottoms of the pots were submerged in approximately 3 cm distilled water until the plants reached a previously determined treatment date (i.e. day 37 post-planting, rosettes ~30 mm in diameter). *A. thaliana* the seedling stage, plants were culled and/or redistributed, based on the appearance of health: *A. thaliana* were culled to three seedlings per pot, such that one plant per group remained. *B. rapa* were culled to 10 plants per pot, *Z. mays* were culled/rearranged to three plants per pot, and *H. annuus* were culled/rearranged to one plant per pot. *Z. mays* and *H. annuus* germination was not as successful as *B. rapa* and *A. thaliana*, and required rearrangement of plants between pots to ensure equal distribution of plants between replicates.

Immediately prior to LiCl treatment, pots were rearranged between nine tubs (six pots each, no longer submerged in DI water) such that each tub, now serving as a treatment group, had similar size

and quality plants. Spike solution was evenly applied to the top of each pot as 100 mL (25 mL delivered to each quadrant) of 15 mM LiCl in 1/64 strength HP media twice weekly, with control plants receiving 100 mL 1/64 HP media only. Two pots were randomly selected from each treatment group for weekly spectra collection and harvest. After each application of hydroponic media, the plants were rotated within the tubs and the tubs were rearranged among the growth shelves to account for potential variation in lighting or other environmental conditions.

2.2. Equipment, setup, and collection of spectra

Reflectance spectra were collected using a FieldSpec Pro (FSP 350-2500P; Analytical Spectral Devices (ASD), Boulder, CO) which is a full range (350 nm – 2500 nm) portable spectroradiometer (with sampling intervals/spectral resolutions of 1.4 nm/3 nm and 2 nm/10 nm for 350-1000 nm and 1000-2500 nm respectively) (ASD 2002). CP spectra were collected using a leaf clip attachment on individual leaves. The CP provides light (3.825 V, 4.05 W low intensity bulb) and collects reflectance spectra. The leaf clip attachment has both a white (for white reference) and black (to minimize back scatter) background. Triplicate CP spectra were collected on one leaf from each of typically three separate plants per pot for *A. thaliana*. For *Z. mays,* one reading was taken on each of 3 to 4 leaves for each plant, depending on how many leaves the plant had. For *H. annuus*, one reading was taken on each of the first set of mature leaves, and two readings on each of the second set of mature leaves, the first toward the stem and the second toward the leaf tip. Multiple readings were taken on single leaves for *H. annuus* to get an overall representation of reflectance as *H. annuus* leaves have a large area. For *B. rapa*, one reading was taken on a single leaf per plant for four plants.

Figure 5.1: Contact probe with leaf clip; spectra acquisition from Brassica rapa.

FOV spectra were collected using an 8° probe (i.e. a viewing angle of 8°). Incident light was provided by two halogen lamps (Pro Lamp, 14.5 V, 50W, P/N 145378, ASD, Boulder, CO) angled at 30 degrees from horizontal. The lights were 180° apart at 30.5 cm from the center of pot on the horizontal and 76.2 cm above the table surface. The fore optics probe was centered between the lights at 66.7 cm above the plane of the pot surface (see Figure 4.4), resulting in a spot size diameter of 9.32 cm. Reflective surfaces were covered with absorbent material to minimize noise and thus variability in spectra, and dark room conditions were approximated by surrounding the lights and fore optics with a black felt canopy. Tripod surfaces were also wrapped in black felt. The white reference was a calibrated Spectralon (25.4 × 25.4 cm, LabSphere, North Sutton, NH) panel of 99% reflectance that was elevated to a height equivalent to a grow pot. Grow pots were placed on black paper plates when collecting spectra and the table top was lined with a light-absorbent black rubber. Four spectra, each collected at a different arbitrary rotation of the pot to get an overall assessment of the reflectance of

the sample, were saved for each FOV session. FOV spectra were always acquired prior to CP because it is possible for the CP to injure the plant and therefore affect subsequent FOV readings.

2.3. Collection of physical measures

2.3.1. Relative water content

As metal stress is known to mimic drought stress (Thenkabail et al. 2012), plants were harvested after spectra collection each week to determine relative water content and chlorophyll content. To determine relative water content, sufficient leaves were removed to obtain between 1000 and 2000 mg of fresh mass for each replicate (i.e. pot). Samples were placed in weigh boats, fresh mass was obtained, samples were dried to a constant mass, and dry mass was obtained. A sample's relative water content was then expressed as Equation 5-1:

$$\text{RWC} = 1 - \frac{\text{dry mass}}{\text{fresh mass}} \tag{5-1}$$

2.3.2. Chlorophyll content

The concentrations of chlorophyll *a* (Chl *a*) and chlorophyll *b* (Chl *b*) were determined for each replicate (i.e. pot) (Knudson et al. 1977; Li et al. 2009; Papista et al. 2002). Four circular leaf subsamples were collected from representative leaves of the plants in a pot using a #3 cork borer (Fisher Scientific, Pittsburgh, PA). Leaf samples were stored in the dark at 4°C in capped 20 mL vials (KG-33 borosilicate glass; Kimble Chase, Vineland, New Jersey) containing 2 mL 100% ethanol for three days before absorbance (*A*) at 665 nm, 649 nm, 629 nm, and 696 nm, with an offset at 750 nm, was determined for 1.5 mL subsamples for each vial using a NanoDrop 2000c UV-Vis spectrophotometer (Thermo Scientific, Wilmington, DE). Disposable methacrylate cuvettes with transmission from 300 to 800 nm > 80% were used with the 1.5 mL subsample (Cole Palmer, Vernon Hills, Illinois). Chlorophyll content was determined using appropriate, previously published equations (Ritchie 2006; Equation 5-2 and Equation 5-3):

$$\text{Chl } a\ (\mu g/mL) = -5.2007 \cdot A_{649} + 13.5275 \cdot A_{665} \quad (5\text{-}2)$$

$$\text{Chl } b\ (\mu g/mL) = 22.4327 \cdot A_{649} - 7.0741 \cdot A_{665} \quad (5\text{-}3)$$

where A_x is absorbance at *x* nm.

2.4. Data analysis

2.4.1. Vegetation indices

Twelve VI (Table 5.1) were considered for applicable spectra acquisition technique(s) (i.e. FOV and/or CP), including indices from the literature as well as indices selected by the author through previous experience with Cs stress effects on *A. thaliana* and visual examination of plant appearance.

Table 5.1: List of vegetation indices considered, including name and abbreviation if applicable, the relevant acquisition technique(s), formulation, and either potential predictive characteristics along with the corresponding reference or indication that the listed index is newly considered by the authors.

Abbreviation/Name		Relevant acquisition technique	Formulation	Potential indicator of:	Reference
NORMALIZED DIFFERENCES					
NDVI	Non-destructive vegetation index	FOV	$\frac{R_{800} - R_{670}}{R_{800} + R_{670}}$	Green biomass; leaf area	Rouse et al. (1974)
PRI	Photochemical reflective index	FOV CP	$\frac{R_{531} - R_{570}}{R_{531} + R_{570}}$	Photosynthetic radiation-use efficiency	Gamon, Peñuelas, and Field (1992)
SIPI	Structural independent pigment index	FOV CP	$\frac{R_{800} - R_{445}}{R_{800} - R_{680}}$	Carotenoid to chlorophyll a ratio	Peñuelas, Baret, and Filella (1995)
PSND	Pigment specific normalized difference	FOV CP	$\frac{R_{800} - R_{680}}{R_{800} + R_{680}}$	Chlorophyll content	Serrano (2008)
SIMPLE RATIOS					
WI	Water index	FOV CP	$\frac{R_{900}}{R_{970}}$	Plant water content	Peñuelas et al. (1997)
--	--	FOV CP	$\frac{R_{750}}{R_{550}}$	Some correlation with metal content	Davids and Tyler (2003)
--	--	FOV CP	$\frac{R_{1110}}{R_{810}}$	Metal stress	Maruthi-Sridhar et al. (2007a)
--	--	FOV CP	$\frac{R_{725}}{R_{675}}$	Some correlation with chlorophyll content; appeared independent of soil moisture	Davids and Tyler (2003)
--	--	FOV CP	$\frac{R_{950}}{R_{750}}$	*Selected by author*	--

--	--	FOV CP	$\frac{R_{1390}}{R_{1454}}$	*Selected by author*	--
--	--	FOV CP	$\frac{R_{1676}}{R_{1933}}$	*Selected by author*	--
DERIVATIVE ANALYSIS					
YI	Yellowness index	FOV CP	$-0.1*\left(\frac{R_{580}-2R_{624}+R_{668}}{\Delta\lambda^2}\right)$	Chlorosis	Adams, Philpot, and Norvell (1999)

2.4.2. Statistical analysis

Two-way ANOVAs were performed by species to test the following null hypotheses:

- The means of the particular VIs or endpoint by treatment level (0, 15) are equal
- The means of the particular VIs or endpoint by week (1,2,3) are equal
- There is no interaction between the treatment level and week

In other words, ANOVAs are conducted by species to determine the significance of the effects of treatment level and length of treatment. Two-way ANOVAs were conducted similarly for relative water content and chlorophyll content. Balanced ANOVAs were also performed for all species combined by week, treatment level, and species.

Box plots by time and treatment level for relative water content, chlorophyll content, and selected vegetation indices are also presented. Pearson correlation coefficients were calculated for each VI (calculated separately at each view) and the aforementioned endpoints. The highest (absolute value) correlation coefficients were used to determine VI for which to perform a linear regression. Linear regression was used to determine the applicability of the selected VI in predicting the corresponding endpoint, and was also used to compare spectra collection methods. Statistics were performed using Minitab version 16 (Minitab Inc., State College, PA).

3. Results

3.1. Spectra

Reflectance spectra are shown by week and technique (CP or FOV) for each species are shown below (Figure 5.2 through Figure 5.5).

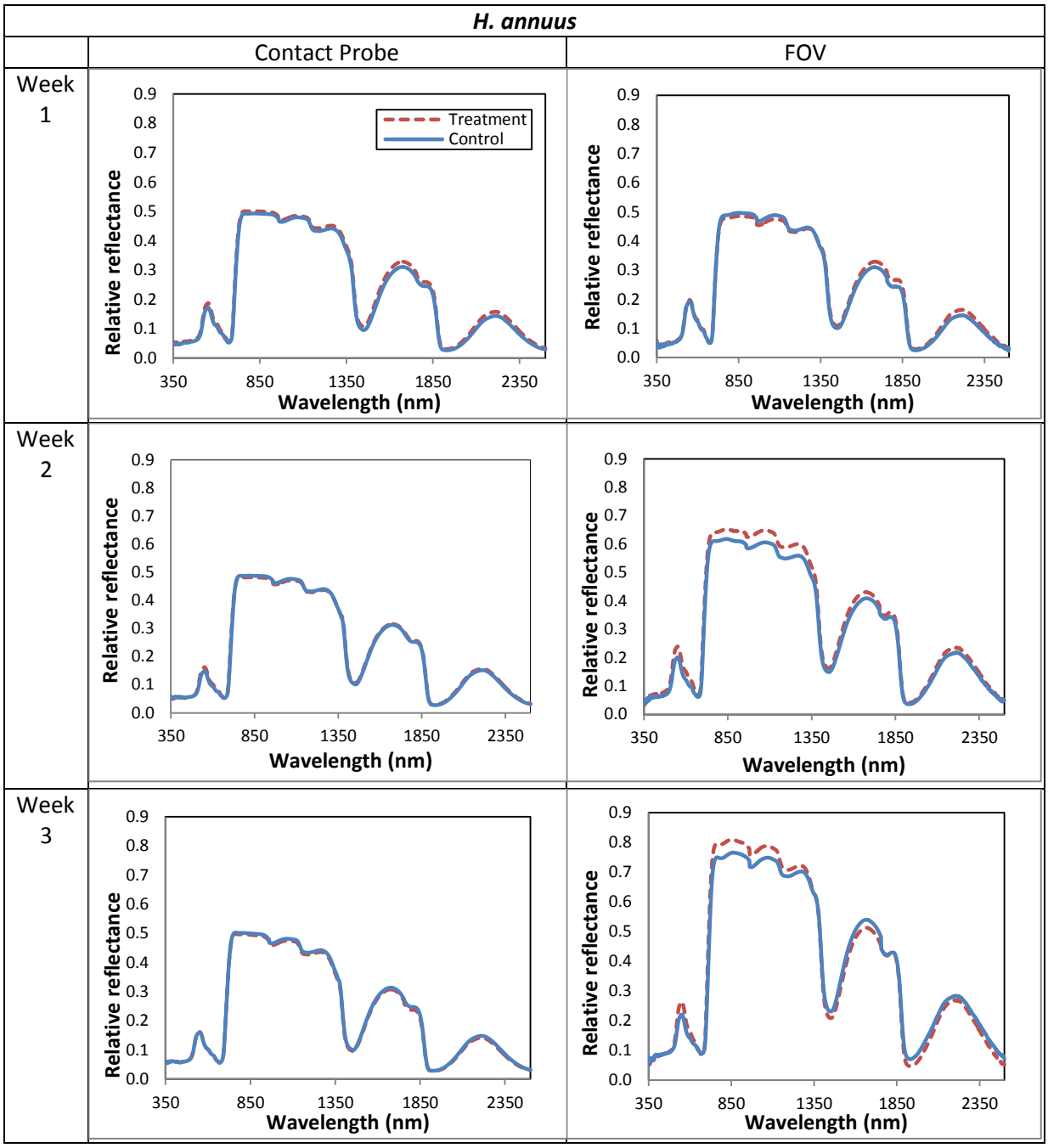

Figure 5.2: Relative reflectance spectra for sunflower; control and treatment spectra are shown each week for both CP and FOV.

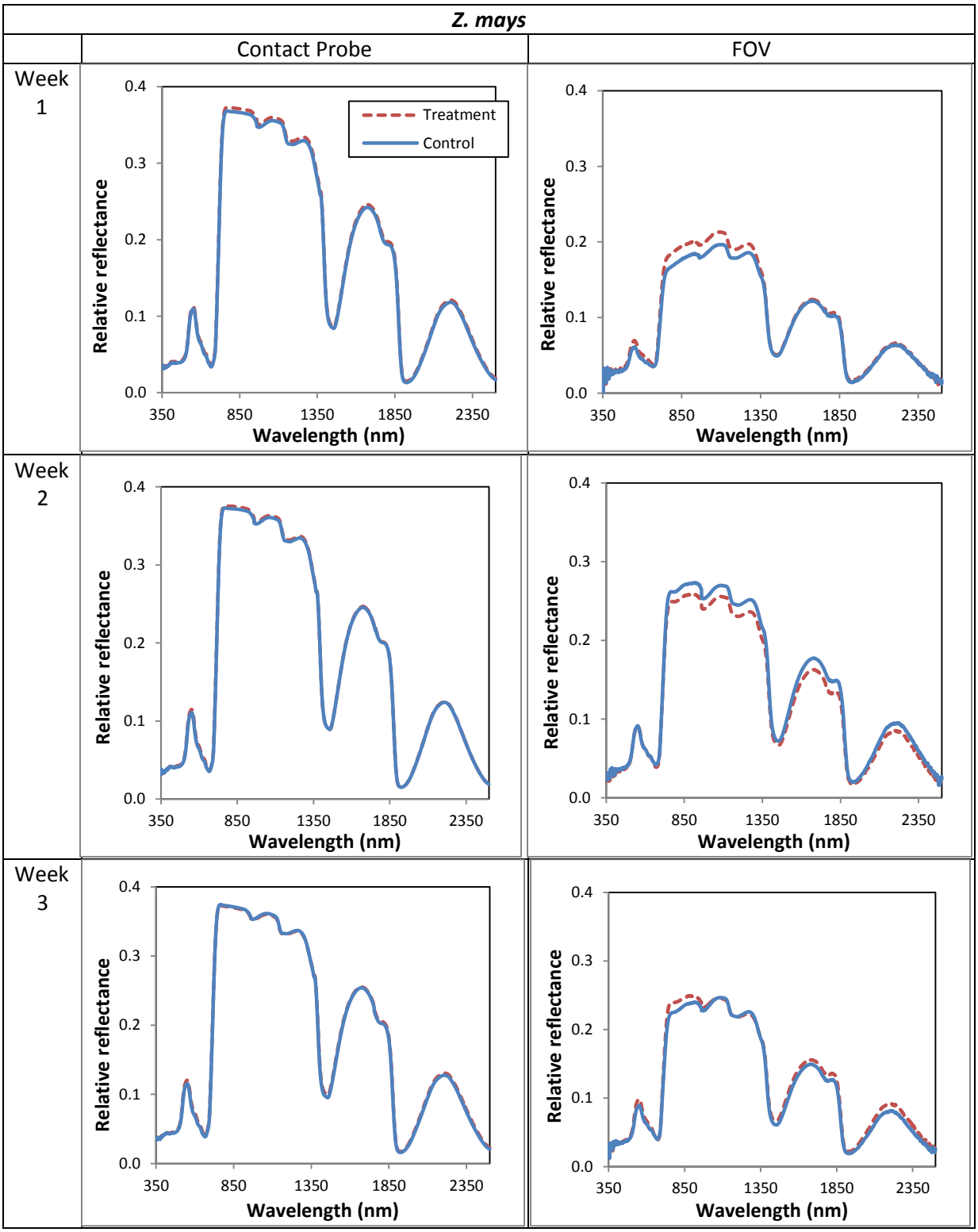

Figure 5.3: Relative reflectance spectra for corn; control and treatment spectra are shown each week for both CP and FOV.

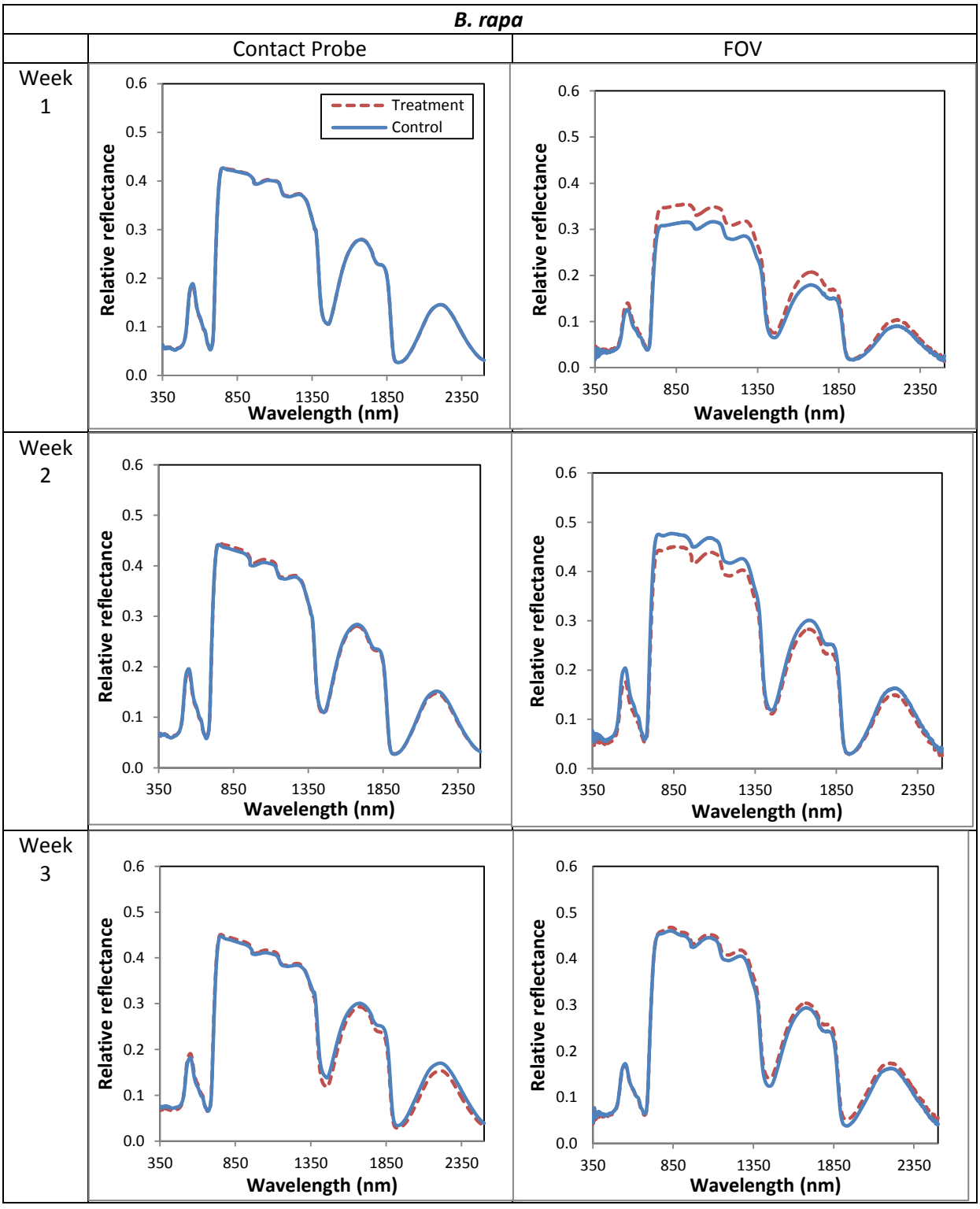

Figure 5.4: Relative reflectance spectra for B. rapa; control and treatment spectra are shown each week for both CP and FOV.

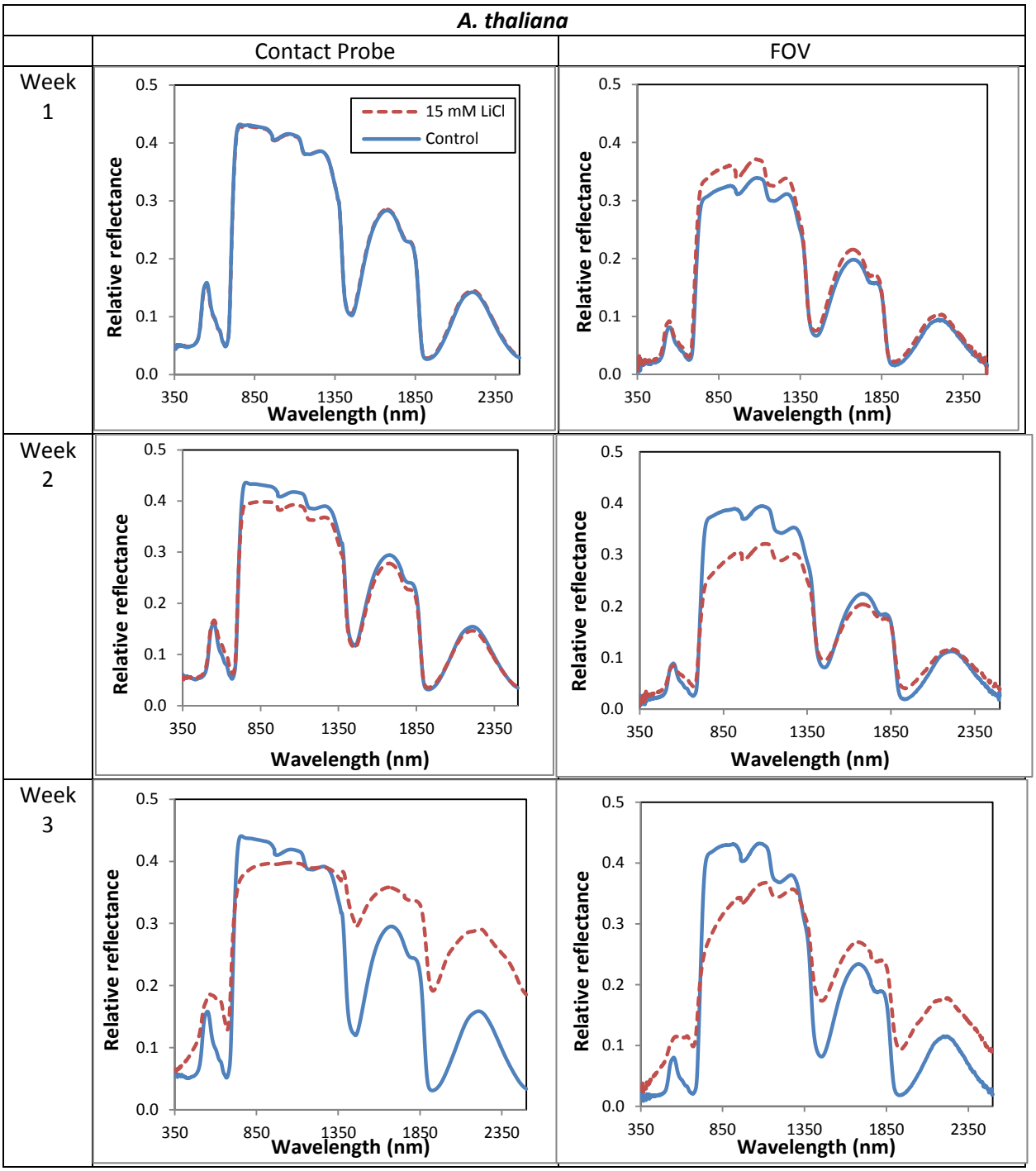

Figure 5.5: Relative reflectance spectra for A. thaliana; control and treatment spectra are shown each week for both CP and FOV.

Mean reflectance spectra relative to the control for each species are contained in Figure 5.6, with single week spectra shown in Appendix B2.

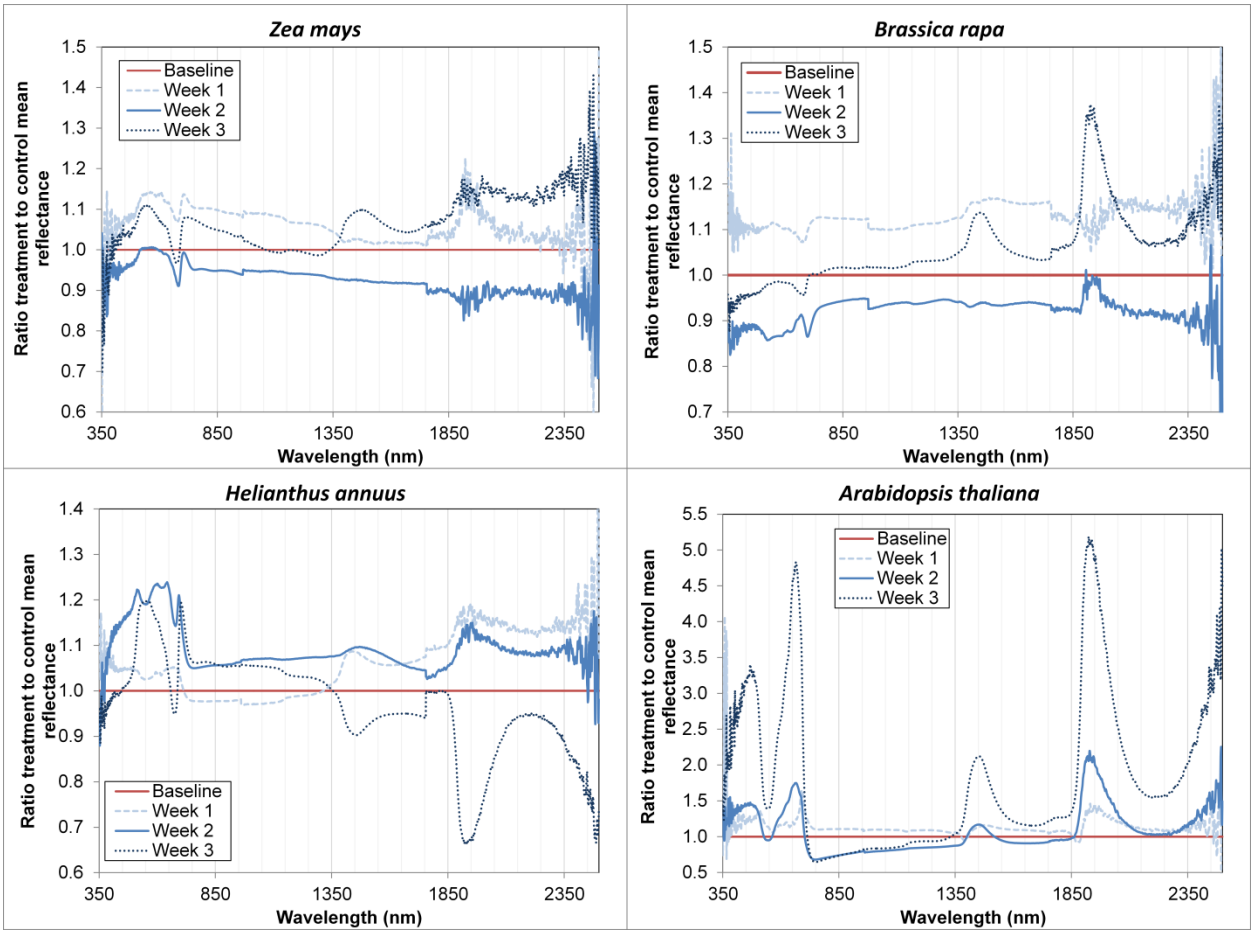

Figure 5.6: Reflectance spectra relative to control for all four species.

3.1. Visual consideration

A. thaliana had noticeable symptoms of lithium exposure starting in week 1, from a slight yellowing (chlorosis) at the leaf tips in week 1 to necrosis and definite reduction in biomass in week 3. *H. annuus* had a significant biomass increase from week 1 to week 2, although growth differences were less obvious from week 2 to week 3. There were no noticeable pigment changes for *H. annuus* between treatment and control groups, and only one plant was found to show slight symptoms of toxicity (small chlorotic spots on leaf tips). *B. rapa* increased in biomass each week, and showed some symptoms of toxicity around leaf edges in weeks 2 and 3. *Z. mays* demonstrated dramatic increase in biomass week to week and showed no symptoms of toxicity. Photographs of the samples at each week are shown in Appendix B3.

3.2. Vegetation indices

P-values from the two-way ANOVAs conducted for the twelve VI considered in Table 5.1 are contained in Appendix B4; these values consider Li toxicity as a whole, rather than the specific symptoms. Significant P-values ($p<0.05$) are shown underlined and in bold, and indicate rejection of the null hypothesis and an acceptance that there is a statistically significant difference between the particular means (or interaction between the factors considered). From these values we see that methods of spectra acquisition as well as the results between species are generally not consistent. For example, nearly all *A. thaliana* VIs had significant P-values for treatment, time, and the interaction between treatment and time, for both spectra acquisition techniques. For other species, however, significant P-values differ between VI, spectra acquisition techniques, endpoints, and time/treatment.

3.3. Endpoints

Boxplots of endpoints by treatment level and time are shown in Figure 5.7 through Figure 5.9, and boxplots of relevant VI are shown in Appendix B5. The variation in relative water content for *A. thaliana* was much higher than the other species, so is shown on a separate graph. Similarly, in Appendix B, some *A. thaliana* graphs are shown separately as not to overpower other species' results.

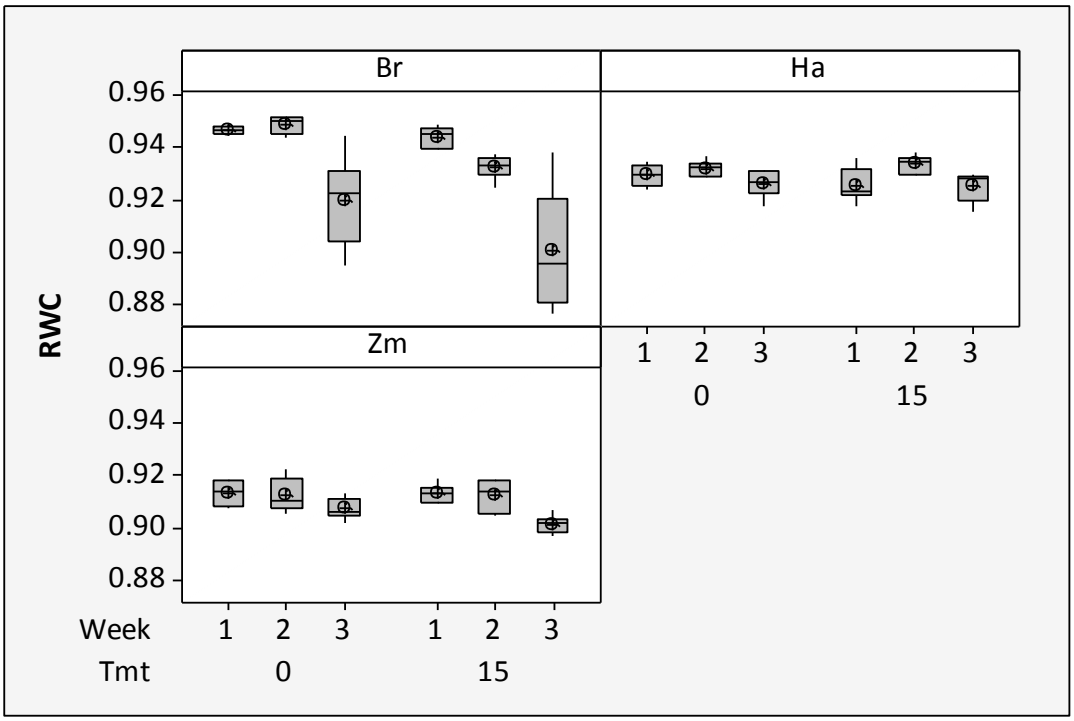

Figure 5.7: Boxplot of relative water content for B. rapa, H. annuus, and Z. mays by week and treatment level.

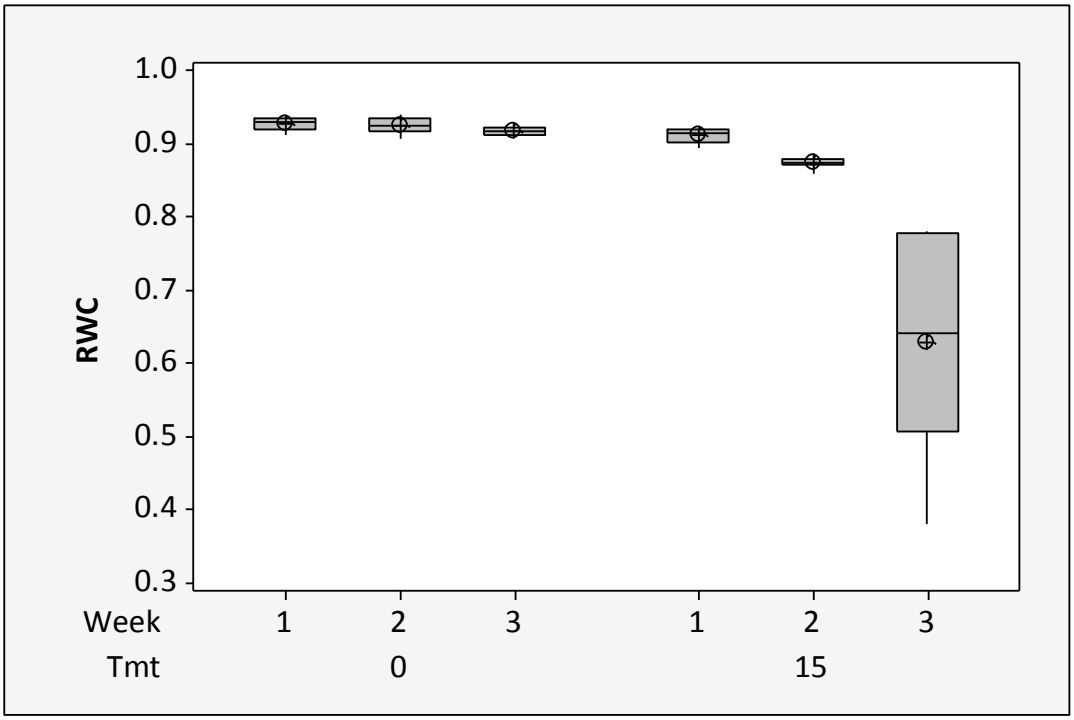

Figure 5.8: Boxplot of relative water content for A. thaliana by week and treatment level.

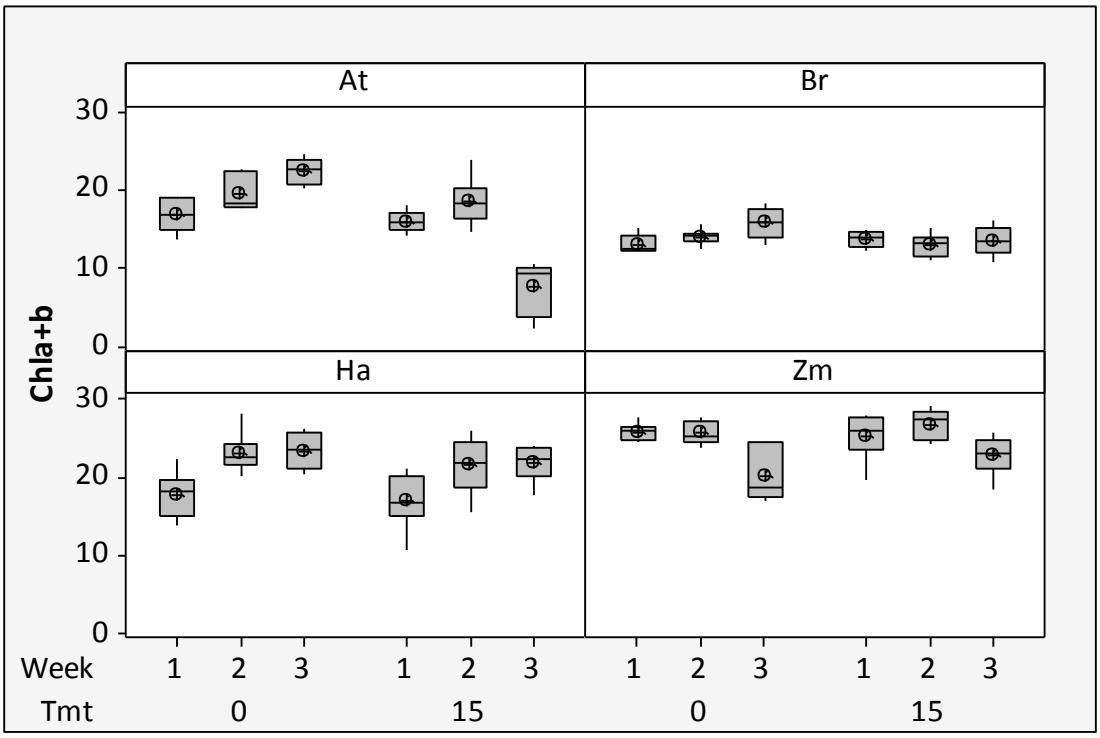

Figure 5.9: Boxplot of chlorophyll content for A. thaliana, B. rapa, H. annuus, and Z. mays by week and treatment level.

Results (P-values) of two-way ANOVA for relative water content and chlorophyll content are listed in Table 5.2 along with the relevant VI, determined by the largest Pearson correlation coefficient.

Table 5.2: Results of two-way ANOVAs for RWC and chlorophyll content, along with most relevant VI.

	Sunflower		Corn		*B. rapa*		*A. thaliana*	
	RWC	Chl a+b	RWC	Chl a+b	RWC	Chl a+b	RWC	Chl a+b
Tmt Level	0.514	0.200	0.206	0.169	**0.003**	0.102	**<0.001**	**<0.001**
Week	**0.003**	**<0.001**	**<0.001**	**<0.001**	**<0.001**	0.103	**<0.001**	**0.001**
Interaction	0.404	0.955	0.249	0.293	0.206	0.063	**<0.001**	**<0.001**
Relevant VI	R_{1110}/R_{810}	R_{750}/R_{550}	R_{1390}/R_{1454}	PSND	R_{1390}/R_{1454}	SIPI	SIPI	SIPI

Results (P-values) of the balanced ANOVA conducted for relative water content and chlorophyll content considering all species together is shown in Table 5.4, along with the relevant VI, determined by the largest Pearson correlation coefficient.

Table 5.3: Results of balanced ANOVAs for RWC and chlorophyll content, along with most relevant VI, across all species, and across H. annuus, Z. mays, and B. rapa.

	All species		*H. annuus, Z. mays, B. rapa*	
	RWC	Chl a+b	RWC	Chl a+b
Tmt Level	**0.001**	**0.005**	0.009	0.542
Week	**<0.001**	**0.008**	**<0.001**	**0.027**
Interaction	**<0.001**	**<0.001**	**<0.001**	**<0.001**
Relevant VI	SIPI	R_{1676}/R_{1933}	R_{1390}/R_{1454}	R_{750}/R_{550}

We consider all species, as well as all species excluding *A. thaliana*, as *A. thaliana* results are much more significant than other species and dominate the results.

Linear regression was used to relate the most appropriate VI to the appropriate endpoint, and to compare results provided by the two different spectra collection techniques. R^2 (%) values for the linear regressions are shown in Table 5.4, with corresponding scatterplots for individual species shown in Figure 5.10 through Figure 5.17; details of the regressions are contained in Appendix B6.

Table 5.4: Linear regressions between endpoints and the most relevant VI for each species and spectra acquisition technique.

Species	Endpoint vs VI	CP	FOV
Sunflower	RWC vs R_{1110}/R_{810}	19.9	6.3
	Chl a+b vs R_{750}/R_{550}	72.0	53.6
Corn	RWC vs R_{1390}/R_{1454}	44.8	23.7
	Chl a+b vs PSND	39.4	3.3
B. rapa	RWC vs R_{1390}/R_{1454}	25.0	62.9
	Chl a+b vs SIPI	23.8	0.3
A. thaliana	RWC vs SIPI	51.4	91.1
	Chl a+b vs SIPI	46.2	70.4
All species	RWC vs SIPI	53.7	78.2
	Chl a+b vs R_{1676}/R_{1933}	50.2	2.7
H. annuus, Z. mays, B. rapa	RWC vs R_{1390}/R_{1454}	4.7	33.0
	Chl a+b vs R_{750}/R_{550}	80.5	32.0

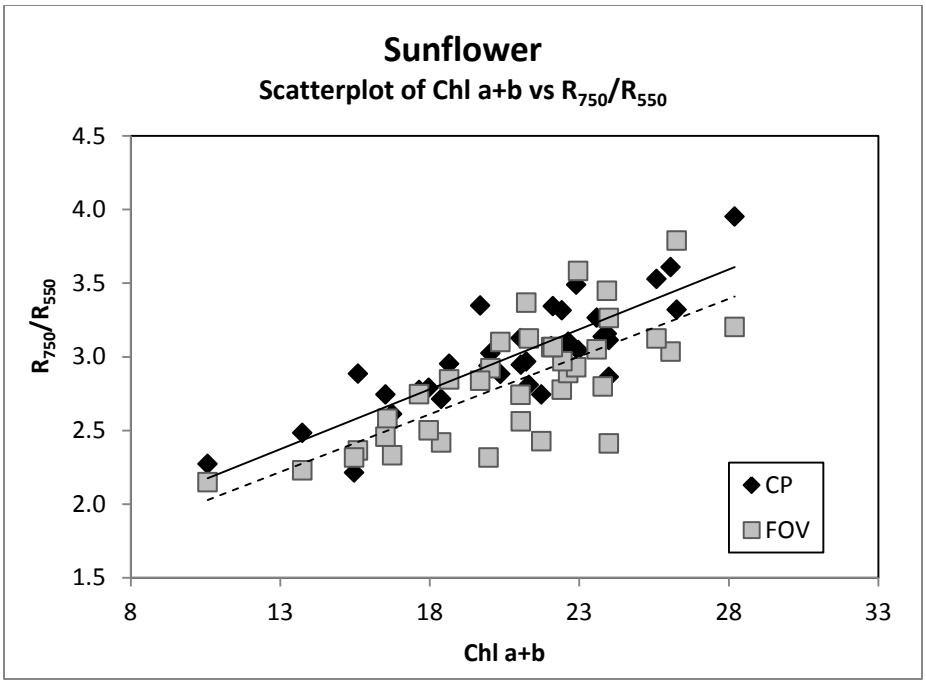

Figure 5.10: Scatterplot of Chl a+b vs R_{750}/R_{550} for sunflower.

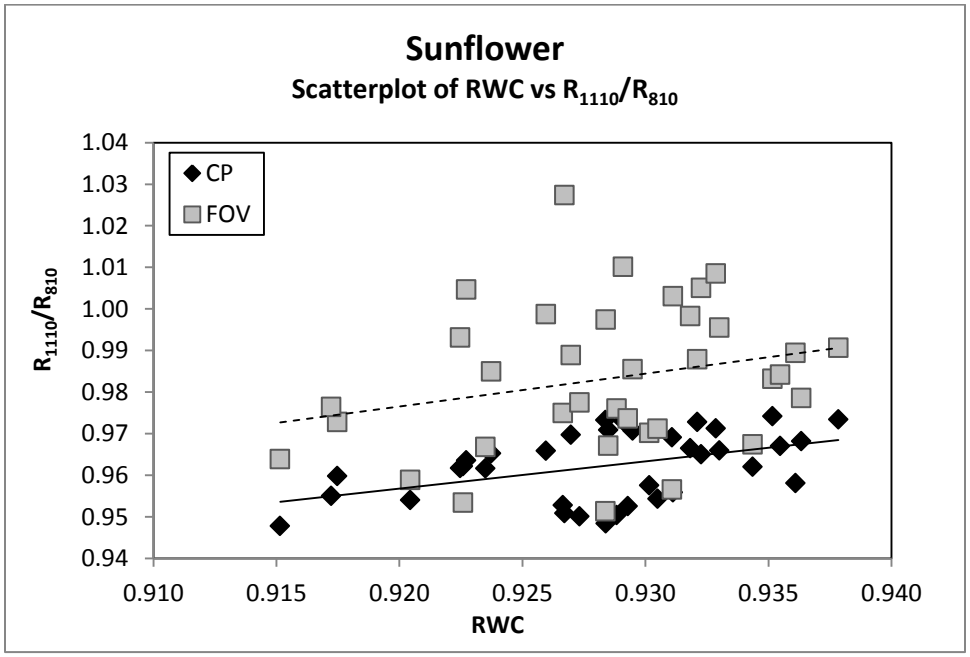

Figure 5.11: Scatterplot of RWC vs R_{1110}/R_{810} for sunflower.

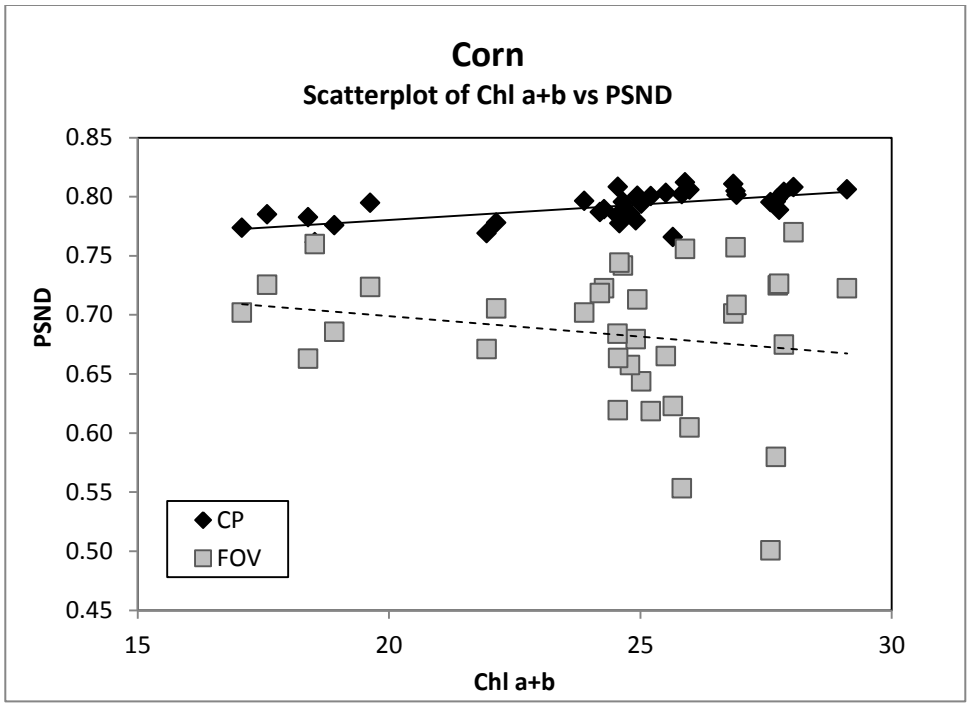

Figure 5.12: Scatterplot of Chl a+b vs PSND for corn.

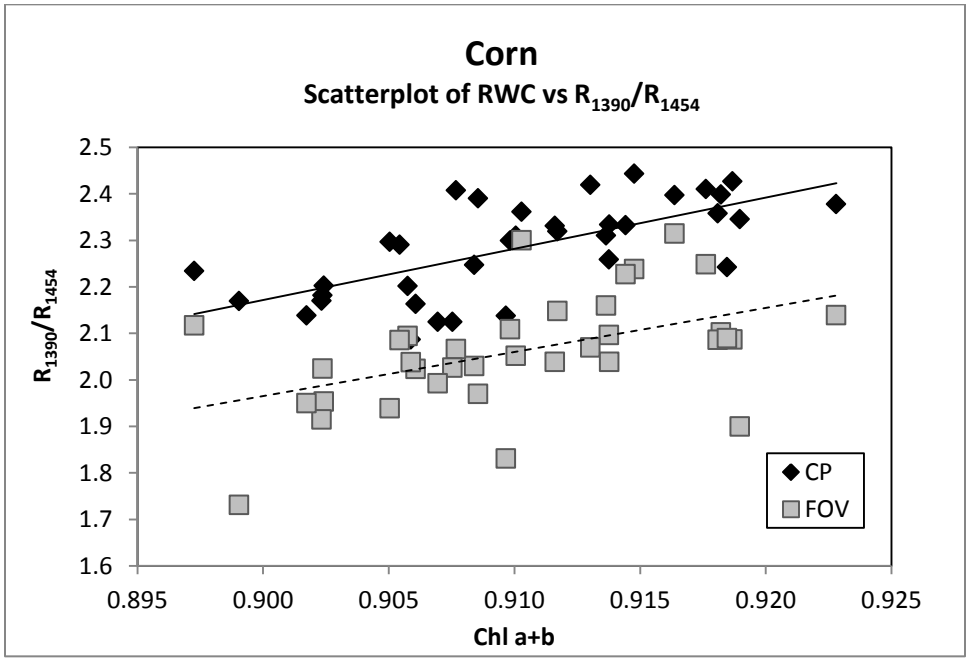

Figure 5.13: Scatterplot of RWC vs R_{1390}/R_{1454} for corn.

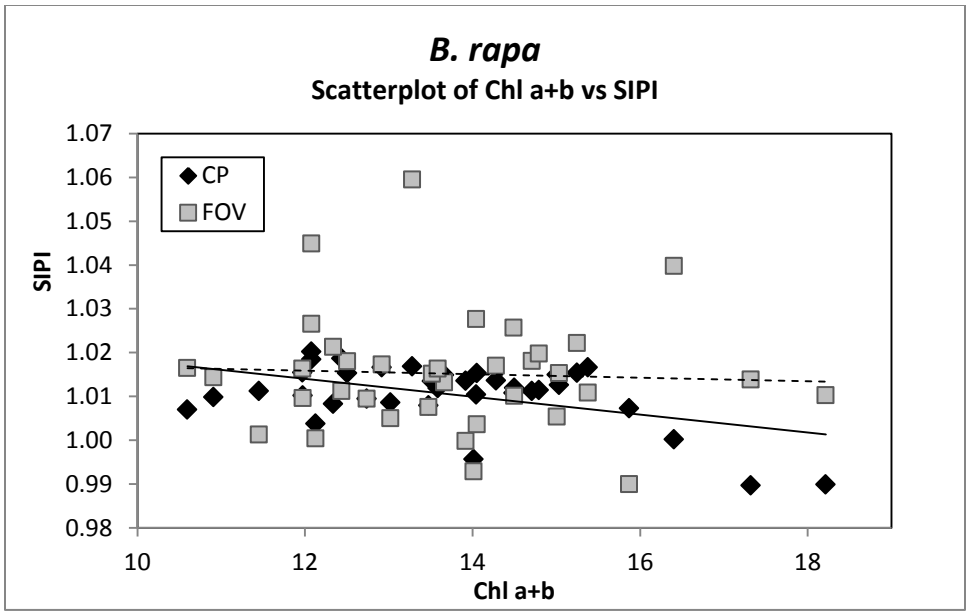

Figure 5.14: Scatterplot of Chl a+b vs SIPI for B. rapa.

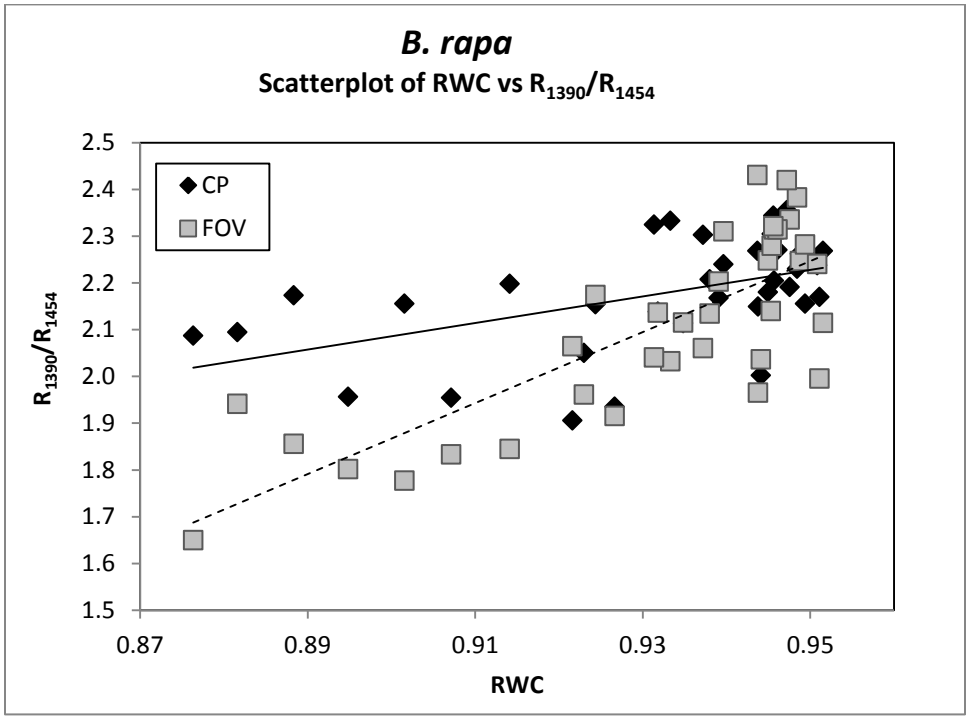

Figure 5.15: Scatterplot of RWC vs R_{1390}/R_{1454} for B. rapa.

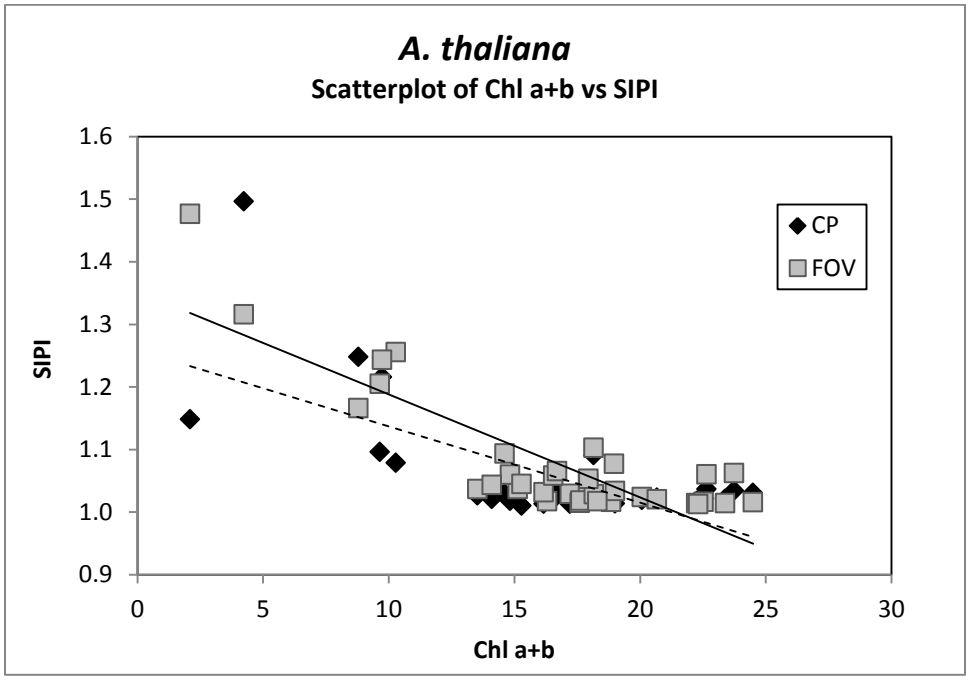

Figure 5.16: Scatterplot of Chl a+b vs SIPI for A. thaliana.

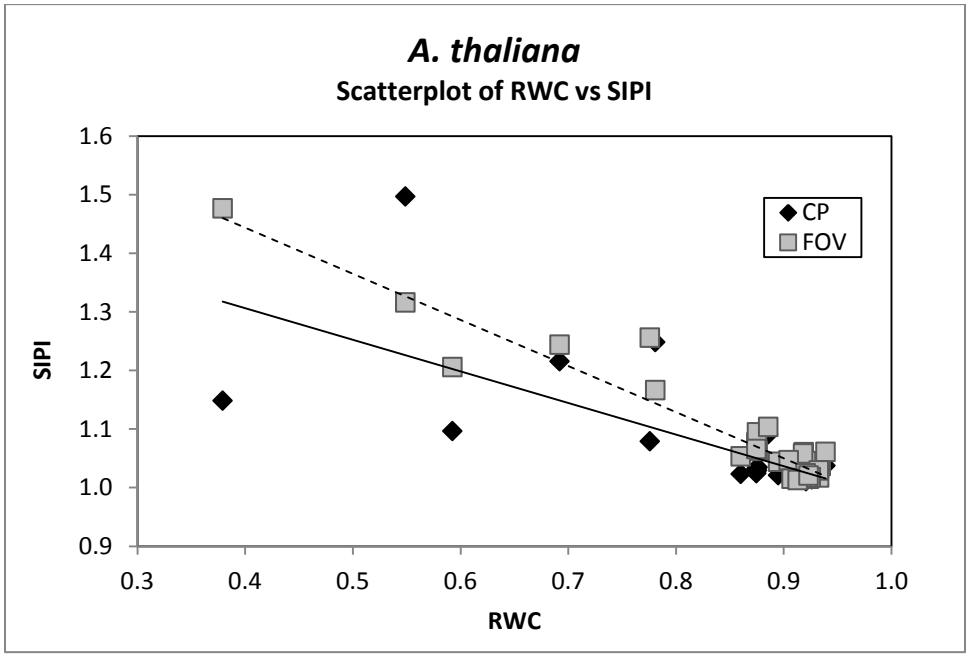

Figure 5.17: Scatterplot of RWC vs SIPI for A. thaliana.

4. Discussion

For *H. annuus, Z. mays,* and *B. rapa* there were few, if any, noticeable differences in CP reflectance spectra between treatment and control groups. There were slight differences in the FOV reflectance spectra of these species, which are discussed below. There were obvious differences in CP spectra and FOV spectra for *A. thaliana*, as well as in endpoints and visual consideration of the *A. thaliana* plants. Thus, Li is shown to be highly toxic to *A. thaliana* and although lithium tolerant mutants exist (Bueso et al. 2007), the wild type (considered here) is not a candidate for phytoremediation of Li contamination.

4.1. Relevant VI

There were six vegetation indices that proved to be the best predictors of relative water content and chlorophyll content, depending on the species. R_{1110}/R_{810}, the best predictor for relative water content in *H. annuus*, has been shown to be related to metal stress (Maruthi-Sridhar et al. 2007a). R_{750}/R_{550} , the best predictor of chlorophyll content in sunflower, was shown by Davids and Tyler (2003) to have some correlation with metal content. PSND (the best predictor of chlorophyll content in *Z. mays*) and SIPI (the best predictor of relative water content and chlorophyll content in *A. thaliana* as well as chlorophyll content in *B. rapa* and relative water content across all species) are related to pigment composition (Penuelas et al. 1995; Serrano 2008). R_{1390}/R_{1454} (the best predictor of relative water content in *Z. mays*, *B. rapa*, and the combination of *H. annuus, B. rapa,* and *Z. mays*) and R_{1676}/R_{1933} (the best predictor of chlorophyll content across all species) were selected by the author based on visual assessment of reflectance spectra collected.

Although R_{950}/R_{750} proved to be one of the best predictors of Cs toxicity in *A. thaliana* in Chapter 4, and there were significant differences in this VI for *A. thaliana* in this study, none of the other species showed a treatment response for this VI (P-values shown in Appendix B4).

4.2. Comparison of plant species

The temporal increase in FOV acquired reflectance (for both treatment and control groups) in the near-IR for sunflower is due to the increase in biomass of the plants (see photographs in Appendix B3). Not only do the plants get taller, and therefore become closer to the fore optics, but there was also an increase in number and size of leaves. Sunflower leaves are broad and grow parallel to horizontal, resulting in a large reflective surface perpendicular to the fore optics. Corn quickly increases in biomass and height, similar to sunflower, although corn leaves are narrow and grow at an angle (as opposed to horizontal), meaning there is less leaf surface directly exposed to the fore optics.

Excess metal exposure negatively affects photosynthetic processes and typically induces a general stress reaction in plants (Sherameti and Varma 2010). Photosynthetic pigments typically decrease with metal exposure, which has obvious consequences for photosynthesis and plant growth. Inhibition of photosynthesis is one effect that most metals have in common when present at toxic concentrations; reduction in photosynthetic efficiency will be seen as an increase in reflectance in the visible range, as less light is being utilized for photosynthesis and chlorophyll production (Thenkabail et al. 2012). *A. thaliana* was the only species to show significant change in chlorophyll content by treatment level (Table 5.2), which corresponds to the increase in reflectance in the visible region. From the boxplot, it appears as if chlorophyll content in *B. rapa* increases slightly in control plants while staying the same for lithium treated plants, although these differences did not prove statistically significant.

Metals can also disrupt the plant-water balance (Thenkabail et al. 2012), which is seen as an increase in reflectance in the mid-infrared region, as water absorbs fairly strongly at 1450 nm, 1940 nm, and 2500 nm (Van der Meer and de Jong SM 2006), with slight increase in the near infrared region (slight water absorption) (Knipling 1970). This is evidenced by the FOV spectra for *B. rapa* in week 3; in the mid-IR region there is less absorbance by the treatment group at wavelengths associated with water

absorption. This is not seen in the corresponding CP spectra, however. It is possible that this is because CP readings are taken in the center of the leaf, and lithium toxicity symptoms are first seen at leaf edges. Water content was significantly altered in *A. thaliana*, with obvious shifts in reflectance spectra. RWC for the treatment group changed in time as the control for *H. annuus* and *Z. mays*, meaning that the shift in water content week to week was not due to lithium exposure.

There will be an increase in light scattering within a plant containing a greater proportion of cell surfaces exposed to intercellular air space, due to different indices of refraction of these materials. As near infrared light is not used for photosynthesis, increasing light scatter in the infrared region means less transmission of light through the plant and more reflection back to the fore optics. Differences in plant structure will therefore affect reflectance of light in the near infrared; larger leaf areas will result in higher reflectance, whereas cell degradation or reduction in leaf thickness will result in lower reflectance, as there will be less light scattering within the plant leaf (Slaton et al. 2001). It appears that there may be structural degradation at week 2 for corn and *B. rapa,* as treatment reflectance is lower than control reflectance, but in week 3 these differences do not appear. There is a slight increase in IR reflectance (treatment compared to control) in week 3 for *B. rapa*, although this is likely due to a reduction in water content, as discussed above.

A. thaliana FOV control reflectance increased in the near IR each week, corresponding to the increase in biomass of the control plants. Treatment reflectance in the near IR was lower than the control reflectance for both the CP and FOV in weeks 2 and 3; the lower CP reflectance indicates a difference in leaf structure. Lower FOV reflectance indicates a lower biomass comparatively, and a shift in the shape indicates a structural difference.

Z. mays, B. rapa, and *A. thaliana* all showed increased reflectance in the treatment group as compared to the control in week 1, and *H. annuus* showed increased reflectance in the treatment group compared to the control in weeks 2 and 3. This implies a possibly stimulatory effect at these time

points. Although *Z. mays* and *H. annuus* did not demonstrate any obvious symptom of lithium toxicity (with one sunflower plant as an exception, see Appendix B3), *B. rapa* did show slight symptoms of toxicity around the leaf edges starting in week 1. However, Kent (1941a, 1941b) suggested that plants could simultaneously experience both stimulatory effects and toxicity symptoms from lithium exposure, due to differing concentrations of lithium within the plant, and McStay (1980) saw stimulated growth along with slight chlorosis in leaves of snap bean (*Phaseolus vulgaris*) exposed to 4 ppm lithium nitrate ($LiNO_3$).

4.3. Comparison of spectra collection techniques

The contact probe was the better predictor for corn and sunflower endpoints, although endpoints for these plants do not provide indication of lithium exposure at the levels considered in this study. Some of the vegetation indices acquired by CP correlated reasonably well with the same indices determined by FOV (Figure 5.18, for example), yet these relationships are inconsistent (Table 5.5).

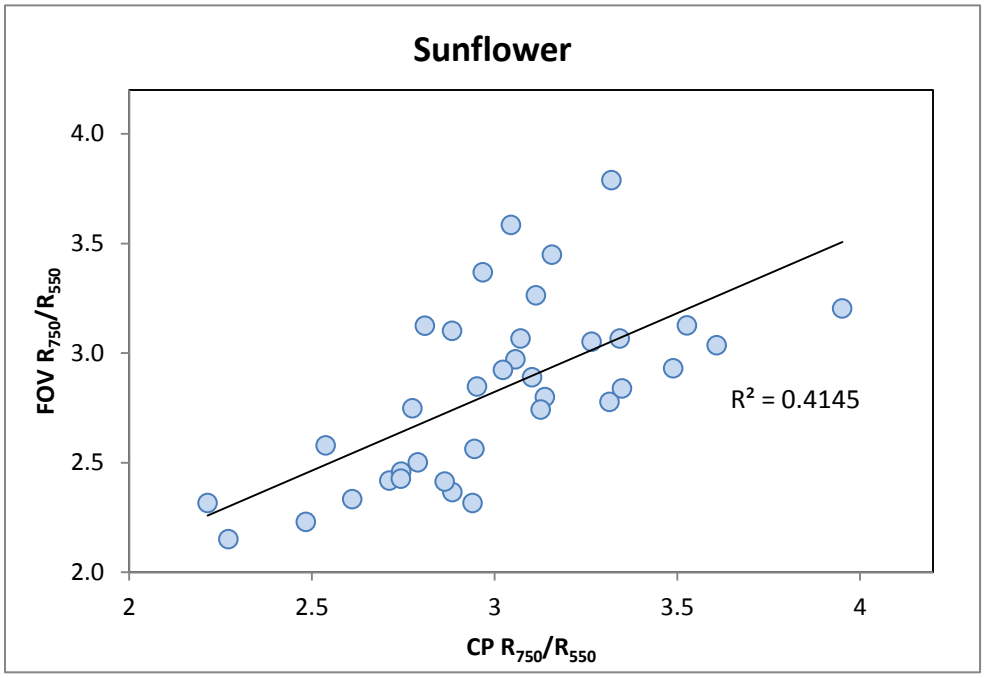

Figure 5.18: Example relationship between FOV and CP; shown for sunflower and R_{750}/R_{550}.

Table 5.5: R^2 (%) values for regression of contact probe and FOV VI values.

Species	VI	R^2 (%) for CP vs FOV
Sunflower	R_{1110}/R_{810}	0.90
	R_{750}/R_{550}	41.5
Corn	R_{1390}/R_{1454}	31.3
	PSND	0.40
B. rapa	R_{1390}/R_{1454}	32.0
	SIPI	7.60
A. thaliana	SIPI	51.4
All species	SIPI	50.2
	R_{1676}/R_{1933}	4.30
H. annuus, Z. mays, B. rapa	R_{1390}/R_{1454}	32.0
	R_{750}/R_{550}	23.6

For example, the relationship between CP and FOV for SIPI is different depending on which species or combination of species is considered. Care should be given applying VI across views as CP and FOV generally provide different results, depending on the endpoint of concern. Different VI should be developed and applied for CP than FOV when utilizing a single reflectance spectra acquisition technique. It is possible that the combination of spectra collection techniques could provide the overall best approximation of plant stress status by accounting for both whole plant and leaf optical properties; multi-index use should be given future consideration in studies utilizing both CP and FOV.

4.4. Comparison of toxicity symptoms in *A. thaliana*

Although treatment levels were different, the early symptoms of Cs and Li toxicity in *A. thaliana* are slightly different. Most noticeably, Cs affected younger leaves while Li affected mature leaves; early symptoms of Cs and Li toxicity for *A. thaliana* are shown in Figure 5.19. The greater effects on mature

leaves may be the result of the greater concentrations that have been reported for Li in older leaves (Hawrylak-Nowak et al. 2012, Naranjo et al. 2003; Kent 1941; McStay et al. 1980).

Figure 5.19: Early symptoms (week 1) of cesium toxicity and lithium toxicity.

Reflectance spectra can be expected to be different for different species, but when treatment reflectance spectra is considered relative to a control, stress may be able to be quantified across species. For example, *B. rapa* and *Z. mays* responded similarly to lithium treatment even though they are very different types of plants, and the same VI were the best predictors of relative water content and chlorophyll content for these species. However, the general difference in toxicity symptoms, as seen between Cs and Li in *A. thaliana*, and seen between species treated with Li, explains why reflectance spectra for different contaminants and species did not always respond in similar ways.

5. Conclusion

From this study, certain vegetation indices seem promising for selected endpoints (Table 5.4) and particular species, especially for *A. thaliana,* but the variable responses of plants to Li makes applying VI across species less reliable. Treating species with different levels of Li to induce a similar level of toxicity may be a more appropriate assessment of vegetation indices than assessing a certain level of Li across all species. Additionally, it would be statistically beneficial to perform these experiments on a larger scale, although the time required to acquire individual spectra by hand is a

limiting factor. Although limited positive results were seen in the laboratory, environmental and sampling conditions were controlled; therefore, care should be given if the intent is to extrapolate to field studies. Measurements taken in the field may not be as consistent or informative as measurements taken in the laboratory due to extraneous and potentially unknown environmental factors. VI determined separately by CP and FOV were occasionally well-related, but this relationship was inconsistent between species, further supporting the conclusion in the previous study that CP and FOV are not interchangeable. These techniques should either be used as compliments or independently, depending on the application.

REFERENCES

Adams ML, Philpot WD, and Norvell WA. 1999. Yellowness index: an application of spectral second derivatives to estimate chlorosis of leaves in stressed vegetation. International Journal of Remote Sensing, 20:3663-3675.

Agelet L and Hurburgh C. 2010. A tutorial on near infrared spectroscopy and its calibration. Critical Reviews in Analytical Chemistry, 40:246-260.

Al-Abbas AH, Barr R, Hall JD, Crane FL, and Baumgardner MF. 1974. Spectra of normal and nutrient-deficient maize leaves. Agronomy Journal, 66:16-20.

Analytical Spectral Devices (ASD). 2002. FieldSpec® Pro: User's Guide. Revision C. Boulder: ASD.

Aral H and Vecchio-Sadus A. 2008. Toxicity of lithium to humans and the environment—a literature revew. Ecotoxicology and Environmental Safety, 70:349-356

Bandaru V. 2010. Quantifying arsenic-induced morphological changes in spinach leaves: Implications for remote sensing. International Journal of Remote Sensing, 31:4163-4177.

Bartolo ME and Carter JV. 1992. Lithium decreases cold-induced microtubule depolymerization in mesophyll cells of spinach. Plant Physiology, 99:1716-1718

Berger B, Parent B, and Tester M. 2010. High-throughput shoot imaging to study drought responses. Journal of Experimental Botany, 61:3519-3528.

Berridge MJ. 1993. Inositol trisphosphate and calcium signaling. Nature, 361:315-325.

Bingham FT, Bradford GR, and Page AL. 1964. Toxicity of lithium to plants. California agriculture, 6-7

Blackmer TM, Schepers JS, and Varvel GE. 1994. Light reflectance compared with other nitrogen stress measurements in corn leaves. Agronomy Journal, 86:934-938.

Bock C, Poole G, Parker P, and Gottwald T. 2010. Plant disease severity estimated visually, by digital photography and image analysis, and by hyperspectral imaging. Critical Reviews in Plant Science, 29:59-107.

Boyko A, Golubov A, Bilichak A, and Kovalchuk I. 2010. Chlorine ions but not sodium ions alter genome stability of *Arabidopsis thaliana*. Plant and Cell Physiology, 51:1066-1078.

Broadley MR and Willey NJ. 1997. Differences in root uptake of radiocesium by 30 plant taxa. Environmental Pollution, 97:11-15.

Broadley MR, Escobar-Gutiérrez AJ, Bowen HC, Willey NJ, and White PJ. 2001. Influx and accumulation of Cs^+ by the akt1 mutant of *Arabidopsis thaliana (L.) Heynh*. lacking a dominant K^+ transport system. Journal of Experimental Botany, 52:839-844.

Bueso E, Alejandro S, Carbonell P, Perez-Amador MA, Fayos J, Belles JM, Rodriguez PL, and Serrano R. 2007. The lithium tolerance of the *Arabidopsis* cat2 mutant reveals cross-talk between oxidative stress and ethylene. The Plant Journal, 52:1052-1065.

Burns D, ed. 2001. Handbook of Near-Infrared Analysis. New York: Marcel Dekker, Inc.

Cameron JR, Daniels F, Johnson N, and Kenney G. 1961. Radiation dosimeter utilizing the thermoluminescence of lithium fluoride. Science, 124:333-334.

Capehart T. 2013. Corn: Background. United States Department of Agriculture: Economic Research Service. www.ers.usda.gov/topics/crops/corn.aspx. Accessed: 13 Feb 2014.

Card D, Peterson D, and Matson P. 1988. Prediction of leaf chemistry by the use of visible and near infrared reflectance spectroscopy. Remote Sensing of Environment, 28:123-147.

Carter G. 1993. Responses of leaf spectral reflectance to plant stress. American Journal of Botany, 80:239-243.

Carter G and Knapp A. 2001. Leaf optical properties in higher plants: Linking spectral characteristics to stress and chlorophyll concentration. American Journal of Botany, 88:677-684.

Chaerle L and Van Der Stragen D. 2000. Imaging techniques and the early detection of plant stress. Trends in Plant Science, 5:495-500.

Collins W, Chang S, Raines G, Canney F, and Ashley R. 1983. Airborne biogeophysical mapping of hidden mineral deposits. Economic Geology, 78:737-749.

Curran PJ, Dungan JL, and Gholz HL. 1990. Exploring the relationship between the reflectance red edge and chlorophyll content in slash pine. Tree Physiology, 7:33-48.

Curran P, Dungan J, Macler B, Plummer S, and Peterson D. 1992. Reflectance spectroscopy of fresh whole leaves for the estimation of chemical concentration. Remote Sensing of Environment, 39:153-166

Crowley KD and Ahearne JF. 2002. Managing the environmental legacy of U.S. nuclear weapons production. American Scientist, 90:514-523.

Daughtry CST, Walthall CL, Kim MS, Brown de Colstoun E, and McMurtey JE III. 2000. Estimating corn leaf chlorophyll concentration from leaf and canopy reflectance. Remote Sensing of Environment, 74:229-239.

Davids C and Tyler A. 2003. Detecting contamination-induced tree stress within the Chernobyl exclusion zone. Remote Sensing of Environment, 85:30-38.

Dunagan S, Gilmore M, and Varekamp J. 2007. Effects of mercury on visible/near-infrared reflectance spectra of mustard spinach plants (*Brassica rapa P*). Environmental Pollution, 148:301-311.

Ercoli L, Mariotti M, Masoni A, and Massantini F. 1993. Relationship between nitrogen and chlorophyll content and spectral properties in corn leaves. European Journal of Agronomy, 2:113-117.

Filella I and Peñuelas J. 1994. The red edge position and shape as indicators of plant chlorophyll content, biomass, and hydric status. International Journal of Remote Sensing, 15:1459-1470.

Gamon G, Peñuelas J, and Field C. 1992. A narrow-waveband spectral index that tracks diurnal changes in photosynthetic efficiency. Remote Sensing of Environment, 41:35-44.

Gates D, Keegan H, Schleter J, and Weidner V. 1965. Spectral properties of plants. Applied Optics, 4:11-20.

Gausman H, Allen W, Cardenas R, and Richardson A. 1970. Relation of light reflectance to histological and physical evaluations of cotton leaf maturity. Applied Optics, 9:545-552.

Gillaspy GE, Keddie JS, Oda K, and Gruissem W. 1995. Plant inositol monophosphatase is a lithium-sensitive enzyme encoded by a multigene family. The Plant Cell, 7:2175-2185.

Gitelson A, Chivkunova O, and Merzlyak M. 2009. Nondestructive estimation of anthocyanins and chlorophylls in anthocyanic leaves. American Journal of Botany, 96:1861-1868.

Grzesiak M, Filek W, Hura T, Kocurek M, and Pilarski J. 2010. Leaf optical properties during and after drought stress in triticale and maize genotypes differing in drought tolerance. Acta Physiologiae Plantarum, 32:433-442.

Hampton CR, Bowen HC, Broadley MR, Hammond JP, Mead A, Payne K, Pritchard J, and White PJ. 2004. Cesium toxicity in *Arabidopsis*. Plant Physiology, 136:3824-3837.

Hawrylak-Nowak B, Kalinowska M, and Szymańska M. 2012. A study on selected physiological parameters of plants grown under lithium supplementation. Biological Trace Element Research, 149:425-430.

Horler D, Dockray M, and Barber J. 1983. The red edge of plant leaf reflectance. International Journal of Remote Sensing, 4:273-288.

Horler D, Barber J, and Barringer A. 1980. Effects of heavy metals on the absorbance and reflectance spectra of plants. International Journal of Remote Sensing, 1:121-136.

International Aatomic Energy Agency (IAEA). 2004. Management of waste containing tritium and carbon-14. Technical Reports Series No. 421. IAEA: Vienna.

International Commission on Radiological Protection (ICRP). 2007. The 2007 Recommendations of the International Commission on Radiological Protection. ICRP Publication 103. Ann. ICRP 37 (2-4).

International Commission on Radiological Protection (ICRP). 2008. Nuclear decay data for dosimetric calculations. ICRP Publication 107. Ann. ICRP 38 (3).

Jones H and Schofield P. 2008. Thermal and other remote sensing of plant stress. General and Applied Plant Physiology, 34:19-32.

Kanter U, Hauser A, Michalke B, Dräxl S, and Schäffner AR. 2010. Cesium and strontium accumulation in shoots of *Arabidopsis thaliana*: Genetic and physiological aspects. Journal of Experimental Botany, 61:3995-4009.

Kent NL. 1941a. Absorption, translocation and ultimate fate of lithium in the wheat plant. New Phytologist, 40:291-298.

Kent NL. 1941b. The influence of lithium salts on certain cultivated plants and their parasitic diseases. Annals of Applied Biology, 28:189-209.

Knapp A and Carter G. 1998. Variability in leaf optical properties among 26 species from a broad range of habitats. American Journal of Botany, 85:940-946.

Knipling E. 1970. Physical and physiological basis for the reflectance of visible and near-infrared radiation from vegetation. Remote Sensing of Environment, 1:155-159.

Knudson LL, Tibbitts TW, and Edwards GE. 1977. Measurement of ozone injury by determination of leaf chlorophyll concentration. Plant Physiology, 60: 606-608.

Kooistra L, Salas E, Clevers J, Wehrens R, Leuven RSEW, Nienhuis PH, and Buydens LMC. 2004. Exploring field vegetation reflectance as an indicator of soil contamination in river floodplains. Environmental Pollution, 127:281-290.

Kszos AL and Stewart AJ. 2003. Review of lithium in the aquatic environment: Distribution in the united states, toxicity and case example of groundwater contamination. Exotoxicology, 12:439-447.

Le Lay P, Isaure MP, Sarry JE, Kuhn L, Fayard B, Le Bail JL, Bastien O, Garin J, Roby C, and Bourguignon J. 2006. Metabolomic, proteomic and biophysical analyses of A*rabidopsis thaliana* cells exposed to a cesium stress. Influence of Potassium Supply. Biochimie, 88:1533-1547.

Li X, Gao P, Gjetvaj B, Westcott N, and Gruber MY. 2009. Analysis of the metabolome and transcriptome of *Brassica carinata* seedlings after lithium chloride exposure. Plant Science, 177:68-80.

Lichtenthaler HK, Gitelson A, and Lang M. 1996. Non-destructive determination of chlorophyll content of leaves of a green and an aurea mutant of tobacco by reflectance measurements. Journal of Plant Physiology, 148:483-493.

Lichtenthaler H, Wenzel O, Buschmann C, and Gitelson A. 1998. Plant stress detection by reflectance and fluorescence. Annals New York Academy of Sciences, 851:271-285

Mariotta M, Ercoli L, and Masoni A. 1996. Spectral properties of iron-deficient corn and sunflower leaves. Remote Sensing of Environment, 58:282-288.

Maruthi-Sridhar BB, Han FX, Diehl SV, Monts DL, and Su Y. 2007a. Monitoring the effects of arsenic and chromium accumulation in chinese brake fern (*Pteris vittata*). International Journal of Remote Sensing, 28:1055-1067.

Maruthi-Sridhar BB, Han FX, Diehl SV, Monts DL, and Su Y. 2007b. Spectral reflectance and leaf internal structure changes of barley plants due to phytoextraction of zinc and cadmium. International Journal of Remote Sensing, 28:1041-1054.

Maruthi-Sridhar BB, Vincent R, Roberts S, and Czajkowski K. 2011. Remote sensing of soybean stress as an indicator of chemical concentration of biosolid amended surface soils. International Journal of Applied Earth Observation and Geoinformation, 13:676-681.

Masoni A, Ercoli L, Mariotti M, and Barberi P. 1994. Changes in spectral properties of ageing and senescing maize and sunflower leaves. Physiologia Plantarum, 91:334-338.

McStay NG, Robers HH, and Anderson CE. 1980. Effects of lithium on *Phaseolus vulgaris L*. The Science of the Total Environment, 16:185-191.

Masoni A, Mariotti M, and Ercoli L. 1997. Effect of water stress and nitrogen nutrition on maize (*Zea mays* L.) leaf spectral properties. Rivista-di-Agronomia, 31:441-448.

Milton N, Ager C, Eiswerth B, and Power M. 1989. Arsenic and selenium induced changes in spectral reflectance and morphology of soybean plants. Remote Sensing of Environment, 30:263-269.

Milton N, Eiswerth B, and Ager C. 1991. Effect of phosphorus deficiency on spectral reflectance and morphology of soybean plants. Remote Sensing of Environment, 36:121-127.

Mulkey TJ. 2005. Alteration of growth and gravitropic response of maize roots by lithium. Gravitational and Space Biology, 18:119-120.

Naranjo, Romero, Belles, Montesinos, Vicente, Serrano. 2003. Lithium treatment induces a hypersensitive-like response in tobacco. Planta, 217:417-424.

The National Science Foundation (NSF). 2013. *Arabidopsis*: The Model Plant. The Multinational Coordinated *Arabidopsis thaliana* Functional Genomics Project. Accessed December 5. http://www.nsf.gov/pubs/2002/bio0202/model.htm#content

Ourcival J, Joffre R, and Rambal S. 1999. Exploring the relationships between reflectance and anatomical and biochemical properties in *Quercus ilex* leaves. New Phytologist, 143:351-364.

Papista E, Acs E, and Boddi B. 2002. Chlorophyll-a determination with ethanol--a critical test. Hydrobiologia, 485:191-198.

Pasquini C. 2003. Near infrared spectroscopy: Fundamentals, practical aspects and analytical applications. Journal of the Brazilian Chemical Society, 14:198-219.

Peng Y and Gitelson A. 2012. Remote estimation of gross primary productivity in soybean and maize based on total crop chlorophyll content. Remote Sensing of Environment, 117:440-448.

Peñuelas J, Gamon JA, Fredeen AL, Merino J, and Field CB. 1994. Reflectance indices associated with physiological changes in nitrogen- and water-limited sunflower leaves. Remote Sensing of Environment, 48:135-146.

Peñuelas J, Baret F, and Filella I. 1995. Semi-empirical indices to assess carotenoids/chlorophyll a ratio from leaf spectral reflectance. Photosynthetica, 31:221-230.

Peñuelas J, Pinol J, Ogaya R, and Filella I. 1997. Estimation of plant water concentration by the reflectance water index WI (R900/R970). International Journal of Remote Sensing, 18:2869-2875.

Peñuelas J and Filella I. 1998. Visible and near-infrared reflectance techniques for diagnosing plant physiological status. Trends in Plant Science, 3:151-156.

Peñuelas J and InoueY. 1999. Reflectance indices indicative of changes in water and pigment contents of peanut and wheat leaves. Photosynthetica, 36:355-360.

Pinder J and McLeod K. 1999. Indications of relative drought stress in longleaf pine from thematic mapper data. Photogrammetric Engineering and Remote Sensing, 65:495-501.

Prasad MNV. 2007. Sunflower (*Helianathus annuus* L.) – a potential crop for environmental industry. Helia, 30:167-174.

Qi Z, Hampton CR, Shin R, Barkla BJ, White PJ, and Schachtman DP. 2008. The high affinity K+ transporter AtHAK5 plays a physiological role in planta at very low K+ concentrations and provides a cesium uptake pathway in *Arabidopsis*. Journal of Experimental Botany, 59:595-607.

Reddy GS, Rao CLN, Venkataratnam L, and Rao PVK. 2001. Influence of plant pigments on spectral reflectance of maize, groundnut and soybean grown in semi-arid environments. International Journal of Remote Sensing, 22:3373-3380.

Ritchie RJ. 2006. Consistent sets of spectrophotometric chlorophyll equations for acetone, methanol and ethanol solvents. Photosynthetic Research, 89:27-41.

Rouse JW, Haas RH, Deering DW, and Sehell JA. Monitoring the vernal advancement and retrogradation (green wave effect) of natural vegetation. Final Rep. RSC 1978-4, Remote Sensing Center, Texas A&M University, College Station.

Sahr T, Voigt G, Paretzke HG, Schramel P, and Ernst D. 2005. Cesium-affected gene expression in *Arabidopsis thaliana*. New Phytologist, 165:747-754.

Salt DE, Blaylock M, Kumar N, Dushenkov V, Ensley BD, Chet I, and Raskin I.1995. Phytoremediation: a novel strategy for the removal of toxic metals from the environment using plants. Biotechnology, 13:468-474.

Salt DE, Smith RD, and Rasin I. 1998. Phytoremediation. Annual Review of Plant Physiology and Plant Molecular Biology, 49:643-668.

Schlemmer M, Gitelson A, Schepers J, Ferguson R, Peng Y, Shanahan J, and Rundquist D. 2013. Remote estimation of nitrogen and chlorophyll contents in maize at leaf and canopy levels. International Journal of Applied Earth Observation and Geoinformation, 25:47-54.

Schrauzer GN. 2002. Lithium: Occurrence, dietary intakes, nutritional essentiality. Journal of the American College of Nutrition, 21:14-21.

Schwaller M, Schnetzler C, and Marshall P. 1981. The changes in leaf reflectance of sugar maple seedlings (*Acer saccharum marsh*) in response to heavy metal stress. NASA Technical Memorandum 82150.

Serbin S, Dillaway D, Kruger E, and Townsend P. 2012. Leaf optical properties reflect variation in photosynthetic metabolism and its sensitivity to temperature. Journal of Experimental Botany, 63:489-502.

Serrano L. 2008. Effects of leaf structure on reflectance estimates of chlorophyll content. International Journal of Remote Sensing, 29:5265-5274.

Sherameti I and Varma A eds. 2010. Soil heavy metals. Soil Biology, Vol 19. Berlin: Springer-Verlag. 492 pp.

Shull C. 1929. A spectrophotometric study of reflection of light from leaf surfaces. Botanical Gazette, 87:583-607.

Sims D and Gamon J. 2002. Relationships between leaf pigment content and spectral reflectance across a wide range of species, leaf structures, and development stages. Remote Sensing of Environment, 81:337-354.

Slaton M, Hunt E, and Smith W. 2001. Estimating near-infrared leaf reflectance from leaf structural characteristics. American Journal of Botany, 88:278-284.

Sneva FA. 1979. Lithium toxicity in seedlings of three cool season grasses. Plant and Soil, 53:219-224.

Su Y, Maruthi-Sridhar BB, Han F, Diehl S, and Monts D. 2007. Effect of bioaccumulation of Cs and Sr natural nuclides and impact of foliar structure and plant spectral reflectance of Indian mustard (*Brassica juncea*). Water Air and Soil Pollution, 180:65-74.

Suter L and Widmer A. 2013. Phenotypic effects of salt and heat stress over three generations in *Arabidopsis thaliana*. PLoS ONE 8:e80819. doi:10.1371/journal.pone.0080819.

Thenkabail PS, Lyon JG, and Huete A. 2012. Hyperspectral remote sensing of vegetation. Boca Raton: CRC Press.

Van der Meer FD and de Jong SM, eds. 2006. Imaging Spectrometry. Dordrecht: Springer.

Vanaja M, Yadav SK, Archana G. Jyothi Lakshmi N, Ram Reddy PR, Vagheera P, Abdul Razak SK, Maheswar M, Venkateswarlu B. 2011. Response of C4 (maize) and C3 (sunflower) crop plants to drought stress and enhanced carbon dioxide concentration. Plant Soil Environment, 57:207-215.

Viña A, Gitelson A, Nguy-Robertson A, and Peng Y. 2011. Comparison of different vegetation indices for the remote assessment of green leaf area index of crops. Remote Sensing of Environment, 115:3468-3478.

Wang Q and Pingheng L. 2012. Hyperspectral indices for estimating leaf biochemical properties in temperate deciduous forests: Comparison of simulated and measured reflectance data sets. Ecological Indicators, 14:56-65.

Wang X, Wang H, Wang J, Sun R, Wu J, Liu S, Bai Y, Mun JH, Bancroft I, Cheng F, Huang S, Li X, Hua W,Wang J, Wang X, Freeling M, Pires JC, Paterson AH, Chalhoub B, Wang B, Hayward A, Sharpe AG, Park BS, Weisshaar B, Liu B, Li B, Liu B, Tong C, Song C, Duran C, Peng C, Geng C, Koh C, Lin C, Edwards D,Mu D, Shen D, Soumpourou E, Li F, Fraser F, Conant G, Lassalle G, King GJ, Bonnema G, Tang H, Wang H, Belcram H, Zhou H, Hirakawa H, Abe H, Guo H, Wang H, Jin H, Parkin IA, Batley J, Kim JS, Just J, Li J,Xu J, Deng J, Kim JA, Li J, Yu J, Meng J, Wang J, Min J, Poulain J, Wang J, Hatakeyama K, Wu K, Wang L,Fang L, Trick M, Links MG, Zhao M, Jin M, Ramchiary N, Drou N, Berkman PJ, Cai Q, Huang Q, Li R,Tabata S, Cheng S, Zhang S, Zhang

S, Huang S, Sato S, Sun S, Kwon SJ, Choi SR, Lee TH, Fan W, Zhao X, Tan X, Xu X, Wang Y, Qiu Y, Yin Y, Li Y, Du Y, Liao Y, Lim Y, Narusaka Y, Wang Y, Wang Z, Li Z, Wang Z,Xiong Z, and Zhang Z; Brassica rapa Genome Sequencing Project Consortium. 2011. The genome of the mesopolyploid crop species *Brassica rapa*. Nature Genetics, 43:1036-1039.

White PJ and Broadley MR. 2000. Tansley Review No. 113. Mechanisms of cesium uptake by plants. New Phytologist, 147:241-256.

White PJ and Broadley MR. 2001. Chloride in soils and its uptake and movement within the plant: a review. Annals of Botany, 88:967-988.

White PJ, Swarup K, Escobar-Gutierrez AJ, Bowen HC, Willey NJ, and Broadley MR. 2003. Selecting plants to minimise radiocesium in the food chain. Plant and Soil, 249:177-186.

Wong KK and He Y. 2013. Estimating grassland chlorophyll content using remote sensing data at leaf, canopy, and landscape scales. Canadian Journal of Remote Sensing, 39:155-166.

Woodhouse R, Heeb M, Berry W, Hoshizake T, and Wood M. 1994. Analysis of remote reflection spectroscopy to monitor plant health. Advances in Space Research, 14:199-202.

Wuana RA and Okieimen FE. 2010. Phytoremediation potential of maize (Zea mays L.). A review. African Journal of General Agriculture, 6:275-287.

Yoder B and Pettigrew-Crosby R. 1995. Predicting nitrogen and chlorophyll content and concentrations from reflectance spectra (400-2500 nm) at leaf and canopy scales. Remote Sensing of Environment, 53:199-211.

Zhao D, Raja Reddy K, Kakani VG, Read JJ, and Carter GA. 2003. Corn (*Zea mays* L.) growth, leaf pigment concentration, photosynthesis and leaf hyperspectral reflectance properties as affected by nitrogen supply. Plant and Soil, 257:205-217.

Zhu YG and Smolders E. 2000. Plant uptake of radiocesium: a review of mechanisms, regulation and application. Journal of Experimental Botany, 51:1635-1645.

APPENDIX B1: DETAILS OF CHAPTER 4 ENDPOINT AND VEGETATION INDEX REGRESSIONS

Regression	Regression Equation	R^2 value	P value
RWC vs $CP_{950/750}$	RWC = 1.85 - 0.959 $CP_{950/750}$	0.330	<0.001
RWC vs $LFOV_{950/750}$	RWC = 1.07 – 0.151 $LFOV_{950/750}$	0.133	0.007
RWC vs $HFOV_{950/750}$	RWC = 1.03 - 0.107 $HFOV_{950/750}$	0.143	0.005
$CP_{950/750}$ vs $LFOV_{950/750}$	$CP_{950/750}$ = 0.847 + 0.120 $LFOV_{950/750}$	0.234	<0.001
$CP_{950/750}$ vs $HFOV_{950/750}$	$CP_{950/750}$ = 0.890 + 0.0780 $HFOV_{950/750}$	0.214	<0.001
$LFOV_{950/750}$ vs $HFOV_{950/750}$	$LFOV_{950/750}$ =0.426 + 0.587 $HFOV_{950/750}$	0.745	<0.001
Chla+b vs $HFOV_{REP}$	Chla+b = - 137 + 0.219 $HFOV_{REP}$	0.249	<0.001
Chla+b vs $LFOV_{REP}$	Chla+b = - 113 + 0.186 $LFOV_{REP}$	0.183	0.001
Chla+b vs CP_{REP}	Chla+b = -164 + 0.260 CP_{REP}	0.010	0.471
CP_{REP} vs $LFOV_{REP}$	CP_{REP} = 651 + 0.0713 $LFOV_{REP}$	0.182	0.001
CP_{REP} vs $HFOV_{REP}$	CP_{REP} = 648 + 0.0757 $HFOV_{REP}$	0.200	0.001
$LFOV_{REP}$ vs $HFOV_{REP}$	$LFOV_{REP}$ = 68.8 + 0.905 $HFOV_{REP}$	0.798	<0.001
CLAI vs $HFOV_{SREP}$	CLAI = 0.105 + 59.3 $HFOV_{SREP}$	0.573	<0.001
CLAI vs $LFOV_{SREP}$	CLAI = 0.109 + 51.8 $LFOV_{SREP}$	0.275	<0.001
CLAI vs CP_{SREP}	CLAI = 0.050 + 48.4 CP_{SREP}	0.059	0.076
CP_{SREP} vs $LFOV_{SREP}$	CP_{SREP} = 0.00931 + 0.130 $LFOV_{SREP}$	0.069	0.055
CP_{SREP} vs $HFOV_{SREP}$	CP_{SREP} = 0.00944 + 0.131 $HFOV_{SREP}$	0.111	0.014
$LFOV_{SREP}$ vs $HFOV_{SREP}$	$LFOV_{SREP}$ = 0.00345 + 0.678 $HFOV_{SREP}$	0.731	<0.001
CLAI vs $HFOV_{SREP}$	CLAI = 0.105 + 59.3 $HFOV_{SREP}$	0.573	<0.001
GF vs $HFOV_{1676/1933}$	GF = - 0.247 + 0.0636 $HFOV_{1676/1933}$	0.785	<0.001
GF vs $LFOV_{1676/1933}$	GF = - 0.230 + 0.0538 $LFOV_{1676/1933}$	0.783	<0.001
GF vs $CP_{1676/1933}$	GF = 0.775 – 0.0378 $CP_{1676/1933}$	0.072	0.049
$CP_{1676/1933}$ vs $LFOV_{1676/1933}$	$CP_{1676/1933}$ = 10.3 – 0.0950 $LFOV_{1676/1933}$	0.048	0.111
$CP_{1676/1933}$ vs $HFOV_{1676/1933}$	$CP_{1676/1933}$ = 10.6 – 0.140 $HFOV_{1676/1933}$	0.075	0.045
$LFOV_{1676/1933}$ vs $HFOV_{1676/1933}$	$LFOV_{1676/1933}$ = 0.432 + 1.11 $HFOV_{1676/1933}$	0.886	<0.001
CF vs $HFOV_{1676/1933}$	CF = 1.29 – 0.0972 $HFOV_{1676/1933}$	0.825	<0.001
CF vs $LFOV_{1676/1933}$	CF = 1.29 – 0.0845 $LFOV_{1676/1933}$	0.867	<0.001
CF vs $CP_{1676/1933}$	CF = 0.066 + 0.0210 $CP_{1676/1933}$	0.010	0.470
$CP_{1676/1933}$ vs $LFOV_{1676/1933}$	$CP_{1676/1933}$ = 10.3 – 0.0950 $LFOV_{1676/1933}$	0.048	0.111
$CP_{1676/1933}$ vs $HFOV_{1676/1933}$	$CP_{1676/1933}$ = 10.6 – 0.140 $HFOV_{1676/1933}$	0.075	0.045
$LFOV_{1676/1933}$ vs $HFOV_{1676/1933}$	$LFOV_{1676/1933}$ = 0.432 + 1.11 $HFOV_{1676/1933}$	0.886	<0.001
RWC vs $LFOV_{WI/NDVI}$	RWC = 1.01 – 0.0788 $LFOV_{WI/NDVI}$	0.241	<0.001
RWC vs $HFOV_{WI/NDVI}$	RWC = 0.993 - 0.0639 $HFOV_{WI/NDVI}$	0.254	<0.001
$LFOV_{WI/NDVI}$ vs $HFOV_{WI/NDVI}$	$LFOV_{WI/NDVI}$ =0.352 + 0.705 $HFOV_{WI/NDVI}$	0.798	<0.001

APPENDIX B2: RATIO OF TREATMENT TO CONTROL MEAN RELATIVE REFLECTANCE

1. *H. annuus*

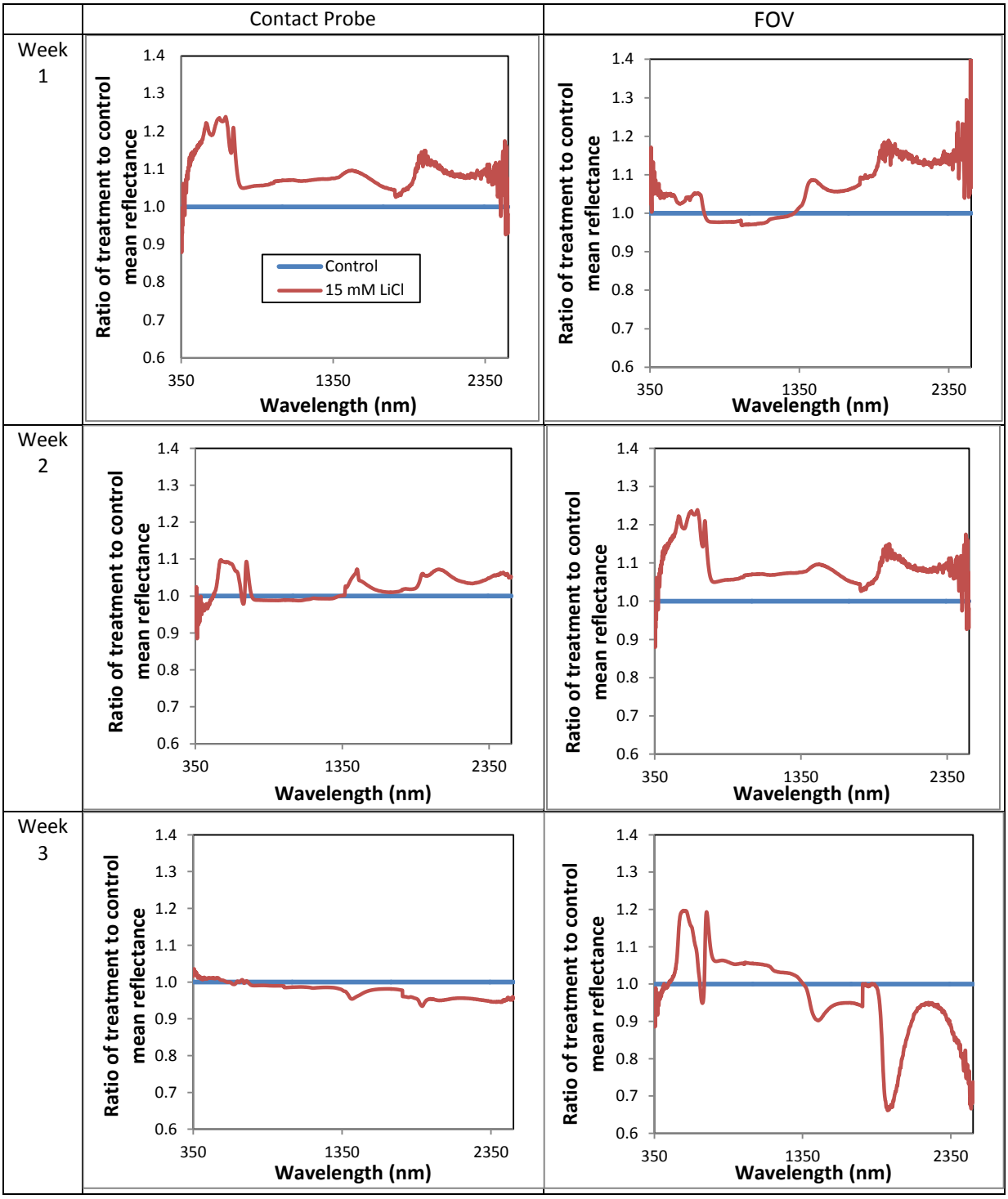

2. *Z. mays*

	Contact Probe	FOV
Week 1	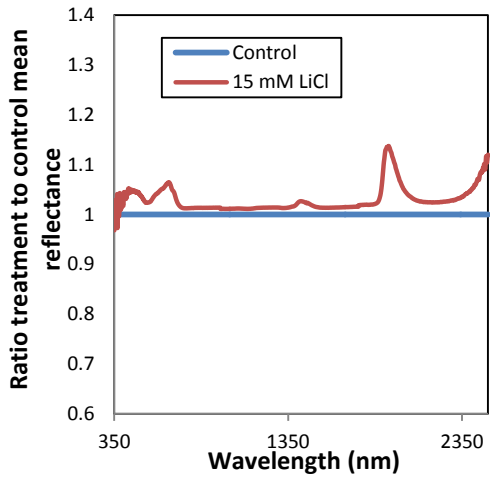	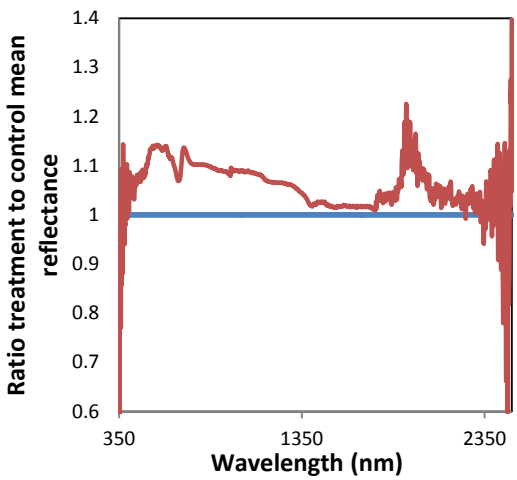
Week 2	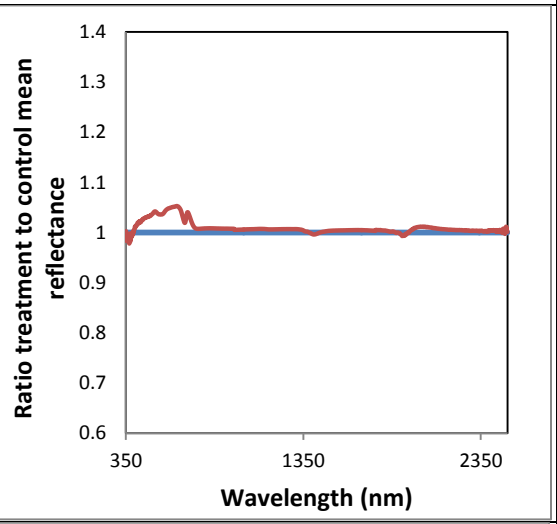	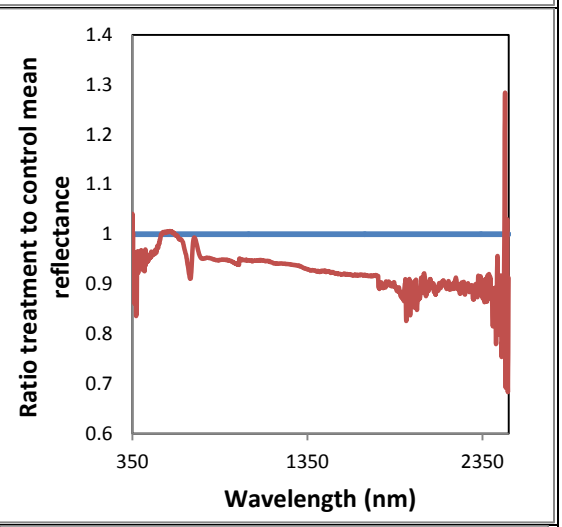
Week 3	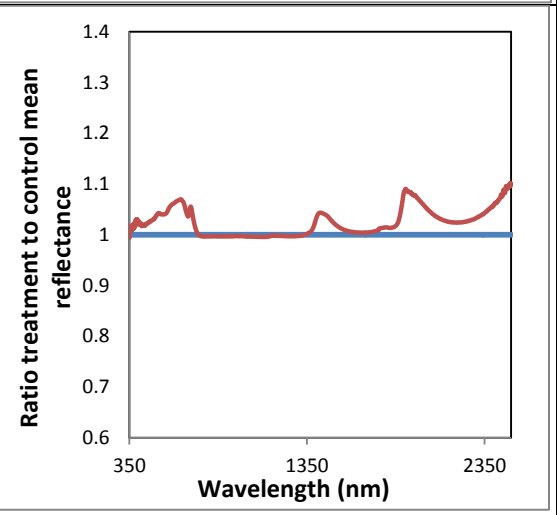	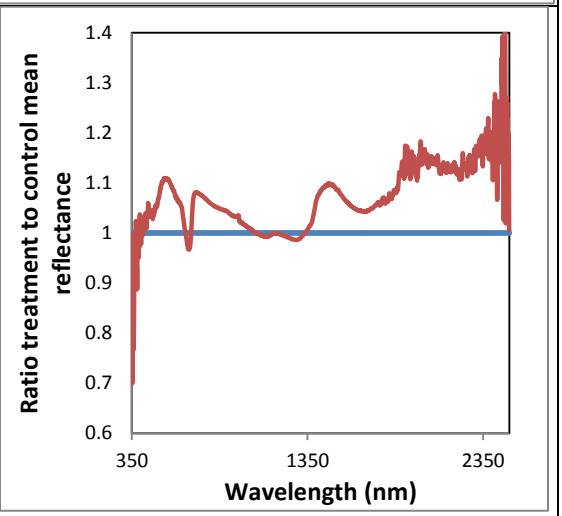

3. *B. rapa*

	Contact Probe	FOV
Week 1	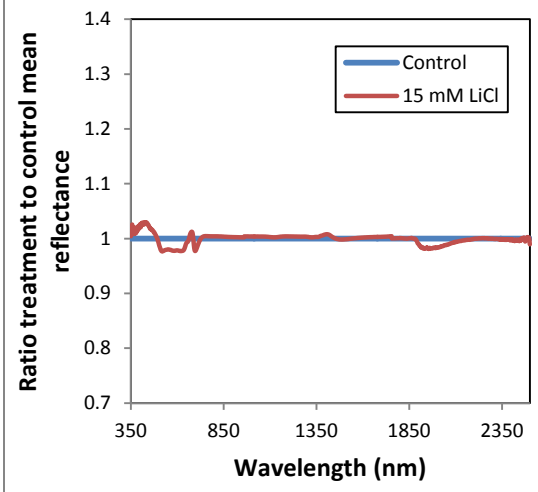	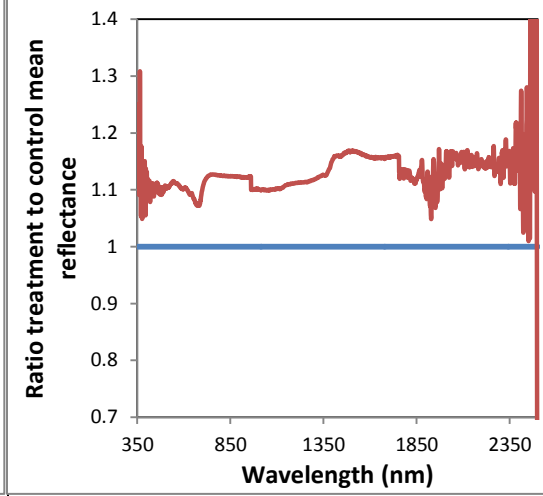
Week 2	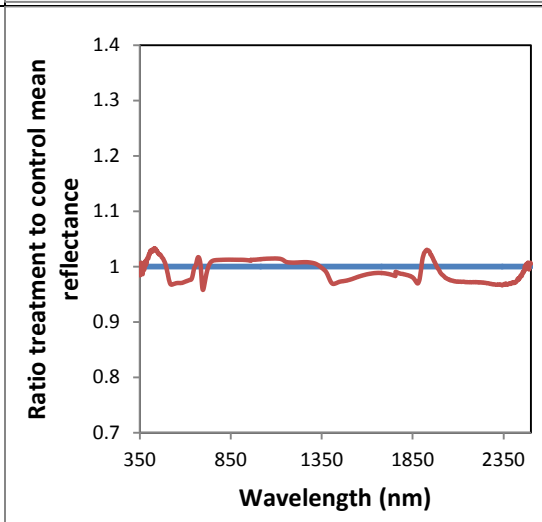	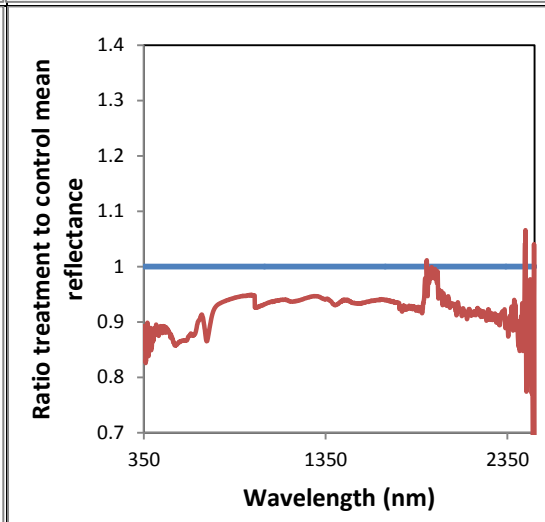
Week 3	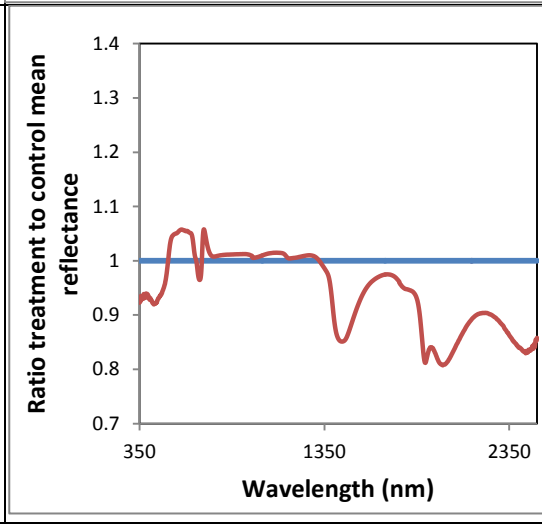	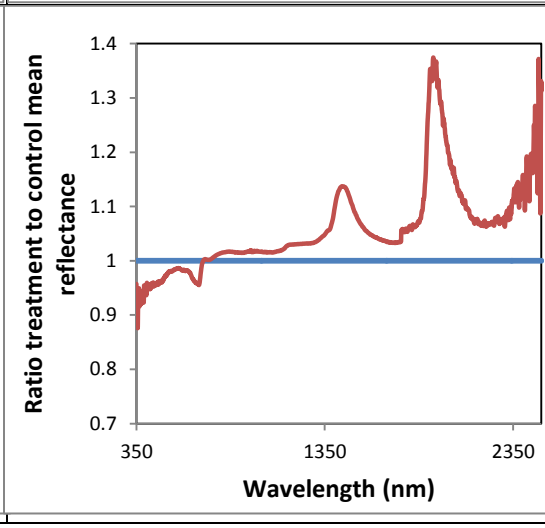

4. *A. thaliana*

4.1. Individual

	Contact Probe	FOV
Week 1	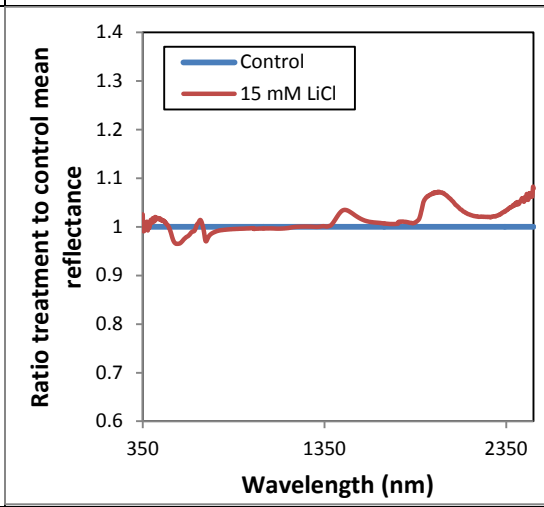	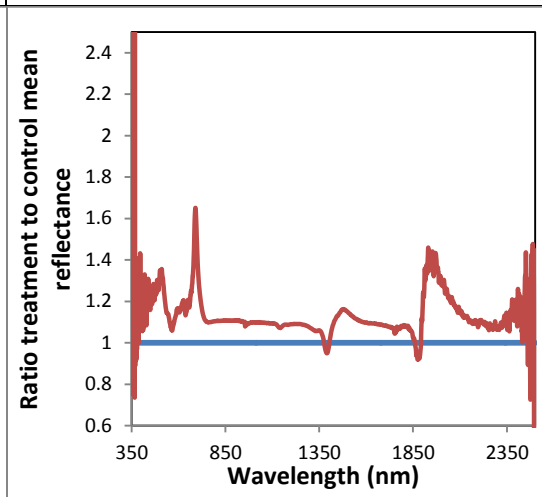
Week 2	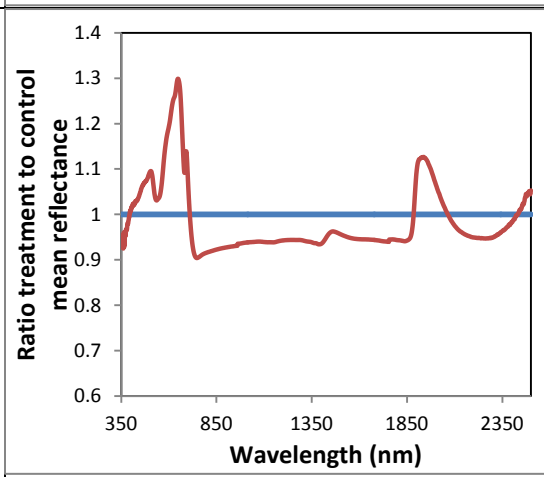	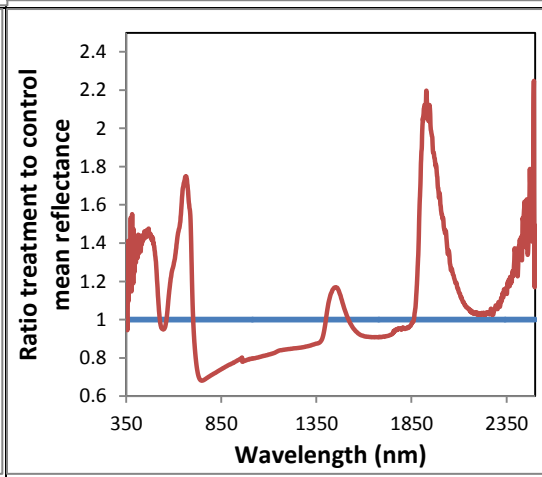
Week 3	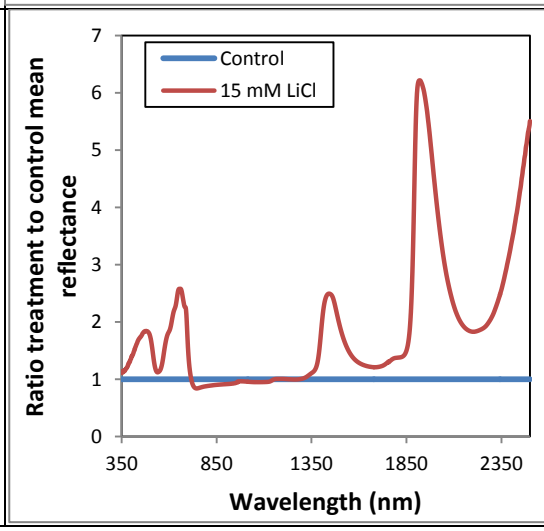	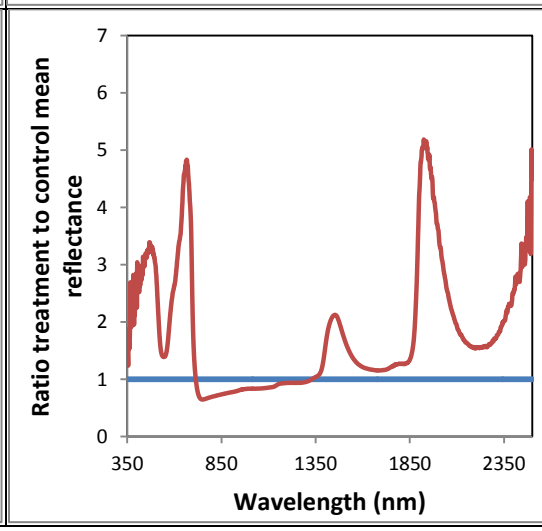

4.2. Each week, as determined by contact probe

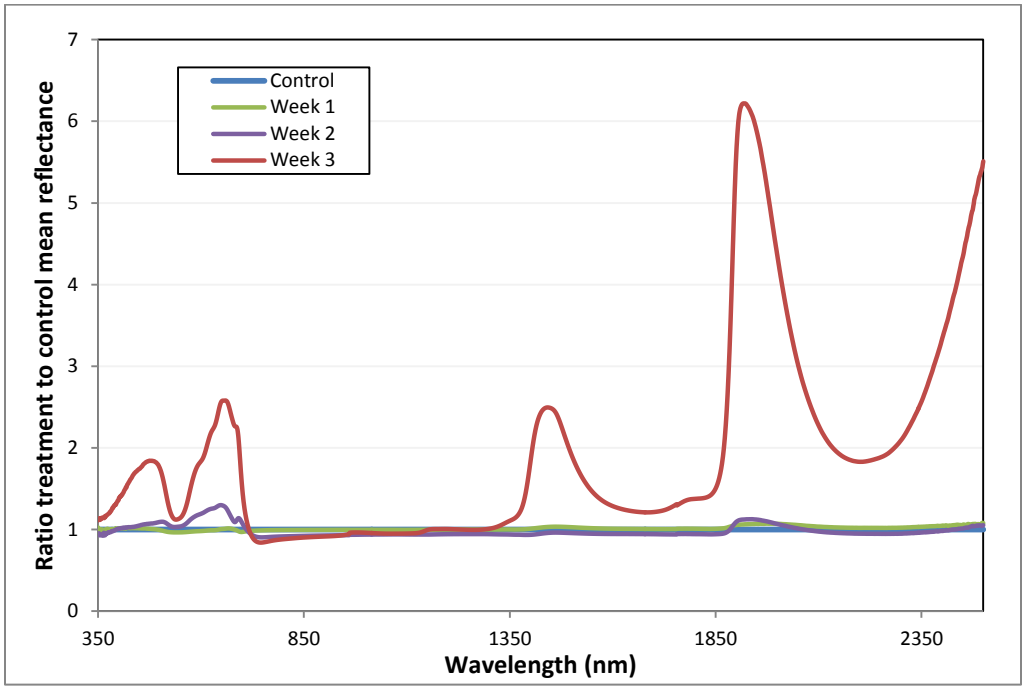

4.3. Each week as determined by field of view

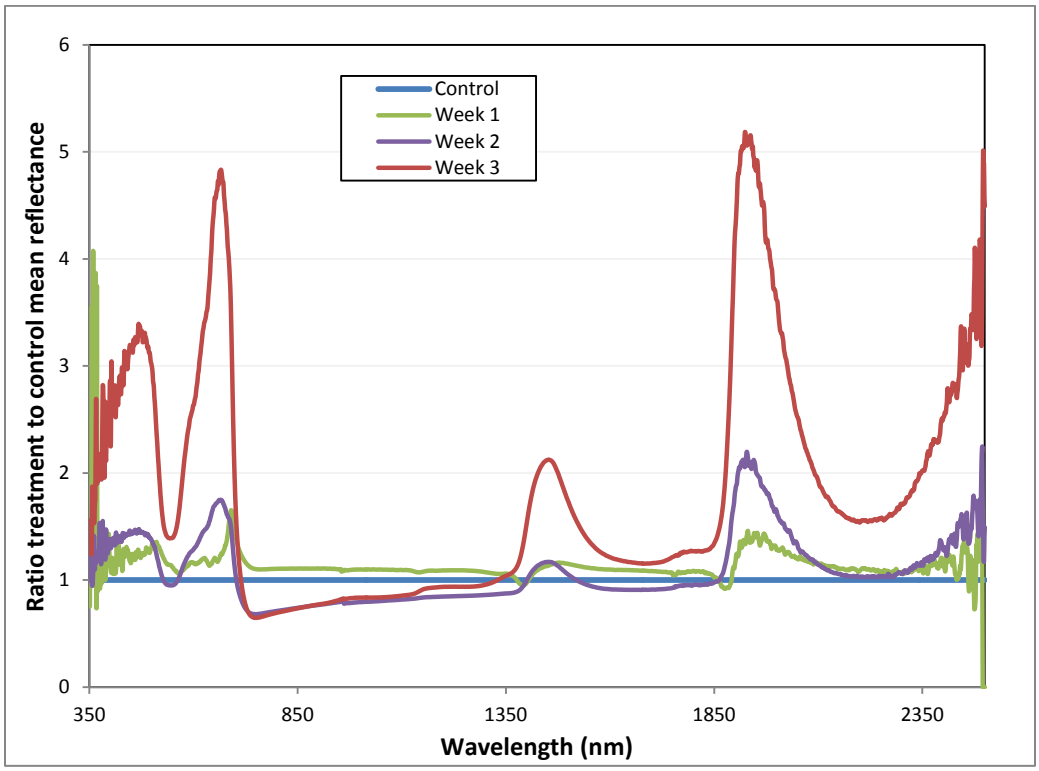

APPENDIX B3: PHOTOGRAPHS OF 15 mM LiCl TREATED PLANTS, WITH CONTROLS

Photographs from the experiments discussed in Chapter 5 are shown in the sections below.

1. *H. annuus*

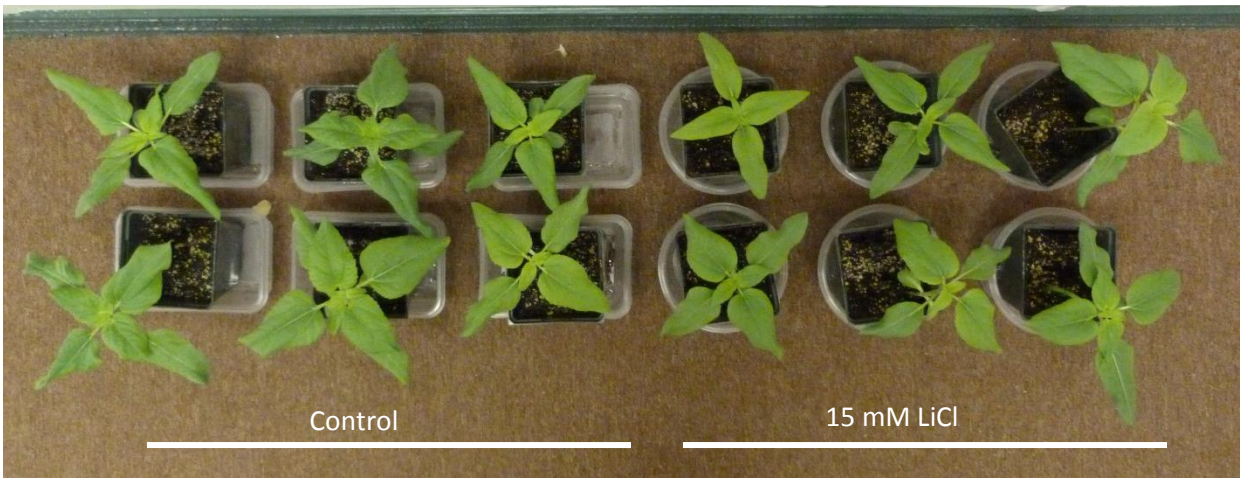

Figure B3.1: Sunflower plants, control and treatment group, week 1 (no flash); round containers hold treatment (15 mM LiCl) pots, and square containers hold control pots (as pictured)

Figure B3.2: Sunflower plants, control and treatment group, week 2 (no flash) ; round containers hold treatment (15 mM LiCl) pots, and square containers hold control pots (as pictured)

Figure B3.3: Sunflower plants, control and treatment group, week 3 (no flash); the treatment group is the six pots on the right hand side of the picture (as shown)

Figure B3.4: Sunflower plants, control and treatment group, week 3 (flash); the treatment group is the six pots in the right hand picture

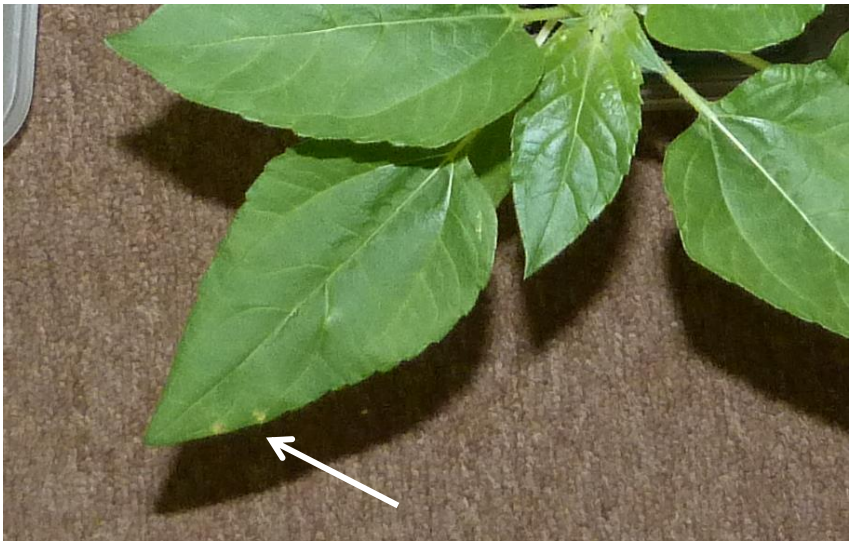

Figure B3.5: Example of slight Li toxicity in a sunflower plant (week 3, with flash): small spots of chlorosis on the tip of a mature leaf (arrow). This particular plant is also pictured in the bottom row, second from right in Figure B3.4.

2. *B. rapa*

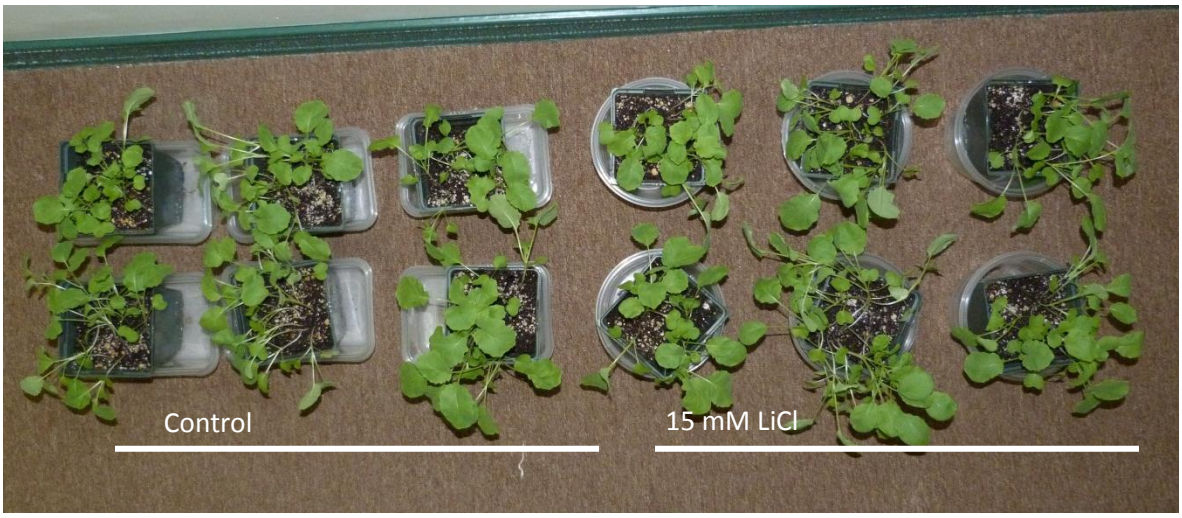

Figure B3.6: B. rapa plants, control and treatment group, week 1 (flash) ; round containers hold treatment (15 mM LiCl) pots, and square containers hold control pots (as pictured)

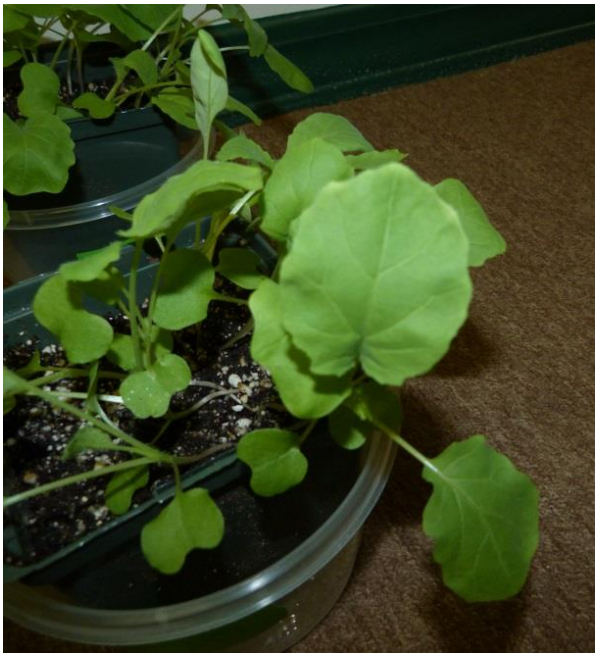

Figure B3.7: B. rapa plant, week 1 (flash); example of slight chlorosis around the edges of the leaf

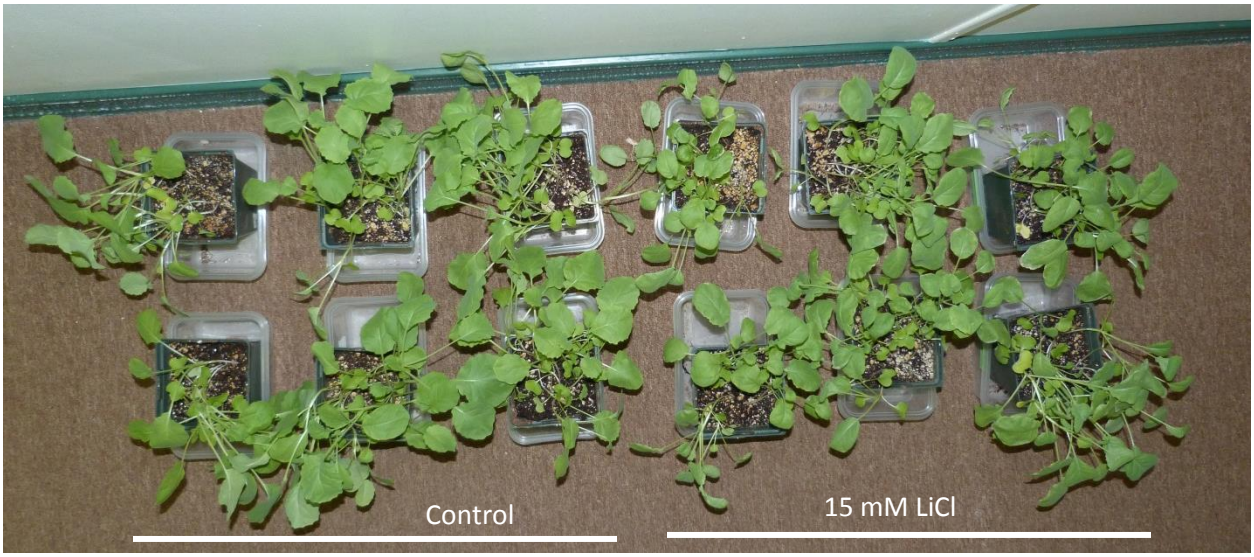

Figure B3.8: B. rapa plants, control and treatment group, week 2 (flash); the treatment group is the six pots on the right hand side

Figure B3.9: B. rapa plant, week 2 (flash); example of necrosis and chlorosis around the edges of the leaves

Figure B3.10: B. rapa plants, control and treatment group, week 3 (flash); the treatment group is the six pots on the right hand side

Figure B3.11: B. rapa plant, week 3 (flash)

3. *Z. mays*

Figure B3.12: Corn plants, control and treatment group, week 1 (no flash); the treatment group is the six pots on the right hand side

Figure B3.13: Corn plants, control and treatment group, week 1 (no flash); the treatment group is the six pots on the right hand side

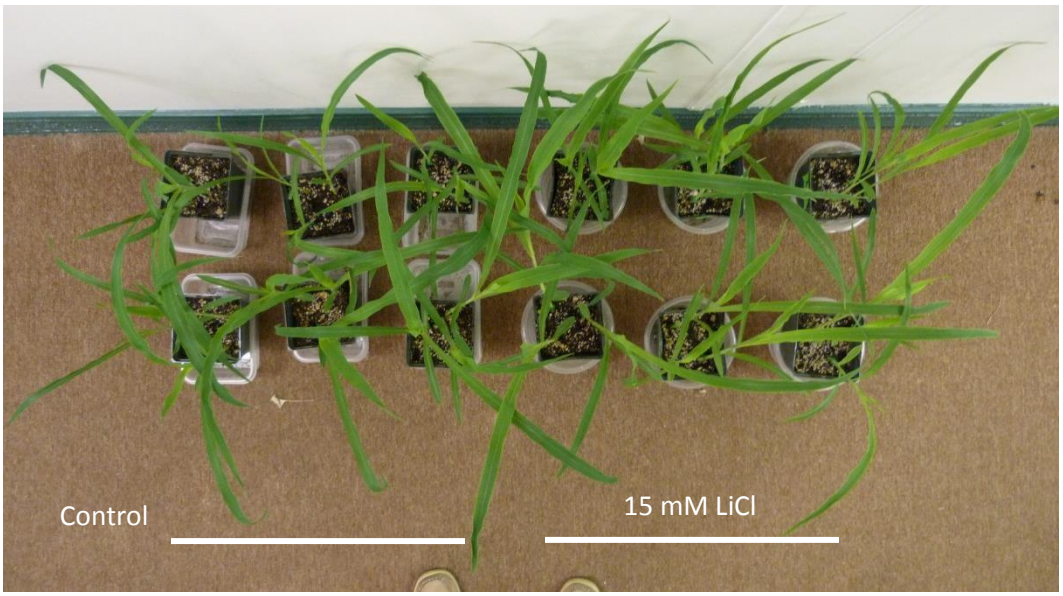

Figure B3.14: Corn plants, control and treatment group, week 2 (no flash); round containers hold treatment (15 mM LiCl) pots, and square containers hold control pots (as pictured)

Figure B3.15: Corn plants, control and treatment group, week 2 (no flash); round containers hold treatment (15 mM LiCl) pots, and square containers hold control pots (as pictured)

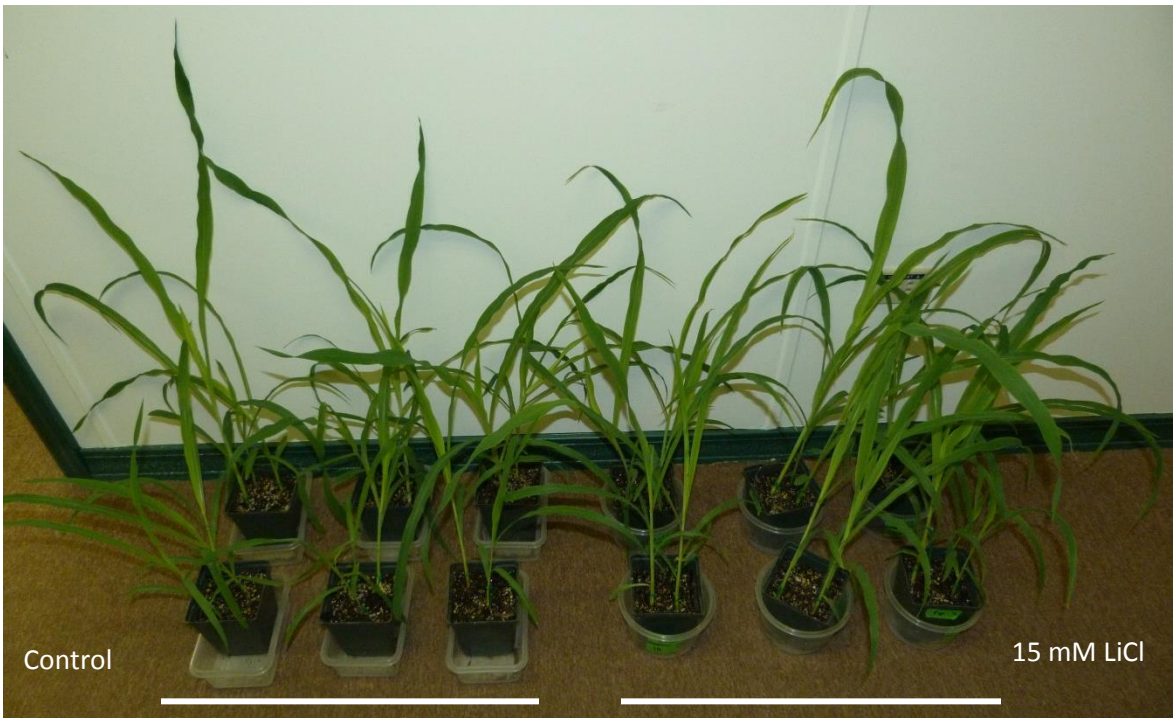

Figure B3.16: Corn plants, control and treatment group, week 3 (no flash); round containers hold treatment (15 mM LiCl) pots, and square containers hold control pots (as pictured)

4. *A. thaliana*

Figure B3.17: A. thaliana plants, control and treatment group, week 1 (flash); round containers on the right hand side hold treatment (15 mM LiCl) pots, and square containers hold control pots (as pictured)

Figure B3.18: A. thaliana plants, control and treatment group, week 2 (flash); round containers on the right hand side hold treatment (15 mM LiCl) pots, and square containers hold control pots (as pictured)

Figure B3.19: A. thaliana plants, control and treatment group, week 3 (flash); round containers on the right hand side hold treatment (15 mM LiCl) pots, and square containers hold control pots (as pictured)

APPENDIX B4: ANOVA RESULTS

Table B4.1: ANOVA results (p-values) for H. annuus

	RWC	Chl a+b
Tmt Level	0.514	0.200
Week	**0.003**	**<0.001**
Interaction	0.404	0.955

	NDVI		PRI		WI		SIPI	
	FOV	CP	FOV	CP	FOV	CP	FOV	CP
Tmt Level	0.677	--	0.494	0.598	0.721	0.282	0.322	0.449
Week	0.084	--	**<0.001**	**0.025**	**0.002**	**<0.001**	**0.036**	0.086
Interaction	**0.007**	--	0.621	0.573	0.247	0.269	0.185	0.723

	PSND		YI		1110/810		950/750	
	FOV	CP	FOV	CP	FOV	CP	FOV	CP
Tmt Level	0.736	0.417	0.151	0.713	0.950	**0.008**	0.620	0.307
Week	0.079	0.107	**<0.001**	0.931	0.683	**<0.001**	0.686	**<0.001**
Interaction	**0.006**	0.592	0.665	0.618	0.211	**0.005**	0.160	0.955

	750/550		725/625		1390/1454		1676/1933	
	FOV	CP	FOV	CP	FOV	CP	FOV	CP
Tmt Level	**0.003**	0.135	0.735	0.933	0.604	**0.020**	0.254	0.096
Week	**<0.001**	**0.015**	**0.001**	**0.008**	**<0.001**	0.242	**<0.001**	0.959
Interaction	0.459	0.749	**0.002**	0.222	**0.001**	0.152	**<0.001**	0.159

Table B4.2: ANOVA results (p-values) for Z. mays

	RWC	Chl a+b
Tmt Level	0.206	0.169
Week	**<0.001**	**<0.001**
Interaction	0.249	0.293

	NDVI		PRI		WI		SIPI	
	FOV	CP	FOV	CP	FOV	CP	FOV	CP
Tmt Level	0.551	--	0.804	**0.001**	0.569	0.523	0.469	0.172
Week	**0.011**	--	0.505	**0.002**	**0.001**	**0.009**	0.057	**<0.001**
Interaction	0.979	--	0.819	0.582	0.687	0.814	0.863	0.238

	PSND		YI		1110/810		950/750	
	FOV	CP	FOV	CP	FOV	CP	FOV	CP
Tmt Level	0.480	**0.043**	**0.020**	**0.004**	0.181	0.473	0.221	0.773
Week	**0.016**	**<0.001**	**<0.001**	**0.046**	**0.000**	0.542	**<0.001**	**<0.001**
Interaction	0.994	0.658	0.596	0.254	0.595	0.975	0.851	0.779

	750/550		725/625		1390/1454		1676/1933	
	FOV	CP	FOV	CP	FOV	CP	FOV	CP
Tmt Level	0.141	0.173	0.292	0.052	0.488	0.371	0.494	0.064
Week	**0.002**	0.081	**0.007**	**<0.001**	0.115	**<0.001**	0.165	**0.005**
Interaction	0.857	0.875	0.882	0.584	0.468	0.790	0.928	0.331

Table B4.3: ANOVA results (p-values) for B. rapa

	RWC	Chl a+b
Tmt Level	**0.003**	0.102
Week	**<0.001**	0.103
Interaction	0.206	0.063

	NDVI		PRI		WI		SIPI	
	FOV	CP	FOV	CP	FOV	CP	FOV	CP
Tmt Level	0.282	--	0.267	**0.005**	0.061	0.205	0.773	0.486
Week	0.078	--	0.113	**<0.001**	0.774	**<0.001**	0.616	**<0.001**
Interaction	0.739	--	0.428	**0.021**	0.310	0.050	0.703	**0.029**

	PSND		YI		1110/810		950/750	
	FOV	CP	FOV	CP	FOV	CP	FOV	CP
Tmt Level	0.220	0.145	0.906	0.535	0.470	0.389	0.215	0.712
Week	0.096	**<0.001**	0.113	**<0.001**	**0.008**	**<0.001**	**0.007**	**<0.001**
Interaction	0.810	**0.045**	0.572	**<0.001**	0.587	0.395	0.291	0.243

	750/550		725/625		1390/1454		1676/1933	
	FOV	CP	FOV	CP	FOV	CP	FOV	CP
Tmt Level	0.106	0.580	0.388	0.504	0.253	**0.003**	0.388	**0.015**
Week	**0.005**	**0.001**	**0.008**	**<0.001**	**<0.001**	**<0.001**	**<0.001**	**<0.001**
Interaction	0.634	**0.013**	0.882	**0.005**	0.864	**0.005**	0.419	**<0.001**

Table B4.4: ANOVA results (p-values) for A. thaliana

	RWC	Chl a+b
Tmt Level	**<0.001**	**<0.001**
Week	**<0.001**	**0.001**
Interaction	**<0.001**	**<0.001**

	NDVI		PRI		WI		SIPI	
	FOV	CP	FOV	CP	FOV	CP	FOV	CP
Tmt Level	**<0.001**	--	**<0.001**	**<0.001**	**0.007**	**<0.001**	**<0.001**	**0.003**
Week	**<0.001**	--	**<0.001**	**<0.001**	0.452	**<0.001**	**<0.001**	**<0.001**
Interaction	**<0.001**	--	**<0.001**	**<0.001**	**0.002**	**<0.001**	**<0.001**	**<0.001**

	PSND		YI		1110/810		950/750	
	FOV	CP	FOV	CP	FOV	CP	FOV	CP
Tmt Level	**<0.001**	**<0.001**	**<0.001**	**<0.001**	**<0.001**	**<0.001**	**<0.001**	**<0.001**
Week	**<0.001**	**<0.001**	**<0.001**	**<0.001**	0.108	**<0.001**	**<0.001**	**<0.001**
Interaction	**<0.001**	**<0.001**	**<0.001**	**<0.001**	**<0.001**	**<0.001**	**<0.001**	**<0.001**

	750/550		725/625		1390/1454		1676/1933	
	FOV	CP	FOV	CP	FOV	CP	FOV	CP
Tmt Level	**<0.001**	**<0.001**	**<0.001**	**<0.001**	**<0.001**	**<0.001**	**<0.001**	**<0.001**
Week	0.656	**0.003**	0.054	**<0.001**	**0.003**	**<0.001**	**<0.001**	**<0.001**
Interaction	**<0.001**	**<0.001**	**<0.001**	**<0.001**	**<0.001**	**<0.001**	**<0.001**	**<0.001**

Table B4.5: ANOVA results (p-values) across all species

	RWC	Chl a+b
Tmt	**0.001**	**0.005**
Week	**<0.001**	**0.008**
Species	**<0.001**	**<0.001**

	NDVI		PRI		WI		SIPI	
	FOV	CP	FOV	CP	FOV	CP	FOV	CP
Tmt	**0.001**	--	**0.033**	**<0.001**	0.769	**0.042**	**0.006**	**0.021**
Week	**0.048**	--	**0.005**	**0.010**	0.243	0.232	0.081	**0.018**
Species	**<0.001**	--	0.396	**<0.001**	**0.026**	**<0.001**	**<0.001**	**<0.001**

	PSND		YI		1110/810		950/750	
	FOV	CP	FOV	CP	FOV	CP	FOV	CP
Tmt	**0.001**	**0.002**	**<0.001**	**<0.001**	**0.067**	**0.003**	**0.003**	**<0.001**
Week	0.057	**<0.001**	0.245	**0.019**	0.053	0.927	0.476	0.341
Species	**<0.001**	**<0.001**	**<0.001**	**<0.001**	**<0.001**	**<0.001**	**<0.001**	**<0.001**

	750/550		725/625		1390/1454		1676/1933	
	FOV	CP	FOV	CP	FOV	CP	FOV	CP
Tmt	**<0.001**	**0.001**	**<0.001**	**<0.001**	**<0.001**	**0.003**	**<0.001**	**<0.001**
Week	0.147	0.543	0.428	**<0.001**	**<0.001**	**<0.001**	**<0.001**	**<0.001**
Species	**<0.001**	**<0.001**	**<0.001**	**<0.001**	**<0.001**	**<0.001**	**0.001**	**<0.001**

Table B4.6: ANOVA results (p-values) across all species, excluding A. thaliana

	RWC	Chl a+b
Tmt	0.009	0.542
Week	**<0.001**	0.027
Species	**<0.001**	**<0.001**

	NDVI		PRI		WI		SIPI	
	FOV	CP	FOV	CP	FOV	CP	FOV	CP
Tmt	0.393	--	0.528	0.058	0.244	0.258	0.346	0.620
Week	**0.036**	--	0.062	**<0.001**	**0.033**	0.247	**0.010**	0.351
Species	**<0.001**	--	**<0.001**	**<0.001**	0.203	**<0.001**	**<0.001**	**<0.001**

	PSND		YI		1110/810		950/750	
	FOV	CP	FOV	CP	FOV	CP	FOV	CP
Tmt	0.299	0.318	0.142	0.304	0.175	0.496	0.567	0.763
Week	0.058	**<0.001**	0.279	0.050	**<0.001**	**<0.001**	**<0.001**	**<0.001**
Species	**<0.001**	**<0.001**	**<0.001**	**<0.001**	**<0.001**	**<0.001**	**<0.001**	**<0.001**

	750/550		725/625		1390/1454		1676/1933	
	FOV	CP	FOV	CP	FOV	CP	FOV	CP
Tmt	0.076	0.084	0.216	0.436	0.399	0.609	0.595	0.130
Week	**<0.001**	0.067	**0.013**	**<0.001**	**<0.001**	**<0.001**	**<0.001**	**<0.001**
Species	**<0.001**	**<0.001**	**<0.001**	**<0.001**	**<0.001**	**<0.001**	**<0.001**	**<0.001**

APPENDIX B5: BOXPLOTS FOR SELECTED VEGETATION INDICES

1. Field of view

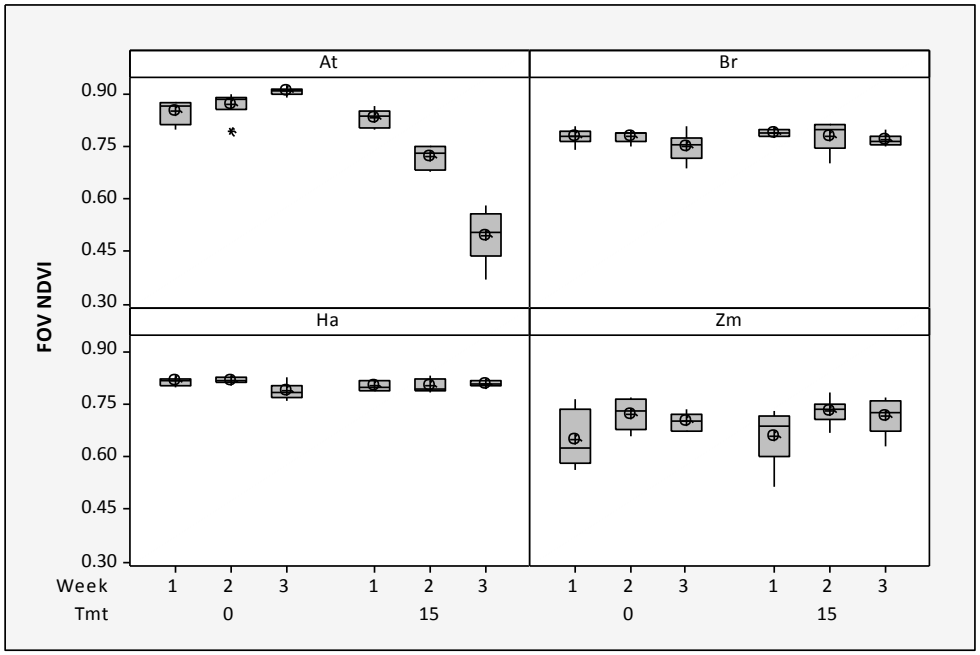

Figure B5.1: Boxplot of NDVI determined by FOV for A. thaliana, B. rapa, H. annuus, and Z. mays by week and treatment level

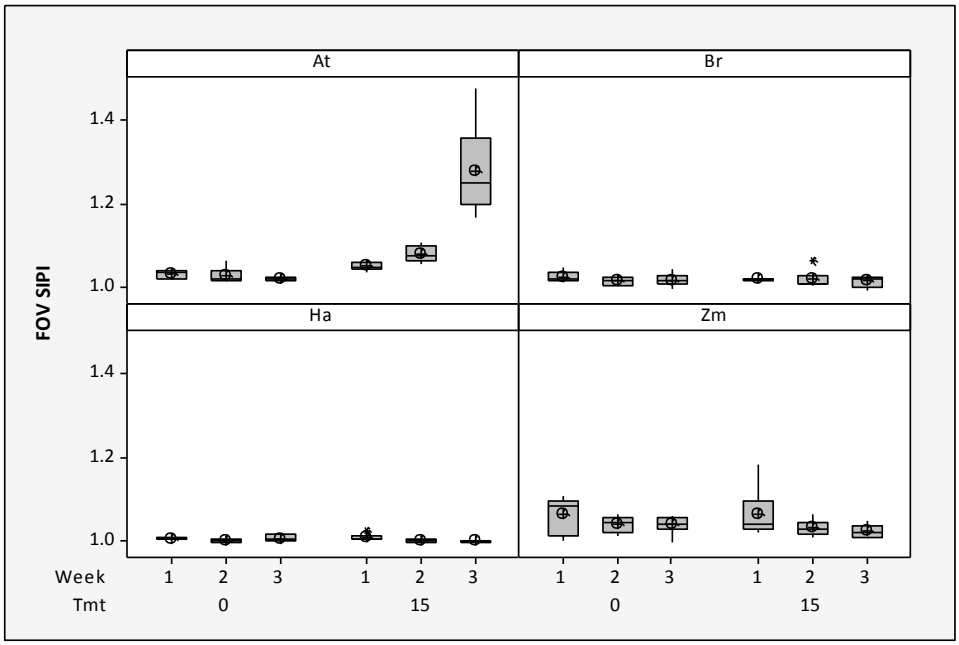

Figure B5.2: Boxplot of SIPI determined by FOV for A. thaliana, B. rapa, H. annuus, and Z. mays by week and treatment level

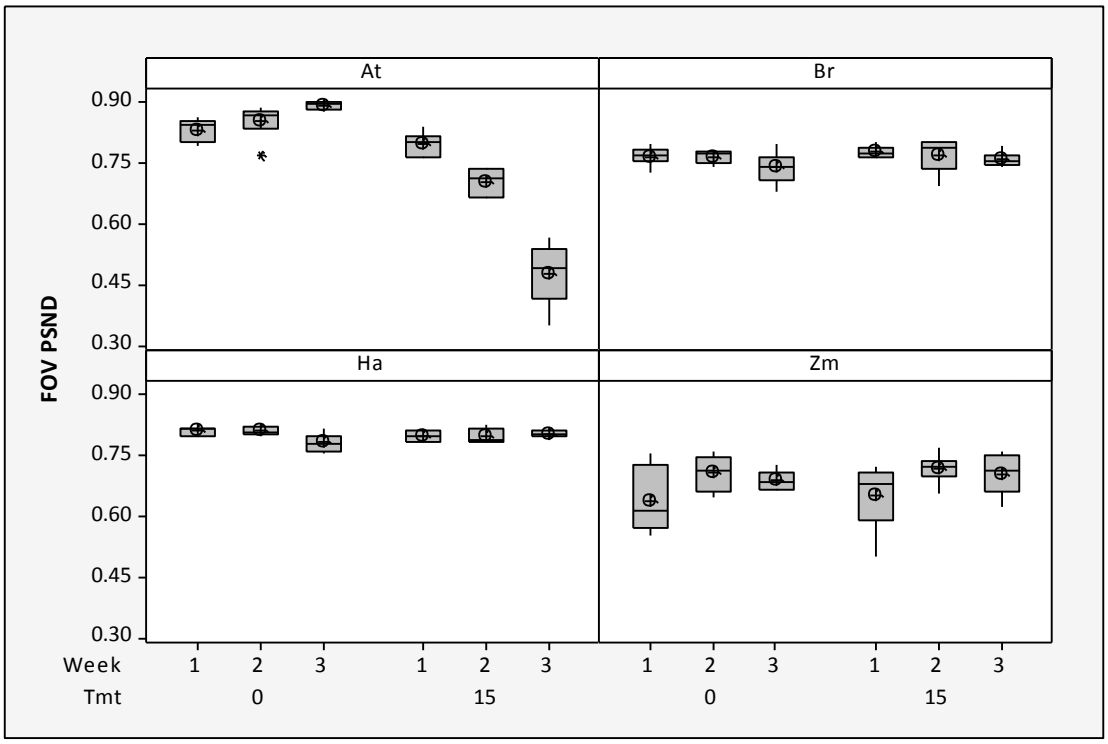

Figure B5.3: Boxplot of PSND determined by FOV for A. thaliana, B. rapa, H. annuus, and Z. mays by week and treatment level

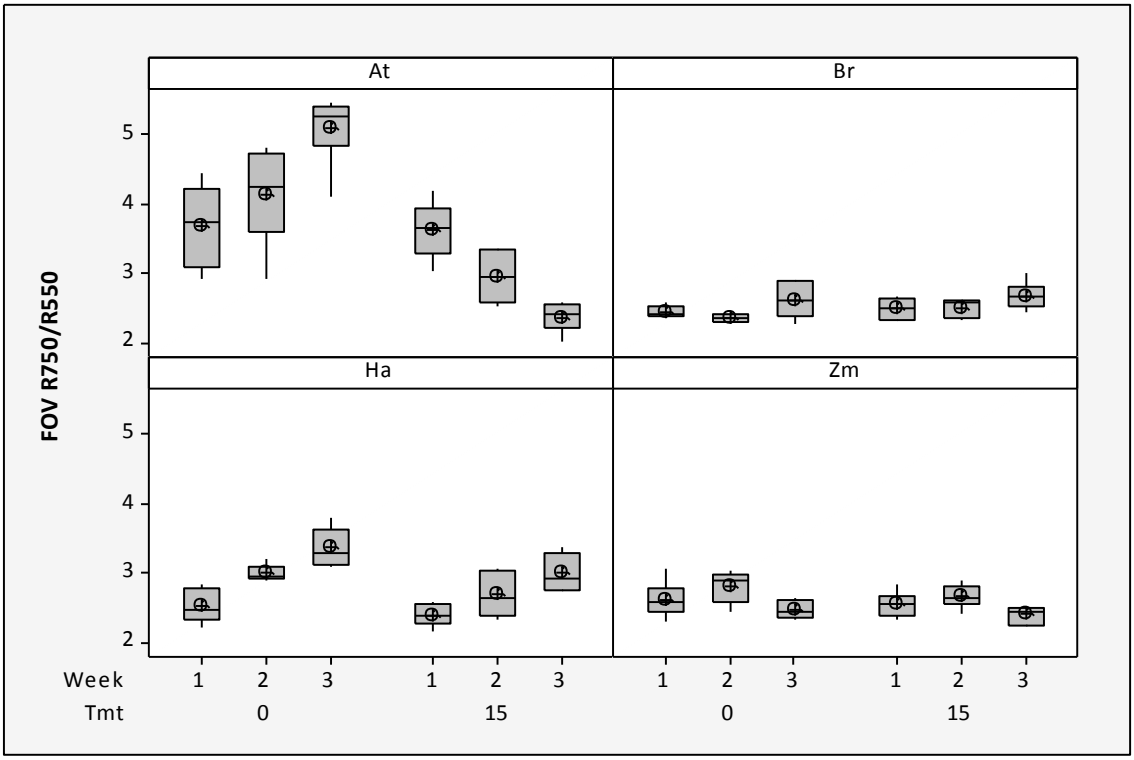

Figure B5.4: Boxplot of R_{750}/R_{550} determined by FOV for A. thaliana, B. rapa, H. annuus, and Z. mays by week and treatment level

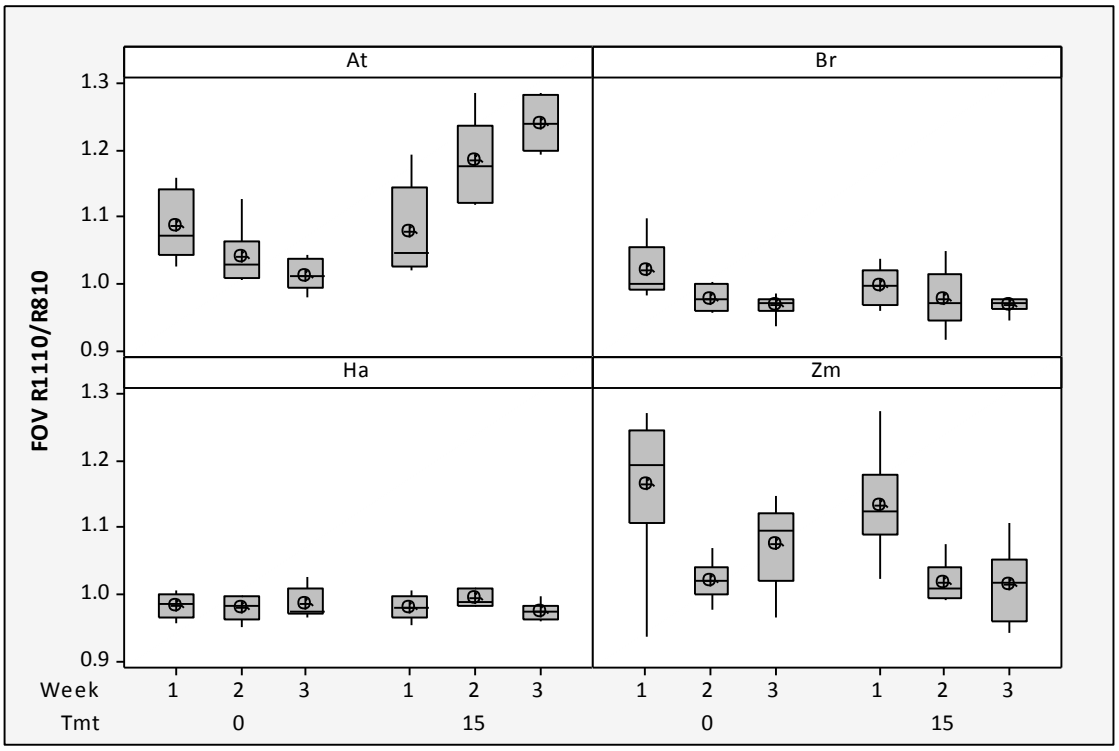

Figure B5.5: Boxplot of R_{1110}/R_{810} determined by FOV for A. thaliana, B. rapa, H. annuus, and Z. mays by week and treatment level

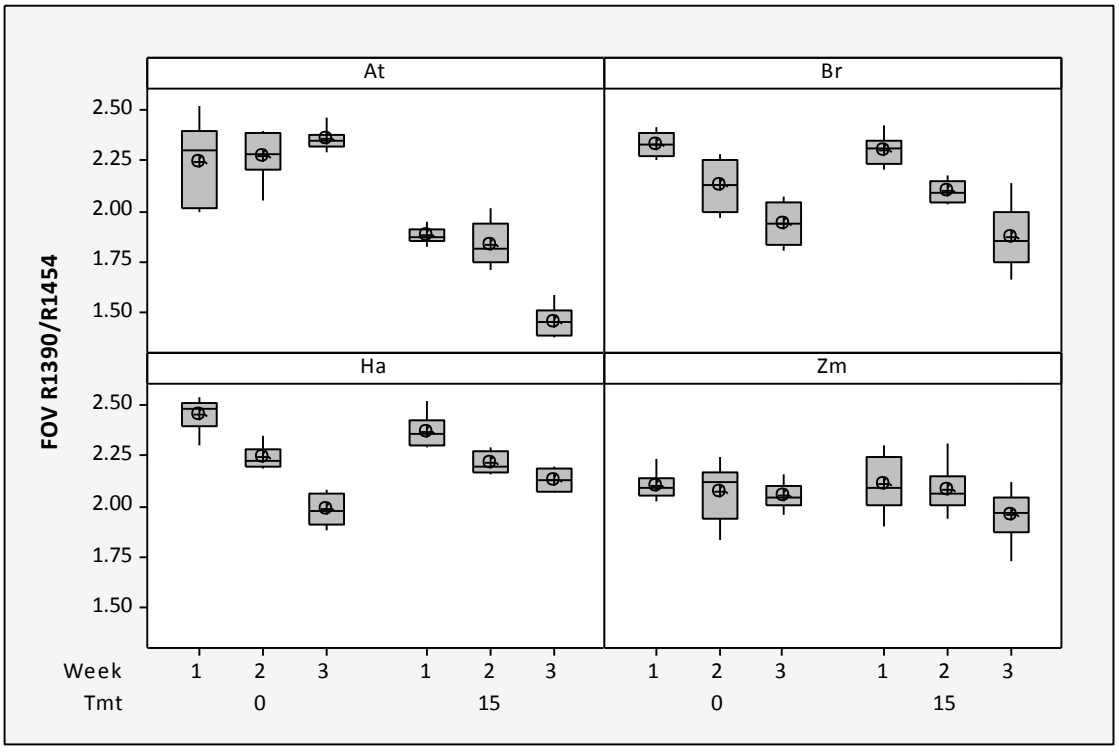

Figure B5.6: Boxplot of R_{1390}/R_{1454} determined by FOV for A. thaliana, B. rapa, H. annuus, and Z. mays by week and treatment level

2. Contact probe

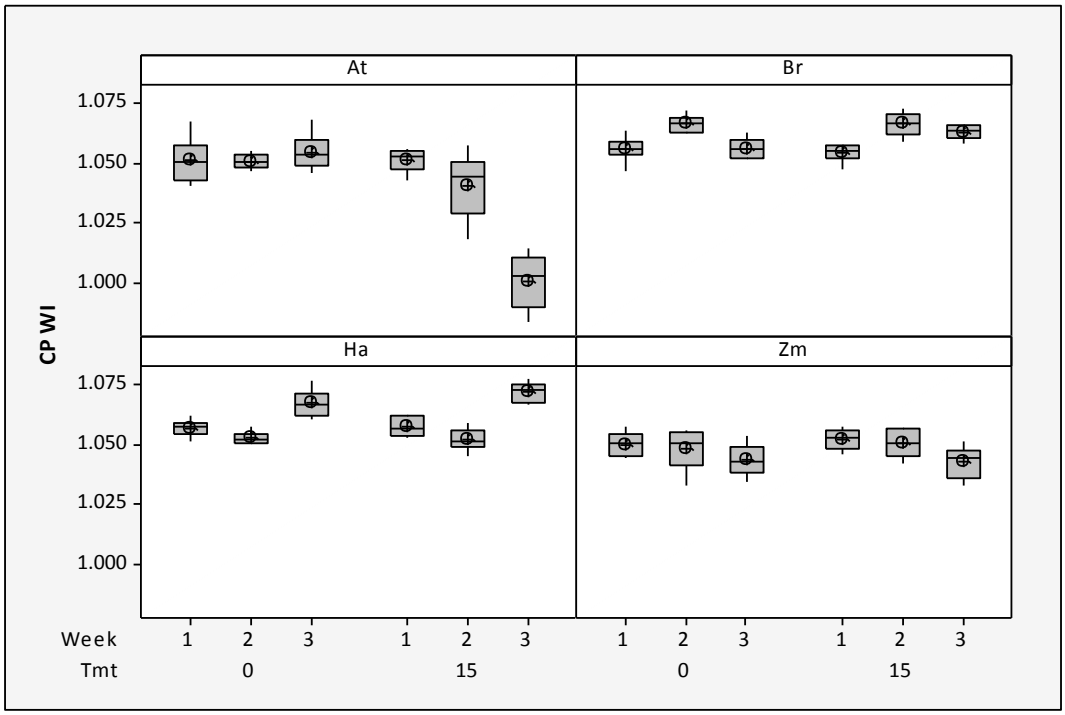

Figure B5.7: Boxplot of WI determined by CP for A. thaliana, B. rapa, H. annuus, and Z. mays by week and treatment level

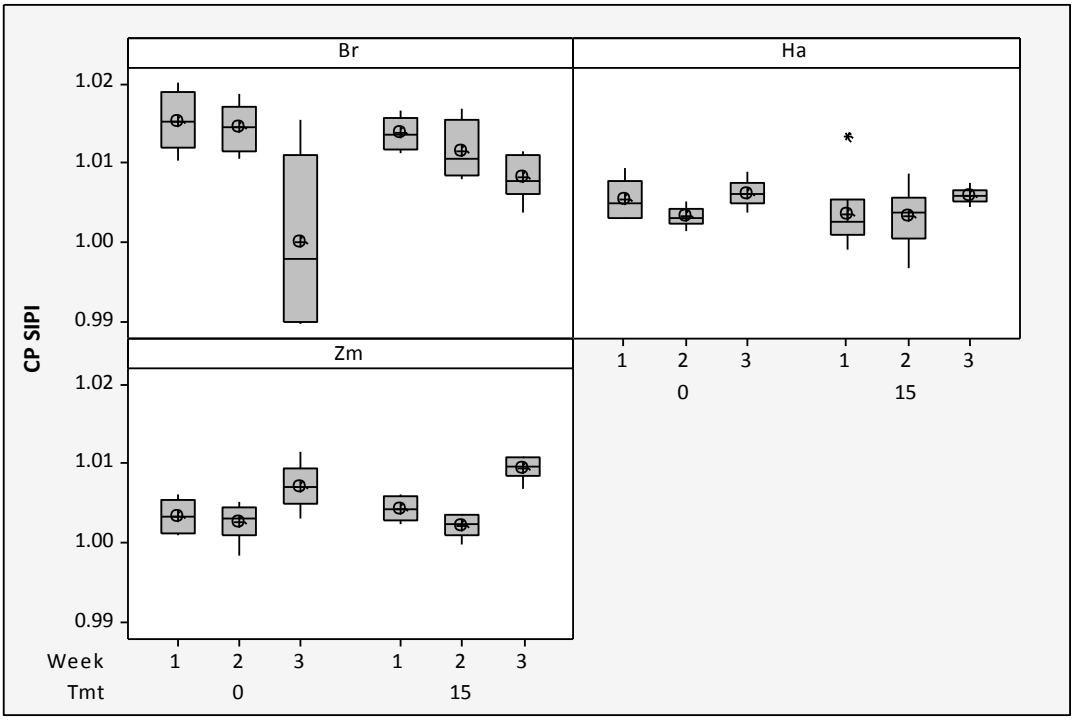

Figure B5.8: Boxplot of SIPI determined by CP for B. rapa, H. annuus, and Z. mays by week and treatment level

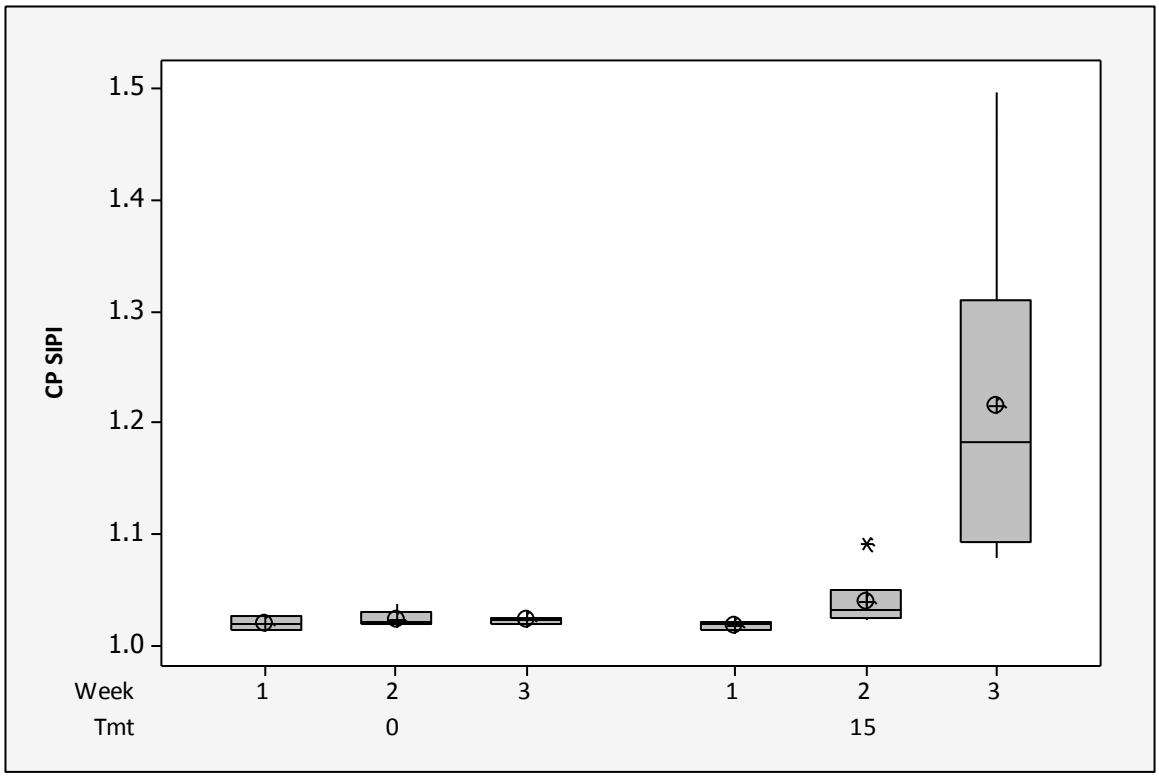

Figure B5.9: Boxplot of SIPI determined by CP for A. thaliana by week and treatment level

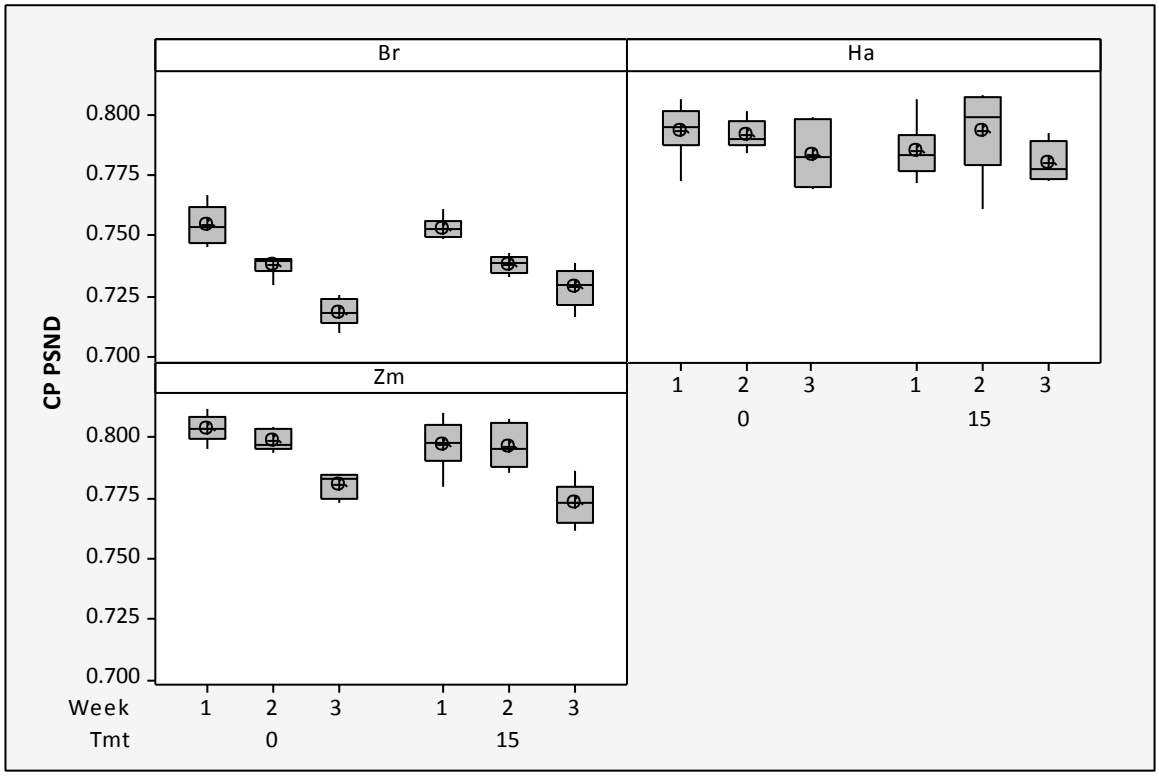

Figure B5.10: Boxplot of PSND determined by CP for B. rapa, H. annuus, and Z. mays by week and treatment level

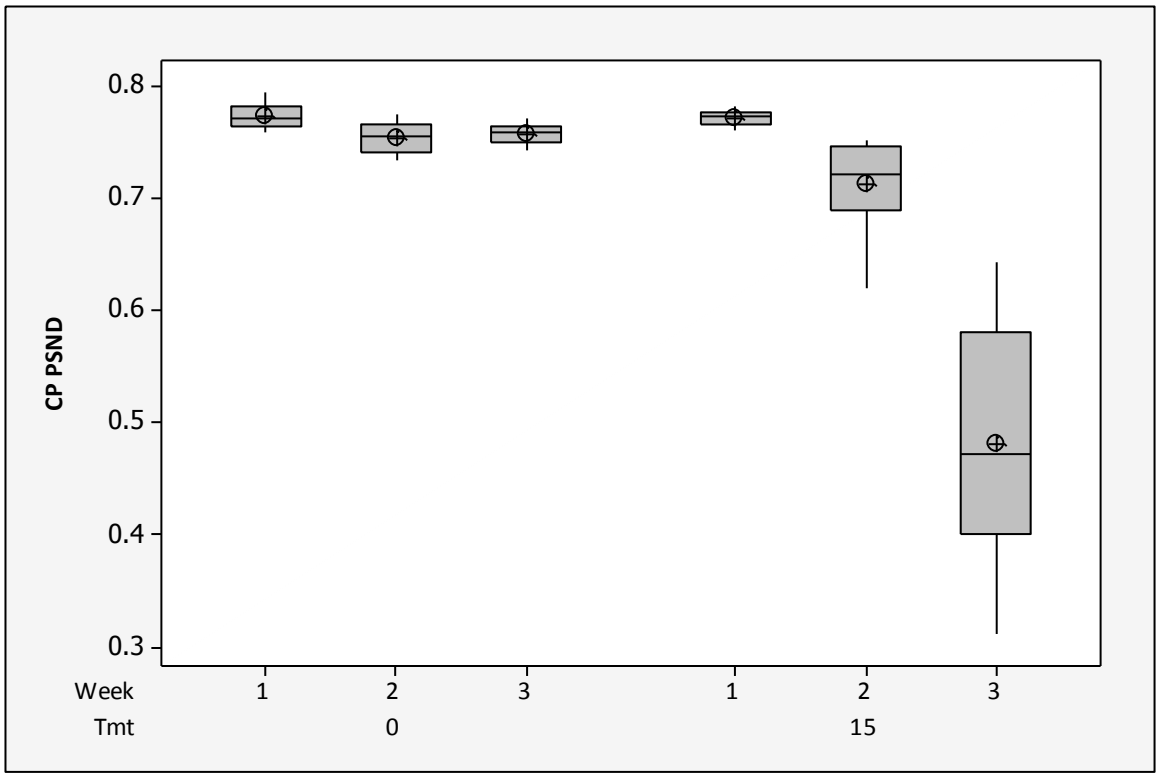

Figure B5.11: Boxplot of PSND determined by CP for A. thaliana by week and treatment level

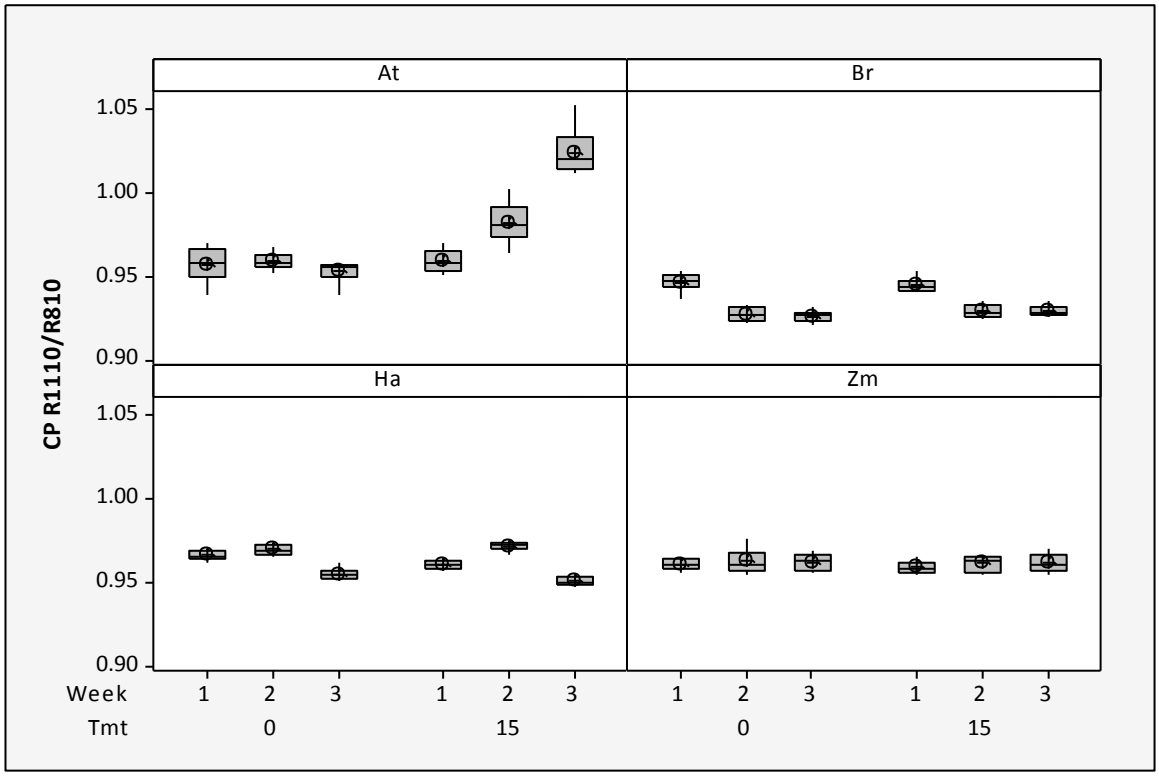

Figure B5.12: Boxplot of R_{1110}/R_{810} determined by CP for B. rapa, H. annuus, and Z. mays by week and treatment level

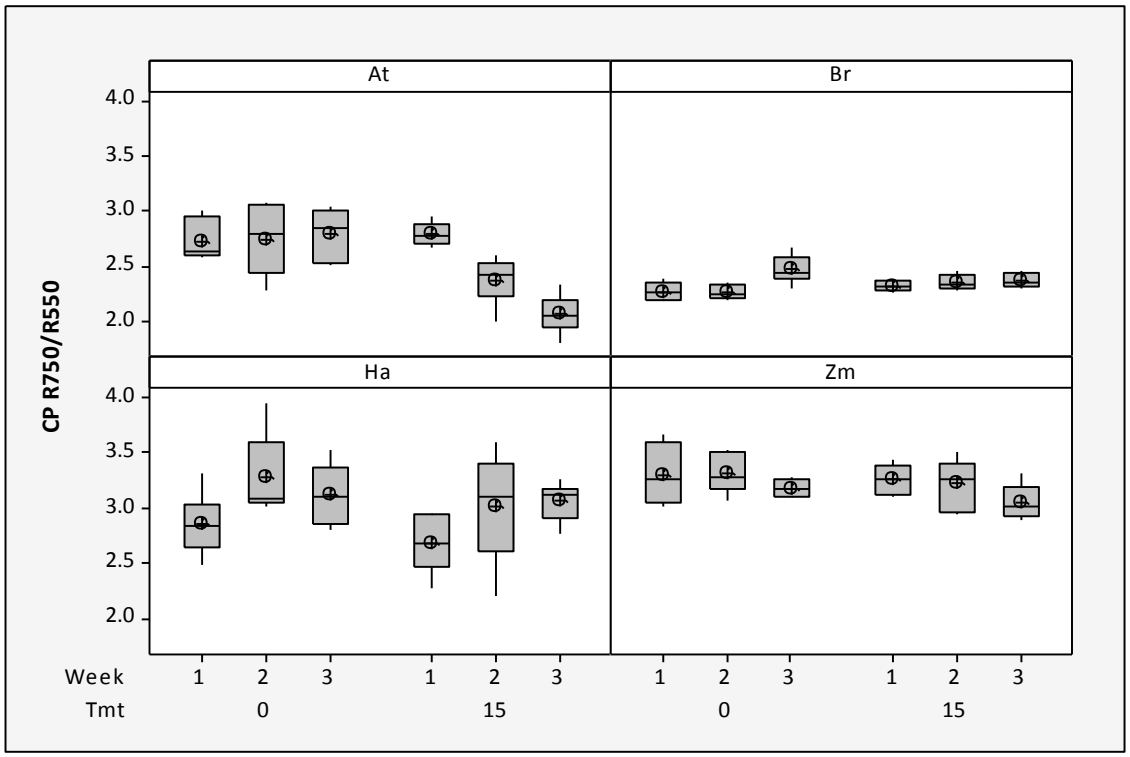

Figure B5.13: Boxplot of R_{750}/R_{625} determined by CP for B. rapa, H. annuus, and Z. mays by week and treatment level

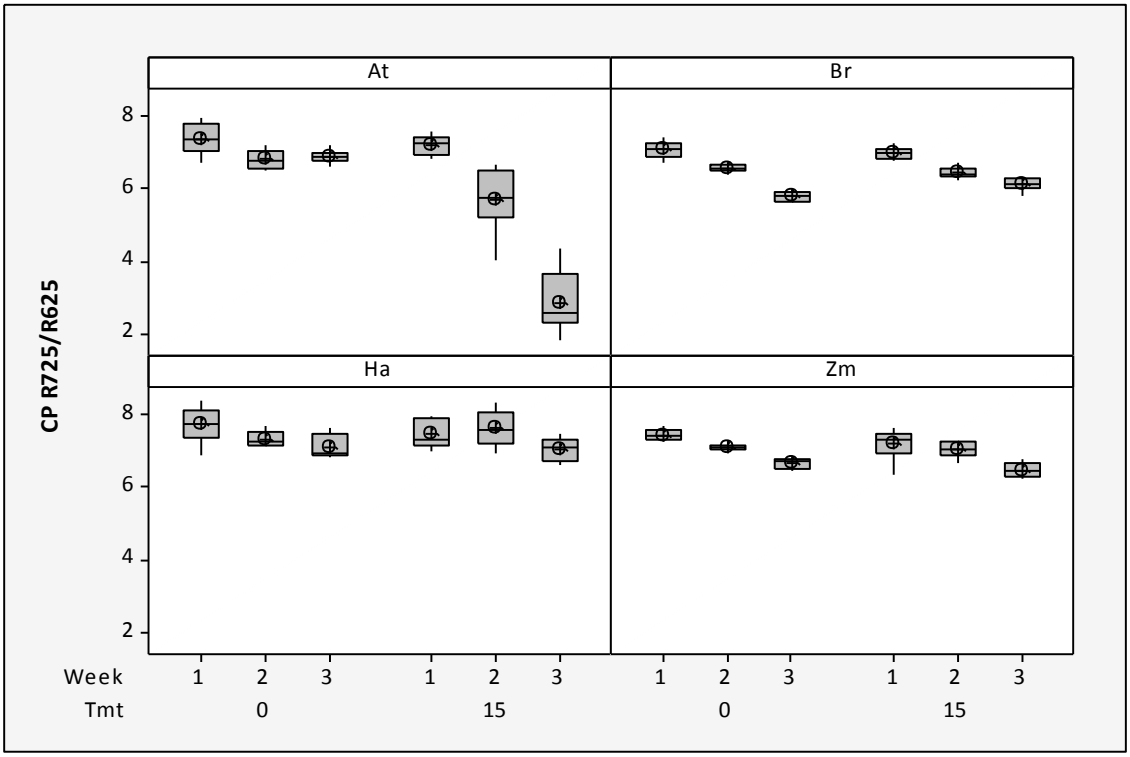

Figure B5.14: Boxplot of R_{725}/R_{625} determined by CP for B. rapa, H. annuus, and Z. mays by week and treatment level

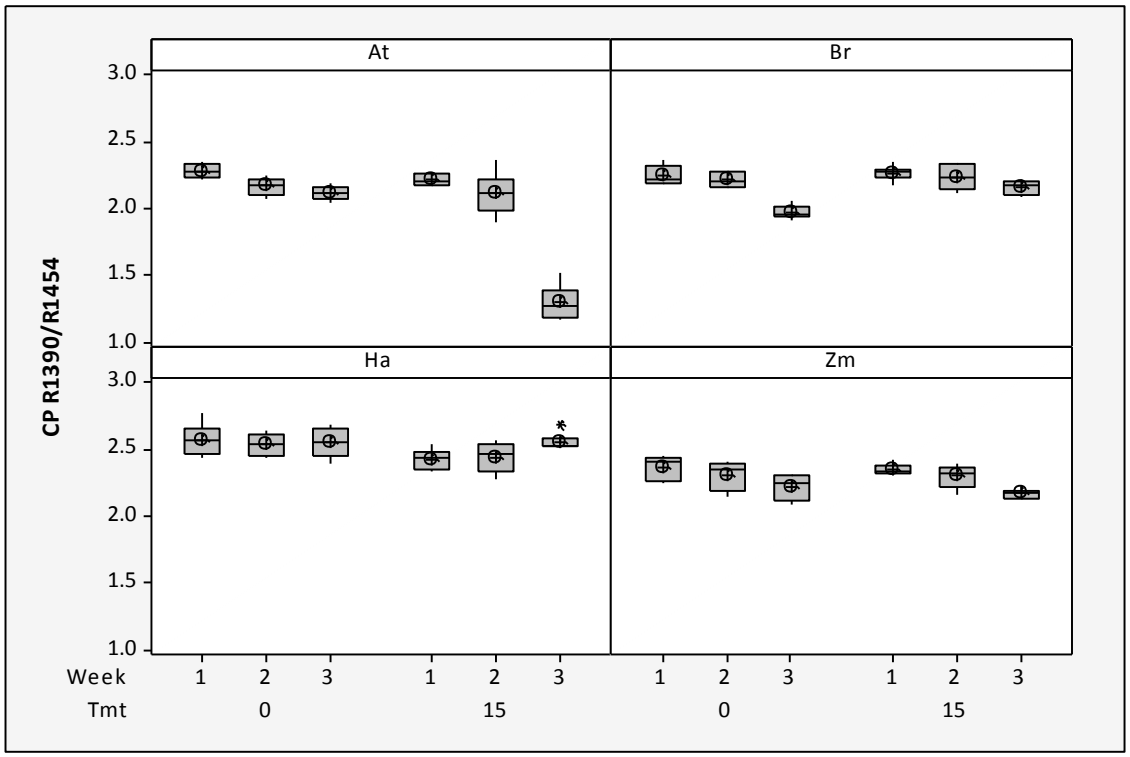

Figure B5.15: Boxplot of R_{1396}/R_{1454} determined by CP for B. rapa, H. annuus, and Z. mays by week and treatment level

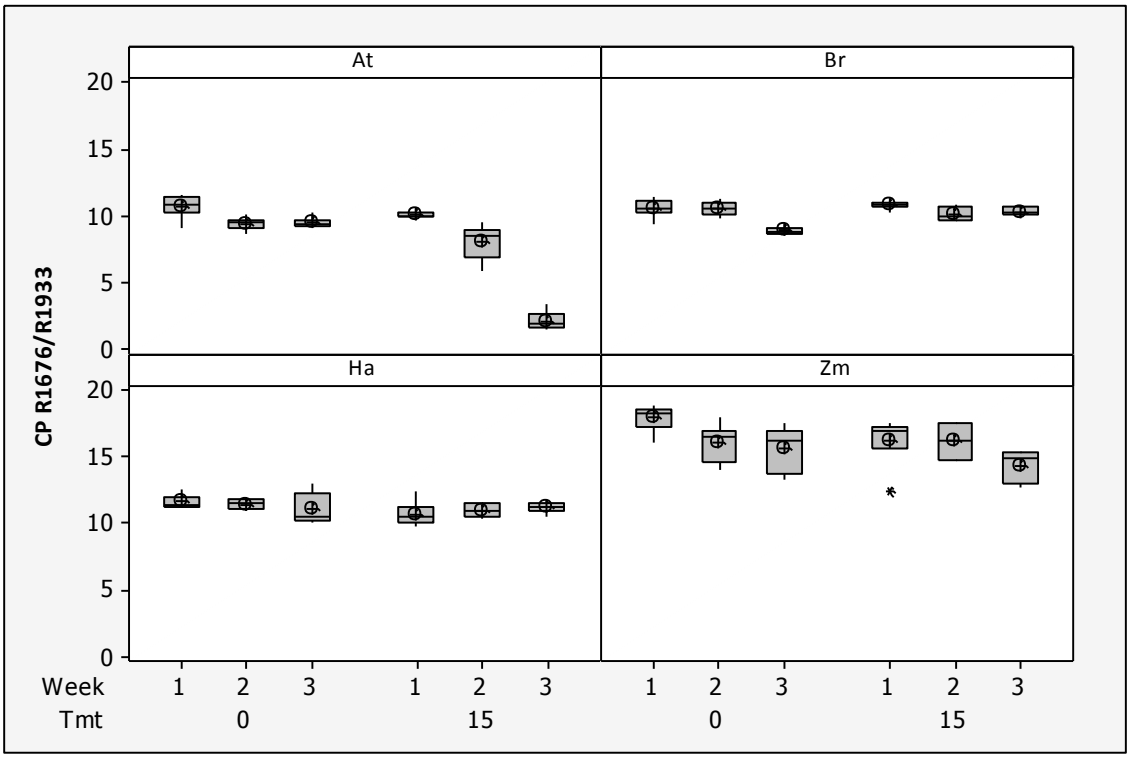

Figure B5.16: Boxplot of R_{1676}/R_{1933} determined by CP for A. thaliana, B. rapa, H. annuus, and Z. mays by week and treatment level

APPENDIX B6: DETAILS OF CHAPTER 5 ENDPOINT AND VEGETATION INDEX REGRESSIONS

Species	Regression	Regression Equation	R^2 value	P value
A. thaliana	RWC vs CP_{SIPI}	RWC = 1.87 - 0.949 CP_{SIPI}	0.512	<0.001
	RWC vs FOV_{SIPI}	RWC = 2.11 – 1.16 FOV_{SIPI}	0.911	<0.001
	CP_{SIPI} vs FOV_{SIPI}	CP_{SIPI} =0.348 + 0.656 FOV_{SIPI}	0.514	<0.001
	Chla+b vs CP_{SIPI}	Chla+b = 56.7 – 37.9 CP_{SIPI}	0.462	<0.001
	Chla+b vs FOV_{SIPI}	Chla+b = 62.8 – 42.8 FOV_{SIPI}	0.704	<0.001
H. annuus	RWC vs $FOV_{1110/810}$	RWC =0.850 + 0.0799 $FOV_{1110/810}$	0.063	0.139
	RWC vs $CP_{1110/810}$	RWC = 0.635 + 0.305 $CP_{1110/810}$	0.199	0.006
	$CP_{1110/810}$ vs $FOV_{1110/810}$	$CP_{1110/810}$ =0.919 + 0.0435 $FOV_{1110/810}$	0.009	0.587
	Chla+b vs $CP_{750/550}$	Chla+b = -5.82 + 8.85 $CP_{750/550}$	0.720	<0.001
	Chla+b vs $FOV_{750/550}$	Chla+b = 1.43 + 6.84 $FOV_{750/550}$	0.536	<0.001
	$CP_{750/550}$ vs $FOV_{750/550}$	$CP_{750/550}$ = 1.37 + 0.577 $FOV_{750/550}$	0.415	<0.001
Z. mays	RWC vs $FOV_{1390/1454}$	RWC =0.859 + 0.0250 $FOV_{1390/1454}$	0.237	0.003
	RWC vs $CP_{1390/1454}$	RWC = 0.817 + 0.0407 $CP_{1390/1454}$	0.448	<0.001
	$CP_{1390/1454}$ vs $FOV_{1390/1454}$	$CP_{1390/1454}$ = 1.31 + 0.472 $FOV_{1390/1454}$	0.313	<0.001
	Chla+b vs CP_{PSND}	Chla+b = -94.8 + 151 CP_{PSND}	0.394	<0.001
	Chla+b vs FOV_{PSND}	Chla+b = 31.0 – 9.62 FOV_{PSND}	0.033	0.286
	CP_{PSND} vs FOV_{PSND}	CP_{PSND} =0.802 - 0.0142 FOV_{PSND}	0.004	0.708
B. rapa	RWC vs $FOV_{1390/1454}$	RWC =0.757 + 0.0828 $FOV_{1390/1454}$	0.629	<0.001
	RWC vs $CP_{1390/1454}$	RWC = 0.741 + 0.0878 $CP_{1390/1454}$	0.250	0.002
	$CP_{1390/1454}$ vs $FOV_{1390/1454}$	$CP_{1390/1454}$ = 1.47 + 0.336 $FOV_{1390/1454}$	0.320	<0.001
	Chla+b vs CP_{SIPI}	Chla+b = 132 - 117 CP_{SIPI}	0.238	0.003
	Chla+b vs FOV_{SIPI}	Chla+b = 20.3 – 6.4 FOV_{SIPI}	0.003	0.769
	CP_{SIPI} vs FOV_{SIPI}	CP_{SIPI} =0.861 + 0.147 FOV_{SIPI}	0.076	0.103
All species	RWC vs CP_{SIPI}	RWC =1.90 - 0.973 CP_{SIPI}	0.537	<0.001
	RWC vs FOV_{SIPI}	RWC = 1.92 - 0.980 FOV_{SIPI}	0.782	<0.001
	CP_{SIPI} vs FOV_{SIPI}	CP_{SIPI} = 0.409 + 0.589 FOV_{SIPI}	0.499	<0.001
	Chla+b vs $CP_{1676/1933}$	Chla+b = 5.9 + 1.14 $CP_{1676/1933}$	0.502	<0.001
	Chla+b vs $FOV_{1676/1933}$	Chla+b = 15.9 + 0.319 $FOV_{1676/1933}$	0.027	0.051
	$CP_{1676/1933}$ vs $FOV_{1676/1933}$	$CP_{1676/1933}$ = 9.04 + 0.252 $FOV_{1676/1933}$	0.043	0.013
B. rapa, H. annuus, Z. mays	RWC vs $FOV_{1390/1454}$	RWC =0.815 + 0.0510 $FOV_{1390/1454}$	0.330	<0.001
	RWC vs $CP_{1390/1454}$	RWC = 0.878 + 0.0196 $CP_{1390/1454}$	0.047	0.024
	$CP_{1390/1454}$ vs $FOV_{1390/1454}$	$CP_{1390/1454}$ = 1.47 + 0.336 $FOV_{1390/1454}$	0.320	<0.001
	Chla+b vs $CP_{750/550}$	Chla+b = -10.9 + 10.7 $CP_{750/550}$	0.805	<0.001
	Chla+b vs $FOV_{750/550}$	Chla+b = 1.14 + 7.02 $FOV_{750/550}$	0.170	<0.001
	$CP_{750/550}$ vs $FOV_{750/550}$	$CP_{750/550}$ = 1.03 + 0.692 $FOV_{750/550}$	0.236	<0.001